

Vitaly Adushkin
Ivan Nemchinov
Editors

Catastrophic Events Caused by Cosmic Objects



Springer

CATASTROPHIC EVENTS CAUSED BY COSMIC OBJECTS

Catastrophic Events Caused by Cosmic Objects

Edited by

VITALY ADUSHKIN

*Institute for Dynamics of Geospheres,
Russian Academy of Sciences, Moscow, Russia*

and

IVAN NEMCHINOV

*Institute for Dynamics of Geospheres,
Russian Academy of Sciences, Moscow, Russia*

 Springer

A C.I.P. Catalogue record for this book is available from the Library of Congress.

ISBN 978-1-4020-6451-7 (HB)

ISBN 978-1-4020-6452-4 (e-book)

Published by Springer,

P.O. Box 17, 3300 AA Dordrecht, The Netherlands.

www.springer.com

Book cover: Our planet experienced many impacts during its evolution. The impact of a large asteroid is shown. If such an asteroid would hit the Earth nowadays, mankind would perish.

This is an extended and updated version and translation of the original work in Russian “Catastrophicheskie vozdeystviya kosmicheskikh tel”, published by the Commercial Publishing Centre “Academkniga”, 2005.

The English edition contains a revised Chapter 1 and new results have been added to Chapter 10.

Printed on acid-free paper

All Rights Reserved

© 2008 Springer

No part of this work may be reproduced, stored in a retrieval system, or transmitted in any form or by any means, electronic, mechanical, photocopying, microfilming, recording or otherwise, without written permission from the Publisher, with the exception of any material supplied specifically for the purpose of being entered and executed on a computer system, for exclusive use by the purchaser of the work.

TABLE OF CONTENTS

Preface	vii
Acknowledgments	ix
List of Contributors	xi
1. Main Factors of Hazards Due to Comets and Asteroids <i>Ivan Nemchinov, Valery Shuvalov and Vladimir Svetsov</i>	1
2. Size-Frequency Distribution of Asteroids and Impact Craters: Estimates of Impact Rate <i>Boris Ivanov</i>	91
3. Cometary Hazards <i>Marina Kuzmitcheva and Boris Ivanov</i>	117
4. Bolides in the Earth Atmosphere <i>Olga Popova and Ivan Nemchinov</i>	131
5. Geologic Effects of Large Terrestrial Impact Crater Formation <i>Boris Ivanov</i>	163
6. Thermal Radiation and Fires after Impacts of Cosmic Objects <i>Vladimir Svetsov</i>	207
7. Tunguska Catastrophe of 30 June 1908 <i>Vladimir Svetsov and Valery Shuvalov</i>	227
8. High-Velocity Impact Ejecta: Tektites and Martian Meteorites <i>Natalia Artemieva</i>	267
9. Marine Target Impacts <i>Valery Shuvalov, Irina Trubetskaya and Natalia Artemieva</i>	291

10. Ionospheric and Magnetospheric Effect	313
<i>Ivan Nemchinov, Valery Shuvalov, Aleksey Kovalev, Igor Kosarev and Yulius Zetzer</i>	
11. Impacts and Evolution of Early Earth	333
<i>Galina Pechernikova and Andrei Vityazev</i>	
Index	351

PREFACE

Butterflies that live for only a day in the warmth of summer know nothing of the cold of night, let alone the driving rain of autumn or the winter frost. In the same way humankind has been ignorant of the cataclysms in the early biosphere and geosphere caused by the impacts of large asteroidal bodies millions of years before the first *Homo sapiens*. In recent times, however, overwhelming evidence has shown that impact catastrophe played a major role in the evolution of Earth and life, and that the hazard posed by the collision of asteroids and comets also exists today.

During recent years, national and international science programs have examined the evidence of impact consequences in the remote past and modeled the potential consequences of impacts in the near future. This book is a revised translation of an original publication, printed in Russia in 2005, documenting research on the environmental consequences of impacts by scientists from Institute of Dynamics of Geospheres of the Russian Academy of Sciences. The work is a result of focused investigations during the last 15 years, supported by Russian and foreign grants. Some of the material contained within this book has been reported at international conferences and published in journals; however, some of these results is unknown to English-speaking readers. This book is aimed to fill this gap.

We think that the chapters written by Russian experts in various aspects of the new science of impacts of cosmic bodies will be of great interest to the broad spectrum of researchers working in different fields of Earth and space science. Being written at a level understandable to astrophysicists and geophysicists, geologists, geochemists, and biologists, the book will be useful both to experts and students just entering the field.

The book is organized and written so that, having familiarized themselves with the preface and Table of Contents, the readers can address each chapter independently of the others. Each chapter contains the appropriate references to the main previous work in a particular science and possible connections to neighboring fields.

ACKNOWLEDGMENTS

The authors are grateful to their Russian and foreign colleagues who participated in various stages of joint studies, kindly helped, and strongly (but always constructively) criticized our results. We thank J. Borovička, A.P. Boss, J.A. Burns, Z. Ceplecha, H. Dypvik, R. Gersonde, W. Hartmann, C. Koeberl, E.M. Kolesnikov, E. Levy, M. Lindström, J. Lunine, H.J. Melosh, B. Milkereit, G. Neukum, L. Nyquist, U. Reimold, R. Spalding, P. Spurný, D. Stöffler, A. Teterov, N.V. Vasilyev, S.J. Weidenschilling, and G.W. Wetherill.

We thank V.V. Novikova, L.M. Beletskaya, L.A. Kiryushkina, and L.P. Markelova for their help in preparing the manuscript for publication.

LIST OF CONTRIBUTORS

ADDRESS FOR ALL CONTRIBUTORS:

Institute for Dynamics of Geospheres,
Russian Academy of Sciences,
38 Leninsky Prosp., bldg. 1,
Moscow 119334, Russia
Fax: (495)137-65-11

PERSONAL CONTACT INFORMATION:

Vitaly Adushkin
adushkin@idg.chph.ras.ru

Galina Pechernikova
pechernikova@idg.chph.ras.ru

Natalia Artemieva
artemeva@psi.edu

Olga Popova
olga@idg.chph.ras.ru

Boris Ivanov
baivanov@idg.chph.ras.ru

Valery Shuvalov
shuvalov@idg.chph.ras.ru

Igor Kosarev
kosarev@idg.chph.ras.ru

Vladimir Svetsov
svetsov@idg.chph.ras.ru

Aleksey Kovalev
akoval@idg.chph.ras.ru

Irina Trubetskaya
trub@idg.chph.ras.ru

Marina Kuzmitcheva
kuzm@idg.chph.ras.ru

Andrei Vityazev
avit@idg.chph.ras.ru

Ivan Nemchinov
ivvan@idg.chph.ras.ru

Yulius Zetzer
zetzer@idg.chph.ras.ru

CHAPTER 2

SIZE-FREQUENCY DISTRIBUTION OF ASTEROIDS AND IMPACT CRATERS: ESTIMATES OF IMPACT RATE

BORIS IVANOV

*Institute for Dynamics of Geospheres, Russian Academy of Sciences, Moscow 119334, Russia
E-mail: baivanov@idg.chph.ras.ru*

Abstract: The size-frequency distribution (SFD) of small bodies in the Solar System provides an important insight into the origin and evolution of these bodies. Main members of the small-body population are asteroids and comets. The direct way to determine small bodies' SFD is direct optical and radar observations. However, the long distance to a telescope, typically based on Earth, puts severe restrictions on the completeness of observations when asteroids smaller than ~ 10 km in the Main Belt and smaller than ~ 1 km in the near-Earth asteroid (NEA) population are counted (Ivezic et al. 2001; Stuart 2001). SFD of Jupiter-family (JF) comets and long-periodic (LP) comets are known approximately due to the presence of coma at small heliocentric distances and relatively small statistics of observations (Tancredi et al. 2000; see also Chap. 3).

1 INTRODUCTION AND BASIC TERMINOLOGY

The technique that is complementary to direct telescopic observations is the measurement of impact craters' SFDs that are formed on planetary surfaces by impacts of asteroids and comets. This technique is an indirect one, demanding knowledge of the scaling laws needed to relate sizes of bodies, created impact craters, projectiles, and sizes of the craters formed. Moreover, one should know (or assume) the velocity spectrum of impacts at a planet of interest (a target), related to population of different orbits. (The impact velocity depends on orbital parameters such as semi-major axis, eccentricity, and orbit inclination.) The next specific feature is that a finite time period is needed to accumulate an appreciative amount of impact craters at the surface of interest. For enough large craters (diameter D of $n \times 10$ and $n \times 100$ km) the accumulation time of a statistically meaningful number of craters extends to 10^5 to 10^6 years. Consequently, observed SFD of craters present relationships averaged over historically long time periods, which is important if the projectile SFD may vary in time. That is why the

“crater count” technique in application to small-body SFD restoration should be applied with caution, comparing results with direct observations as completely as is possible today.

The presented review analyzes and compares “crater count”-based SFD and recent observational data on Main Belt asteroids and NEA. One unavoidable assumption is that the cometary input into the cratering history is relatively small ($\sim 15\%$ and less) for terrestrial planets. (The reciprocal statement is valid for satellites of outer planets.) However, from the SFD point of view more exact estimates should be postponed before much larger statistics on comet sizes are accumulated (Rickman et al. 2001).

Leaving the Main Belt, asteroids may hit the Sun, be ejected beyond the terrestrial planet region, or form impact craters on the surface of planetary bodies (including other asteroids). The population of impact craters has been studied to date on Mercury, Venus, Earth, the Moon, Mars, Martian satellites, and a few asteroids (Gaspra, Ida, Mathilde, Eros, and Itokawa), and possibly the nuclei of a couple of comets. (Borelly and Wild 2 provided counted features that are remnants of impact craters.) The relative age of planetary surfaces may be estimated by counting the number of impact craters of a given size, accumulated per unit surface area. (Younger surfaces accumulate fewer craters than older ones.) Absolute interplanetary dating is possible provided one knows the bombardment flux, impact conditions, and scaling laws to calculate comparative crater diameter on different planets for a fixed projectile size.

Problems of crater-based surface dating are discussed in detail in the fundamental publication of Basaltic Volcanism project (Hartmann et al. 1981) and in recent reviews (Hartmann and Neukum 2001; Ivanov et al. 2001; Neukum et al. 2001b). In addition to comparative model “cratering” ages study of impact crater population allows investigators to reconstruct the so-called production function, which is a replica of SFD of projectiles, not yet changed by planetary resurfacings and mutual impact crater overlapping. (The former are often named as “saturation equilibrium” observed for small craters on the oldest exposed planetary surfaces.) The observed crater SFD may be compared with a potential projectile SFD, giving an insight into the evolution of small bodies and planets in the Solar System. In some ancient planetary areas the cratering chronology may be traced back to an era of late heavy bombardment (3.3 to ~ 4 Ga ago), now hidden in terrestrial geologic records.

Impact craters observed on planetary surfaces are created by a few distinct families of celestial small bodies (projectiles). The main projectile families include asteroids evolved from Main Belt orbits, Jupiter family comets (JFC) visiting the inner Solar System from the trans-Neptunian region (named Kuiper or Kuiper-Edward belt), and LP comets, dropped out from the remote Oort comet cloud (Morrison et al. 2002; Weissman et al. 2002). Two other projectile families that are less important for terrestrial planets are Trojan asteroids (occupying Lagrange points in the Jovian orbit) and Halley-type comets. All these families have different

probabilities of collision and different spectra of possible impact velocities as they rotate around the Sun in different orbits.

Small bodies in each family listed in the preceding have survived or have been produced in the course of their collision evolution. As a result, the size-frequency distribution of bodies in each family can be different.

Dynamic models of small-body orbital evolution together with the permanently expanding volume of astronomical observations of small bodies allow investigators to create a kind of knowledge database to constrain possible projectile family parameters. Bottke et al. (2002) demonstrated that Main Belt asteroids having initial orbits with $a > 2.4$ AU are the most probable source of planetary crossers, responsible for $>90\%$ of impact craters now visible on terrestrial planets. The exact fraction number of craters created by LP comets is not very well understood (Weissman et al. 2002). Jupiter family comets are not numerous enough to compete in the cratering rate of terrestrial planets. (On satellites of giant planets JFC are now believed to be the main crater-forming family of small bodies.) For reasons discussed later one can make a trial comparison of cratering records on terrestrial planets assuming temporarily that asteroids are the main family of crater-forming projectiles.

2 LUNAR PRODUCTION FUNCTION

The Moon is the main test site to study the impact crater chronology. Active volcanic activity ended in most areas >3 Ga ago (with the exception of small possibly younger basaltic lava flows; Hiesinger et al. 2000). During the last 3 Ga the lunar surface has been modified by newly formed impact craters. The moon was relatively well studied during the Apollo and Luna space missions. Lunar rock samples returned to Earth provide a unique opportunity to correlate the number of craters, accumulated in the vicinity of sampling sites, and isotopic ages of rocks (Neukum et al. 2001a; Stöffler and Ryder 2001). Hence, one can estimate the rate of cratering on the moon; i.e., the number of impact craters accumulated on a unit area per unit of time.

Figure 1 demonstrates the correlation between number of counted craters with diameters >1 km per unit area $N(1)$ and the measured age of lunar rocks. The main features here are: (1) approximately linear growth of $N(1)$ with surface age up to ~ 3 Ga, and (2) the exponentially increased cratering rate for older surfaces. This period of recorded high impact rate on the young moon is often called the late heavy bombardment (LHB) period. (See Hartmann et al., 2002, for the history of this term and hypothesis of the LHB nature.) Neukum (1983) proposed to present the cratering rate decay in time in the form of the equation for the number of impact craters accumulated at the surface of the age T . Expressing the number of craters through the point $N(D = 1 \text{ km})$ one can write this Equation as:

$$N(1) = 5.44 \times 10^{-14} (e^{6.93T} - 1) + 8.38 \times 10^{-4} T \quad (1)$$

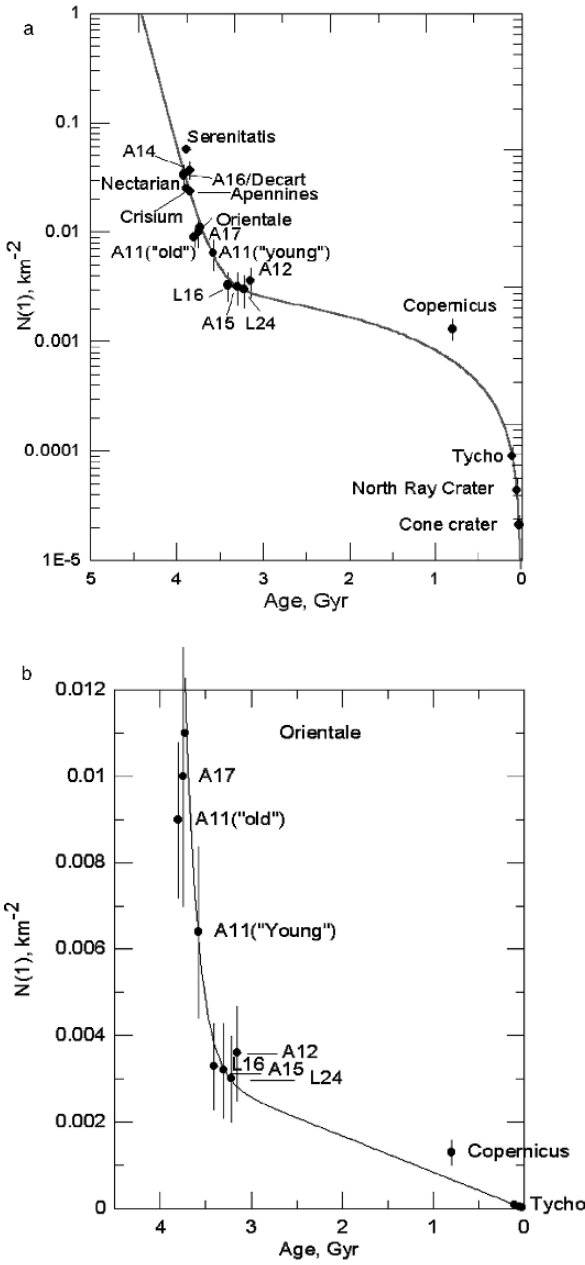


Figure 1. The number of craters with $D > 1$ km, formed in given areas with various age. (a) semi-logarithm coordinates, (b) the part of data in linear scales for both axis. The black curve is constructed with the Equation (1). Reprinted from Neukum et al. (2001a) with permission from Springer

where $N(1)$ is the crossing point of the $N(D)$ curve with the $D = 1$ km axis, normalized per area of crater counting (in km^2), and T is the age of surface in billions of years (Ga).

The modern ($T < 3$ Ga) constant flux is believed to be mainly the flux of Moon-crossers, derived from the Main Belt of asteroids. The nature of the enhanced ancient (LHB) flux ($T > 3.3$ Ga) is still under discussion. Most probable hypotheses include (Hartmann 2002; Gomes et al. 2005):

- The remnants (“leftovers”) of planetesimals not incorporated into planets before their differentiation and crust formation (now of concern; Bottke et al. 2006)
- The flux of comets from the formation zone of Neptune and Uranus
- The flux of asteroids from the ancient asteroid belt due to the migration of the orbits of Jupiter and Saturn ~ 0.5 Ga after the Solar System formed.

As illustrated in the following, observed impact craters allow investigators to conclude that LHB projectiles have an SFD similar to the modern asteroid belt. Hence, one can assume that LHB bodies have experienced a similar collision evolution as asteroids.

To study SFD of planetary impact craters quantitatively, one can introduce the so-called production function (PF). The PF is the SFD of craters that would be observed at the once completely renovated (erased) planetary surface before the area was saturated with impact craters. (Saturation or equilibrium area density impact craters are observed in old planetary surfaces, when each newly formed crater destroys one or several previously formed craters. On lunar maria the equilibrium state is observed for craters $< 200\text{--}300$ m in diameter.) The PF in the whole range of possible impact crater diameters rarely may be observed because of the different geologic histories of different planetary areas. However, the PF may be restored piece by piece by combining data for large craters in the oldest areas and smaller craters in the younger areas. Here the PF is illustrated using two mostly detailed approaches, by W. Hartmann and G. Neukum (see Neukum et al. 2001a for a review).

In the early days of lunar crater counting (Öpik 1960) researchers used telescopic observations of the near side of the moon. Observations allowed them to count craters $> 5\text{--}10$ km in diameter. It was found that craters have an SFD close to the power law $N(> D) \sim D^{-2}$. Later, spacecraft images of the lunar surface enabled researchers to count impact craters as small as 10 m in diameter. After a few years of discussions about the best applicable power law, after more data had been accumulated, it was recognized that the lunar crater PF is not a simple power law, where in all craters the diameter range would have SFD presented in the form $N(> D) \sim D^{-m}$. Thorough analysis of telescopic data (Chapman and Haefner 1967) has shown that the local slope of the SFD curve (the derivative $d\log N/d\log D$) varies with the crater size. Later Shoemaker (1965) found from high-resolution spacecraft images that small craters have steeper SFD than large craters, $N(> D) \sim D^{-2.9}$. Different researchers have used different approximations to take into account the “wavy” nature of the impact crater SFD, undulating around the general trend; in any surface small craters are less numerous than larger craters.

Observed impact crater SFDs on various planets are similar in their main details to a crater population produced by the modern asteroids leaving the Main Belt. Just as the early Solar System could have different small body populations, it can be proved that these ancient populations also experienced some collision evolution, but it cannot be proved that the Main Belt asteroids were the main populations during the LHB period.

Separated impact crater counts in various size ranges may be generalized as a universal relation, the PF. Production function is defined as the impact crater SFD accumulated on an ideal planetary surface once obliterated and preserved all impact craters formed after the starting obliteration event (e.g., lava flow deposition, the floor of a large crater, and its continuous ejecta zone). The real cratering records may be quite different from the ideal PF due to a set of surface processes, individual for each terrestrial planetary body.

There is no general agreement yet about the detailed structure of the production function on terrestrial planets. However, all proposed PFs are similar in their main features. The following illustrates the issue of PF construction with the most widely cited PFs proposed by W. Hartmann and G. Neukum (see the review by Neukum et al. 2001a).

2.1 Hartmann Production Function (HPF)

HPF has been designated as a table of $N(D)$ data, selected by W. Hartmann from many sources to present $N(D)$ dependence for an average lunar mare surface. Here the resurfacing event, erasing the surface, is assumed to be the mare basalt emplacement. It was believed that the time period of basalt emplacement was short in comparison with the whole geologic history of the moon (as measured from returned lunar basalt samples; Stöffler and Ryder 2001).

Recent papers about photogeologic analysis of nonsampled lunar basalt flows (Hiesinger et al. 2000, 2003) estimate the relative area of younger and older flows of mare basalts. Figure 2 illustrates the age distribution model of mare basalt (Hiesinger et al. 2003). One can see that visible volcanic activity in some areas could have ended as recently as 1.5 Ga ago. However, the median age of basalt flows is about 3.4 Ga. About 60% of visible mare surfaces were covered by basalts; the model age was ~ 2.8 to ~ 3.5 Ga. According to the modeled accumulation rate of impact craters (Fig. 1) one can assume that looking back in time during this basalt emplacement period, the number of craters increased from a factor 0.65 to 1.35 relative to the number of accumulated craters with a median surface age of 3.4 Ga. Hence, the accuracy (synchrony) of HPF values, combined areas with a slightly different age, may be estimated as a factor of 1.35.

Original HPF is presented in a so-called incremental form. It represents the number of counted craters normalized to 1 km^2 , N_H , with diameters in the diameter bin interval $D_L < D < D_R$, where D_L and D_R are left and right bin boundaries, and $D_R/D_L = 2^{1/2}$. The right boundary of one interval is equal to the left boundary of the next diameter bin (going from smaller to larger diameters). The data can be plotted

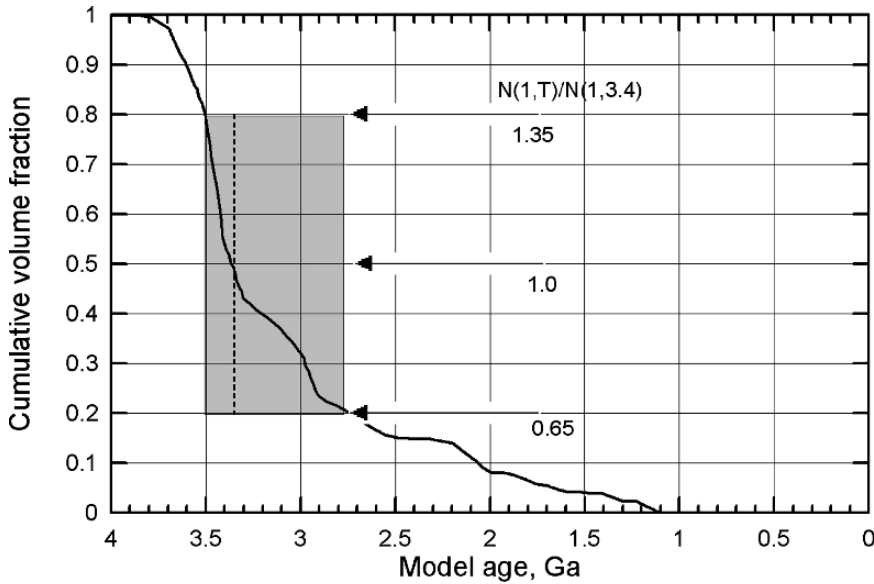


Figure 2. Relative fraction of lunar mare surface covered with basalts of various ages (Hiesinger et al. 2003)

versus the geometric average of the bin boundary values $D_{av} = (D_L \times D_R)^{1/2}$. Graphic representation of the latest version of the HPF (Hartmann 2005) is presented in Fig. 3a.

In Fig. 3a one can see that the number of craters per bin varies 8 to 10 orders of magnitude for the whole range of crater diameters. The crater-counting community has proposed a standard way to present the data in a relative form (R-plot), where the original data are normalized to a power law function $\sim D^{-3}$. It helps to decrease the vertical range of plotted values. The standard definition of R is as follows

$$R(D_{av}) = D_{av}^3 N_H / (D_R - D_L) \tag{2}$$

Here the differential number of craters ($\Delta N / \Delta D$) is multiplied by a “streamline” function, D_{av}^3 . Hence, the R -representation of the SFD presents the deviation of the differential SFD of the simple unique power law. If the differential number of craters, $\Delta N / \Delta D$, decreases with the crater diameter as D^{-3} , it is represented in the R -plot by a horizontal line of a constant R -value. SFD, steeper than D^{-3} , is a decreasing function in the R -plot, and SFD, less steep than D^{-3} , is an increasing function in the R -plot. This is demonstrated in Fig. 3b for the HPF. In the following, $D \approx 300$ m, the HPF, describes an equilibrium state of small craters on mare surfaces, the interval $300 \text{ m} < D < 1.4 \text{ km}$ HPF in the R -plot is a decreasing function, and in the range $1.4 \text{ km} < D < 64 \text{ km}$ the R -plot for HPF is an increasing function of D .

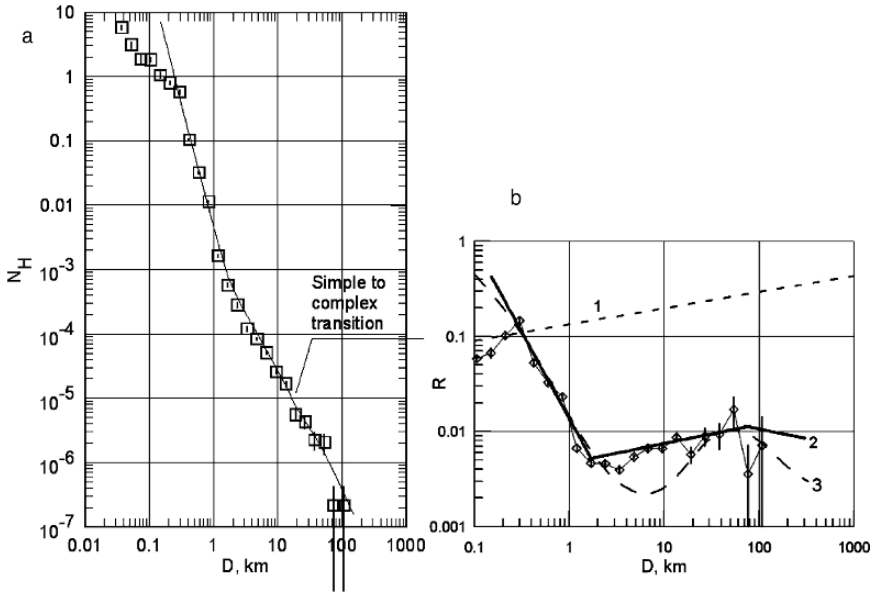


Figure 3. Hartmann’s Production Function (HPF) in the incremental form (a) and R-plot (b) is shown as tabulated data points (squares). Thick lines corresponds to the piece-wise power law representation (Equation 3), dashed curve in (b) presents here for comparison Neukum’s Production Function, discussed later in this chapter. Dashed line 1 in (b) corresponds to the “empirical saturation” SFD, proposed by Hartmann (1984). Reprinted from Neukum et al. (2001a) with permission from Springer

To work logically with HPF, Hartmann (2005; see also Ivanov et al. 2001) proposes piece-wise exponential relations, which use 10-base logarithms:

$$\log N_H = -2.616 - 3.82 \log D_L, 0.3\text{km} < D < 1.41\text{km} \tag{3}$$

$$\log N_H = -2.920 - 1.80 \log D_L, 1.41\text{km} < D < 64\text{km} \tag{4}$$

$$\log N_H = -2.198 - 2.20 \log D_L, D > 64\text{km} \tag{5}$$

For $D < 0.3$ km lunar mare craters are in equilibrium, and the HPF should be assumed from data for younger surfaces, where small craters have not reached yet saturated area density (Hartmann 2005). Graphic representation of Equations (3)-(5) is shown in Fig. 3.

2.2 Neukums’ Production Function (NPF)

Following the idea of Chapman and Haefner (1967) about the variation of the local SFD slope depending of the crater diameter range, G. Neukum (1983; see also

Table 1. Coefficients for Equation (6)

a_i	“Old” $N(D)$ (Neukum 1983)	“New” $N(D)$ (Neukum et al 2001a)	Coefficient “sensitivity”*	$R(D_p)$ (this work)**
a_0	-3.0768	-3.0876		+2.906
a_1	-3.6269	-3.557528	$\pm 3.8\%$	+0.5376
a_2	+0.4366	+0.781027	$\pm 3.9\%$	+0.8392
a_3	+0.7935	+1.021521	$\pm 2.5\%$	-0.4390
a_4	+0.0865	-0.156012	$\pm 1.6\%$	-2.1581
a_5	-0.2649	-0.444058	$\pm 0.88\%$	-0.5956
a_6	-0.0664	+0.019977	$\pm 1.3\%$	+1.9629
a_7	+0.0379	+0.086850	$\pm 0.78\%$	+1.0633
a_8	+0.0106	-0.005874	$\pm 1.8\%$	-0.6303
a_9	-0.0022	-0.006809	$\pm 1.8\%$	-0.6015
a_{10}	-5.1810^{-4}	$+8.2510^{-4}$	$\pm 5.6\%$	-3.76710^{-2}
a_{11}	$+3.9710^{-5}$	$+5.5410^{-5}$	$\pm 24.1\%$	-0.1031
a_{12}	-	-	-	$+4.359110^{-2}$
a_{13}	-	-	-	$+7.269810^{-3}$
a_{14}	-	-	-	$+4.540910^{-4}$
Application $0.01 < D \text{ (km)} < 300$ limits				From 3 m to 20 km

*Coefficient “sensitivity” presents limits of the given coefficient variation (while other coefficients are “frozen”) resulted in factor of 2 maximum deviation from the nominal $N(D)$ in the range of the polynomial solution applicability.

**The coefficient a_0 is calculated from the lunar crater chronology to estimate the frequency of impacts on modern Earth. The average impact probability for Earth-crossers are taken as 3.5 Ga^{-1} .

Neukum and Ivanov 1994) proposed an analytical presentation of the lunar crater production SFD in a wide range of crater diameters. He also suggested that the shape of the production SFD had been more or less stable from $\sim 4 \text{ Ga}$ ago to the present. Neukum also proposed the time dependence of the crater accumulation rate, discussed in Equation (1). The analytical NPF can be presented as:

$$\log_{10}(N_{>D}) = \log_{10}(a_0) + \sum_1^{n_{\max}} a_n [\log_{10}(D)]^n \quad (6)$$

Coefficients a_n are listed in Table 1. The coefficient a_0 presents the logarithm of the number of craters larger 1 km in diameter $N(1)$, accumulated in 1 Ga per unit area. According to Neukum (1983) $10^{a_0} = N(1) = 8.38 \times 10^{-4} \text{ km}^{-1} \text{ Ga}^{-1}$.

Equation (6) is valid for the crater diameter range from 10 m to 300 km. Equation (1) estimates the variation of $N(1)$ with the surface age. Neukum et al. (2001a; in comparison with Neukum 1983) derived updated coefficients from new crater counts.

Equation (6) can also be used to present the SFD for projectiles. This problem is discussed later in this section. For further discussion the last column of Table 1 lists coefficients for the R-plot of lunar projectile SFDs.

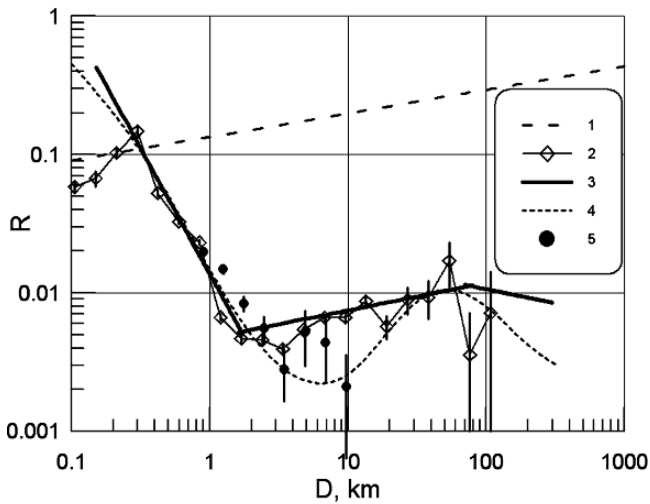


Figure 4. R-plot for recent crater counts by Namiki and Honda (2003) in comparison with HPF and NPF shown earlier in Fig. 3b. 1—Empirical saturation crater density after Hartmann (1984); 2—HPF; 3—piece-wise power law approximation for HPF; 4—NPF for the age of 3.4 Ga; 5—averaged data from crater counts by Namiki and Honda (2003)

2.3 Comparison of HPF and NPF

Figure 3b illustrates R-plots for NPF and HPF for mare crater counts. Both HPF and NPF well present observational data for crater diameters $D < 1$ km. However, in the crater diameter range $1 < D$ (km) < 40 the NPF is well below the HPF, giving a main discrepancy of a factor of 3 at $D \sim 6$ km.

One should be cautious using PFs in this diameter range, as data published by various authors show very different SFD behaviors for impact craters. Additional investigations are hardly needed to refine the SFD for post-mare craters in the diameter range mentioned here. New crater counts were published for the lunar mare last year. For example, Fig. 4 presents data published by Namiki and Honda (2003) for NPF and HPF. One can see that the “true” PF for impact craters in the crater diameter range of $3 \text{ km} < D < 30 \text{ km}$ may be between that of HPF and NPF.

Production function may be used to interpolate crater counts obtained on surfaces of various ages. Comparisons show that assumptions about the stability of the PF through time (100 different craters per unit area) fit data for the lunar surfaces well (Fig. 5).

Despite the discrepancy in NPF and HPF, both PFs assume the constancy of the general shape of PF through ~ 4 Ga of planetary geologic history. The alternative point of view is defended by R. Strom (Strom and Neukum 1988; Strom et al. 1992), who claims that the modern PF is appreciably different from the PF during

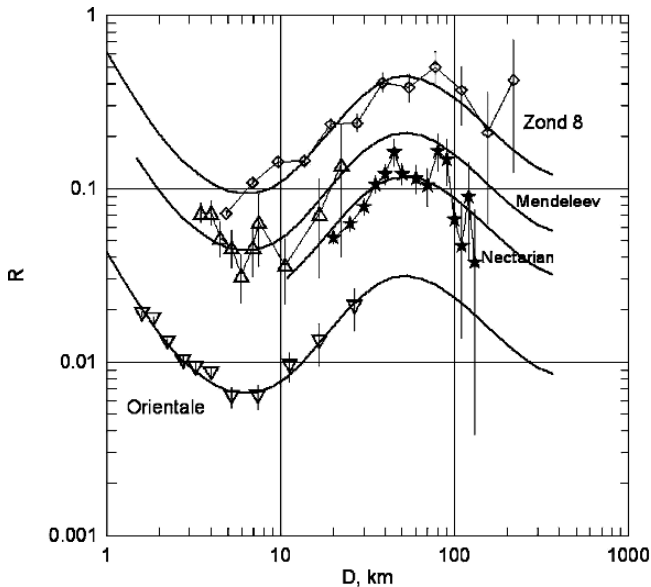


Figure 5. R-plot for the Neukum production function (NPF, solid curves) for various lunar areas, differ a factor of 100 in the crater number per unit area. Observational data are for the lunar highland imaged by the Russian spacecraft Zond-8 (Ronca et al. 1981), Mendeleev crater, Nectarian craters (Wilhelms et al. 1987), and Orientale basin (Neukum et al. 2001a)

the LHB epoch. This discussion is complicated because Strom uses geologic data to select impact craters of the same age. This technique is not particularly reliable, as the “freshness” of an impact crater on other planets depends strongly on the resolution of available images. Most of Strom’s data for Mars are based on Viking imagery (Strom et al. 1992). The Mars imaging campaign, including the Mars Global Surveyor, Odyssey, Mars Express, and HiRISE, is ongoing. One should discuss recent publications cautiously until new data are analyzed properly.

3 IMPACT CRATERS ON TERRESTRIAL PLANETS

Lunar impact crater SFD, presented in the previous section, may be transferred to other planets. The “lunar-derived” impact crater SFD model may be compared with real crater counts on Mercury, Venus, Earth, and Mars. The basic procedure, as described by Hartmann (1977), includes finding the average impact velocity, specific for each planetary body, and the application of the impact crater scaling laws, describing the relation of the projectile mass and final crater diameter (see, e.g., Ivanov et al. 2001).

Table 2. Average impact probability and average impact velocity on terrestrial planets for observed planetary crossers $H < 17$, listed in the MPC catalog (file astorb.dat) in November 2005

Planetary body	$N_{H<17}$	Average impact rate,* 10^{-15} $\text{km}^{-2} \text{yr}^{-1}$	Average collision probability per one body (planetary crosser), Ga^{-1}	Average impact velocity, $\text{km}\cdot\text{s}^{-1}$	R_b^{**}
Mercury	34	0.72	1.6	35.4	0.92
Venus	89	0.88	4.5	24.2	1.12
Earth	194	1.3	3.4	19.3	1.68
The Moon	194	0.78	0.16	17.5	1
Mars, current orbit, $e=0.0934$	2680	3.8	0.21	9.4	4.93****
Mars, $e = 0.05^{***}$	1433	2.4	0.24	10.2	3.10****
Mars, $e = 0.01$	869	2.0	0.34	10.5	2.58****

*Average impact rate is the global number of impacts per a time unit, divided by the surface area of a planet.

***"Bolide ratio" is the ratio of the impact rate of projectile of the same size per unit area to the same value for the moon (for the moon $R_b = 1$ by definition).

***This value of eccentricity is close to the average value for a time span of 10 Ma and longer still limited to the available Mars orbit modeling duration (Ward 1992).

****Not corrected for the incomplete observation of Mars crossers (see Ivanov et al. (2001) for an example of a correction).

3.1 Average Impact Velocity

The distribution of impact on impact velocity (the frequency of impacts within a given velocity range) depends on the orbital parameters of planet-crossing bodies. A set of Earth-crosser population models have been published for the Earth–Moon system (e.g., Rabinowitz 1993; Bottke et al. 2002; Stuart and Binzel 2004).

In addition to results of orbit evolution and observation bias modeling, one can construct a good approximation of impact velocity frequency using orbits of observed planetary crossers listed in the permanently updated catalog of small body orbits astorb.dat (<ftp://ftp.lowell.edu/pub/elgb/astorb.dat>). Using Öpik approach, extended for the typical case of two bodies in elliptic orbits (Wetherill 1967), one can estimate probability and velocity of impact for observed small bodies.

Table 2 summarizes these estimates for the astorb.dat as it was in October 2006.

For Earth Table 2 lists the average impact velocity of $19.3 \text{ km}\cdot\text{s}^{-1}$, which is $\sim 5\%$ less than the typical model with unbiased population estimates (Stuart 2001; Bottke et al. 2002; Morbidelli et al. 2002; Stuart and Binzel 2004).

Table 2 illustrates a set of principal characteristics of terrestrial planets' modern bombardment rate:

1. The average impact velocity decreases with an increase in the target planet's distance from the Sun. For Mercury, the average impact velocity is above $30 \text{ km}\cdot\text{s}^{-1}$, whereas for Mars it is around $10 \text{ km}\cdot\text{s}^{-1}$.

2. The average asteroid impact probability is 0.2 to 4 Ga⁻¹. This means that an asteroid should orbit around the Sun 0.25 to 5 Ga at the currently observed orbit before impacting a target planet. This is dynamically impossible for a given planetary-crosser, as close encounters with terrestrial planets and resonances result in relatively short (1–10 Ma) average life spans (Gladman et al. 2000). The given asteroid has a much greater chance of hitting the Sun or being ejected to the margin of a solar system than to experience a crater-forming collision with a planet. Without a supply of new bodies, the population of planetary crossers would become extinct in ~100 Ma (Hartmann et al. 2002). To maintain an approximately constant impact rate in the modern (post-LHB) inner solar system, it is essential that new asteroids be delivered from the main belt into planetary-crossing orbits. Hence, Table 2 makes the additional assumption that currently observed osculating orbits have the same population of small bodies on average. For example, if the average time for a typical orbit is ~300 Ma before a collision with Earth, and the half-life of a given asteroid in this orbit is ~10 Ma, then one can estimate that this orbit will be repopulated ~30 times before one new impact crater will be created on the surface of the Earth. The strong role of orbit repopulation illustrates the importance of evolution modeling of small bodies' behavior in the Solar System (Ipatov 2000).
3. The average cratering rate for projectiles of the same size per unit area (although crater diameters would vary because of different impact velocities and surface gravities), differs for all terrestrial planets much less than one order of magnitude from Mercury to Mars. The most dramatic difference gives the comparison between Earth and the Moon: With the same projectile flux "at infinity," the larger cross-section of Earth results in 20 impacts per one impact on the moon (for the same size projectile). However, the normalization of the impact rate with the planetary surface gives the Moon–Earth impact rate ratio of the order of 1.7. Hartmann (1997) designates the ratio of impact frequency of same-size projectiles per unit area the "bolide ratio," R_b (Table 2, last column). For all terrestrial planets the value of R_b varies from 0.9 to ~5 in comparison with the moon.
4. Mars has the most variable orbit of all terrestrial planets; it changes its eccentricity and inclination per ~2 Ma (Ward 1992; Laskar et al. 2004). During the period of largest eccentricity, Mars (in the aphelion) approaches the main belt, and experiences frequent impacts from numerous so-called shallow Mars-crossers. During the whole cycle of the Mars eccentricity, its impact rate may vary by a factor of 4. Mars' current orbital eccentricity of 0.0934 (close to the maximum), should also have had an enhanced impact rate during the last 1 to 2 Ma.

The average velocity of impacts does not give a full representation of the impact velocity range. For example, observed asteroids could strike the planet Mercury with a velocity of 13–50 km·s⁻¹. Figure 6 illustrates the frequency of impacts on the Earth and Moon for all observed asteroids with $H < 17$.

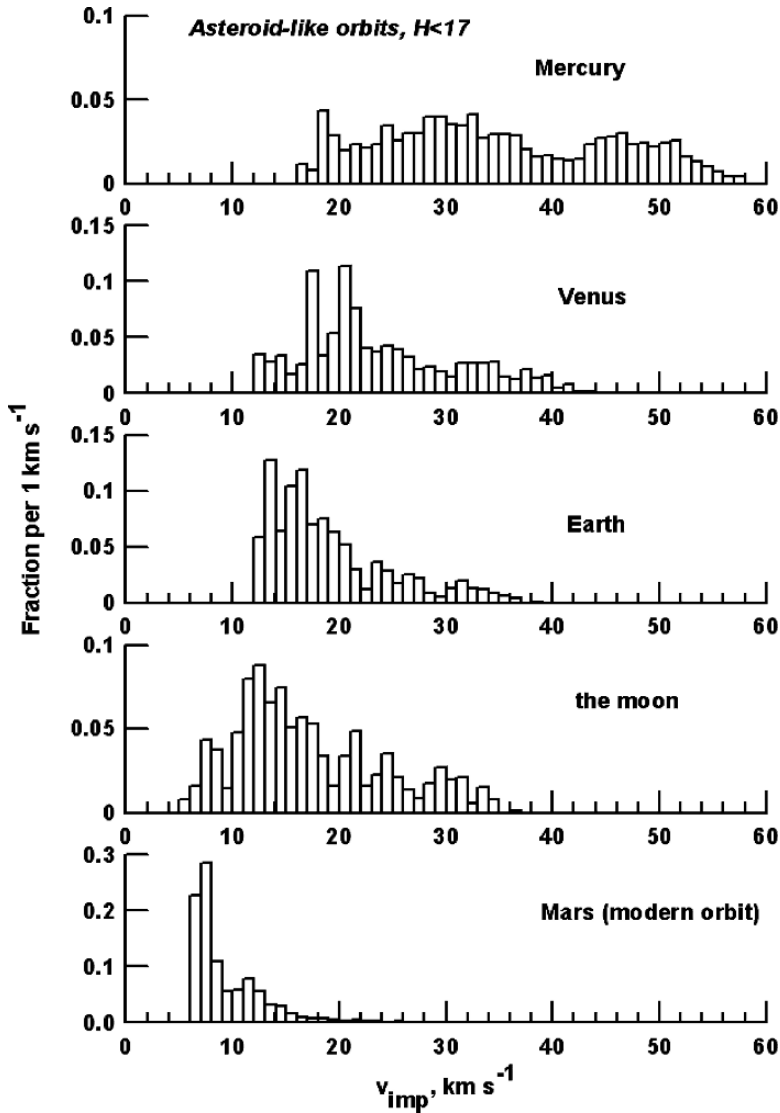


Figure 6. Frequency of the impact velocity for terrestrial planets and the Moon, presented as the fraction of all impacts, f_v , in velocity bins with the width of 1 km s^{-1}

3.2 From Impact Crater Diameters to Projectile Size

For simplicity this subsection follows the assumption that the majority of impact craters are formed by asteroids. The authors will remain open-minded to the problem of the comet impact fraction in the observed population of impact craters until

better knowledge is accumulated about LP comet SFD. For the same reason, the authors assume a density of 2.7 g cm^{-3} , which is typical for S-type asteroids (Britt et al. 2002), the most numerous subpopulation of projectile impacts on the Earth (Stuart and Binzel 2004). The conversion of crater SFD to projectile SFD is presented by Ivanov et al. (2001). The procedure uses the Schmidt and Housen (1987) scaling law to relate the projectile diameter and the rim and transient impact crater diameter. For complex craters (Melosh and Ivanov 1999), the transient cavity diameter is estimated with the semiempirical model (Croft 1985; Chapman and McKinnon 1986; McKinnon et al. 1991).

The Schmidt-Housen scaling law is experimentally derived for two broad classes of targets: nonporous material and porous material (Schmidt and Housen 1987). Originally the experimental data were reduced by the scaling theory with a set of dimensionless parameters, π . The Schmidt-Housen scaling law expresses in crater diameter terms of dimensionless (scaled) π -value for transient crater diameter, D_{at} , named $\pi_D = D_{at}(\rho/m)^{1/3}$ (ρ is the target material density, and m is the projectile mass), and the other π -value for the projectile, $\pi_2 = 1.61gD_p/v^2$ (g is the gravity acceleration, D_p is the projectile diameter, and v is the impact velocity). For target materials without an appreciable cohesion (e.g., dry sand), the scaling law is well approximated with the exponential relation:

$$\pi_D = K_D \pi_2^\beta \quad (7)$$

where K_D and β are experimentally derived coefficients. For nonporous rocks $K_D = 1.6$; $\beta = 0.22$, whereas for porous rocks (e.g., dry sand) $K_D = 1.68$; $\beta = 0.17$.

Rocks with nonzero effective cohesion scaling laws are more complicated. The description of a more general scaling rule derivation from the exponential Schmidt-Housen scaling, presented in the preceding, has been offered in a set of papers (Holsapple and Schmidt 1979; Holsapple and Housen 2007). Neukum and Ivanov (1994) propose a simplified version of the strength-gravity transition description. With the updated numerical coefficients the approximate scaling rules may be presented here in the following form (see also Ivanov et al. 2001):

for low-porous rocks:

$$\frac{D_{at}}{D_p} = 1.21 \frac{(\delta/\rho)^{0.427} \nu^{0.564}}{[g(D_{sg} + D)]^{0.282}} \quad (8)$$

for porous materials such as sand or lunar regolith:

$$\frac{D_{at}}{D_p} = 1.31 \frac{(\delta/\rho)^{0.401} \nu^{0.41}}{[g(D_{sg} + D)]^{0.205}} \quad (9)$$

These relations allow investigators to estimate the projectile diameter and impact velocity for a given transient cavity diameter. For the most frequent impacts of S-type asteroids projectile density may be taken as $\sim 2.7 \text{ g cm}^{-3}$ (Britt et al. 2002).

The transient cavity diameter D_{at} is estimated from the value for the rim crest diameter, D . For simple craters experimental data show with reasonable accuracy that the transient cavity diameter may be estimated as:

$$D_{at} \approx D/1.25 \quad (10)$$

For complex (collapsed) craters the similar relation is not yet well defined, and tentatively Croft's (1985) model may be used (see also Chapman and McKinnon 1986; McKinnon et al. 1991):

$$D_{at} \approx D_{sc}^{0.15} D^{0.85} \quad (11)$$

where D_{sc} is the effective boundary separated simple and complex (collapsed) craters of impact crater diameters.

The nonporous scaling law gives the best approximation for large craters. For small lunar craters, created in the lunar regolith, the porous scaling law gives a reasonable fit between the modern projectile flux and the youngest (<100 Ma) lunar impact crater production rate (Ivanov 2006).

In numerous previous publications (e.g., Neukum and Ivanov 1994; Ivanov et al. 2001; Ivanov et al. 2001, 2002; Werner et al. 2002), the porosity effect was not taken into account for small lunar crater formation. Consequently, sizes of small projectiles (with diameters below ~ 100 m) were too small (due to larger efficiency of cratering according to the assumed nonporous scaling), and the number of small projectiles in the SFD was underestimated. This discrepancy is pointed out by many authors (e.g., Stuart and Binzel 2004). Here the authors have attempted to correct the projectile SFD derived from lunar crater records.

The usual point of view is that a lunar regolith of 5- to 15-m thickness is overlaid with a competent rock basement (as witnessed by the presence of concentric impact craters of ~ 100 m in diameter; Quaide and Oberbeck 1968). Definitely, the material under regolith has an increased cohesion compared with the surface regolith layer. However the review of previously published data on seismic sounding of the Moon shows that the layer just under regolith has an amazingly low velocity of longitudinal elastic waves about $1 \text{ km}\cdot\text{s}^{-1}$ in the upper 1 km (Cooper et al. 1974; Vinnik et al. 2001; Chenet et al. 2006). Such low seismic velocities allow investigators to assume highly fractured and fragmented ~ 1 km near-surface lunar rocks. This fragmented state increases the macroporosity of near-surface lunar bedrock. Impacts in porous rocks result in fast shock wave decay and enhanced energy conversion into heat due to dynamic closing of porous space. Despite the apparent low strength of porous rocks, dynamic effects may result in smaller final crater sizes than in more competent but nonporous rocks. This effect is partially masked in low-velocity experiments (Schmidt and Housen 1987), but well-expressed in numerical modeling (Wünnemann et al. 2006).

Assume that for small craters one can use the porous rock scaling law. This was confirmed by comparison of the modern NEA flux and recent lunar cratering rate by Ivanov (2006). For large craters ($D > 20$ km) the usage of the nonporous scaling law

offers a best guess as 1-km and larger projectiles penetrate through the fragmented ~ 1 -km-thick layer, as revealed by lunar seismic sounding. The intermediate crater diameter range is extrapolated with a smooth transition from nonporous to porous scaling laws. Assuming that all impacts have an average impact velocity of $18 \text{ km}\cdot\text{s}^{-1}$ and an average impact angle of 45° , the lunar crater NPF is converted into a smooth projectile SFD. Resultant points for the projectile SFD are approximated with the same polynomial formula as for impact craters (Equation 4) to the 14th power of $\log(D_p)$. Coefficients for the projectile SFD are listed in Table 1.

To illustrate ranges at which porous and nonporous scaling laws are used, apply the projectile polynomial SFD to the backward construction of the lunar crater SFD. Figure 7b compares the crater counts for Orientale basin and the crater SFD modeled with the polynomial projectile SFD. One can see that the proposed tentative projectile SFD gives a good fit to the crater SFD below $D \sim 2 \text{ km}$. The nonporous scaling law provides a good fit for the crater SFD above $D \sim 20 \text{ km}$. Intermediate range corresponds to the yet-unknown intermediate scaling law for the real lunar crust, with porosity gradually decreasing with depth (shaded area in Fig. 7a). More indirect evidence in favor of the porosity hypothesis is seen in Fig. 7a: the same diameter number of craters counted inside the Orientale (assumed) crater rim is larger than the number of craters counted outside in the area of the deposited crater ejecta. The additional thickness of ejecta layer increases the effective thickness of porous fragmented material and the same impacts “outside” craters have smaller diameters than “inside” craters. The effect visible in Fig. 7b is not strong enough, however; much more investigation and modeling are needed to properly take into account the target effect while crater counts are compared in various areas.

3.3 Terrestrial Impact Craters

This section compares the lunar crater SFD recalculated to the Earth with data on terrestrial crater counts. The comparison of the lunar data with crater counts on other terrestrial planets has been published previously (e.g., Neukum et al. 2001a)

Hartmann (1965, 1966) is one of the first who recognized that large terrestrial impact craters survive on the surface longer than small craters, as small craters are eroded faster. This effect prevents the construction of terrestrial PF for craters smaller than $\sim 10 \text{ km}$. Results of the lunar crater chronology recalculation to the Earth are shown in Fig. 8. Here the model PF is shown for a set of accumulation tie intervals from 10^4 years to 3.4 Ga. The PF expresses the number of impact craters with diameters larger D on the whole Earth’s surface if this surface is a solid (continental) one. More exactly, the PF presents the number of impact events around the Earth where the impact energy scale is expressed through the diameter of an impact crater created on land. The actual number of impact craters is controlled by the presence of oceans, where small craters on the floor cannot be formed because of the shielding effect of sea water. One observational data set for continental craters (Hughes 2000) is shown for comparison after recalculation to the whole Earth surface.

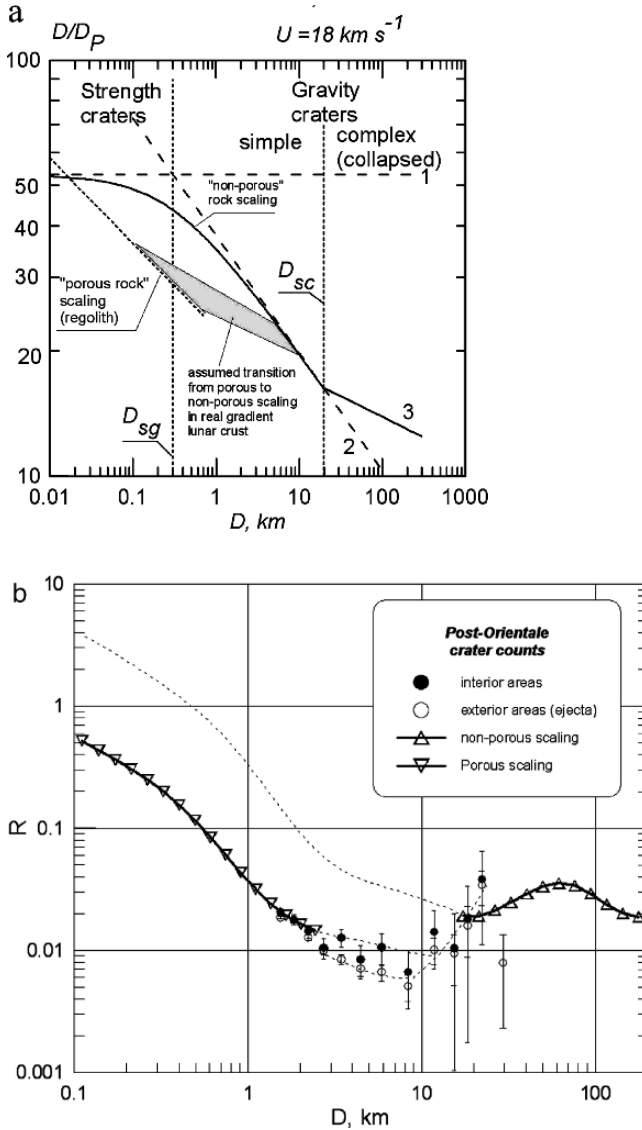


Figure 7. (a) The scaling law for porous and nonporous targets presented as the ratio of crater and projectile diameters for the average impact velocity of $18 \text{ km}\cdot\text{s}^{-1}$. (b) Illustration of difference between porous and nonporous scaling laws applied for reproduction of the Orientale basin crater count with the preliminary lunar projectile SFD (Equation 6) with coefficients from the right column of Table 1

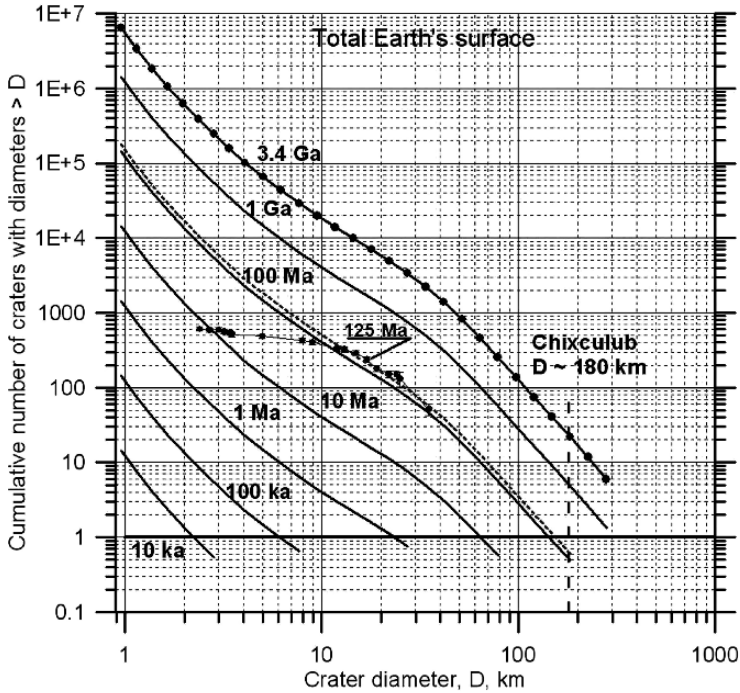


Figure 8. Cumulative number of impacts for the whole Earth surface. The scale of impact is presented with the diameter of impact craters formed in continents. (Oceanic impacts may not result in crater formation.) Curves for selected accumulation times are calculated from the lunar impact crater chronology assuming the porous scaling law for small lunar craters and nonporous scaling for large lunar craters. The model SFD for projectiles with the density 2.7 g cm^{-3} is presented by Equation (6) with coefficients listed in Table 1. Black dots present independent estimates by Hughes (2000) with the “nearest neighbor” technique for recognized terrestrial impact craters in selected continental areas. These estimates are recalculated to the whole area of the globe. Dotted curve shows the good fit of recalculated lunar chronology to Earth

The crossing of isochrones with the horizontal line $N_{>D} = 1$ gives an estimate of the average time interval between impacts formed by craters of a given diameter. For example, impacts of craters with diameters $>5 \text{ km}$ on land occur approximately once per 100,000 years (100 ka), and of those $>30 \text{ km}$, once per 1 Ma. Impacts of craters with diameters of 200 km (the largest craters found to date; see Chap. 5) occur on average once per 100 Ma. During the last 3 Ga Earth has experienced about 30 such impacts. If the total area of continents was roughly the same as it is now (\sim one-third of the total globe’s surface), the PF estimates that ~ 10 land craters with diameters of 200 km and larger were formed. Taking into account the violent geologic history of Earth, one can say that the finding three such craters (Sudbury, age of 2 Ga; Vredefort, age of 1.8 Ga; Chicxulub, age of 65 Ma) would not contradict to the lunar-based estimate.

4 SIZE-FREQUENCY DISTRIBUTION OF ASTEROIDS

4.1 Main Belt Asteroids

Telescopic observations and satellite infrared survey (IRAS) resulted in the recognition of all Main Belt asteroids with diameters larger than ~ 40 km (van et al. 1970; Gradie et al. 1989; Cellino et al. 1991). To count smaller asteroids researchers have proposed the power law $dN/dD_p \sim D_p^{-k}$, where the exponent k is the range of 2.95 to 3.5 (the so-called Palomar-Leiden [PL] slope; van et al. 1970); a typical value for the similar fragmentation cascade (Dohnanyi 1969; Davis et al. 1994) has used the geometric average of aforementioned values (Cellino et al. 1991) to process the IRAS experiment data.

More recent improved observations have shown that the asteroid SFD is not a simple power law, but demonstrates “wavy” deviation from the general power trend (e.g., Jedicke et al. 2002).

Several explanations of the asteroid SFD’s wavy character are proposed by various models of asteroid collision evolution (Campo et al. 1994a, 1994b; Durda et al. 1998; Davis et al. 2002). Campo et al. (1994a) produced SFD waves by removing the smallest fragments from the collision cascade. Here the deficiency of small fragments results in the enhanced survivability of larger bodies, creating SFD waves. Durda et al. (1998) used numerical modeling results of the catastrophic breakup (Love and Ahrens 1996; Melosh and Ryan 1997; Benz and Asphaug 1999). Here transition from the “strength” regime of fragmentation (the material strength that controls the energy of a catastrophic collision) to the “gravity” regime (fragments re-accumulates due to self-gravity, producing so-called rubble-pile asteroids) creates a wave in the collisionally evolved asteroid fragment cascade.

Figure 9 presents direct observational data (Davis et al. 1994; Jedicke and Metcalfe 1998) in comparison with estimates of the preliminary projectile SFD based on the lunar impact crater SFD. One can see a set of similar features in both SFDs (Fig. 5).

Comparison of SFDs for asteroids and assumed lunar projectiles is in favor of the assumption that lunar LHB craters are created by projectiles having SFDs similar to the modern Main Belt asteroids. This means it was a collisionally evolved population. Our limited knowledge of the comet SFD (Chap. 3) favors the minor input of comets in cratering on terrestrial planets. Much more work needs to be done to verify that asteroids were the main cratering population throughout terrestrial planetary history.

4.2 Near-Earth Asteroids

Figure 10 compares most of the known data about NEA SFD with the preliminary projectile SFD derived from lunar craters. Here the number of NEAs is converted into a global probability of impacts of asteroids larger than a given diameter. As for Main Belt asteroids, the lunar projectile SFD is a good proxy

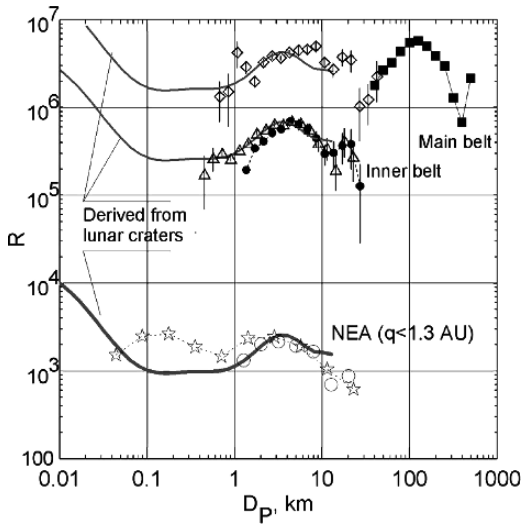


Figure 9. R-plot for size-frequency distribution of Main Belt asteroids from telescopic observations (Davis et al. 1994; Jedicke and Metcalfe 1998; Ivezić et al. 2001; Ivezić et al. 2002): signed data point for C-asteroids (diamonds) and S-asteroids (triangles) in comparison with the projectile SFD derived from lunar impact craters. Known near-Earth asteroids are shown as open circles, and LINEAR data (Stuart 2001) are shown as stars

for poorly known SFDs for small NEAs. The most impressive result of this comparison is that the modern impact rate on Earth, measured from satellite observations of bolides (Brown et al. 2002b) within error bars corresponds to the small lunar crater formation rate, averaged for the time period of 10 to 100 Ma (Ivanov 2006).

5 CONCLUSIONS

One of the vital problems in a study of Solar System evolution is the analysis of small body motion: The asteroid population at planetary-crossing orbits (“projectiles” for modern impact bombardment) is permanently renovating due to migration of Main Belt asteroids. The practically important question is impact frequency depending on the asteroid size. Year to year direct telescopic observations improve our knowledge about asteroids’ SFD. However, telescopic counting of asteroids to date gives reliable numbers only for bodies larger than ~ 1 km in diameter. The parallel usage of known SFDs of lunar and planetary impact craters, after recalculating to projectiles, allows investigators to extrapolate the SFDs to smaller sizes of ~ 1 m and below. Celestial bodies in this small-size range enter the terrestrial atmosphere frequently enough to be measured by ground-based and/or satellite observations. Hence, impact crater size–frequency relations connect independent observational data in different size ranges.

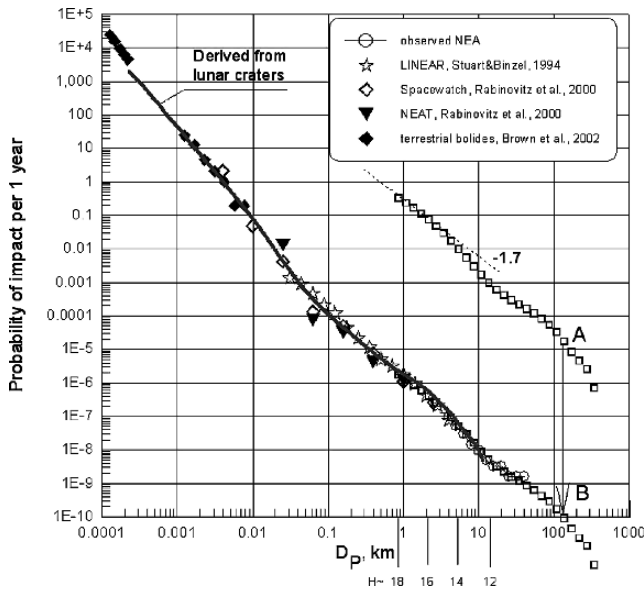


Figure 10. Cumulative SFD for NEA recalculated to the global probability of collision for bodies of various diameters. The plot is constructed using astronomical observations and modeling (Rabinowitz et al. 2000; Stuart and Binzel 2004), satellite global recording of bolides (Nemtchinov et al. 1997b; Brown et al. 2002b) in comparison with the lunar projectile SFD recalculated to terrestrial conditions (thick gray curve). Recent estimates for the Main Belt SFD is shown with squares (and labeled A) after Jedicke et al. (2002). The same SFD is shown scaled to the NEA absolute numbers (labeled B) to illustrate the similarity of SFDs for NEA and Main Belt asteroids with diameters > 1 km

Available data on the size–frequency and time frequency of impact crater formation on the Moon, Earth, and other terrestrial planets witness that the simple hypothesis about constancy of impact bombardment rate and size–frequency throughout the last ~ 3.3 Ga (after the end of the LHB) is a good starting approximation for further investigations of the fundamental problem of Solar System evolution.

The SFD of asteroids (projectiles) and impact craters looks wavy in comparison with simple power law relations. These waves tell a great deal about the collision evolution of small bodies in the early and modern Solar System. If it is proved that the main reason for wavy small-body SFDs is self-gravity, which changes the specific energy of catastrophic breakups, it will become obvious that positions of wave maxima and minima should vary depending on impact strength and average impact velocity in a population. This means that the SFD wavy curve may be different, for example, for the modern asteroid belt and planetesimals in the early Solar System. Consequently, SFD shapes for modern and ancient (e.g., LHB) projectiles may be different. Comparison of ancient and modern impact crater SFDs may be used to restrict amplitudes of these possible differences. The picture to date, suggests that LHB projectiles should have passed through the collision evolution

mill before becoming crater-forming projectiles for terrestrial planets; however, this is still an open question.

One more open question is the role of comets in the formation of currently observed crater populations on terrestrial planets. The similarity of ancient and younger impact crater SFDs allows investigators to assume, as a starting approximation, that collision evolution played the main role in impact cratering by asteroid-like bodies with generally similar features. Consequently, the role of comets, which is currently minor for terrestrial planets, should not be much more important during the LHB. From this point of view, comet input may be masked if the comet SFD is similar to the asteroid SFD. Did comets pass through collision evolution? If so, is the final comet SFD similar enough to the asteroid SFD to produce similar wavy SFDs for older and younger impact crater populations? Where did comet collision evolution take place: In the feeding zone of giant planet formation or only in the Kuiper belt? These and many other questions may be investigated with the help of improved knowledge about the SFDs of impact craters on the Moon, Earth, and other terrestrial planets.

REFERENCES

- Benz W, Asphaug E (1999) Catastrophic disruptions revisited. *Icarus* 142:5–20
- Bottke W, Levison HF, Nesvorný D, Dones L (2006) Can planetesimals leftover from terrestrial planet formation produce the lunar Late Heavy Bombardment? Presented at AAS/Division of Planetary Sciences Meeting #38, abstr #66.01
- Bottke J, William F, Morbidelli A et al (2002) Debaised orbital and absolute magnitude distribution of the Near-Earth Objects. *Icarus* 156(2):399–433
- Britt DT, Yeomans D, Housen K, Consolmagno G (2002) Asteroid density, porosity, and structure. In: Bottke W, Cellino A, Paolicchi P, Binzel RP (eds) *Asteroids III*. University of Arizona Press, Tucson, pp 485–500
- Brown PG, Spalding RE, ReVelle DO et al (2002b) The flux of small near-Earth objects colliding with the Earth. *Nature* 420(6913):294–296
- Campo Bagatin A, Cellino A, Davis DR et al (1994a) Wavy size distributions for collisional systems with a small-size cutoff. *Planet Space Sci* 42(12):1079–1092
- Campo Bagatin A, Farinella P, Petit J-M (1994b) Fragment ejection velocities and the collisional evolution of asteroids. *Planet Space Sci* 42(12):1099–1107
- Cellino A, Zappala V, Farinella P (1991) The size distribution of main-belt asteroids from IRAS data. *Mon Not R Astronom Soc* 253:561–574
- Chapman CR, Haefner RR (1967) A critique of methods for analysis of the diameter–frequency relation for craters with special application to the Moon. *J Geophys Res* 72:549–557
- Chapman CR, McKinnon WB (1986) Cratering of planetary satellites. In: Burns JA, Matthews MS (eds) *Satellites*. University of Arizona Press, Tucson, pp 492–580
- Chenet H, Lognonné P, Wieczorek M, Mizutani H (2006) Lateral variations of lunar crustal thickness from the Apollo seismic data set. *Earth Planet Sci Lett* 243:1–14
- Cooper MR, Kovach RL, Watkins JS (1974) Lunar near-surface structure. *Rev Geophys Space Phys* 12:291–308
- Croft SK (1985) The scaling of complex craters. *J Geophys Res* 90:C828–C842
- Davis DR, Durda DD, Marzari F et al (2002) Collisional evolution of small-body populations. In: Bottke W, Cellino A, Paolicchi P et al (eds) *Asteroids III*. University of Arizona Press, Tucson, pp 545–558
- Davis DR, Ryan EV, Farinella P (1994) Asteroid collisional evolution: results from current scaling algorithm. *Planet Space Sci* 43:599–610

- Dohnanyi JS (1969) Collisional model of asteroids and their debris. *J Geophys Res* 74:2531–2554
- Durda D, Greenberg R, Jedicke R (1998) Collisional models and scaling laws: a new interpretation of the shape of the Main-Belt asteroid distribution. *Icarus* 135:431–440
- Gladman B, Michel P, Froeschlé C (2000) The Near-Earth object population. *Icarus* 146:176–189
- Gomes R, Levison HF, Tsiganis K, Morbidelli A (2005) Origin of the cataclysmic Late Heavy Bombardment period of the terrestrial planets. *Nature* 435:466–469
- Gradie JC, Chapman CR, Tedesco EF (1989) Distribution of taxonomic classes and the compositional structure of the asteroid belt. In: Binzel R, Gehrels T, Matthews MS (eds) *Asteroids II*. University of Arizona Press, Tucson, pp 316–335
- Hartmann WK (1965) Terrestrial and lunar flux of meteorites in the last two billion years. *Icarus* 4:157–165
- Hartmann WK (1966) Martian cratering. *Icarus* 5:565–576
- Hartmann WK (1984) Does crater “saturation equilibrium” occur in the solar system? *Icarus* 60:56–74
- Hartmann WK (2005) Martian cratering 8: Isochron refinement and the chronology of Mars. *Icarus* 174:294–320
- Hartmann WK, Neukum G (2001) Cratering chronology and the evolution of Mars. *Space Sci Rev* 96(1/4):165–194
- Hartmann WK, Ryder G, Dones L, Grinspoon D (2002) The time-dependent intense bombardment of the primordial Earth/Moon system. In: Bottke W, Cellino A, Paolicchi P, Binzel RP (eds) *Asteroids III*. Univ. of Arizona Press, Tucson, AZ, pp 493–512
- Hartmann WK, Strom RG, Weidenschilling SJ et al (1981) Chronology of planetary volcanism by comparative studies of planetary craters. *Basaltic Volcanism on the Terrestrial Planets*. Elmsford, NY: Pergamon Press, pp 1050–1127
- Hiesinger H, Head JW, Wolf U et al (2003) Ages and stratigraphy of mare basalts in Oceanus Procellarum, Mare Nubium, Mare Cognitum, and Mare Insularum. *J Geophys Res* 108(E7):5065, doi:10.1029/2002JE001985
- Hiesinger H, Jaumann R, Neukum G et al (2000) Ages of mare basalts on the lunar nearside. *J Geophys Res* 105:29239–29276
- Holsapple KA, Housen KR (2007) A crater and its ejecta: an interpretation of Deep Impact. *Icarus* 187:345–356
- Holsapple KA, Schmidt RM (1979) A material-strength model for apparent crater volume. In: *Proceedings Lunar Planet Sci Conference 10th*. Pergamon Press, NY, pp 2757–2777
- Hughes DW (2000) A new approach to the calculation of the cratering rate of the Earth over the last 125 ± 20 Myr. *Mon Not Roy Astronom Soc* 317:429–437
- Ipatov SI (2000) Migration of celestial bodies in the solar system. Editorial URSS, Moscow (in Russian), p 320
- Ivanov BA (2001) Mars/Moon cratering rate ratio estimates. *Space Sci Rev* 96(1/4):87–104
- Ivanov BA (2006) Earth/Moon impact rate comparison: searching constraints for lunar secondary/primary cratering proportion. *Icarus* 183:504–507
- Ivanov BA, Neukum G, Bottke WF Jr, Hartmann WK (2002) The comparison of size-frequency distributions of impact craters and asteroids and the planetary cratering rate. In: Bottke WF, Cellino A, Paolicchi P, Binzel RP (eds) *Asteroids III*. University of Arizona Press, Tucson, pp 89–101
- Ivanov BA, Neukum G, Wagner R (2001) Size-frequency distribution of planetary impact craters and asteroids. *Collisional processes in the solar system*. Marov MY, Rickman H (eds). *Astrophys Space Sci Library* 261. Kluwer Academic Publishers, Dordrecht, pp 1–34
- Ivezic Z, Juric M, Lupton RH et al (2002) Asteroids observed by the Sloan Digital Survey. In: Tyson JA, Wolff Sidney (eds) *Survey and other telescope technologies and discoveries*. *Proceedings of the SPIE* 4836:98–103
- Ivezic Z, Tabachnik S, Rafikov R et al (2001) Solar system objects observed in the Sloan digital sky survey commissioning data. *Astronom J* 122:2749–2784
- Jedicke R, Larsen J, Spahr T (2002) Observational selection effects in asteroid surveys. In: Bottke WF, Cellino A, Paolicchi P, Binzel RP (eds) *Asteroids III*. University of Arizona Press, Tucson, pp 71–87

- Jedicke R, Metcalfe TS (1998) The orbital absolute magnitude distributions of Main Belt asteroids. *Icarus* 131:245–260
- Laskar J, Correia ACM, Gastineau M, Joutel F, Levrard B, Robutel P (2004) Long term evolution and chaotic diffusion of the insolation quantities of Mars. *Icarus* 170:343–364
- Love SG, Ahrens TJ (1996) Catastrophic impacts on gravity dominated asteroids. *Icarus* 124:141–155
- McKinnon WB, Chapman CR, Housen KR (1991) Cratering of the Uranian satellites. In: Bergstrahl JT et al (eds) *Uranus*. University Arizona Press, Tucson, pp 629–692
- Melosh HJ, Ivanov BA (1999) Impact crater collapse. *Ann Rev Earth Planet Sci* 27:385–415
- Melosh HJ, Ryan EV (1997) Asteroids: shattered but not dispersed. *Icarus* 129:562–564
- Morrison D, Harris AW, Sommer G et al (2002) Dealing with the impact hazard. In: Bottke W, Gellino A, Paolicchi P, Binzel RP (eds) *Asteroids III*. University of Arizona Press, Tucson, pp 739–754
- Nemchinov IV, Svetsov VV, Kosarev IB et al (1997b) Assessment of kinetic energy of meteoroids detected by satellite-based light sensors. *Icarus* 130(2):259–274
- Neukum G (1983) *Meteoritenbombardement und datierung planetarer oberflächen*. Ludwig-Maximilians-University, Munich, p 186
- Neukum G, Ivanov BA (1994) Crater size distributions and impact probabilities on Earth from Lunar, terrestrial-planet, and asteroid cratering data. In: Gehrels T (ed) *Hazards due to comets and asteroids*. University of Arizona Press, Tucson, pp 359–416
- Neukum G, Ivanov BA, Hartmann W (2001a) Cratering records in the inner Solar System in relation to the lunar reference system. *Space Sci Rev* 96(1/4):55–86
- Neukum G, Oberst J, Hoffmann H et al (2001b) Geologic evolution and cratering history of Mercury. *Planet Space Sci* 49:1507–1521
- Öpik EJ (1960) The frequency of crater diameters in mare Imbrium. *Astronom J* 65:55
- Quaide WL, Oberbeck VR (1968) Thickness determinations of the lunar surface layer from lunar impact craters. *J Geophys Res* 73(16):5247–5270
- Rabinowitz DL, Helin E, Lawrence K et al (2000) A reduced estimate of the number of kilometer-sized Near-Earth Asteroids. *Nature* 403:165–166
- Rickman H, Fernandez JA, Tancredi G et al (2001) The cometary contribution to planetary impact rates. In: Marov MY, Rickman H (eds) *Collisional proceedings in the solar system*. 261, Kluwer Academic Publishers, Dordrecht, pp 131–142
- Ronca LB, Basilevsky AT, Kryuchkov VP, Ivanov BA (1981) Lunar craters evolution and meteoroidal flux in pre-mare and post-mare times. *Moon Planets* 245:209–229
- Schmidt RM, Housen KR (1987) Some recent advances in the scaling of impact and explosion cratering. *Int J Impact Engng* 5:543–560
- Shoemaker EM (1965) Preliminary analysis of the fine structure of the lunar surface in Mare Cognitum. In *Jet Propulsion Lab Cal Tech*, Tech Rep 32–700, pp 75–134
- Stöffler D, Ryder G (2001) Stratigraphy and isotope ages of lunar geologic units: chronological standard for the inner Solar System. *Space Sci Rev* 96(1/4):9–54
- Stuart JS (2001) A near-Earth asteroid population estimate from the LINEAR survey. *Science* 294:1691–1693
- Stuart JS, Binzel RP (2004) Bias-corrected population, size distribution, and impact hazard for the near-Earth objects. *Icarus* 170(2):295–311
- Tancredi G, Fernandez JA, Rickman H et al (2000) A catalog of observed nuclear magnitudes of Jupiter family comets. *Astronom Astrophys Suppl Ser* 146:73–90
- van Houten CJ, van Houten-Groeneveld I, Herget P et al (1970) The Palomar-Leiden survey of faint minor planets. *Astronom Astrophys Suppl Ser* 2:339–448
- Vinnik LP, Chenet H, Gagnepain-Beyneix J, Lognonné P (2001) First seismic receiver functions on the Moon. *Geophys Res Lett* 28:3031–3034
- Ward WR (1992) Long-term orbital and spin dynamics of Mars. In: Kieffer HH, Jakosky BM, Snyder CW, Matthews MS (eds) *Mars*. University of Arizona Press, Tucson, pp 298–320
- Weissman PR, Bottke WF, Jr, Levison HF (2002) Evolution of comets into asteroids. In: Bottke W, Cellino A, Paolicchi P, Binzel RP (eds) *Asteroids III*. University of Arizona Press, Tucson, pp 669–686

- Werner SC, Harris AW, Neukum G, Ivanov BA (2002) NOTE: The near-Earth asteroid size-frequency distribution: a snapshot of the lunar impactor size-frequency distribution. *Icarus* 156:287–290
- Wilhelms DE, McCauley JF, Trask NJ (1987) *The geologic history of the moon*. Washington, DC: U.S. G.P.O., pp 302
- Wünnemann K, Collins GS, Melosh HJ (2006) A strain-based porosity model for use in hydrocode simulations of impacts and implications for transient crater growth in porous targets. *Icarus* 180: 514–527

CHAPTER 3

COMETARY HAZARDS

MARINA KUZMITCHEVA AND BORIS IVANOV

Institute for Dynamics of Geospheres, Russian Academy of Sciences, Moscow 119334, Russia
E-mail: kuzm@idg.chph.ras.ru; baivanov@idg.chph.ras.ru

Abstract: A relative role of comets versus asteroids in the bombardment of the inner planets remains questionable. The uncertainty originates from two main problems. The first is that we do not know with adequate accuracy the real sizes of the cometary nuclei that often look detectable with active comas. The second problem lies in the “fading” of comets; and it is important to value a portion of “dormant” comets in a total population of bodies whose orbits intersect with the Earth and planets. This chapter lays out the authors’ vision of the modern aspects of these problems.

1 COMETARY TAXONOMY

Comets are divided in two groups according to time of orbital revolution: the long-period comets (LP) with time of revolution >200 years and the short-period (SP) comets with time of revolution <200 years. In their turn SP comets are divisible into Jupiter-family (JF) comets, with a time of revolution <20 years, and Halley-type comets, with an intermediate time of revolution of 20–200 years. A boundary between LP and SP comets corresponds to the semiaxis $a = (200)^{2/3} = 34.2$ AU. It indicates a difference among comets whose aphelia lie inside or near our planetary system and comets that fly away far from the Sun. Influence of planets on comets with time of revolution >200 years is not correlated with passing on perihelion. A revolution time of 200 years is about equal to the period of telescopic astronomical exploration (Wiegert and Tremaine 1999).

At the end of 1978 for the two preceding centuries of astronomical observations, 113 objects were classified as periodical comets, 72 from 113 were observed in two and more apparitions, 41 were observed in a single apparition; 28 comets, detected earlier, were lost. The majority are short-period ones (Shoemaker and Wolf 1982). Up until 1998 approximately 145 JF comets were known; five or six of which intersect the Earth’s orbit. Twenty-two active Halley-type comets with perihelia <1.3 AU are also known, which may approach Earth. The flux of long-period comets at a distance of 3 AU from the Sun is evaluated as 36 per year (Zahnle et al. 2003).

A specific group of “sun-grazing” comets consists of bodies with a very small perihelion, <0.02 AU. Owing to Sun-exploring missions, small-size (down to diameters of 10 meters) have been detected with a rate of several objects per year, but only the largest ones (with diameters of 1–1.5 km) have survived passing through the perihelion (Biesecker et al. 2002). All of them are treated as debris of one or a few parent bodies. Today these comets are the subject of intense exploration (Sekanina and Chodas 2004; Nemchinov et al. 2005). Since a sun-grazing comet falls into pieces both before and after its perihelion passage, such a comet creates small cometary debris not far from the Earth. This scenario is discussed in the following.

2 ORIGIN OF COMETS: COMET RESERVOIRS

It is generally agreed that comets originate from planetesimals, which accumulated in the feeding zone of giant planets, and then were scattered into the trans-Neptunian zone (the Kuiper-Edgeworth belt) and the periphery of the Solar System (the Oort cloud). Hence, comets can contain 50–90% of volatiles.

In numerical N-body simulations it has been shown that planetesimals decelerated by gas drag grow in mutual collisions. In the course of accumulation a peak in size-frequency distribution (SFD) for bodies with diameters of 10–100 m arises, a speed of mutual collisions also has a minimum of 1-km bodies. Therefore, growing planetesimals should be of low mechanical strength, with caverns, and consist of structural blocks of 10–100 m, which makes them similar to comet nuclei (Weidenschilling 1997).

Comets can come back into the inner part of the planetary system under the action of galactic tides, the close approach of the nearest stars, the resonance influence of giant planets, and collisions. During the life of the Solar System, comets in the Kuiper belt can have undergone collisional evolution, and heat and gravity stratification may occur in the interiors of the most massive comets (Davis and Farinella 1997; Durda and Stern 2000).

From 1992 (the first observations) to 2002 astronomers discovered almost 600 Kuiper belt objects (KBO) with diameters >100 km. There may be 70,000 such objects (Jewitt et al. 1996; Levison and Duncan 1997). The least detected bodies have diameters of 10 km (Cochran et al. 1995). Among KBOs, three different dynamical groups are separated (classic KBO, scattered KBO, and Plutinos). The scattered objects on inclined orbits are affected by the gravity perturbations of Neptune, and are considered a main source of the short-period comets in the inner planetary region.

The Oort cloud contains the most peripheral objects in the Solar System. It is supposed to be a storage place for long-period comets. The number of these comets is determined to be as large as 10^{12} – 10^{13} with semiaxes $10^{3.5}$ – $10^{4.5}$ AU. The bodies are >10 km (Stern and Weissman 2001). They preserve the significant amount of volatiles that give rise to the early appearance of comas, bursts, and even breakup.

3 ORBITAL AND PHYSICAL EVOLUTION OF COMETS

The results of numerical simulations of SP comets' orbital behavior conducted by several research groups form a statistical description of comet orbital evolution. This method has also been used for LP and Halley-type comets.

By numerical simulations (Levison and Duncan 1994, 1997; Tancredi 1994; Fernandez et al. 2002) it has been shown that a typical ecliptic comet (the former KBO) lives in the Solar System for 45 million years before being ejected from the System or falling into the Sun. During this time the comet turns to and from the Jupiter and Halley-type families ~ 10 times. A median time of the one visit to JF is 13,500 years (Tancredi 1994). The comet may be active for 4,200 years. Afterward a dusty mantle is formed on the surface of the comet that prevents a coma from developing (Rickman et al. 1990).

In modeling, it is often said (Levison and Duncan 1997) that a comet may be visible (active) if its perihelion is < 2.5 AU. A characteristic "fading" time is evaluated to estimate the proportion of "dormancy" due to mantle formation in a whole cometary population. Levison and Duncan have estimated the ratio of dormant to active comets to be 10:20. Can a comet be reactivated? Tancredi (1994) has supposed that it is possible if a dormant comet is found in an orbit with a short perihelion for the next visit to a JF.

A modern study shows the essential reduction in the number of dormant comets in the vicinity of the Earth (Fernandez et al. 2002). Near-Earth comets are dormant; they spend no more than 40% of their total time in the region of the inner planets, because comets are physically disintegrated into meteor streams. In May of 2006 the comet Sqhwassmann-Wachmann 3 demonstrated a spectacular example of such breakup.

Numerical simulation of the orbital evolution of long-period comets has shown that some of them may have orbits similar to Halley-type comets (Levison and Duncan 1994). "New" comets come to the Sun from the Oort cloud. The best agreement with the observable population of LP comets can be achieved if the fading rate is proportional to $m^{-0.6}$, where m is a number of recoveries (Wiegert and Tremaine 1999). Consequently, the observable population of LP comets contains 20% of new comets.

4 SIZES OF COMETS AND THEIR MULTIPLICITY

An impact rate onto the Earth is proportional to the number of minor bodies that intersect its orbit. Because of inopportune observational conditions, observational period limitations, remoteness of the object from the observer, and so on, not every hazardous object can be detected. A complete population is reconstituted with the help of an observed population as well as with ratio of size and luminosity, SFDs deduced from crater records, the proportion of dormant and active comets, and so on.

The systematic astrometric measurement of comets began in 1957 (Roemer 1965, 1966; Roemer and Lloyd 1966; Roemer et al. 1966). These data became the basis

for the study of the SFDs of different cometary populations. Comet nuclei are currently under investigation (Fernandez et al. 1992; Licandro et al. 2000; Tancredi et al. 2000). A divergence of modern data on stellar magnitudes with Roemer's <1.0 and looks comparable with color variations in magnitude and variations due to rotation of nonspherical nuclei.

The absolute stellar magnitude, H , of a comet nucleus is sensible to the presence of coma, so to eliminate this influence all measurements are carried out at maximal distances from the Sun. Cometary nuclei are treated as spherical bodies with surface photometric properties like those for asteroids. The nucleus radius R_N is defined as:

$$\log R_N = 2.4986 - 0.2 \cdot H_V - 0.5 \log p_V, \quad (1)$$

where p_V is albedo, and H_V is the absolute stellar magnitude. Cometary albedos are low, and are equal to 0.02–0.05; therefore, the radius of a comet nucleus with a reference magnitude $H = 18$ and albedo 0.04 is equal to 1.66 km.

Photometric data H_V , $\sigma(H_V)$ and nucleus radii R estimated for 18 JF comets (Licandro et al. 2000) are pictured in Table 1 ($\sigma(H_V)$ is an order of magnitude, q and Q are perihelion and aphelion in AU). The comet 37P/Forbes has the smallest radius (1 km) among these; the comet 65P/Gunn has the largest radius of 11 km, in the latter case the comet was very active. LP comet nuclei are usually greater than those of SP comets.

Table 1. Magnitudes of comet nuclei and estimates of their radii. The table is adapted from Licandro et al. (2000) and reprinted with kind permission of Elsevier

Comets	H_V	$\sigma(H_V)$	R, km	q	Q
49P/Ashbrook-Jackson	15.2	0.14	3.0	2.32	5.34
37P/Forbes	17.6	0.2	1.0	1.44	5.24
82P/Gehrels 3	>> 15.4	0.2	<2.8	2.35	5.61
26P/Grigg-Skjellerup	16.9	0.06	1.4	0.99	4.93
65P/Gunn	>> 12.4	0.11	<< 11.0	2.46	4.74
52P/Harrington-Abell	16.9	0.2	1.4	1.78	5.94
103P/Hartley 2	>> 14.1	0.07	<< 5.0	0.96	5.84
48P/Johnson	14.9	0.2	3.5	2.31	4.99
96P/Machholz 1	14.8	0.1	3.6	0.13	5.91
97P/Metcalf-Brewington	16.9	0.22	1.4	1.59	6.25
137P/Shoemaker-Levy 2	14.5	0.1	4.2	1.84	6.98
74P/Smirnova-Chernykh	>> 12.5	0.04	<< 10.5	3.57	4.81
64P/Swift-Gehrels	16.7	0.1	1.5	1.35	7.43
98P/Takamizawa	14.9	0.2	3.5	1.59	5.89
8P/Tuttle	13.3	0.05	7.3	1.00	10.34
53P/Van Biesbroeck	> 13.6	0.2	< 6.3	2.40	8.34
43P/Wild 2	>> 14.0	0.2	<< 5.3	1.58	5.37
43P/Wolf-Harrington	> 15.3	0.05	<< 2.9	1.61	5.37

The majority of SP comets have perihelia $q < 4.5$ AU. Shoemaker and Wolf (1982) supposed that a number of comets grows linearly with q ($q > 1.1$):

$$N(< q) = 64q - 58. \quad (2)$$

Today it is certain that all comets with $q < 1.3$ AU have already been found, since the annual number of newly detected comets is extremely low (Marsden 1986; Marsden and Williams 2003). For $1.3 < q < 2$ AU the number of comets is written as follows:

$$N(< q) = 100q - 100. \quad (3)$$

In Fig. 1, a cumulative distribution of $N(> d)$ (where N is a number of bodies whose diameters are larger than d) of JF comets is presented in comparison with the same distribution of Main Belt asteroids and Jupiter Trojans. An approximation of the distributions onto smaller diameters (shown as a solid thick line) is made with SFD of impactors based on lunar crater records (Ivanov et al. 2001). On the whole, Main Belt asteroids are substantially more numerous than JF comets, of course (by a factor of 10^4). Small comets are discussed in a separate section.

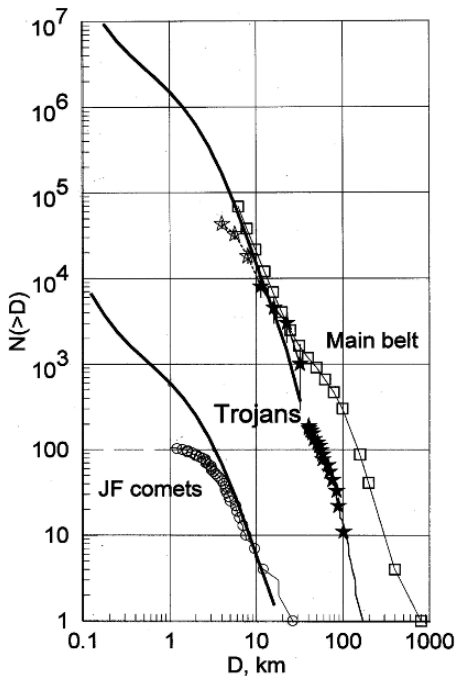


Figure 1. Populations of small bodies in the Solar System

It is more difficult to monitor LP than SP comets, although they stay active longer. A number of LP comets have been evaluated by Everhart's relation ($q > 1.3$ AU):

$$N(< q) = 500q - 175. \quad (4)$$

Thus, LP comets are more manifold than SP comets. A definite deficit of LP comets may occur near the Sun due to the influence of the Sun and planets (Kresak 1978): $N(< q) \propto q^{1.5}$. Some numerical simulations of the Oort cloud evolution give a steeper dependence: $N(< q) \propto q^2$ (Weissman et al. 1989; Zahnle et al. 2003). If about 36 active LP comets pass through the area of 3 AU near the Sun per year, then (Wiegert and Tremaine 1999; Zahnle et al. 2003):

$$\dot{N}(< q) = 36(q/3AU)^2. \quad (5)$$

Today 22 active Halley-type comets are known to pass near the Sun at a distance < 1.3 AU as frequently as 0.46 per year. Levison et al. (2002) suppose that $N(< q) \propto q$ for Halley-type comets, and the comets already found are 26% of the total population, with perihelia < 1.3 AU; therefore, the per-year flux is expressed as:

$$\dot{N}(< q) = 1.8 \cdot (q/3AU). \quad (6)$$

Comets are main impactors of planets and moons in the outer Solar System (Shoemaker and Wolf 1982). Size-frequency distributions (SFD) for hitting bodies (comets) have been obtained from SFDs for crater fields with known scaling laws. The following cumulative SFDs $N(> d) \propto d^{-b}$ have been obtained on different moons based on Galileo team data (Zahnle et al. 2003):

- For ~ 100 craters with diameters > 1 km on Europa, the degree $b = 0.9$ for comets with $d < 1$ km. It appears that the SFD becomes steeper for $d > 1$ km.
- For crater fields on Ganymede, $b = 1.7$ for comets in a size range $2 < d < 5$ km and $b = 2.5$ for comets with a size of $5 < d < 20$ km.

For Jovian moons the comet population looks depleted in small bodies. For the Neptunian moon Triton the SFD for impactors is much steeper: $b = 2.5$. Such a distribution is formed in bodies with strengths independent of their sizes under a cascade of disruptive collisions (Williams and Wetherill 1994). It appears reasonable to suggest that many smaller comets disappear while migrating from Neptune to Jupiter. SFDs deduced for the outer planetary system are presented in Fig. 2.

5 SMALL COMETS

The existence of small comets has been discussed for many years. This chapter does not discuss "Frank's small comets" (Frank et al. , 1986), because they appear to be artifacts. Shatters of disintegrated normal comets can be considered as small comets (e.g., Shoemaker-Levy 9, LINEAR C/1999 S4, Machholz 2, Schwassmann-Wachmann 3) their number can be qualified. All estimates of the cratering rate

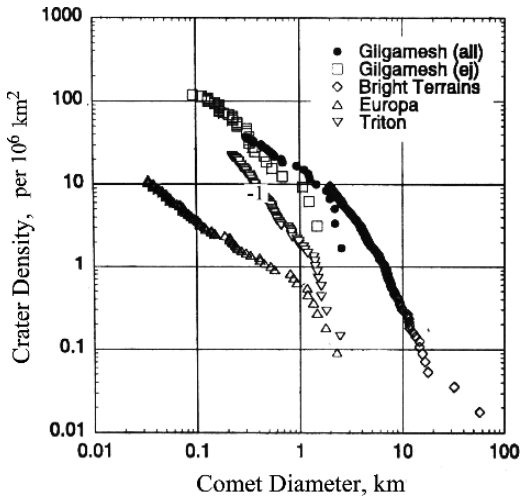


Figure 2. Size distribution of impacting bodies obtained from the observations of young surfaces of moons in the outer Solar System (Zahnle et al. 2003)

for small-scale craters are based on extrapolation of impactor SFD into a range of small bodies that are not available yet for direct observations (Shoemaker and Wolf 1982; Brandt et al. 1996; Zahnle et al. 2003). This chapter discusses plausible causes of depleting small comets in comparison with the power law extrapolation.

First, there are causes that could be named “generic.” The preceding considered a scenario in which comets were accumulated in a zone of giant planets and then were separated dynamically into the Kuiper Belt and the Oort cloud. If small comets could disappear at the early stage, the deficit would be revealed in the distribution of LP comets. Planetesimals under accretion were affected by gas drag (Whipple 1972). The smallest bodies fall into the Sun; comparatively large ones, kilometer-sized and greater, move around the Sun along Keplerian orbits. From numerical simulations it follows that a deficit of nuclei <100 m, but this gap may be filled by debris of bodies shattered in mutual collisions (Weidenschilling 1997).

Suppositions of the second type may be qualified as “evolutionary.” Numerical modeling of orbital dynamics of comets (Tancredi 1994; Banaszkiewicz and Rickman 1996), if one takes “fading” into account, a permanent decrease in comet nuclei mass develops. Formation of a mantle of dusty particles on a surface of nuclei leads to reduction in evaporation rate by orders of magnitude, and coma develops due to jets from active areas. The following model of mantling has been accepted (Rickman et al. 1990; Coradini et al. 1997): Dusty particles are captured by gas flow of evaporating volatiles, but the most massive of those are held by the gravity of the nucleus. Solar radiation controls evaporation and, hence, the mantling rate. If the diameter of a comet is less than some critical value, the process of mantle formation has no time to protect a nucleus from evaporation. For a

distance from the Sun equal to 1 AU and a rate of mantling 10^{-3} sm·year $^{-1}$ this critical diameter is 1.6 km (Banaszkiewicz and Rickman 1996).

Small comets could emerge in the Kuiper belt as a result of a cascade of mutual disruptive collisions. The Kuiper Belt contains as many as 10^3 bodies if compared with asteroids of the Main Belt, but the relative speed of collisions is 10 times less. For the age of the Solar System, collisions were able to modify size distribution of the population. By numerical simulations of a collisional evolution in the Kuiper belt (Farinella and Davies 1996; Durda and Stern 2000) it has been shown that in the population 10–50% of primordial bodies with diameters 20 km could survive, and comets with diameters of a few kilometers were probably collision debris, although in the initial population that sort of body would be necessary to run a collisional cascade. This debris could then migrate to Jupiter through gravity resonances.

It is supposed that there are $2 \cdot 10^4$ SP comets with a typical lifetime of $3 \cdot 10^5$ years; hence, a comet flux of 0.06 per year is needed to maintain the population. In the Kuiper Belt 10 comets with diameters of 2–10 km emerge per year, and some percentage of them migrate into the planetary region. A flux of 100-m debris is almost 10^3 times higher in accordance with power law SFD. How long can the debris survive among JF comets?

Kuzmitcheva and Ivanov (2002) have evaluated a lifetime controlled by sublimation of small comets on orbits typical for JF comets. Nuclei of known SP comets are almost inactive in a sense that gas evaporates from about 10% of their surface. Nevertheless, the gravity of small comets is too low to form a dusty mantle. Heating of a comet by solar radiation is described with heat conductivity and balance on the surface without influence of coma, which is reasonable at a distance >0.5 AU from the Sun. Energy balance on the surface at a distance r from the Sun is written as:

$$\chi(1 - A_V)F_0 r^{-2} = (1 - A_{ir})\sigma \cdot T_s^4 + H(T_s)Z(T_s) - K(T_s)\frac{\partial T}{\partial \xi}, \quad (7)$$

where T_s is temperature in K, $K(T_s)$ is heat conductivity, ξ is depth, A_V and A_{ir} are albedo in visible and infrared, F_0 is a solar constant, H is a specific heat of sublimation, Z is a rate of sublimation, σ is a Stefan-Boltzmann constant, and χ describes a geometry of irradiation. In values K and Z a porosity of cometary matter and shielding of a comet's surface by dust particles are taken into account. Comet albedo is as low as 0.02 to 0.05, so one neglects the energy expense due to sublimation and into the nucleus, as comet surface temperature becomes close to the black body temperature. With the contribution of cosmic rays a surface temperature of a fast-rotating black body at a distance r from the Sun is expressed as follows:

$$T_m = 290 \cdot r^{-0.48}, \quad (8)$$

where T_m is in K and r is in AU.

Results of simulations for the comet with a radius of 100 m are shown in Figs. 3 and 4. In Fig. 3 (the upper panel) the radius reduction rate and surface temperature

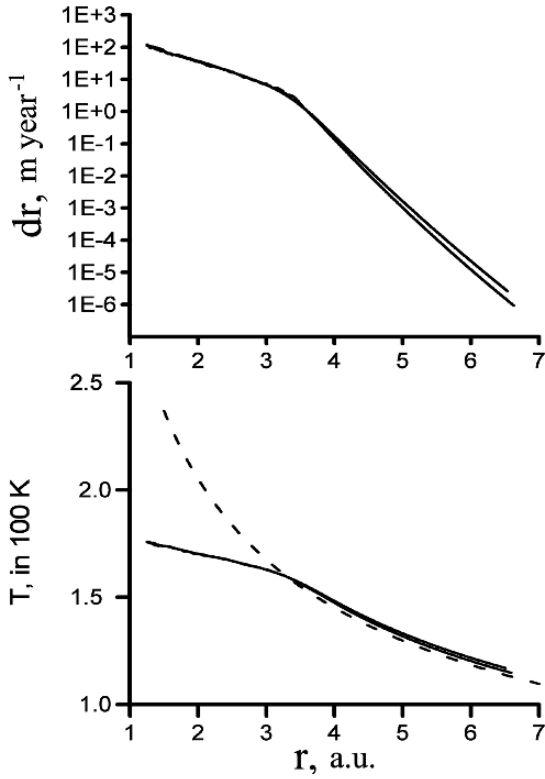


Figure 3. Surface temperature of a comet nucleus and a rate of radius decrease versus distance to the Sun

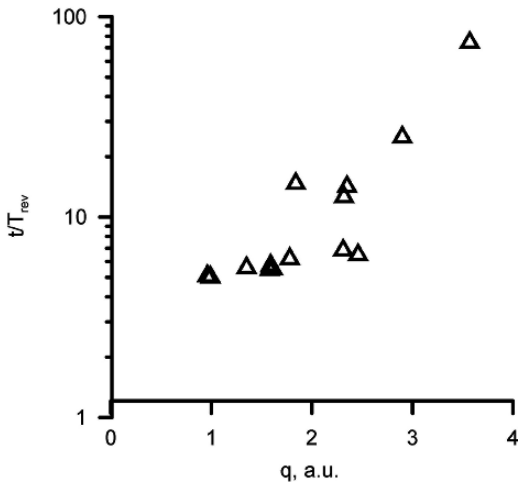


Figure 4. Lifetime of comets with 100-m radii in orbits of short-period comets as a function of perihelion

(the lower panel) versus the distance from the Sun are presented. The low branches of solid curves refer to motion from aphelion to perihelion; the upper ones pertain to reverse motion. For comparison the model temperature T_m is plotted as a dashed line. One can see that the radius reduction rate depends strongly on the surface temperature. Heat conductivity of porous cometary matter is low, and while a comet moves to perihelion, the rate of sublimation grows. A heated layer is whirled away, and the surface temperature falls lower than the model's.

Almost all comets under consideration have orbits with an eccentricity of 0.5, and the radius reduction mainly takes place near perihelion. In Fig. 4 lifetimes of small comets referred to times of revolution versus perihelion distances q (in AU) are presented. All bodies within a radius of 100 m and $q < 2$ AU are vaporized for about of 10 revolutions, equal to 50–150 years. Lifetimes of small comets decrease with a decrease in size. The deficit of small bodies in the vicinity of Jupiter in comparison with those in Neptune's zone (Zahnle et al. 2003) confirms the authors' results concerning the sublimation of small comets.

What happens to debris if a comet disintegrates in the vicinity of the Earth? It is known that 10 JF comets that disappeared due to disintegration had perihelia < 1.3 AU (Fernandez et al. 2002). Disintegration looks very probable for sun-grazing comets, even in post-perihelion motion.

The authors have assumed that a comet breaks down at a distance of 1 AU and have taken the results for small JF comets. Extrapolating to a distance of 1 AU, the surface temperature of about 175 K and the radius reduction rate of $1.5 \cdot 10^2$ m \cdot year $^{-1}$ have been extrapolated. Thus, a lifetime of a 100-m comet is only about 8 months. If the surface temperature rises up to 200 K, the lifetime decreases to 1 week.

Asher and Stell (1998) investigated the problem of a possible origin of the Tunguska bolide from 2P/comet Encke. (Its diameter is 1–3 km, perihelion is 0.33 AU, eccentricity is 0.85, and major semiaxis is 2.21 AU.) The Tunguska event differs by only 1 day from the maximum of a diurnal meteor shower of β -taurids associated with the comet. Since the perihelion of this comet is rather close to the Sun, it was supposed that the comet was broken down on passing through the perihelion similar to other disintegrated comets. Today (as in 1908) the orbit of this comet does not intersect an orbit of the Earth, but the orbital parameters vary due to dynamic action. It has been shown that a piece of the comet could encounter the Earth $< 10,000$ years after a partial disintegration of the comet. In the authors' opinion, a small comet fragment could not survive such a time period near the Earth, provided that cometary matter is more or less homogeneous.

In connection with numerous observations of minute sun-grazing comets that are considered as debris of parent comets, it was proposed that comets could be disintegrated far from the Sun and not due to tidal mechanism. Since the reasons of primary disintegration of parent bodies are unknown, their times of revolution are estimated to be from 4.5 to 350 years. Orbits of observable sun-grazing comets do not intersect the Earth's orbit.

6 THE COMPARATIVE ROLE OF COMETS AND ASTEROIDS IN THE BOMBARDMENT OF TERRESTRIAL PLANETS

The comparative role of comets and asteroids remains questionable because of the previously mentioned uncertainties. This section summarizes existent appraisals. In the first place it is necessary to remind a history the hypothetically great importance of comet impacts in comparison with those of asteroids.

Since the Voyager mission passed by Jupiter, moons with crater fields have been discovered. Shoemaker and Wolf (1982) published their estimates for cratering on these bodies. They have come to the conclusion that JF comets are main impactors for moons of these giant planets. This thesis remains accepted today (Zahnle et al. 2003). An alternative situation is presented for the terrestrial planets, including the Earth and Moon, in which the impact probability of asteroids and LP comets exceeds that of JF and SP comets. To compare a relative role of asteroids and LP comets, Shoemaker focused on ideas concerning the orbital evolution of minor bodies accepted at that time. It was adopted that the evolution of asteroids is controlled by close approaches with planets; therefore, a lifetime of minor bodies in orbits intersecting the orbits of planets was evaluated. A quasi-stationary population of bodies in such orbits was supposed to be maintained by collisions in the Main Belt. Shoemaker has evaluated the low probability of disruptive large asteroid collisions that lead to the deficiency of impactors to form craters on the Earth $> \sim 30$ km. Shoemaker decided that LP comets created the residual craters.

The successful development of methods of celestial mechanics has led to the principal renewal of ideas about asteroidal transitions in the orbits, intersecting with the inner planets. Orbital evolution of the Main Belt asteroids is controlled by gravitational resonances with Jupiter and Saturn. The pioneering work of Farinella et al. (1994) was followed with a wide exploration of orbital dynamics, which showed that a phase space is filled by strong and weak resonances that control fast or slow diffusion of small bodies to orbits intersecting the orbits of terrestrial planets. Modern methods of numerical simulations of orbital evolution in combination with progress in astronomical observations have permitted researchers to build a new system of ideas on evolution and intensity of asteroid flux cratering terrestrial planets (Froeschle et al. 1995; Bottke et al. 2000,2002; Gladman et al. 2000). Shoemaker's prior conclusion about the dominant role of LP comets in the formation of large craters is not necessarily in accord with new concepts. Table 2 presents typical relative values of parabolic comets' impact frequencies.

In accordance with the assumption that 40 ± 10 unobservable comets exist for every detected comet, values of the impact frequency of JF comets have been obtained for Jupiter and terrestrial planets (Table 3) (Nakamura and Kurahashi 1998). Although all the estimates are valid with an accuracy of factor 3, one can see what a rare event an impact of a periodical comet onto the Earth is if compared with impacts onto Jupiter, which humanity watched in 1994.

Table 2. Typical comparative estimates of frequency of impacts of parabolic comets on planets, impact velocity, and rate of accumulation of comet impact craters (Zimbelman 1984; Steel 1993)

Planet	Everhart (1967) Impact number; Jupiter = 100	Zimbelman (1984) Impact number*; Jupiter = 100	Rate of crater accumulation per unit surface (Earth = 1)	Most probable impact velocity, km-s ⁻¹
Mercury	0.06	0.15	6.3	89.3
Venus	0.50	0.55	1.7	66.0
Earth	0.36	0.42	1	56.2
Moon	—	0.03	2.1	59.8
Mars	0.04	0.08	0.7	45.3
Jupiter	100.00	100.00	no craters	63.6

*Average impact probability for a parabolic comet with the Earth is $(3 \pm 1) \times 10^{-9}$ per one comet passage through perihelion (Dones et al. 1999).

Table 3. Estimates of impact frequencies for periodic comets

Planet	Average probability of a single comet impact,* years ⁻¹	Full impact probability for the population N(D > 1 km)~7000*	Averaged time between impacts
Venus	4.0×10^{-11}	$\sim 28 \times 10^{-6}$	~4 My
Earth	5.0×10^{-11}	$\sim 35 \times 10^{-6}$	~3 My**
Mars	5.7×10^{-12}	$\sim 4 \times 10^{-6}$	~25 My
Jupiter	$(3.6 - 4.5) \times 10^{-7}$	$\sim 7 \times 10^{-4}$	~400 years

*Estimates taking into account orbit dynamics of a periodic comet (Nakamura and Kurahashi 1998).

**A mean time between impacts of asteroids with $M < 18$ on the Earth is 0.5–1 My, i.e., asteroids impact the Earth three to six times more frequently than comets of commensurate size (see Chap. 2).

7 SUMMARY

For the Earth, comets are an auxiliary population of impactors. Impact probabilities of small cometary debris migrating from the Kuiper belt are negligible in comparison with that of small asteroids. Nevertheless, the evolution of the cometary population and their flux into the inner planetary area are modeled with obvious uncertainties since cometary store reservoirs are found far from the Sun. Nuclei of all “old” comets have low albedos. It is harder to detect them than asteroids of the same size; consequently, the “inactive” ecliptic comets can be extremely hazardous (Napier et al. 2004). Progress in the detection of asteroids in the inner part of the Solar System will permit researchers to draw up a full catalog of hazardous bodies earlier or later, although the appearance of new comets always remains unpredictable. Hence, exploring comets and a search for collision marks with comets on terrestrial planets will be important and tangible.

REFERENCES

- Asher DJ, Stell DI (1998) On the possible relation between the Tunguska bolide and comet Encke. *Planet Space Sci* 46(2/3):205–211
- Banaszkiewicz M, Rickman H (1996) Modeling of cometary evolution by kinetic theory: Method and first results. *Earth Moon Planets* 72:203–210
- Biesecker DA, Lamy P, Llebaria A et al (2002) Sungrazing comets discovered with the SOHO/LASCO coronagraphs 1996–1998. *Icarus* 157:323–348
- Botke WF, Jedicke R, Morbidelli A et al (2000) Understanding the distribution of Near-Earth asteroids. *Science* 288:2190–2194
- Botke J, William F, Morbidelli A et al (2002) Debiased orbital and absolute magnitude distribution of the Near-Earth Objects. *Icarus* 156(2):399–433
- Brandt JC, A'Hearn MF, Randall CE et al (1996) On the existence of small comets and their interactions with planets. *Earth Moon Planets* 72:243–249
- Cochran AL, Levison HF, Stern SA et al (1995) The discovery of Halley-sized Kuiper belt objects using the Hubble space telescope. *Astrophys J* 455:342–346
- Coradini A, Capaccioni F, Capria MT et al (1997) Transition elements between comets and asteroids. I. Thermal evolution models. *Icarus* 129:317–336
- Davis DR, Farinella P (1997) Collisional evolution of Edgeworth-Kuiper Belt objects. *Icarus* 125:50–60
- Dones L, Gladman B, Melosh HJ et al (1999) Dynamical lifetimes and final fates of small bodies: Orbit integrations vs opik calculations. *Icarus*. 142(2):509–524
- Durda DD, Stern SA (2000) Collision rates in the present-day Kuiper Belt and Centaur regions: applications to surface activation and modification on comets, Kuiper Belt Objects, Centaurs, and Pluto-Charon. *Icarus* 145:220–229
- Everhart E (1967) Intrinsic distributions of cometary perihelia and magnitudes. *Astron. J* 72:1002–1011
- Farinella P, Davies ME (1996) Short-period comets: primordial bodies or collisional fragments? *Science* 273:938–941
- Farinella P, Froeschle Ch, Froeschle C et al (1994) Asteroids falling onto the Sun. *Nature* 371:315–317
- Fernandez JA, Gallardo T, Brunini AN (2002) Are there many inactive Jupiter-family comets among the Near-Earth asteroid population? *Icarus* 159:358–368
- Fernandez JA, Rickman H, Kamel L (1992) The population size and distribution of perihelion distances of the Jupiter family. In: Fernandez JA, Rickman H (eds) *Periodic comets*. Universidad de la Republica, Facultad de Ciencias, Montevideo, Uruguay, pp 143–157
- Frank LA, Sigwarth JB, Craven JD (1986) On the influx of small comets into the earth's upper atmosphere. I. Observations. II. Interpretation. *Geophys Res Lett* 13:303–310
- Froeschle C, Hahn G, Gonczi R et al (1995) Secular resonances and the dynamics of Mars-crossing and Near-Earth asteroids. *Icarus* 117:45–61
- Gladman B, Michel P, Froeschlé C (2000) The Near-Earth object population. *Icarus* 146:176–189
- Ivanov BA, Neukum G, Wagner R (2001) Size-frequency distribution of planetary impact craters and asteroids. *Collisional Processes in the Solar System*. Marov MY, Rickman H (eds). *Astrophys Space Sci Library* 261. Kluwer Academic Publishers, Dordrecht, pp 1–34
- Jewitt D, Luu J, Chen J (1996) The Mauna Kea-Cerro-Tololo (MKCT) Kuiper Belt and Centaur Survey. *Astronomical Journal* 112:1225
- Kresak L, Pittich EM (1978) The intrinsic number density of active long-period comets in the inner solar system. *Bull Astronom Instit Czechoslovakia* 29:299–309
- Kuzmitcheva MY, Ivanov BA (2002) Probable populations of projectiles for Galilean moons. Conference Asteroids, Comets, Meteors (ACM2002). Berlin, July 29–August 2, 2002. Technical University Berlin. Berlin. Germany (ESA-SP-500), pp 851–853
- Levison HF, Duncan MJ (1994) The long-term dynamical behavior of short-period comets. *Icarus* 108:18–36
- Levison HF, Duncan MJ (1997) From the Kuiper Belt to Jupiter-Family comets: the spatial distribution of ecliptic comets. *Icarus* 127:13–32

- Levison HF, Morbidelli A, Dones L et al (2002) The mass disruption of Oort Cloud comets. *Science* 296:2212–2215
- Licandro J, Tancredi G, Lindgren M et al (2000) CCD photometry of cometary nuclei, I: Observations from 1990–1995. *Icarus* 147:161–179
- Marsden BG (1986) Catalogue of cometary orbits. *Intern Astronom Union Circular* 4168, 2
- Marsden B, Williams G (2003) Catalogue of cometary orbits. *Smithsonian Astrophysical Observatory*, p 169
- Nakamura T, Kurahashi H (1998) Collisional probability of periodic comets with the terrestrial planets—an invalid case of analytic formulation. *Astronom J* 115:848–854
- Napier WM, Wickramasinghe JT, Wickramasinghe NC (2004) Extreme albedo comets and the impact hazard. *Month Not R Astronom Soc* 355:191–195
- Nemchinov IV, Kosarev IB, Kovalev AT et al (2005) Impacts of comets onto the Sun and coronal mass ejections. *Geophysical Research Abstracts* 7, 04384. SRef-ID: 1607-7962/gra/EGU05-A-04384
- Rickman H, Fernandez JA, Gustafson BAS (1990) Formation of stable dust mantles on short-period comet nuclei. *Astronom Astrophys* 237:524–535
- Roemer E (1965) Observations of comets and minor planets. *Astronom J* 70:397–402
- Roemer E (1966) The dimensions of cometary nuclei. In: *Les Congres et Colloques de Universite de Liege. Colloque international tenu al'Universite de Liege* 5,6 et 7 julliet 1965, 37:23–28
- Roemer E, Lloyd RE (1966) Observations of comets, minor planets, and satellites. *Astronom J* 71: 443–457
- Roemer E, Thomas M, Lloyd RE (1966) Observations of comets, minor planets, and Jupiter VI H. *Astronom J* 71:591–601
- Sekanina Z, Chodas PW (2004) Fragmentation hierarchy of bright sungrazing comets and the birth and orbital evolution of the Kreutz System. I Two-superfragment model. *Astronom J* 607(1):620–639
- Shoemaker EM, Wolf RF (1982) Cratering time scales for the Galilean satellites. In: *Morrison D (ed) Satellites of Jupiter*. University of Arizona Press, Tucson, pp 277–339
- Steel DI (1993) Collisions in the solar system. V – Terrestrial impact probabilities for parabolic comets. *Monthly Notices of the Royal Astronomical Society* 264:813
- Stern SA, Weissman PR (2001) Rapid collisional evolution of comets during the formation of the Oort cloud. *Nature* 409:589–591
- Tancredi G (1994) Physical and dynamical evolution of Jupiter family comets: Simulations based on the observed sample. *Planet Space Sci* 42:421–433
- Tancredi G, Fernandez JA, Rickman H et al (2000) A catalog of observed nuclear magnitudes of Jupiter family comets. *Astronom Astrophys Suppl Ser* 146:73–90
- Weidenschilling SJ (1997) The origin of comets in the Solar Nebula: a unified model. *Icarus* 127:290–306
- Weissman PR, Dobrovolskis AR, Stern SA (1989) Constraints on impact rates in the Pluto-Charon system and the population of the Kuiper comet belt. *Geophys Res Lett* 16:1241–1244
- Whipple FL (1972) On certain aerodynamic processes for asteroids and comets. In: *From plasma to planet*. Elvius A (ed) Wiley, New York, pp 211–232
- Wiegert P, Tremaine S (1999) The evolution of long-period comets. *Icarus* 137:84–121
- Williams DR, Wetherill GW (1994) Size distribution of collisionally evolved asteroidal populations—analytical solution for self-similar collision cascades. *Icarus* 107:117–128
- Zahnle K, Schenk P, Levison H et al (2003) Cratering rates in the outer Solar System. *Icarus* 163(2): 263–289
- Zimbelman JR (1984) Planetary impact probabilities for long-period comets. *Icarus* 57:48–54

CHAPTER 4

BOLIDES IN THE EARTH ATMOSPHERE

OLGA POPOVA AND IVAN NEMCHINOV

Institute for Dynamics of Geospheres, Russian Academy of Sciences, Moscow 119334, Russia
E-mail: olga@idg.chph.ras.ru; ivvan@idg.chph.ras.ru

Abstract: The incremental influx of cosmic material on the Earth shows few maxima in the dependence on the size of falling meteoroids (Ceplecha 1992). The largest one corresponds to the impact of asteroid-sized bodies—about 3 km in size and mass of about 10^{14} kg. The second maximum reaches almost the same value and corresponds to the bodies with masses of 10^4 – 10^6 kg (i.e., with diameters about 1–10 m). The information about these meteoroids is scarce. These bodies create the appearance of very bright meteors in the Earth's atmosphere (bolides and superbolides). Sizes of these bodies are one to two orders of magnitude smaller than the sizes of meteoroids, which create asteroid hazards. It is possible to observe bolides and superbolides on a regular basis.

1 BOLIDES NETWORKS

The first photographic bolide network (Prairie Network, USA) was operated in 1964–1975. Sixteen photographic stations covered an area about $1.7 \cdot 10^6 \text{ km}^2$ (McCrosky et al. 1976, 1977). The European bolide Network (EN) was established in the early 1970s. About 50 stations cover about 10^6 km^2 in Germany, the Czech and Slovak Republics as well as parts of Belgium, Switzerland, and Austria. The European bolide Network is currently in operation (Oberst et al. 1998). The Canadian bolide Network operated from 1971 to 1985. Its 12 stations covered about 10^6 km^2 (Halliday et al. 1996). There is also a small camera network in Great Britain, which was established by amateur astronomers in 1973. The first two stations of the Spain bolide Network started regular observations in 2003. Extensive meteor observations were carried out in the Astrophysical Institute in Tadzhikistan (Babadzhanov 1986).

Recently a new bolide network (Desert Network) was established in the desert region of Western Australia (Bland et al. 2006). The aim of this project is to observe fireballs, calculate orbits, triangulate fall positions, and recover meteorites in a place with large number of clear sky nights and suitable conditions for locating meteorites. Currently it comprises three autonomous cameras and covers an area of approximately $(0.3\text{--}0.4) \times 10^6 \text{ km}^2$.

The bolides networks have detected more than 1,000 bolides. The largest bolides (brighter than -15^m) registered by EN are collected in Table 1 (Oberst et al. 1998; Spurný and Porubčan 2002; Spurný et al. 2003).

Number, date of event, maximal intensity (in stellar magnitudes, m_{max}), mass estimate (M), classification according Ceplecha et al. (1998), beginning (H_B), maximal light (H_M) and end (H_E) altitudes and entry velocity (V_B) are listed. The Prairie Network had recorded three bolides brighter than -15^m (McCrosky et al. 1976, 1977).

In a few cases bolide networks detected bolides, and then meteorites were found. Meteorites Příbram, Czechoslovak Republic, 1959 (Ceplecha 1961), Lost City, USA, 1970 (Ceplecha 1996), Innisfree, Canada, 1977 (Halliday et al.1981), and Neuschwanstein, Germany, 2002 (Spurný et al. 2003; ReVelle et al. 2004) were recorded as bolides during their flight. Bolide networks appear to be less effective in the search for meteorites than was initially expected, but bolide networks are a unique source of information about meteoroids' physical properties as well as the spatial and temporal distribution of extraterrestrial matter in the near Earth space.

The flights of three more meteorites were recorded by video cameras of occasional eyewitnesses: Peekskill, Canada, 1992 (Brown et al.1994), Moravka, Czech Republic, 2000 (Borovička et al. 2001; Borovička and Kalenda 2003), Villalbeto de la Peña, Spain, 2004 (Trigo-Rodríguez et al. 2004; Llorca et al. 2005). Besides, the falls of six meteorites were detected by satellite observational network (SN): St. Robert, Canada, 1994 (Brown et al. 1996); Juancheng, China, 1997 (Wacker et al. 1998); Tagish Lake, Canada, 2000 (Hildebrand et al. 2000; Brown et al. 2002a); Moravka, Czech Republic, 2000 (Borovička et al. 2001; Borovička

Table 1. Brightest EN bolides

Event	Date	Name	m_{max}	M, kg	type	H_B km	H_M km	H_E km	V_B km·s ⁻¹
19241	07.04.1959	Příbram	-19.2	11000	I	98	46	13	20.89
EN 151068	15.10.1968	Cechtice	-15.5	800	II	72	45	30	19.02
EN 100469	10.04.1969	Otterskirchen	-15.4	2500	II	84	45	24	16.08
EN 241170	24.11.1970	Mt.Riffler	-15.1	1500	I	83	41	26	21.17
EN 170171	17.01.1971	Wirzburg	-17.0	3200	IIIb/II	75	60	45	15.7
EN 041274	04.12.1974	Šumava	-21.5	3000	IIIb	99	73	55	27.0
EN 010677	01.06.1977	Freising	-16.9	2600	II	78	47	27	27.0
EN 140977A	14.09.1977	Brno	-16.2	1500	II	97.8	60	40	30.2
EN 070591	07.05.1991	Benešov	-19.5	4000	I-II	98	26	16	21.1
EN 220293	22.02.1993	Meuse	-17.3	3000	IIIb	77	-	21.5	26.7
EN 221095	22.10.1995	Visla	-17.1	900	I	-	-	-	-
EN 251095A	25.10.1995	Tisza	-16.1	890	I	80.5	-	26.5	29.22
EN 231195	23.11.1995	J.Hradec	-16.9	3600	I	93	-	20.4	22.19
EN 171101	17.11.2001	Dolyna	-18.5	4300	-	81	22.2	13.5	18.5
EN 060402	06.04.2002	Neuschwanstein	-17.2	600	-	-	-	-	-

and Kalenda 2003); Park Forest, USA, 2003 (Brown et al. 2004; Simon et al. 2004); Villalbeto de la Peña, Spain, 2004, with the help of optical sensors. Bolides Moravka, Tagish Lake, St. Robert, and Park Forest were also observed by numerous eyewitnesses.

2 SATELLITE OBSERVATIONS (SATELLITE NETWORK)

The European bolide Network records bolides over only about 0.3% of the Earth's surface. In recent years global observational system, which covers almost the total Earth surface, appeared. This satellite system consists of few geostationary satellites, which belong to the US Department of Defense (Tagliaferri et al. 1994). Its primary goal is to register nuclear explosions and missile starts, but it also detects bright light flashes in the atmosphere, which are caused by bolide entries. The satellites are equipped by optical sensors with detail temporal resolution and infrared sensors. The Satellite Network is able to detect superbolides.

Bolides brighter than -17^m are called superbolides. Only a small number of superbolides were registered during the operation of ground-based networks (few decades of recording; Table 1) due to small coverage of the surface. The continuous record, weather independence, and global coverage are the great advantages of the satellite system. The lack of dynamical data records is the main limitation of SN. In the most cases there are no data on meteoroid trajectory (velocity, angle of entry, etc.). The Satellite Network recorded more than 300 bright flashes in the atmosphere associated with meteoroid entries during the 8 years from February 1994 to September 2002 (Brown et al. 2002b). About 60–80% of the Earth's surface is covered during these observations. In average, about 30 events are detected over the globe during a year. The light flashes usually occur at altitudes 30–45 km, their duration is about 1–3 seconds and the energy in radiation is about 0.01–1 kt TNT, i.e., the energy of these events is comparable with the energy of nuclear explosions. Light curves (i.e., the radiation power versus time) were recorded for a number of events (Fig. 1) (McCord et al. 1995; Tagliaferri 1996).

The information collected by SN was available for independent scientific analysis over the few years. Data of optical observations in 1994–1996 (51 events) were considered by Nemtchinov et al. (1997a). Maximal irradiated energy (4.4 kt TNT) was registered on 1 February 1994 in the nearby Marshall Islands. This area is unpopulated and ground-based observations of this event were scarce (McCord et al. 1995).

The satellite observational data were used to determine kinetic energy E_k of meteoroids entering Earth's atmosphere (in the energy range $E_k \sim 0.06 - 40$ kt TNT; Nemtchinov et al. 1997a,b).

Several methods were suggested for SN data interpretation. These approaches allowed researchers to determine parameters of meteoroids, which caused observed light flashes. It was proved that these flashes are created not only by meteoroid flight in the atmosphere, but also by its disruption. It is impossible to explain the

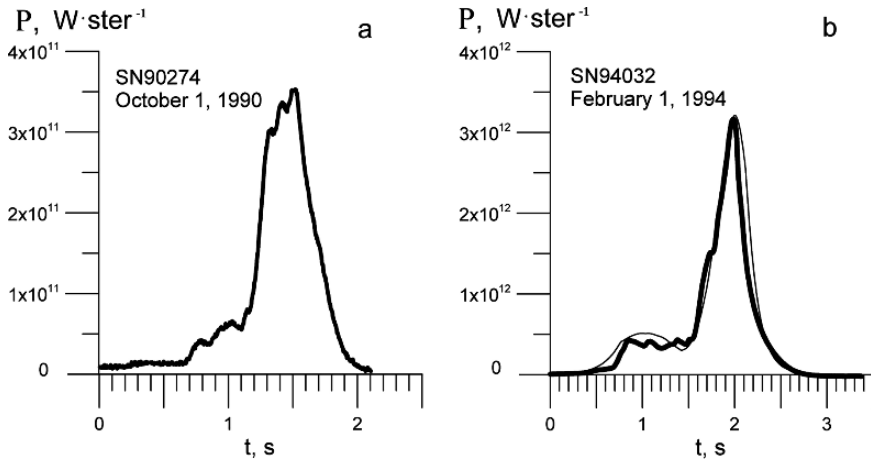


Figure 1. Examples of light curves recorded by SN. (a) bolide 1 October 1990 light curve (SN90274); (b) light curve of one of the largest SN bolides—Marshall Island bolide (1 February 1994; SN94032) (thick line) and its model light curve (thin line). The figure is adapted from Nemtchinov et al. (1997c) and reprinted with the kind permission of Annals of the New York Academy of Sciences

quick intensity growth (Fig. 1) in the framework of a single-body model (Svetsov et al. 1995; Nemtchinov et al. 1997a,b).

3 METEOROID FRAGMENTATION IN THE ATMOSPHERE

Kilometer-sized stony and iron meteoroids release all their energy on the ground. The fate of smaller meteoroids is dependent on their velocity, strength, and composition. The atmosphere affects the consequence of their impacts. The data on the famous Tunguska meteoroid (estimated diameter $D \sim 50\text{--}60$ m) demonstrate that the atmosphere can prevent crater formation and decreases seismic effects even for a body that is hundreds of meters in size.

The greater part of meteoroids is disrupted under aerodynamical loading during the flight through the atmosphere (Ceplecha et al. 1993). There are more than 70 fragments on the video record of the Peekskill bolide (Brown et al. 1994). Seventeen fragments were collected on the scattering field of the Příbram meteorite (Ceplecha 1961). Nine fragments were found for the Innisfree meteorite, and the flight of six separated pieces was recorded (Halliday et al. 1981). A large number of fragments was collected for meteorite falls Mbale (Jenniskens et al. 1994), Thuanthe (Reimold et al. 2003) and Park Forest (Simon et al. 2004).

The fragmentation can occur in different ways (Fig. 2). For example, few large fragments are formed. These pieces initially interact through their shock waves and then continue their flight independently (Melosh 1981, 1989; Artem'eva and Shuvalov 1996; Bland and Artemieva 2003).

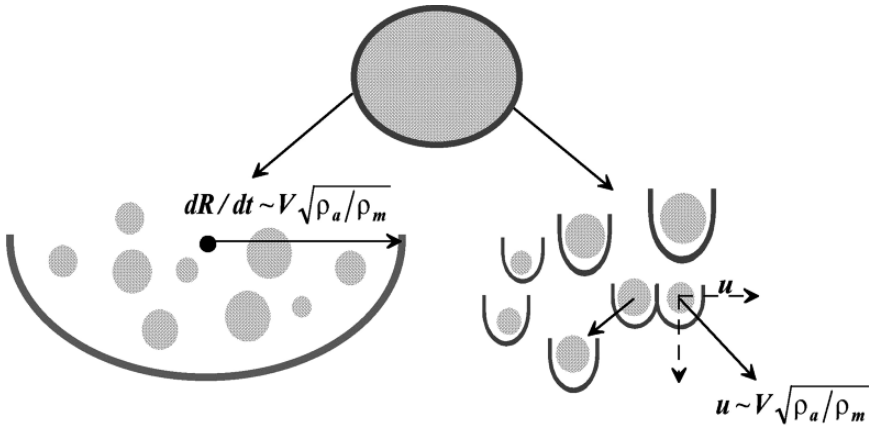


Figure 2. Two different and often used approaches to the meteoroid disruption in the atmosphere

The second mode of fragmentation is the disruption into a cloud of small fragments and vapor, which are united by the common shock wave (Adushkin and Nemchinov 1994; Svetsov et al. 1995). This fragmentation occurs during the disruption of relatively large bodies. The formation of a fragment–vapor cloud was observed in the breakup of the meteoroid on 1 February 1994 (McCord et al. 1995), at the last fragmentation of the Benesov bolide (Borovička and Spurný 1996; Borovička et al. 1998a), and in other cases. Initially formed fragments penetrate together deeper into the atmosphere and the fragmentation proceeds further. If the time between fragmentations is smaller than the time for fragment separation, all the fragments move as a unit, and a swarm of fragments and vapor penetrates deeper, being deformed by the aerodynamical loading like a drop of liquid. This liquid-like or “pancake” model assumes that the meteoroid breaks up into a swarm of small bodies, which continues their flight as a single mass with increasing pancake-like cross-section. The smallest fragments can be evaporated easily and fill the volume between larger pieces. As a whole, this process may be described in the frame of a single-body model. However, large fragments may escape the cloud and continue flight as independent bodies. The total picture of fragmented-body motion is comparatively complicated. Both scenarios are realized in the real events (Borovička et al. 1998a).

3.1 Liquid-like Fragmentation Models

The movement of totally disrupted bodies is often described by hydrodynamic approximation, which is used both in analytical and numerical modeling.

Grigoryan (1979) suggested the idea of lateral spreading of meteoroids after fragmentation. He also noted that during the increase of a cloud lateral cross-section the edges of the cloud are bent backward and are separated from the total mass.

Similar ideas were used in other papers (Hills and Goda 1993; Zahnle 1992; Chyba et al. 1993). Simple differential equations describing the spreading of a fragmented meteoroid were suggested. The results obtained are analogous to each other. The loading at the front of the body has maximal value in the critical point and decreases to the edges. The presence of a pressure gradient causes liquid particles (or quasi-liquid particles of fragmented material) to move along the frontal surface. The velocity of this lateral motion u may be estimated from the following equation according to the paper by Hills and Goda (1993):

$$u = (\rho_a/\rho_m)^{1/2}V, \quad (1)$$

where V is the meteoroid velocity, ρ_m is its density, and ρ_a is the atmosphere density.

As a result, these rather crude considerations provide a simple equation for the fragmented meteoroid's evolution during flight through the atmosphere.

The application of liquid-like models to large meteoroids is quite reasonable. According to the often used strength scaling law (see the following), the fragmentation of a large body starts under smaller loading than the breakup of a smaller meteoroid, because the probability to find cracks increases with an increase in size. Larger fragments are less decelerated and, being under higher loading, continue to break. Smaller fragments are evaporated quicker. The vapor fills the gaps between the fragments and supports a common shock wave, which units fragments and vapor into the cloud.

3.2 Progressive Fragmentation

Relatively small meteoroids may be broken into few fragments. For example, one to three relatively large pieces (10–90% of mass under disruption) were formed during the disruption of the Moravka meteoroid; the other part of the mass was converted into small fragments and dust, which were not seen on the video records.

Progressive fragmentation suggests that meteoroids are disrupted into fragments, which continue their flight as independent bodies and may be disrupted further. Similar models were suggested in numerous papers, beginning with Levin (1956). These papers did not take into account the interaction of resulting fragments, even at the initial stage, until the paper by Passey and Melosh (1980). It was usually suggested that the lateral size of meteorites and crater-strewn fields is caused by various reasons (Frost 1969; Tsvetkov 1987). Passey and Melosh (1980) considered the interaction of fragment shock waves and determined the velocity u , which caused the lateral spreading of fragments:

$$u = K(\rho_a/\rho_m)^{1/2}V. \quad (2)$$

The value of coefficient K is estimated as $K \sim 0.17 - 1.5$ (Passey and Melosh 1980) basing on the crater displacement in known crater-strewn fields. The value

of K is estimated as $K \sim 0.44$ for two quasi-cylindrical fragments, using three-dimensional gas-dynamic simulations (Artem'eva and Shuvalov 1996, 2001). The value of the coefficient K is dependent on the initial shape of the body if the number of formed fragments exceeds 2. For a cubical body disrupting onto a number of equal fragments, the value of K is estimated as $K \sim 0.44$, and for a quasi-sphere as $K \sim 1.1$ (Artem'eva and Shuvalov 1996; Artemieva and Shuvalov 2001). If different-sized pieces are formed in the disruption, the fragment mass difference should be taken into account in lateral velocity estimates.

The appearance of lateral velocity due to interaction among fragments at the initial stage of disruption provides a successful explanation for crater- and meteorite-strewn fields, and for fragment deviation from the trajectory of the main body. This progressive fragmentation model was successfully used for modeling of the Sikhote Alin meteorite fall (Nemtchinov and Popova 1997; Artemieva and Shuvalov 2001), the Benesov bolide (Borovička et al. 1998a), and the Martian crater fields (Popova et al. 2003), as well as other cases.

At the same time the observations of the Moravka fragments' motion (Borovička and Kalenda 2003) demonstrate that the lateral velocities of some fragments exceed the estimates given in Equation (2). At an altitude of 32 km the estimated lateral velocity $u = 35 \text{ m}\cdot\text{s}^{-1}$ for $K = 1$, whereas the observed velocities are about $50 \text{ m}\cdot\text{s}^{-1}$ and even up to $300 \text{ m}\cdot\text{s}^{-1}$ for several fragments. The explosive character of the fragment-separation process caused by rapid evaporation of a large amount of small fragments and dust may explain the observed lateral velocities.

4 RADIATIVE RADIUS AND INTEGRAL RADIATION EFFICIENCY

The amount of observational data is quite large for small ($<0.1 \text{ m}$) meteor bodies mainly because of the bolide network operations. Masses of these bodies are usually determined based on the so-called physical theory of meteors.

One of the main equations is that for the intensity I_m of meteor optical radiation:

$$I_m = \tau_m (-dM/dt) \cdot V^2, \quad (3)$$

where τ_m is the luminous efficiency, and M , V are the meteoroid mass and velocity, respectively. This equation implies that radiation intensity is proportional to the kinetic energy of ablated mass and is determined only by ablation rate.

Equation (3) cannot be applied to the meteoroids with sizes of about 0.1 m and larger because it does not take into account the radiation of heated air:

$$I_a = \tau_i S \rho_a \frac{V^3}{2}, \quad (4)$$

where S is the cross-section, ρ_a is the air density, and τ_i is the luminous efficiency (the coefficient of conversion of incoming air kinetic energy into radiation energy).

Taking into account the meteoroid deceleration equation:

$$M \frac{dV}{dt} = -SC_d \rho_a V^2, \quad (5)$$

where C_d is the drag coefficient, one may obtain:

$$I_a = -\frac{\tau_i}{4C_d} M \frac{dV^2}{dt}. \quad (6)$$

For large bodies, the radiation intensity equation is often written as:

$$I = \tau((-dM/dt)V^2/2 + MV(-dV/dt)), \quad (7)$$

where the single luminous efficiency τ is used for both terms in the right side of Equation (7).

The empirical values derived from the analysis of photographed meteorite falls (Halliday et al. 1981; Ceplecha 1996; ReVelle and Ceplecha 2001; Ceplecha and ReVelle 2005) or theoretically obtained values (Nemchinov et al. 1997a) are used as the luminous efficiency. The value of luminous efficiency is dependent on the spectral passband of observations. The photographic bolide networks usually record radiation in the panchromatic passband, whereas the satellite network registers the intensity of radiation mainly in the infrared spectral range.

A clear pattern of ablation and radiation is required to analyze data on large bolides. Systematic calculations of ablation rate of different-sized meteoroids were carried out by the radiative hydrodynamic model by Golub' (1996). Besides, the luminous efficiencies and spectra of radiation were obtained by these calculations in the framework of the ablating piston model Golub' et al. (1996). The model is based on the analogy between one-dimensional nonstationary motion of a cylindrical piston in air and the two-dimensional quasi-stationary flow around a body (Chernyi 1959; Hayes and Probstein 1959). The formation of a vapor layer due to action of intensive radiation from shocked-compressed air was taken into account. This heated vapor layer radiates and heats the gas in front of the shock wave (Nemchinov et al. 1994). Radiation transfer both in the air and the meteoritic vapor has been taken into account in the model (Golub' et al. 1996). The dominant mechanism of mass losses is vaporization due to thermal radiation falling onto the surface of the meteoroid. The model predicts that the spectrum of a large and/or deeply penetrating body is of a continuum type with superimposed spectral lines.

Meteoroids encounter the Earth's atmosphere at velocities between 11 and 72 km·s⁻¹. These velocities are much larger than the rocket's velocity; the temperature in front of the body is also very high ($T \sim 3 \cdot 10^4 - 5 \cdot 10^4$ K). One would expect that the radiation from the hot front region would be emitted in the ultraviolet (UV) passband; however, the UV radiation is absorbed by cold air. The temperature of the heated air and vapor decreases with an increase in distance from the blunt nose. The maximum of the spectra gradually moves from the UV range into the visible and infrared (IR) ranges; the role of lines in the spectra increases with the distance from the nose where new, colder and colder regions are taken into account. The region of the nearby wake at a distance of several diameters of the body is mainly responsible for emission in the panchromatic wavelength range, while the bolide's head is mainly responsible for UV emission, and the far wake provides mainly the

emission in the IR spectrum (Golub' et al. 1997; Borovička et al. 1998b). Spectra of radiation may essentially differ from the blackbody due to the relatively small optical thickness of heated volume, at least in the continuum. Bolide radiation is composed of atomic line emissions, molecular bands, and continuum radiation.

It should be mentioned that the model (Golub' et al. 1996) and observed spectra of the Benesov bolide (Borovička et al. 1998b) are in general agreement with each other. The shapes of spectra at different altitudes are similar. Predicted spectral lines are found in the observational spectra. The emission temperature of spectral lines is about 5,000–6,000 K both in the model and the observations. The role of the continuum increases with a decrease in altitude of a flight (Borovička et al. 1998b). Few disagreements mentioned in (Borovička et al. 1998b) show that the radiative model needs further development.

There are some limitations of the ablating piston model. A strict boundary between vapor and air is assumed. However, in reality this boundary is unstable and large-eddy and small-scale turbulent mixing of the vapor and air may occur. The model is one dimensional. Besides, the application of the model to the disrupted meteoroid also has restrictions. The simple assumption that formed fragments move and radiate independently after breakup may lead to significant errors when the fragments are still close to each other. Additionally some small fragments may appear in the wake of a larger fragment; consequently, they are in essentially different conditions than the fragments, which move through undisturbed air.

The ablating piston model makes it possible to calculate parameters for numerous combinations of meteoroid sizes, velocities, compositions, and altitudes of flight. The model results allow the determination of radiative radii of different meteoroids. The radiative radius (Nemtchinov et al. 1994, 1995, 1997a,b) is defined from the light curve. The simplest way to determine the size of a body at any moment is to compare the observed intensity with the theoretical values for different sizes for the given velocity and altitude and choose the one that gives the best fit of radiation intensity to light curve.

The rapid increase of a radiative radius during the light flash corresponds to the intensive fragmentation and rapid spreading of the vapor-and-fragment cloud. The radiative radius is dependent on meteoroid composition, and the corresponding radiative mass also is dependent on suggestions about meteoroid shape and density. These are the reasons that radiative mass estimates are uncertain. The same is valid for dynamic mass estimates, which are determined based on meteoroid deceleration in the atmosphere (i.e., according Equation (5)). Combining both approaches increases the reliability of the estimates.

Usually there is no information concerning the trajectory and velocity of large meteoroids detected by the satellite network (Reynolds 1992; Tagliaferri 1993, 1996; Tagliaferri et al. 1994; McCord et al. 1995). As a first approximation, the integral luminous efficiency approach is suggested to determine the kinetic energy of an incoming meteoroid. This approach mainly uses the total energy of a recorded light pulse. The idea of this method is based on the well-known fact that the fraction of the energy transferred into radiation has only a weak dependence on the energy

of the explosion and its altitude under a powerful point-like explosion (Glasstone and Dolan 1977; Svetsov 1994a). The flight of a meteoroid through the atmosphere is similar to a set of cylindrical explosions, with some distribution of energy release along the trajectory. The total released energy may be large enough and reach the range of nuclear explosion energies. However, the area of energy release has an elongated shape, the character's lateral size is not large, and the optical thickness of a luminous area also is not large (especially for relatively small meteoroids and high altitudes of flight). The energy losses may depend on entry velocity and meteoroid (and vapor) composition.

Attempts to explain light curves of satellite bolides without fragmentation have failed (Svetsov et al. 1995; Nemtchinov et al. 1997a). Assuming some fragmentation model and standard equations of meteoroid motion and radiation, one may obtain a radiated power using values of conversion coefficients of released energy to radiation energy (Nemtchinov et al. 1997a). Integrating the radiative power over the time of flight one obtains the radiative energy for a given initial mass, velocity, and meteoroid composition. The integral luminous efficiency may be determined as the relation of total radiative energy (for the time of flight) to the initial kinetic energy:

$$\eta = E_r/E_k, \quad (8)$$

where E_r is the radiative energy accepted by detector, and E_k is the kinetic energy of the meteoroid.

The dependence of integral luminous efficiency on radiated energy E_r is given on Fig. 3 for H-chondrites (open squares) and irons (black circles). Integral luminous efficiency η increases both with size and velocity. The dashed and solid lines (Fig. 3) correspond to the least-square approximation of results for H-chondrites' and iron meteoroids' composition. An apparent strength of 10 MPa (see the following) was adopted for these calculations. The average value of integral luminous efficiency differs both from the maximal value (at the velocity $30 \text{ km}\cdot\text{s}^{-1}$) and the minimal value (at $V \sim 12 \text{ km}\cdot\text{s}^{-1}$) by about two times.

The following approximation of η can be used for iron (Equation 9a) and H-chondrite (Equation 9b) correspondingly:

$$\eta = 0.021 \lg E_r + 0.0031V + 0.037 \quad (9a)$$

$$\eta = 0.021 \lg E_r + 0.0055V + 0.022, \quad (9b)$$

where V is the velocity in $\text{km}\cdot\text{s}^{-1}$, and E_r is the energy of radiation in kt TNT. The luminosity is dependent on meteoroid composition. If the entry velocity is unknown, the simplified dependence for integral luminous efficiency may be used (given for chondrite):

$$\eta = 0.021 \lg E_r + 0.103. \quad (10)$$

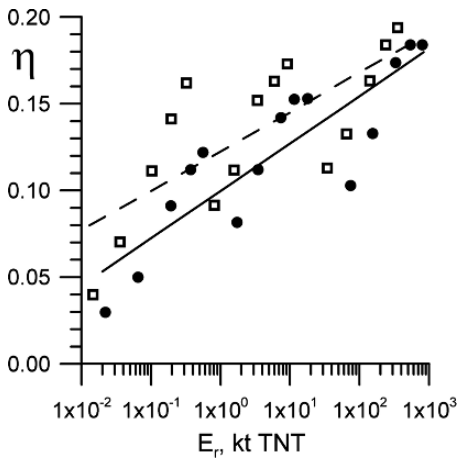


Figure 3. Dependence of luminous efficiency on radiated energy for H-chondrite (open squares) and iron (black circles) bodies with sizes 1, 3, and 10 m (corresponding sequence of η moves right with size) and velocities 12, 15, 20, 25, 30 $\text{km}\cdot\text{s}^{-1}$ (corresponding values η shift up with V increase). Dashed and solid lines are least squares approximations of η for H-chondrites and irons correspondingly. The apparent strength was assumed to be 10 MPa. The figure is adapted from Nemtchinov et al. (1997a) and reprinted with the kind permission of Elsevier

It should be mentioned that the value of η is dependent on the spectral sensitivity of the observational system. The values of coefficients in Equations (9) and (10) are given for photoelectric detectors with an observational passband of 1–3 eV (Tagliaferri et al. 1994). Its maximal sensitivity corresponds to the maximum of blackbody radiation at a temperature of about 6,000 K (Glasstone and Dolan 1977). For the panchromatic films, which are usually used in ground-based observational networks, the value of efficiency η is about 1.5 times lower (Popova and Nemtchinov 1996). The integral luminous efficiency η increases with a meteoroid size and corresponding increase in the optical thickness of a luminous area. For meteoroids <10 meters in size at altitudes >20 km the radiation spectra still differ from the spectra of opaque plasma and are determined by atomic lines and molecular bands. For large bodies (~ 100 m and larger) the radiation is mainly determined by the radiation of shock-heated air (Zel'dovitch and Raiser 1967; Kiselev et al. 1991; Nemtchinov 1994). In this case radiation transfer and heat conduction in the vapor are provided by the radiative heat conduction (Nemtchinov et al. 1994; Loseva et al. 1998).

For meteoroids with masses about 10–100 t and energies $E_k \sim 0.5$ –5 kt TNT the integral luminous efficiency η is about 8–10%. These values are much smaller than the luminous efficiency in nuclear explosions, where $\eta \sim 30\%$ (Glasstone and Dolan 1977). This difference is connected with the different character of energy release in both cases. In meteor events the energy is released permanently along the trajectory and the shapes of luminous volume are essentially different—elongated versus spherical.

Compare the integral efficiency η with integral coefficients of luminosity η_i , determined in the course of individual analysis of several bolides (Svetsov 1994a; Nemtchinov et al. 1997a). The kinetic energies of six bolides, which were determined based on detail light curves, differ from the estimates found with the help of integral luminous efficiency by not more than two times.

In Nemtchinov et al.'s paper (1997a), the bolide kinetic energy E_k is estimated with the help of integral luminous efficiency η for the whole number of bolides registered by the Satellite Network in 1992–1994 and several earlier events (51 events totally).

Currently the data on satellite observations are not released on a permanent basis, but data on few events were published since the publication of the paper by Nemtchinov et al. (1997a). These data are presented in Table 2 and the energy of these meteoroids are estimated using the integral luminous efficiency.

The size of meteoroids may be roughly estimated based on irradiated energy, assuming some average entry velocity (the authors adopt $18 \text{ km}\cdot\text{s}^{-1}$ if there are no other data) and some average density ($\rho_m \sim 3 \text{ g}\cdot\text{cm}^{-3}$). Obtained size estimates D are given in Table 2. Most of the meteoroids listed in Table 2 as well in Nemtchinov et al.'s (1997a) paper may be estimated as 1–5 m in size with initial kinetic energies 0.1–1 kt TNT.

5 METEOROID STRENGTH

Data on meteoroid strength are extremely scarce. Some authors (e.g., Hills and Goda 1993) use meteorite strength values (i.e., $\sigma_a \sim 10\text{--}50 \text{ MPa}$ for chondrites, 200 MPa for irons), and estimate the strength of volatileless comets as $\sim 1 \text{ MPa}$. However, the strength of a large body usually appears to be smaller than the strength of a small piece because of its larger number of cracks and discontinuities. Besides, the energy necessary to separate a fragment from the whole meteoroid is proportional to the body cross-section, whereas the elastic energy stored in the body under aerodynamical loading is proportional to the body volume.

Usually the strength σ of a large meteoroid is expected to decrease in comparison with small sample strength σ_s , according to the statistical strength theory (Weibull 1951). The relation between σ and σ_s is written as:

$$\sigma = \sigma_s (m_s/m)^\alpha, \quad (11)$$

where σ and m are the apparent strength of a large body, σ_s and m_s are those of the sample, and α is the power exponent. There are no precisely determined values of α , but for stony bodies the exponent α is estimated to be in the range of 0.1–0.5 (Svetsov et al. 1995).

The value of meteoroid strength σ in the breakup may be estimated as:

$$0.365\rho_a V^2 = \sigma_a, \quad (12)$$

where ρ_a is the atmospheric density at the breakup altitude, and V is the meteoroid velocity. The corresponding value of strength σ_a may be called apparent strength.

Table 2. Parameters of recent SN bolides. Maximal intensity P_m , irradiated energy E_r , integral luminous efficiency η , kinetic energy E_k , estimated mass M_o and diameter D , entry velocity V_o , height of maximum light H_m , stellar magnitude m_{max} , kinetic energy E_o estimated based on acoustic signals and corresponding mass M_{oa}

N	date	P_m	E_r , kt	η , %	E_k , kt	D, m	H_m , km	m_{max}	V_o , km·s ⁻¹	M_o , t	E_o , kt	M_{oa} , t	E_o/E_k
97117	27.04.1997	3×10^{11}	0.17	8.6	1.98	3		-23					
97282	09.10.1997	1.0×10^{11}	0.045	7.5	0.6	1.7	36	-22	25	8.1	0.3	4	0.5
(El Paso)													
97343	09.12.1997	9.5×10^{10}	0.06	7.8	0.8	1.6	46,	-	30.5	7.42	0.1	1.0	0.13
(Greenland)							28-25 (33-21)						
97248	05.09.1997	2.4×10^{10}	0.05	7.5	0.6	1.9		-20	18	15.6			
97273	30.09.1997	9.0×10^9	0.006	5.6	0.1	1.1		-19	18	2.6			
97274	01.10.1997	1.7×10^{10}	0.02	6.5	0.2	1.4		-20	18	6.0			
98011	11.01.1998	-	-	-	-	-	-	-	18	-			
99014	14.01.1999	2.9×10^{11}	1.2	10.5	11.5	5.2	35	-23	15	400-500			
(Pacific Region)													
99228	16.08.1999		0.01	6.0	0.15	1.2			18	3.9	0.18	4.7	1.2
99188	07.07.1999						28.8		18				
(N. Zealand)													
99339	05.12.1999						74-23		18				
(Alabama)													

(Continued)

Table 2. (Continued)

N	date	P_m	$W \cdot \text{ster}^{-1}$	E_r , kt	η , %	E_k , kt	D, m	H_m , km	m_{\max}	V_0 , km s $^{-1}$	m_0 , t	E_a , kt	M_{on} , t	E_d/E_k
00018 (Tagish Lake)	18.01.2000		0.3	9.1	2.9	3.3	25		15.8	50–200	1.66	97.1	0.57	
00049	18.02.2000		0.9	10.2	8.46	4.65			18	219.3	3.89	101	0.46	
00127 (Moravka)	06.05.2000	1.05×10^{10}	0.01	5.6	0.11	1.0	36–33		22.5	1–3	0.09	1.9	0.82	
00131	10.05.2000	1.05×10^{10}	0.005	5.4	0.08	1.0	55–38		18	2.2				
00238	25.08.2000	–	0.3	9.3	3.6	3.5			18	92.9	2.4	64.8	0.66	
01113	23.04.2001	–	1.1	10.4	10.6	5.0	28.5		18	273.5	~0.6	25.9	0.057	
01204	23.07.2001	–	0.3	9.2	3.3	3.4	82–32		18	85.6	0.3	7.5	0.10	
02068	09.03.2002		0.05	7.62	0.7	2.02			18	18.1	1.05	27.2	1.5	
02157	06.06.2002		0.9	10.21	8.9	4.72			18	230.7	25.8	669	2.9	
02206	25.07.2002		0.06	7.73	0.78	2.1			18	20.19	0.6	15.6	0.77	
02267 (Vitim)	24.09.2002	2.4×10^{11}	0.2	8.8	2.3	2.9	62–30		18	58.7				
03086 (Park Forest)	27.03.2003		0.03	7.2	0.45	1.7			20	9.6				

Different methods are used to determine meteoroid strength at breakup (direct observation of fragments, analysis of dynamic data, flashes on light curves, etc.) (see Popova et al. 2007 for details).

Some data on apparent strength are given in Table 3, mainly for SN meteoroids (Popova et al. 2003). It was suggested that the flash on the light curve corresponds to breakup, and deceleration of the body was roughly taken into account. The apparent strength of meter-sized meteoroids has large scatter (1–10 MPa and even more in some cases). The fragmentation is often a multistage process. For some events (1 February 1994; Greenland bolide, Benesov, Moravka) the first disruption occurs at high altitudes (50–60 km) under loading <1 MPa. There are no light flashes on light curves due to high altitude fragmentations. The strength values listed in Table 3 mainly correspond to the main or essential fragmentations at mid- or low altitudes (45–25 km).

Body strength is expected to be connected with its composition and structure. For carbonaceous chondrite Tagish Lake (Brown et al. 2000, 2001, 2002a) the fragmentation started at a 46-km altitude under loading of about 0.25 MPa, and the main breakup occurred at a 37-km altitude (loading of about 0.7 MPa). However, these values are close to the apparent strength of ordinary stony meteoroids, whereas the structures are essentially different.

For meteoroids some meters in size collected in Table 3, the end heights are quite low (~ 25 – 30 km). Before 1994 14 meteoroids with estimated sizes ~ 1 m were recorded during flight (Cepelcha et al. 1993, 1994). For five of them the end heights were >45 – 50 km, and the heights of maximal intensity were about 90–60 km. These high-altitude bolides probably correspond to cometary bodies. One of these events (the bolide Šumava) (Borovička and Spurný 1996; Nemtchinov et al. 1999) was disrupted under loading of only 0.01–0.1 MPa. The Šumava mass probably reaches $\sim 5,000$ kg. There are no similar bodies in the collections of meteorites.

Given data about light flash altitudes, mass, velocity, strength power law, and fragmentation model, the apparent strength of meteoroids, fragmentation of which is accompanied by light flashes, can be estimated (Popova and Nemtchinov 2002). Compare these model estimates with data obtained from observations. The authors' values agree with the strength estimates at 30- to 40-km altitudes, and are slightly higher for altitudes of 20–25 km (if the deceleration and mass decrease in previous fragmentations are not taken into account). The value of exponent power $\alpha \approx 0.25$ seems preferable. This approach does not allow one to determine breakups at high altitudes (without large energy release).

The authors estimate the strength of stony bodies with $M \sim 1$ ton as 1–10 MPa; these bodies are fragmented mainly at 25- to 49-km altitudes (Fig. 4). It seems reasonable to use these apparent strength estimates for stony bodies with masses 1–1,000 t. The strength of stony bodies is quite low probably due to their collisional history. A lot of cracks or discontinuities develop during multiple collisions in space (Consolmagno and Britt 2004).

The model of a meteoroid without strength at all may be considered as a limiting case. It is conceivable that individual fragments of meteoroid are only slightly

Table 3. Data on large bolides in the atmosphere. Table is adapted from Popova et al. (2003) and reprinted with the kind permission of Meteoritics and Planetary Science

Event	Date	E_r , kt	η , %	E_k , kt	M_{\odot} , ton	D_p , m	V_{\odot} , km.s ⁻¹	H_m , km	$\sigma_a = \rho_a V^2$, MPa
88106 (SN)	15 Apr. 1988	1.70	11	8-9	25-45	2.5-3	48-50 ^{est}	43	<0.9
90274 (SN)	1 Oct. 1990	0.57	9.7	3-5	70-200	3.5-5	15-20 ^{est}	30	1-3
91277 (SN)	4 Oct. 1991	0.14	8.4	0.9	20	2.3	15-20 ^{est}	33	1.2-3
94032 (SN)	1 Feb. 1994	4.39	12.5	31	400	6.3	24	34.21	<0.8, >10
94149 (SN)	29 May 1994	0.090	8.0	0.6-2.5	2-140	1.1-4.5	<50 ^{est}	34	<12
94307 (SN)	3 Nov. 1994	0.56	9.7	3-5	70-200	3.5-5	15-20 ^{est}	34	<0.5-1.7
94350 (SN)	16 Dec. 1994	0.0086	5.9	0.07-0.3	0.25-17	0.5-2.2	<40 ^{est}	30	<20
94166 (SN) (OC)	15 June 1994	0.0031	4.93	0.063	1-3	0.9-1.2	13	36.2	0.6-1
El Paso (SN)	9 Oct. 1997	0.045	7.5	0.6	8	1.7	25	28-30	5.4-10
Greenland (SN)	9 Dec. 1999	0.064	7.8	0.8	8.36	1.7	29.30.5	46, 28-25 33-21	<0.4, 1.3-23 10-40
N.Zealand (SN)	7 Jul. 1999	-	-	-	1-3	0.9-1.2	18 ^{est}	28.8	5-7
Tagish Lake (SN) (CC)	18 Jan. 2000	0.26	9.1	2.85	50-200	3.2-5	15.8	37.25	<0.7, 2-4
01113 (SN) Pacific Region	23 Apr. 2001	1.1	10.4	10.6	200-400	5-6.3	18 ^{est}	28.5	<2
Benešov	14 Jan 1999	1.2	10.4	11.5	500	6.8	15	35	<0.3
Peekskill (OC)	7 May 1991	0.01	6.1	0.16	2-4	1.1-1.4	21	37.24	1.3-2, >12
Mbala (OC)	9 Oct. 1992	-	-	-	~10	1.9	14.7	41, below	>0.4
Přibram (OC)	14 Aug. 1992	-	-	-	0.4-1	0.6-0.9	13.5	25, below	6-7
Moravka (SN) (OC)	7 Apr. 1959	-	-	-	1-5	0.9-1.5	20.9	44-25	0.3-20
Innisfree (OC)	6 May 2000	0.006	5.6	0.1	1-3	0.9-1.2	22	36, below	2-3
Sikhote-Alin (I)	7 Feb. 1977	-	-	-	0.1-0.02	0.4-0.2	14	36, below	1.2-1.5
	12 Feb. 1947	-	-	3.5-13	200-500	-	12-15	28-10	5-30

CC carbonaceous chondrite; D_p meteoroid diameter estimate; *est* only velocity estimate is given; *I* iron; *OC* ordinary chondrite.

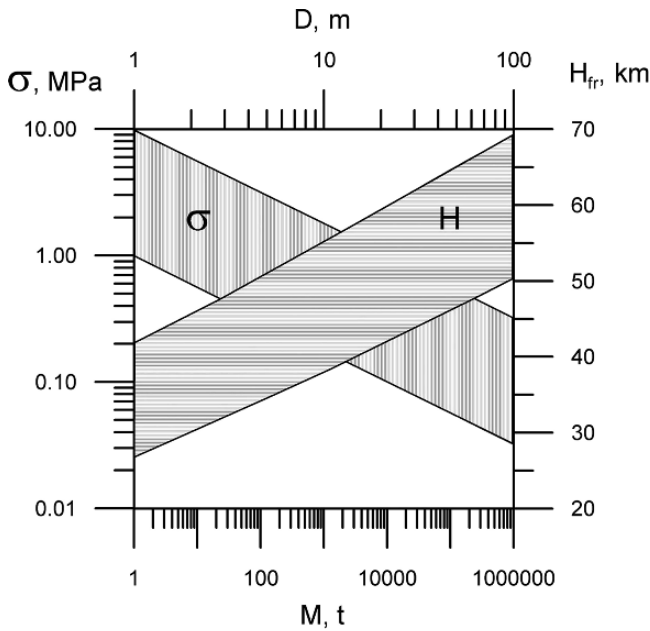


Figure 4. The estimates of strength and altitude of breakup in dependence on body mass

bonded together along contact surface. These fragments start to move relative to each other after the entry. The friction, which is proportional to the loading in direction perpendicular to the contact surface, is the only impediment to fragment motion. On the one hand there is some body orientation during the entry, which produces the maximal velocity along the crack surface (Walsh and Zhu 2004). From the other side it is evident that in the strengthless model it is impossible to obtain large lateral velocities of fragments in the breakup, as observed in the Moravka meteoroid (Borovička and Kalenda 2003). At the same time the motion of pieces along the crack causes the disruption of ridges on the rough contact surface, i.e., the formation of tiny dust, which can rapidly evaporate.

It should be noted here that according to Equation (11) the apparent strength should increase during the progressive fragmentation sequence from one break to another. However, in the disruption of the Moravka meteoroid (Borovička and Kalenda 2003) some fragments were disrupted under loading pressures that were smaller than those under which they were formed. Therefore, the question of meteoroid disruption during atmosphere entry needs further investigation, probably taking into account preceding collisional history. Nevertheless, any consideration cannot change the conclusion concerning the low strength of meter-sized bodies, and argues against the suggestion that the strength of larger bodies (~100 m) may be even lower. This conclusion is very important in the treating asteroid hazards

and considering the possibility of destroying an incoming asteroid by a prolonged mechanical pulse.

6 ACOUSTIC SYSTEM OF OBSERVATIONS

The motion and disruption of large cosmic bodies in the atmosphere are accompanied by powerful acoustic–gravitational (Golitsyn et al. 1977) and acoustic–infrasound disturbances (ReVelle 1976), which may be detected by ground-based stations. Moreover, powerful sound waves impacting the ground cause the appearance of seismic waves (Edwards and Hildebrand 2004). The shock wave is the main source of atmospheric disturbances. The shock wave is converted into a sound wave at distances of about R_a , which may be estimated by the following relation for confined energy release:

$$R_a \approx (E/P_a)^{1/3}, \quad (13)$$

where E is the released energy, and P_a is the pressure at the altitude of energy release. In reality the energy release for a flight without fragmentation is similar to cylindrical explosions, then:

$$R_a \approx (E/P_a L)^{1/2}, \quad (14)$$

where L is the length of energy release zone. The value of R_a may be estimated based on the wake radius R_w , which is defined by effective body radius R_b at the moment of maximal energy release and Mach number M_f . The following relation may be written $R_a \approx R_w \approx R_b \cdot M_f$. Given a velocity of $\sim 30 \text{ km}\cdot\text{s}^{-1}$ (Mach number $M_f = 100$) and diameter $D = 6 \text{ m}$ (i.e., a meteoroid with an energy $\sim 10 \text{ kt}$), one obtains $R_a = 0.3 \text{ km}$. The characteristic time of shock wave transfer into acoustic one is about $\tau_a = R_a/c_a \sim 1 \text{ s}$, where c_a is the sound velocity in the atmosphere. Infrasound waves are a part of acoustic waves in the spectral range between 20 Hz and the normal frequency of atmosphere oscillations ($3 \cdot 10^{-3} \text{ Hz}$). The infrasound waves in the atmosphere are only slightly attenuated, so the bolide infrasound can be detected at large distances. Infrasound disturbances propagate in the atmospheric waveguides, which are formed at different heights by temperature and velocity gradients, at distances of about hundreds or even thousands of kilometers. The infrasound signal at large distances propagates in the lower (between the ground and 40- to 60-km altitude) or the upper waveguide (between the ground and ~ 110 -km altitude). The acoustic gravitational waves propagate even further (thousands of kilometers). In fact these waves are the reaction of large atmosphere masses on the disturbance in which a part of the atmosphere has been forced out of the equilibrium and oscillates.

During 1960–1974 acoustic signals of ten bolides were recorded by the microbarograph network in the United States (ReVelle 1997). For nine meteoroids the initial kinetic energy is in the range 0.2–30 kt TNT. The largest event (8 March

1963; 51°S, 24°E) has the energy about 1.1 Mt. (The signal was recorded at distances of 11,000 and 13,000 km.) The characteristic maximal period is ~ 10 s for energies ~ 10 kt TNT and reaches 50 s for a 1-Mt energy, when the characteristic size is $\sim 2R_b \sim 20$ m. Measured parameters of infrasound waves essentially exceed the duration of the source itself. The determination of a bolide kinetic energy from acoustic signals is based on the empirical dependences between time period and amplitude of acoustic waves obtained during nuclear explosion tests. This relation may be written as follows (ReVelle 1997):

$$E_s = 2 \left(\frac{\tau}{5.92} \right)^{3.34}, \quad (15)$$

where E_s is the source energy in kt TNT, and τ is the period of acoustic signal at the level of maximal amplitude.

A few points should be noted. First, the energy E_s highly depends on the period τ , so one needs to know the period with high accuracy in order to define the energy precisely. For the Park Forest bolide, the observed period differed by about two times (2.3 and 5.6 s) at similar distances from the source (965 and 1,170 km) (Brown et al. 2004). As a result, the difference in the energy estimates reaches an order of magnitude. This difference may be connected with strong winds. For determination of the source energy E_s , based on Equation (15) (or some other approach), one needs to know data on winds (and sound velocity) at different altitudes along the trajectory from the source to the place of registration. Additionally, the shape of the energy release volume in the nuclear explosion has spherical symmetry and differs from the shape of an energy release volume during the meteoroid flight. Multistage fragmentation complicates the pattern and the area of energy release is more similar to several explosions at different altitudes during a 1-s time interval.

For the Neuschwanstein bolide (ReVelle et al. 2004), the acoustic signal at a distance of 256 km from the place of maximal intensity (Spurný et al. 2003) is composed of two parts: an initial signal with duration < 10 s and frequencies > 1 Hz, and a more powerful signal at higher frequencies, which started 1 minute later. The maximal amplitude reaches 1.5 ± 0.33 Pa for the first signal, and 5.36 ± 1.94 Pa for the second (ReVelle et al. 2004). According to the consideration in the ray approximation these signals were formed at different altitudes—from a higher altitude, where the meteoroid may be described as a linear moving source, and from a more compact area with higher concentration of energy release. Photographic methods may help to determine the part played by these areas.

Alas, the statistics are still poor. The number of events for which the energy is determined by the acoustic approach is smaller than the number of events for which the energy is found on the basis of optical observations. It seems that currently the acoustic method is less precise than the optical one, especially if optical observations are supplemented by data on velocity, meteoroid composition, and radiative spectra.

Ten events recorded simultaneously by the acoustic system and satellites were analyzed by Brown et al. (2002b). The authors supplemented the data set by three

photographic bolides. They determined the integral luminous efficiency based on the acoustic energy estimates as the following:

$$\eta_B = (0.1212 \pm 0.0043) E_r^{0.115 \pm 0.075}. \quad (16)$$

The comparison of dependences Equations (10) and (16) is given in Fig. 5a. These dependences do not differ by more than 30%. Estimates by the authors and those by Brown et al. (2002b) are close to each other, in the energy range 0.01–10 kt (Fig. 5b), except for a few cases (Table 2, last column). For SN01204 the energy determined by the acoustic method is an order of magnitude smaller than the energy estimate based on the optical data, and for SN02206 the “acoustic” energy E_a is three times larger than the “optical” one (Table 2).

Brown et al. (2002b) did not use acoustic data for SN0113. The kinetic energy estimate based on acoustic signal for this bolide is smaller than energy of its radiation. The same problem (luminous efficiency about 60–100% if acoustic data are used) occurs in the SN97343 (Greenland bolide) and SN01204 (23 July 2001) cases (ReVelle 2001). These data also were excluded from the analysis by Brown et al. (2002b). At the same time one must note that the energy estimates found on the basis of light curves fall far short of being perfect.

7 RECENT SUPERBOLIDES

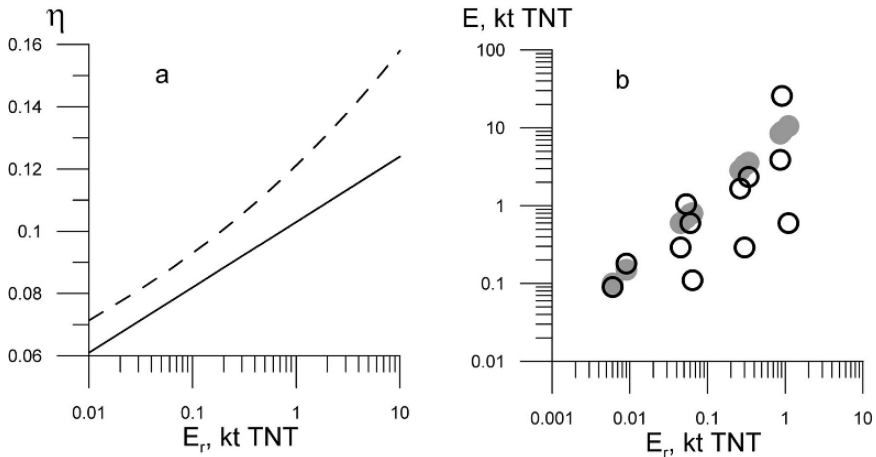


Figure 5. (a) The comparison of integral luminous efficiency dependences on irradiated energy (Equation (10) *solid line*; Equation (16) *dashed line*); (b) Kinetic energy estimates based on our data (circles) and by acoustic signal (*gray circles*) (Brown et al. 2002b)

7.1 Greenland Bolide

When a large meteoroid (SN97343; 12 September 1997; Pedersen et al. 2001) entered the atmosphere over southern Greenland, a large area was illuminated. Observations were visual sightings from the SW coast of Greenland and trawlers in the waters off the coast of Greenland, video recording in Nuuk, and DoD US satellite data. The satellite registration started at an altitude of 46 km, and two bright flashes were recorded at 34 and 25–28 km heights, so the meteoroid was disrupted above these altitudes. A very large area was illuminated, which suggested that this event was unusual. However, the light curve of the Greenland bolide was not exceptional. It is given in Fig. 6a in comparison with the light curve of the Benesov bolide (Table 1).

Short light flashes at the end of the light curves are similar and are easily explained in the frame of the fragmentation model. The lower is the altitude of disruption, the higher is the meteoroid velocity, and the shorter are the resulting flashes. The initial kinetic energy of the meteoroid, which produced the Greenland bolide, is about 0.8 kt TNT according to the estimates based on the energy of the light pulse detected by SN and theoretical values of integral luminosity. This is a rather typical energy for SN meteoroids. The meteoroid’s mass is about 8 t, if the velocity estimate of $29 \text{ km}\cdot\text{s}^{-1}$ is valid (Pedersen et al. 2001). The authors’ estimates have precision of about two times, so the meteoroid mass may be estimated as 4–16 t, and its size is 0.7–1.3 m for an assumed density of $2\text{--}3.7 \text{ g}\cdot\text{cm}^{-3}$. The light curve of the Greenland bolide can be reproduced by modeling, assuming that the Greenland meteoroid has at least two extensive fragmentations (the second consisting of three close events) under loading of $\sim 0.04\text{--}0.6 \text{ MPa}$ ($M \sim 55\text{--}35 \text{ km}$) and $\sim 1\text{--}2 \text{ MPa}$ ($M \sim 30 \text{ km}$). The first disruption was probably more gradual; fragments were formed sequentially, which would permit one to

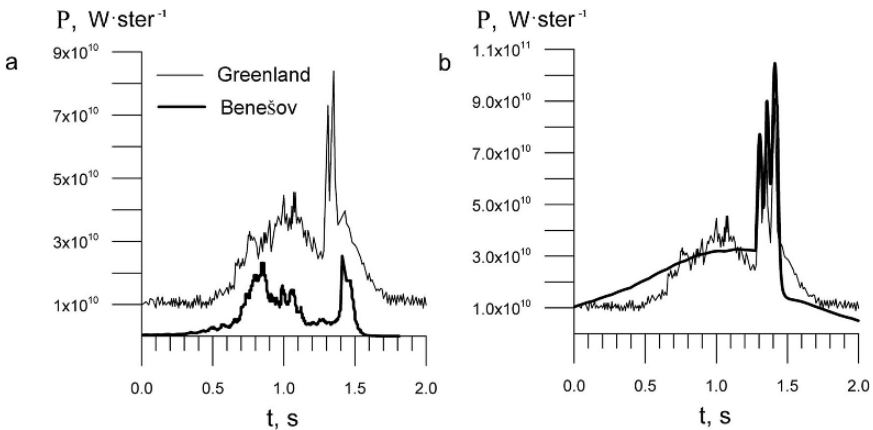


Figure 6. Comparison of Greenland and Benesov bolide light curves (a) Observed (thin) and model (thick) light curves of Greenland bolide (b)

obtain a modeling light curve closer to the observed one. Possibly large fragments continued their flight <25 km altitude, in contrast with the Benesov bolide, for which small fragments were formed in the last disruption. The strength of the Greenland meteoroid fragments (10–20 MPa) disagrees with its probable cometary orbit.

7.2 Vitim Bolide

On 24 September 2002 (16:48:56 UTC), the Vitim bolide was recorded by optical and infrared sensors of the US satellite observation system. The object was detected at an altitude of ~62 km at a point with coordinates 57.91 N, 112.90 E, and traced to an altitude of ~30 km with coordinates 58.21 N, 113.46 E. The optical sensor recorded a bolide signal with radiation energy of the order of $8.6 \cdot 10^{11}$ J.

The initial kinetic energy of this meteoroid is estimated as 10^{13} J (or 2.4 kt of TNT) based on the light pulse energy. Among the data on large meteoric bodies published in the last 15 years, estimates of the initial kinetic energy of only 10 events exceed $\sim 10^{13}$ J.

When analyzing such large bodies probably of asteroidal origin, one may assume that the mean velocity of entry into the atmosphere was approximately $20 \text{ km}\cdot\text{s}^{-1}$. In this case, the mass of the body was approximately 50 t (90 t at $V \sim 17 \text{ km}\cdot\text{s}^{-1}$ and 30 t at $V \sim 25 \text{ km}\cdot\text{s}^{-1}$). Light impulses recorded by the satellite observation system were caused not only by the flight of the meteoroid, but also by its destruction, and the authors used the fragmentation models to consider the breakup of the Vitim meteoroid (Borovička et al. 1998a). The authors' estimates suggest that the main energy was released at altitudes <40 km (Fig. 7), and a large number of fragments was formed. Precise numbers and sizes of fragments are dependent on meteoroid strength used, fragmentation model, and meteoroid velocity. The mass of the greater part of the fragments is estimated as kilogram-weight, and a scattering field with a width of ~1–2 km and length of ~6–15 km probably was formed. Three expeditions worked in the fall area, but meteorites were not recovered (Antipin et al. 2004).

On 24 September 2002, the seismic stations Chara (56.9°N, 118.27°E), Nelyaty (56.49°N, 115.7°E), and Peledui (59.6°N, 112.6°E) recorded two signals that presumably were related to the event considered here. The first signals at each point apparently corresponded to the arrival of a seismic wave induced by a sound wave propagating vertically downward from the source (epicenter of the event), whereas the second signals were related to the influence of a direct infrasonic wave that propagated from the source and spread out in a subaerial waveguide on the seismic recorder.

Altitude and coordinates of the main fragmentation point were obtained based on the arrival time of these signals (Adushkin et al. 2004). The main disruption of the Vitim meteoroid occurred at ~27 km altitude and about above the point (58.3°N; 112.8°E; i.e., 30–40 km northwest of the trajectory determined by satellites). The

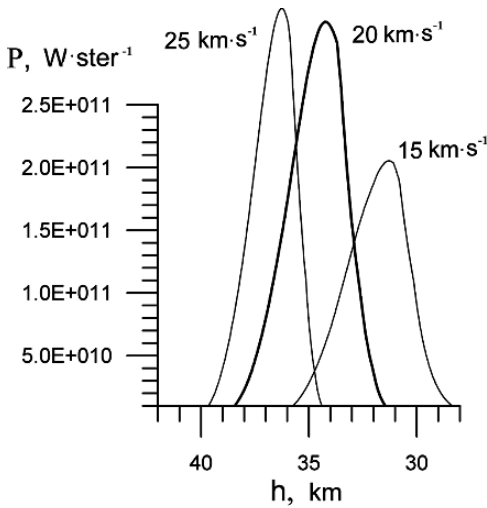


Figure 7. Model Vitim bolide light pulse for different entry velocities. The figure is adapted from Adushkin et al. (2004) and reprinted with the kind permission of Pleiades Publishing, Inc.

uncertainty of coordinate determination is ~ 10 km (because of uncertainty of the arrival time).

On 24 September 2002, continuous recording of infrasonic signals at the Ussuriisk, Zalesovo, Podol'sk, and other stations fixed the infrasonic perturbations of the fields, which can be identified as signals from the bolide. The stations are equipped with highly sensitive microbarographs designed for measurement of atmospheric pressure fluctuations in the frequency range 0.0015–0.5 Hz (at level 0.5). The frequencies in the spectral maximum region of recorded infrasonic signals are close to the Brunt-Vajsjalja frequency in the range 0.0016–0.003 Hz. Therefore, the record of perturbations at these frequencies is related to the propagation of both infrasonic waves and internal gravity waves from the source. Estimates show that the bolide excited internal gravity waves in the atmosphere that were almost an order of magnitude more intense than the infrasonic waves.

The estimates of Vitim meteoroid kinetic energy ($0.8\text{--}1.3 \cdot 10^{13}$ J) based on the registration of distant stations (2,000–4,000 km) agree with the energy determined based on the light pulse.

7.3 Vilalbeto de la Pena

The bolides with detail observational data producing meteorites are the most interesting events. Only nine cases are known so far. More details may be found in recent compilation by Popova et al. (2007). The most recent event (4 January 2004) is Vilalbeto de la Pena meteorite (Trigo-Rodríguez et al. 2004; Llorca et al. 2005). Thirty-three L6 ordinary chondrites with total mass of ~ 5 kg have been

recovered so far. The initial mass of the meteoroid was found to be 760 ± 150 kg by combining luminosity, seismic, infrasound, and cosmogenic radionuclide data (Llorca et al. 2005). The modeling of dynamics and light curve from the video record by Trigo-Rodríguez et al. (2006) gave the mass at the beginning of the video record ($h \sim 33$ km) of 550 ± 150 kg, corresponding to the initial mass of ~ 600 kg. Its entry velocity is estimated as $17 \text{ km}\cdot\text{s}^{-1}$. The initial kinetic energy of this body is ~ 0.02 kt TNT. Light energy is determined based on the video records under assumption that meteoroid radiation is similar to the radiation of a blackbody with 6,000 K temperature. It should be noted that for this relatively small body the difference of real spectrum from the blackbody one is greater than for larger bodies mentioned in the preceding. The fireball light curve extracted from the video shows at least seven flares, the most pronounced of which occurred at a height of 28 km. The first flare was observed at a height of 30 km under a dynamic pressure of 3.9 MPa, but no one can exclude the earlier fragmentation. The dynamic pressure at the main flare was 4.8 MPa, and 5 MPa at the position of the last flare at 22 km. The amplitude of the flares and the existence and appearance of the dust train show that most mass loss in fragmentation occurred in the form of dust. Nevertheless, small meteorites were formed as well, but their distribution shows that they were basically produced in the main fragmentation, which occurred at 28 km.

Number of meteorites whose flight is recorded increases constantly, and will increase further taking into account the interests to these unique events.

8 FREQUENCY OF LARGE BOLIDE IMPACTS

Data on 51 SN events were analyzed by Nemtchinov et al. (1997a,b) during a 22-month period of systematic observation in 1994–1996. The authors divided the total energy range of bolides into few energy bins, the kinetic energy ranging over a factor of four in each bin. The number of events in these energy bins is presented in Fig. 8 (gray cells). Unfortunately, systematic release of satellite data was stopped, but the information on a few events was published on the web site. The authors supplemented the systematic data from Nemtchinov et al. (1997a) by these recent observations. These events fall within the most populated energy bins and do not essentially change the distribution obtained previously. It is interesting to note that since 1994 there has been no registration of events similar to the energy of the 1 February 1994 bolide (~ 40 kt TNT).

The authors calculated the cumulative number of impacts N per year over the entire surface of the Earth depending on impactor energy E (Nemtchinov et al. 1997a) (Fig. 9, open circles). The decrease of cumulative number $N(E)$ at energies $E \leq 0.3$ kt TNT is caused by a decrease in the sensor's sensitivity.

The total energy released in the atmosphere per year in the energy range 0.02–30 kt TNT is about 55.7 kt TNT. About 36–37 meteoroids with energy in this range impact the Earth's atmosphere per year. The average energy of impacts is about 1.5 kt TNT. The largest annual event expected is about 10–15 kt TNT.

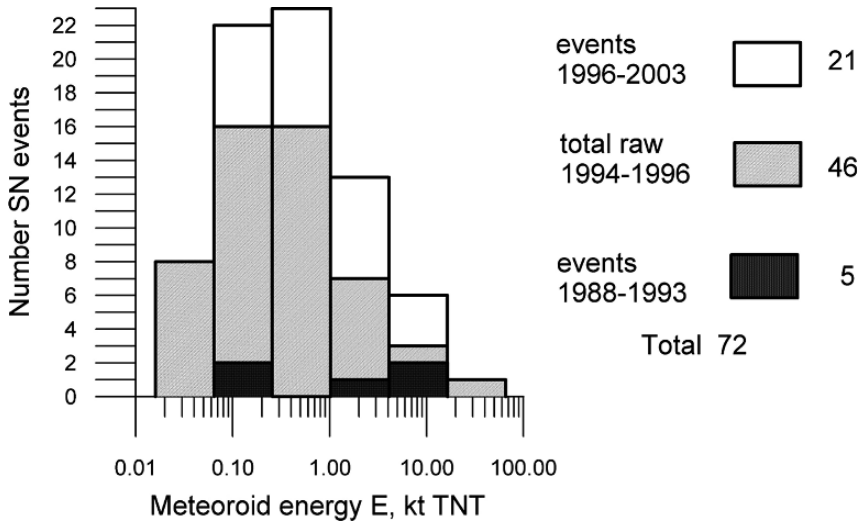


Figure 8. Frequency of events in dependence of meteoroid energy. The figure is adapted from Nemtchinov et al. (1997a) and reprinted with the kind permission of Elsevier

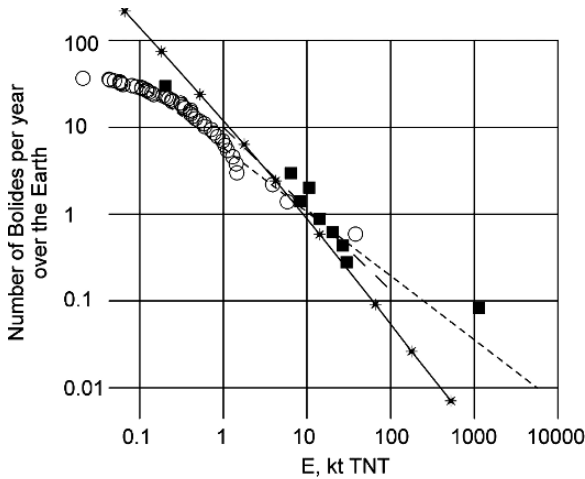


Figure 9. Cumulative number of impacts onto the Earth per year versus energy of impactor: open circles indicate detection by light sensors on board geostationary satellites taking into account the duration of the period of systematic observations (22 months) and correction factor for intermittence of observations in Eastern Hemisphere; black squares indicate observations by the acoustic system (ReVelle and Whitaker 1996); short dashed line indicates approximation of the acoustic observational data; dashed line indicates best estimate of the near Earth object by Shoemaker (1983); stars indicate distribution derived from lunar crater data. The figure is adapted from Nemtchinov et al. (1997a) and reprinted with the kind permission of Elsevier

Besides the data mentioned in the preceding, one more data set was released at the ACM99 Conference. These satellite observations covered about half of the Earth's surface. Seventeen events were recorded. The presenters (Pack et al. 1999) estimated that during the year about 14–59 meteoroids brighter than -18^{mag} enter the Earth's atmosphere. The largest event in this data set occurred on 14 January 1999. Its light energy was $\sim E_r \sim 1.2$ kt, which corresponds to the kinetic energy of ~ 11.5 kt and mass $\sim M \sim 400$ t (assuming the entry velocity $15 \text{ km}\cdot\text{s}^{-1}$). This energy is four times smaller than for the 1 February 1994 event, but the masses of meteoroids are similar. All other meteoroids are smaller. Their energies can be estimated at 0.06–0.4 kt and their sizes >1 m.

The energy–frequency distribution obtained from acoustic observations (ReVelle 1995) is shown by black squares. ReVelle (1995) has derived the following approximation for the energy–frequency distribution from the acoustic observation:

$$N = 7.17E^{-0.731}, \quad (17)$$

where N is the number of events per year with energy greater than E (Fig. 9, short dashed line). According Equation (17) the number of events rapidly increases with a decrease in the sensitivity limit E_s as $E_s^{-1.7}$, because the largest part of impactors are low energy.

In the energy range 0.5–2 kt, the results of acoustic observations and satellite registration are close to each other.

The largest event registered by the acoustic system had an estimated energy of ~ 1 Mt TNT. The appearance of a 1-Mt event is estimated at about once in 25 years. One such event was recorded during 17 years of acoustic observations (up to 1996) (ReVelle 1995; ReVelle and Whitaker 1996). No similar large event has been recorded to the present.

The extrapolation of suggested dependence Equation (17) to the 10-Mt energy (i.e., energy close to the Tunguska event) results in a rate of one event per 100 years. Figure 9 demonstrates that the unique 1-Mt event is situated far from the reminder set of events, with energies of about 10 kt. Consequently the certainty of a large energy impactor rate is low due to the very small number of observed events with large energy.

The total number of acoustically recorded events is about five times smaller than the number of events with optical registration.

The energy–frequency distribution obtained by light data analysis is compared with the best estimate by Shoemaker (1983). This approximation is mainly based on lunar crater data (Fig. 9). The following approximation is used for this best estimate:

$$N = 10E_k^{-0.87}, \quad (18)$$

where E_k is the kinetic energy in kt TNT. This approximation Equation (18) correlates with observational data both acoustic and optical systems in the energy

range <100 kt rather well (Fig. 9), except for the 1-Mt event recorded by the acoustic system. This approximation gives the probability of 1 Mt once in 40 years.

Compare the present data with the energy–frequency distribution obtained directly from lunar crater data (Neukum and Ivanov 1994; Ivanov 2001), not with its approximation by power law Equation (18). These data were approximated by a 12th-degree polynomial and are represented in Fig. 9 by stars. The satellite data agree with the original lunar crater record. The acoustic data also are in agreement with this curve, excluding the isolated 1-Mt event, for which the real interval between events is not known. According to the lunar curve this interval may be ~40–50 years.

The wavy character of the size–frequency distribution of asteroids in the asteroidal band, i.e., deviation from a simple power law (Dohnanyi 1969), was predicted in a number of papers concerning collisions and fragmentation of cosmic bodies (Farinella et al. 1982; Campo Bagatin et al. 1994a; Williams and Wetherill 1994). Wavy structure is explained by the accumulation of small bodies beyond the equilibrium value due to elimination of smaller ones, which are able to break them up. The wave period is determined by the relation between average kinetic energy and strength of colliding bodies. The strength of meter–kilometer bodies decreases with size increase; the strength of 10-km bodies increases due to self-gravitation. Different models of strength–size dependence provide different minima corresponding to the weaker bodies (Durda and Dermott 1997). The weakest are broken more frequently. Accordingly their number is smaller than that from the equilibrium distribution, and the deficiency of impactors causes the excess of larger bodies. Similar wavy structures were found in lunar crater distribution, craters on Mars and Mercury, and the size–frequency distribution in the main asteroid belt (Neukum and Ivanov 1994; Ivanov et al. 2002; Kuzmitcheva and Ivanov 2004). Simple power extrapolation into the range of large energies probably is not adoptable.

Many questions are still open about the process of large meteoroid interaction with the atmosphere. Observational data are still incomplete. It would be advantageous to extend ground-based observational networks, and maintain new networks in places with favorable weather- and meteorite-searching conditions (e.g., Spain, Morocco, and Australia). The first steps in this direction are being completed now. A full set of data, including detailed light curves, photographic trajectories, spectra, acoustic and seismic signals, and data on the composition of found meteorites would increase the precision of initial meteoroid parameter determination in comparison with the usage of integral luminous efficiencies. Known trajectories allow the determination of a parent body's orbit. Data processing should use the elaborated theoretical methods. For example, the optical properties of vapor with the composition of found meteorites should be used in determining instantaneous and integral luminous efficiencies. The fragmentation of meteoroids should be considered when taking into account both the breakup models and details from optical, acoustic, and seismic data.

REFERENCES

- Adushkin VV, Nemchinov IV (1994) Consequences of impacts of cosmic bodies on the surface of the Earth. In: Gehrels T (ed) *Hazards due to comets and asteroids*, University Arizona Press, Tucson, pp 721–778
- Adushkin VV, Popova OP, Rybnov YuS et al (2004) Geophysical effects of the Vitim bolide. *Doklady Earth Sciences* (Translated from *Doklady Akademii Nayk V.* 397) 397A(6):861–864
- Antipin VS, Yazev SA, Kuz'min MI, Perepelov AB, Efremov SA, Mitichkin MA, Ivanov AV (2004) Natural phenomena and the substance in the ablation trail of the Vitim meteoroid (September 25, 2002). *Doklady Physics* 49(10):573–577
- Artem'eva NA, Shuvalov VV (1996) Interaction of shock waves during passage of disrupted meteoroid through atmosphere. *Shock Waves* 5(6):359–367
- Artemieva NA, Shuvalov VV (2001) Motion of a fragmented meteoroid through the planetary atmosphere. *J Geophys Res* 106(E2):3297–3309
- Babadzhanov PB (1986) *Astronomy in Tadzhikistan*. IAU, Asian-Pacific Regional Meeting, 3rd, Kyoto, Japan, Sept 30–Oct 5, 1984. *Astrophys Space Sci* (ISSN 0004–640X)
- Bland PA, Artemieva NA (2003) Efficient disruption of small asteroids by Earth's atmosphere. *Nature* 424:288–291
- Bland PA, Spurny P, Bevan AWR et al (2006) First light for the desert fireball network. *Proceedings of 69th Annual Meeting of the Meteoritical Society*, August 6–11. Switzerland, Zurich. *Meteoritics Planetary Sci* 41:5197
- Borovička J, Kalenda P (2003) The Morávka meteorite fall: 4. Meteoroid dynamics and fragmentation in the atmosphere. *Meteoritics Planetary Sci* 38(7):1023–1043
- Borovička J, Popova OP, Golub' AP et al (1998b) Bolides produced by impacts of large meteoroids into the Earth's atmosphere: comparison of theory with observations. II. Benešov bolide spectra. *Astronom Astrophys* 337:591–602
- Borovička J, Popova OP, Nemtchinov IV et al (1998a) Bolides produced by impacts of large meteoroids into the Earth's atmosphere: comparison of theory with observations. I Benešov bolide dynamics and fragmentation. *Astronom Astrophys* 334:713–728
- Borovička J, Spurný P (1996) Radiation study of two very bright terrestrial bolides. *Icarus* 121:484–510
- Borovička J, Spurný P, Ceplecha Z (2001) The Morávka meteorite fall: fireball trajectory orbit and fragmentation from video records. *Meteoritics Planetary Sci Suppl* 36:A25
- Brown P, Ceplecha Z, Hawkes RL et al (1994) The orbit and atmospheric trajectory of the Peekskill meteorite from videorecords. *Nature* 367:624–626
- Brown P, Hilderband AR, Green DWE et al (1996) The fall of the St.Robert meteorite. *Meteoritics Planetary Sci* 31:502–517
- Brown P, Pack D, Edwards WN et al (2004) The orbit, atmospheric dynamics, and initial mass of the Park Forest meteorite. *Meteoritics Planetary Sci* 39(11):1781–1796
- Brown PG, Hildebrand AR, Zolensky ME et al (2000) The fall, recovery, orbit, and composition of the Tagish Lake meteorite: a new type of carbonaceous chondrite. *Science* 290(5490):320–325
- Brown PG, ReVelle DO, Tagliaferri E, Hildebrand AR (2001) The Tagish Lake meteorite fall: interpretation of physical and orbital data. *Proceedings Meteoroids 2001-Conference*, pp 497–505
- Brown PG, ReVelle DO, Tagliaferri E, Hildebrand AR (2002a) An entry model for the Tagish Lake fireball using seismic, satellite and infrasound records. *Meteoritics Planetary Sci* 37:661–675
- Brown PG, Spalding RE, ReVelle DO et al (2002b) The flux of small near-Earth objects colliding with the Earth. *Nature* 420(6913):294–296
- Campo Bagatin A, Cellino A, Davis DR et al (1994a) Wavy size distributions for collisional systems with a small-size cutoff. *Planet Space Sci* 42(12):1079–1092
- Ceplecha Z (1961) Multiple fall of Pribram meteorites photographed. *BAICz* 12:21–46
- Ceplecha Z (1992) Influx of interplanetary bodies onto Earth. *Astronom Astrophys* 263:361–366
- Ceplecha Z (1993) Meteoroid impacts into the Earth's atmosphere: 1 to 10 m size range. In: Gehrels T (ed) *Hazards due to comets and asteroids*. University of Arizona Press, Tucson, pp 25

- Ceplecha Z (1994) Impacts of meteoroids larger than 1 m into the Earth's atmosphere. *Astronom Astrophys* 286:967–970
- Ceplecha Z (1996) Luminous efficiencies based on photographic observations of Lost-City fireball and implications to the influx of interplanetary bodies onto Earth. *Astronom Astrophys* 311:329–332
- Ceplecha Z, Borovička J, Elford WG et al (1998) Meteor phenomena and bodies. *Space Sci Rev* 84:327–471
- Ceplecha Z, ReVelle DO (2005) Fragmentation model of meteoroid motion, mass loss, and radiation in the atmosphere. *Meteoritics Planetary Sci* 40(1):35–54
- Ceplecha Z, Spurný P, Borovička J, Kečliková J (1993) Atmospheric fragmentation of meteoroids. *Astronom Astrophys* 279(2):615–626
- Chernyi GG (1959) Gas flows with a high supersonic speed. Fizmatgiz, Moscow (in Russian)
- Chyba CF, Thomas PJ, Zahnle KJ (1993) The 1908 Tunguska explosion: atmospheric disruption of a stony asteroid. *Nature* 361(6407):40–44
- Consolmagno GSJ, Britt DT (2004) Meteoritical evidence and constraints on asteroid impacts and disruption. *Planet Space Sci* 52:1119–1128
- Dohnanyi JS (1969) Collisional model of asteroids and their debris. *J Geophys Res* 74:2531–2554
- Durda DD, Dermott SF (1997) The collisional evolution of the asteroid belt and its contribution to the zodiacal cloud. *Icarus* 130:140–164
- Edwards WN, Hildebrand AR (2004) SUPRACENTER: Locating fireball terminal bursts in the atmosphere using seismic arrivals. *Meteoritics Planetary Sci* 39(9):1449–1460
- Farinella P, Paolicchi P, Zappala V (1982) The asteroids as the outcomes of catastrophic collisions. *Icarus* 52:409–433
- Frost MJ (1969) Size and spacial distribution in meteoritic showers. *Meteoritics* 4(3):217–232
- Glasstone S, Dolan PJ (1977) The effects of nuclear weapons. US Department of Defense and US Department of Energy, US Government Printing Office, Washington, DC, p 653
- Golitsyn GS, Grigoryev GI, Dokuchaev VP (1977) Generation of acoustic-gravity waves at motion of meteors in the atmosphere. *Atmos Oceanic Phys* 13(9):633–639 (English translation)
- Golub' AP, Kosarev IB, Nemtchinov IV, Popova OP (1997) Emission spectra of bright bolides. *Solar System Res* 31(2):85–97
- Golub' AP, Kosarev IB, Nemchinov IV, Shuvalov VV (1996) Emission and ablation of a large meteoroid in the course of its motion through the Earth's atmosphere. *Solar System Res* 30(3):183–197
- Grigoryan SS (1979) On the motion and disruption of meteorites in planetary atmospheres. *Kosm Issled* 17(6):875–893
- Halliday I, Griffin AA, Blackwell AT (1981) The Innisfree meteorite fall: a photographic analysis of fragmentation, dynamics and luminosity. *Meteoritics* 16(2):153–170
- Halliday I, Griffin AA, Blackwell AT (1996) Detailed data for 259 fireballs from the Canadian camera network and inferences concerning the influx of large meteoroids. *Meteoritics Planetary Sci* 31: 185–217
- Hayes WD, Probstein RF (1959) Hypersonic flow theory. Academic, New York
- Hildebrand AR, Brown PG, Zolensky ME et al (2000) The fireball and strewnfield of the Tagish Lake meteorites, fell January 18, 2000, In northern British Columbia. *Meteoritics Planetary Sci* 35(5):A73
- Hills JG, Goda MP (1993) The fragmentation of small asteroids in the atmosphere. *Astronom J* 105(3):1114–1144
- Ivanov BA (2001) Mars/Moon cratering rate ratio estimates. *Space Sci Rev* 96(1/4):87–104
- Ivanov BA, Neukum G, Bottke WF Jr, Hartmann WK (2002) The comparison of size-frequency distributions of impact craters and asteroids and the planetary cratering rate. In: Bottke WF, Cellino A, Paolicchi P, Binzel RP (eds) *Asteroids III*. University of Arizona Press, Tucson, pp 89–101
- Jenniskens P, Betlem H, Betlem J et al (1994) The Mbale meteorite shower. *Meteoritics* 29(2):246–254
- Kiselev Yu N, Nemchinov IV, Shuvalov VV (1991) Mathematical modeling of the propagation of intensely radiating shock waves. *Comput Math Mathemat Phys* 31(6):87–101
- Kuzmitcheva MY, Ivanov BA (2004) Modelling of shock evolution of the population of main belt asteroids and the population of remnants of Earth accumulation. *Dynamics of Interacting Geospheres* IDG RAS. Moscow, pp 209–216 (in Russian)

- Levin, B. Yu (1956) *Fizicheskaya teoriya meteorov i meteornoe veshchestvo v Solnechnoi sisteme* (Physical Theory of Meteors and Meteoric Matter in the Solar System) Nauka, Moscow, 294 (in Russian)
- Llorca J, Trigo-Rodríguez JM, Ortiz JL et al (2005) The Villalbeto de la Peña meteorite fall: I. Fireball energy, meteorite recovery, strewn field, and petrography. *Meteoritics Planetary Sci* 40:795
- Loseva TV, Kosarev IB, Nemtchinov IV (1998) Thermal ablation of large cosmic bodies. *Solar System Res* 32(2):149–156
- McCrosky RE, Shao C.-Y, Posen A (1976) Prairie network fireball data I: summary and orbits. *Center Astrophys Prepr Ser* 665
- McCrosky RE, Shao C.-Y, Posen A (1977) Prairie network fireball data II: trajectories and light curves. *Center Astrophys Prepr Ser* 721
- McCord TB, Morris J, Persing D et al (1995) Detection of a meteoroid entry into the Earth's atmosphere on February 1, 1994. *J Geophys Res* 100(E2):3245–3249
- Melosh HJ (1981) Atmospheric breakup of terrestrial impactors. In: Schultz PH, Merrill RB (eds) *Multi-ring basins*. Pergamon Press, New York, pp 29–35
- Melosh HJ (1989) *Impact cratering: a geologic process* (Oxford Monographs on Geology and Geophysics, No. 11). Oxford University Press, New York, p 245
- Nemchinov IV (1994) Intensely radiating shock waves. *Sov J Chem Rhys* 12(3):438–458
- Nemtchinov IV, Jacobs C, Tagliaferri E (1997b) Analysis of satellite observations of large meteoroid impacts. In: Remo J (ed) *Near-Earth Objects*. *Ann NY Acad Sci* 822:303–317
- Nemtchinov IV, Kuzmicheva M Yu, Shuvalov VV et al (1999) Šumava meteoroid: was it a small comet? Evolution and source regions of asteroids and comets. *Proceedings of the IAU Colloquium 173 Svoren J, Pittich EM, Rickman H (eds) Astronom Inst Slovak Acad Sci Tatranska Lomnica*, pp 51–56
- Nemtchinov IV, Popova OP (1997) An analysis of the 1947 Sikhote-Alin event and a comparison with the phenomenon of February 1, 1994. *Solar System Res* 31(5):408–420
- Nemtchinov IV, Popova OP, Shuvalov VV, Svetsov VV (1994) Radiation emitted during the flight of asteroids and comets through atmosphere. *Planet Space Sci* 42(6):491–506
- Nemtchinov IV, Popova OP, Svetsov VV, Shuvalov VV (1995) On the photometric masses and radiation sizes of large meteoroids. *Solar System Res* 29(2):133–150
- Nemtchinov IV, Svetsov VV, Kosarev IB et al (1997a) Assessment of kinetic energy of meteoroids detected by satellite-based light sensors. *Icarus* 130(2):259–274
- Neukum G, Ivanov BA (1994) Crater size distributions and impact probabilities on Earth from Lunar, terrestrial-planet, and asteroid cratering data. In: Gehrels T (ed) *Hazards due to comets and asteroids*. University of Arizona Press, Tucson, pp 359–416
- Oberst J, Molau S, Heinlein D et al (1998) The “European Fireball Network”: current status and future prospects. *Meteoritics Planetary Sci* 33:49–56
- Pack DW, Tagliaferri E, Yoo BB et al (1999) Recent satellite observations of large meteor events. *Asteroids, comets, meteors 1999*. Cornell University, Ithaca, NY, pp 48
- Passy QR, Melosh HJ (1980) Effects of atmospheric breakup on crater field formation. *Icarus* 42(2): 211–233
- Pedersen H, Spalding RE, Tagliaferri E et al (2001) Greenland superbolide event of 1997 December 9. *Meteoritics Planetary Sci* 36:549–558
- Popova O, Hartmann WK, Borovička J, Spurný P, Trigo-Rodríguez J, Gnos E, Nemtchinov I (2007) Very low strengths of interplanetary meteoroids and small asteroids. Submitted to *Icarus*
- Popova OP, Nemtchinov IV (1996) Estimates of PN bolide characteristics based on the light curves. *Meteoritics Planetary Sci (Suppl 31):A110*
- Popova OP, Nemtchinov IV (2002) Strength of large meteoroids entering Earth atmosphere. *Proceedings Conference of Asteroids, Comets, Meteors (ACM 2002)*, Technical University Berlin, pp 281–284
- Popova O, Nemtchinov I, Hartmann WK (2003) Bolidés in the present and past Martian atmosphere and effects on cratering processes. *Meteoritics Planetary Sci* 38(6):905–925
- Reimold WU, Buchanan PC, Ambrose D, Koeberl C (2003) The H4/5 Thuathe meteorite fall of 21 July 2002, Lesotho: history of the fall, strewn field determination, and mineralogical and geochemical characterization. *Meteoritics Planetary Sci (Suppl 38) 5015*

- ReVelle DO (1976) On meteor generated infrasound. *J Geophys Res* 81:1217–1240
- ReVelle DO (1995) Historical detection of atmospheric impacts by large bolides using acoustic-gravity waves. *Int Conf Near-Earth Objects*. April 24–26, 1995. The Explorers Club and United Nations Office for Outer Space Affairs. New York, book of abstracts
- ReVelle DO (1997) Historical detection of atmospheric impacts by large bolides using acoustic gravity waves. In: Remo J (ed) *Near-Earth Objects*. *Ann NY Acad Sci* 822:284–302
- ReVelle DO (2001) Global infrasonic monitoring of large bolides. *Proceedings of the Meteoroids 2001-Conference, Swedish Institute of Space Physics, Kiruna, Sweden, 6–10 August 2001 (ESA SP-495, November 2001)*, pp 483–489
- ReVelle DO, Cepelch Z (2001) Bolide physical theory with application to PN and EN fireballs. *Proceedings of the Meteoroids 2001-Conference, Swedish Institute of Space Physics, Kiruna, Sweden, 6–10 August 2001 (ESA SP-495, November 2001)*, pp 507–512
- ReVelle DO, Whitaker RW (1996) Acoustic efficiency analysis using infrasound from NEOs. *Proceedings of the Comet Day II (5th International Conference Space-96)*. June 1–6, 1996. Albuquerque, NM
- ReVelle DO, Brown PG, Spurný P (2004) Entry dynamics and acoustics/infrasonic/seismic analysis for the Neuschwanstein meteorite fall. *Meteoritics Planetary Sci* 39(10):1605–1626
- Reynolds DA (1992) Fireball observation via satellite. *Proceedings of the Near-Earth-Object Interception Workshop Canavan GH, Solem JC, Rather JDG (eds) Los Alamos National Lab, Los Alamos, NM, pp 221–226*
- Shoemaker EM (1983) Asteroid and comet bombardment of the Earth. *Ann Rev Earth Planet Sci* 11:461–494
- Simon SB, Grossman L, Clayton RN et al (2004) The fall, recovery, and classification of the Park Forest meteorite. *Meteoritics Planetary Sci* 39(4):625–634
- Spurný P, Porubčan V (2002) The EN171101 bolide—the deepest ever photographed fireball. *Proc Asteroids, Comets, Meteors—ACM 2002 Barbara Warmbein (ed) Int Conf 29 July–2 August 2002. Germany, Berlin, pp 269–272*
- Spurný P, Oberst J, Heinlein D (2003) Photographic observations of Neuschwanstein, a second meteorite from the orbit of the Pribram chondrite. *Nature* 423:151–153
- Svetsov VV (1994a) Radiation emitted during the flight: application to assessment of bolide parameters from the satellite recorded light flashes. *Lunar Planet Sci XXV. LPSI, Houston, pp 1365–1366*
- Svetsov VV, Nemtchinov IV, Teterev AV (1995) Disintegration of large meteoroids in Earth's atmosphere: theoretical models. *Icarus* 116:131–153. Errata: *Icarus* 1996 120(2):443
- Tagliaferri E (1993) Asteroid detection by space based sensors. Presented at the Erice International Seminar on Planetary Emergencies. *The Collision of an Asteroid or Comet with the Earth*
- Tagliaferri E (1996) Satellite observations of large meteoroid impacts. *Meteoroid Impact Workshop. Sandia National Laboratories, Albuquerque, NM, June 4–7.*
- Tagliaferri E, Spalding R, Jacobs C et al (1994) Detection of meteoroid impacts by optical sensors in Earth orbit. In: T Gehrels (ed) *Hazards due to comets and asteroids*. University of Arizona Press, Tucson, pp 199–220
- Trigo-Rodríguez JM, Llorca J, Ortiz JL et al (2004) The “Villalbeto de la Peña” meteorite fall: bolide description, recovery, and classification. *Meteoritics Planetary Sci (Suppl 39):A106*
- Trigo-Rodríguez JM, Āorovička, Spurný, JL, Ortiz JA, Docobo AJ, Castro-Tirado, Llorca J (2006) The Villalbeto de la Peña meteorite fall: II. Determination of the atmospheric trajectory and orbit. *Meteoritics & Planetary Science* 41:505–517
- Tsvetkov VI (1987) Sikhote Alin meteorite shower: fragmentation, scattering, trajectory and orbit. *Meteoritika* 46:3–10 (in Russian)
- Wacker JF, Hildebrand AR, Brown P et al (1998) The Juancheng and El Paso superbolides February 15, 1997, and October 9, 1997: preatmospheric meteoroid sizes. *Meteoritics Planetary Sci* 33(4):160
- Walsh JB, Zhu W (2004) Sliding of a rough surface under oblique loading. *J Geophys Res* 109. B05208, doi:10.1029/2004JB003027
- Weibull W (1951) A statistical distribution function of wide applicability. *J Appl Mech* 10:140–147

- Williams DR, Wetherill GW (1994) Size distribution of collisionally evolved asteroidal populations—analytical solution for self-similar collision cascades. *Icarus* 107:117–128
- Zahnle K (1992) Airburst origin of dark shadows on Venus. *J Geophys Res* 97(E8):10243–10255
- Zel'dovitch Ya B, Raiser Yu P (1967) *Physics of shock waves and high-temperature hydrodynamic phenomena*. Academic Press, New York

CHAPTER 5

GEOLOGIC EFFECTS OF LARGE TERRESTRIAL IMPACT CRATER FORMATION

BORIS IVANOV

*Institute for Dynamics of Geospheres, Russian Academy of Sciences, Moscow 119334, Russia
E-mail: baivanov@idg.chph.ras.ru*

To date around 180 impact structures have been identified on Earth. The diameters of these structures are from ~ 10 to $\sim 200\text{--}250$ km. Knowledge about terrestrial impact structures accumulated during many decades includes a large amount of geological and geophysical data. These data are very useful in formulating important constraints for impact model parameters reaching a double goal: (1) to fit parameters in the available mechanical models of planetary crust reaction to the impact event, and (2) to use numerical modeling to make an insight into the possible original structure of partially eroded terrestrial impact structures. This chapter presents results of numerical modeling for selected terrestrial impact craters (Puchezh-Karunki, Popigai, Vredefort, Sudbury, and Chicxulub) and compares model results with available geologic and geophysical data, obtained in the field study of aforementioned structures.

1 INTRODUCTION

The formation of terrestrial planets, as we see them now, was completed ~ 4.5 Ga ago. The complicated collision evolution of planetesimals, condensed previously from the gas-dust nebula, resulted in main planet formation. Leftovers of these processes, namely planetesimals, not incorporated into main planets were the possible population of bombardment projectiles, recorded on the early planetary surfaces of Mercury, the Moon, and Mars as craters of the late heavy bombardment period (LHB). The LHB ended ~ 3.3 Ga ago. After this period slow orbital evolution of small bodies in the Solar System continued to support approximately constant bombardment flux, resulting in the permanent formation of new impact craters on planetary surfaces, including of course, the surface of the Earth. In the central Russia the last visible crater-forming impact event was observed in Bashkiria on

17 May 1990. The impact of a small iron meteoroid resulted in the formation in a potato field of a crater with a diameter of 10 m (Fig. 1). The largest recovered meteoroid fragment has mass of 315 kg. Pre-atmospheric mass of the meteoroid is estimated as $>1,500$ kg (Petaev et al. 1991; Ivanov and Petaev 1992).

To date around 180 impact craters are recognized on the Earth's surface. The oldest structures have an age of ~ 2 Ga. Crater diameters vary from a few meters to ~ 200 km. The preservation level of a crater structure also varies by a wide range.

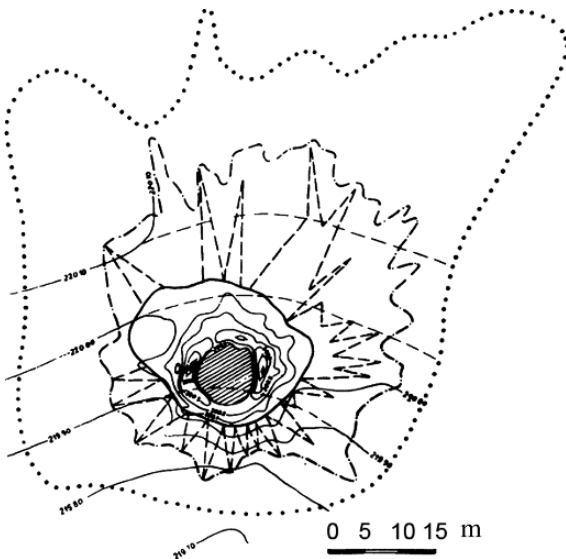


Figure 1. Photo of the Sterlitamak impact crater with diameter of 10 m, formed in Bashkiria, Russia, May 17, 1990 (top panel). The bottom panel presents a draft of the ejecta topography map, constructed by Petaev et al. (1991)

Impact craters have been studied with numerous techniques, including geological and geophysical surveys and deep core drilling. In the last two decades computer numerical modeling of crater-forming processes has proved its usefulness, providing a wide range of possibilities to verify models by comparison with field observations. In return the numerical models allow us to construct the reliable framework for generalization of necessary patchy geological and geophysical observations and search for general laws of planetary impact cratering.

The history of the lunar surface gives an important window to the hidden early evolution of terrestrial planets. The early impacts, which created numerous impact craters and basins, are dated to be as old as ~ 4 Ga. Ancient impact craters are visible on Mercury and Mars, and possibly on ice satellites of Jupiter and Saturn. An equivalently large number of ancient impact craters were inevitably formed on the early Earth surface as well. However, active Earth tectonic-magmatic processes have erased the footprints of these catastrophes. Similar resurfacing occurs on Venus also. On Earth and Venus one can see approximately the same diameter, D , of the largest preserved impact structures on the order of 100–300 km. On Venus the largest recognized impact crater is the Mead crater ($D \sim 260$ km), whereas ten craters have $D > 100$ km. On Earth to date four craters with $D > 100$ km have been found: Popigai (Masaitis et al. 1975), Chicxulub, Sudbery, and Vredefort (see Grieve and Theriault, 2000 for an excellent review).

The *spatial distribution* of known impact craters over the Earth surface is very uneven (Fig. 2). This is the result of several factors, including various levels of geologic survey completeness, and the different geologic histories of different regions.

The *accumulation rate* (the rate of new craters formed) depends mainly on physical and orbital evolution of small bodies in the Solar System (see Chap. 2),



Figure 2. Locations of known terrestrial craters on the Earth's surface

which may be taken as approximately constant for each crater size averaged over ~ 30 Ma and longer periods. Hence, relatively young areas of fast sedimentation on continents and the oceanic floor, permanently renovated by subduction and middle-ocean ridge volcanism, do not accumulate a large number of impact craters visible on the surface: Just-formed craters are quickly erased or buried by endogenic activity. In many areas of the world, impact craters found on the modern surface have been buried for many millions and tens of millions of years under eroded (and now overburdened) layers. It is only recent erosion of these areas that has exposed visible remnants of impact craters on the day surface, allowing relatively easy recognition. A notable example of such recently exhumed craters is Ries and Steinheim craters in Germany. Formed ~ 15 Ma ago, they were buried under the shallow sea sediments, eroded now. The history of impact craters in Fennoscandia in the area of the Caledonian tectonic deformation is very complicated. Recognized impact craters in this area have an age span up to 1–2 Ga. Meanwhile, 13 of 26 known craters formed during the time period between 300 and 700 Ma ago. In the following period only seven known craters with ages of 70–230 Ma formed. This fact is in favor of the idea that in many areas in Fennoscandia one sees the exhumed ancient surface, buried under cover for tens and hundreds of millions of years. Unknown numbers of impact craters seem to be formed in these cover rocks, which are now totally eroded.

A few large impact craters are found in the European part of Russia (mostly in the limits of Russian platform). Their location is shown in Fig. 3.

Excluding erosion remnants of Suavjärvi and Jänisjärvi structures at the east margin of Fennoscandia, visible at the modern surface, most of impact craters in the Russian platform currently are buried under 100–800 m of sedimentary rocks. Buried craters are studied by geophysical techniques and drilling (Fig. 4). The dome-like structural elements such as central peak or rim uplift were drilled first.

Size-frequency and age-frequency distributions of known terrestrial impact craters is shown in Fig. 5. These distributions illustrate that the balance of crater formation and obliteration results in finding still-visible craters as only a small fraction of the total number of impact events in the Earth's history. Assuming a constant impact crater production rate in the past 3 Ga, one can estimate the frequency of crater-forming impacts (Fig. 5). On average one new 10-km crater appears on Earth every 10 Ma, and one 50-km may be formed every ~ 10 Ma. Impacts, resulted in craters with diameters from 100 to 200 km on continents, occurs approximately once per 100 Ma.

The simple illustration of the balance between accumulation and obliteration rate of impact cratering may be presented with a standard balance Equation:

$$dN/dt = N' - N/\tau, \quad (1)$$

where N is the number of visible impact craters of a given diameter, N' is the cratering rate, and τ is the average characteristic time of crater obliteration (i.e., the average time period before a crater becomes unrecognizable with modern geologic



Figure 3. Known impact craters in the European Russia: Suavjärvi (“S,” D ~ 16 km, age ~2.4 Ga), Jänisjärvi (“J,” D ~ 16 km, age ~700 Ma), Mishina Gora (“M,” D ~ 5 km, age ~360 Ma), Kaluga (“<K>1,” D ~ 15 km, age ~380 Ma), Kursk (“<K>2,” D ~ 6 km, age ~250 Ma), Karla (“<K>3,” D ~ 10 km, age ~10 Ma), Puchezh-Katunki (“PK,” D ~ 40 km, age ~170 Ma), Kamensk and Gusev (“K + G,” D ~ 25 km and ~3.5 km correspondingly for the same age of ~65 Ma). Not shown in the figure Kara crater (D ~ 65 km, age ~70 Ma with a possible companion Ust-Kara crater) is situated in Polar Ural region near the Kara river mouth

and geophysical observation techniques). The solution of Equation (1) presents the number of recognizable craters at any given time:

$$N = g\tau N' [1 - \exp(-t/\tau)]. \tag{2}$$

Approximate fit of the curve for number of craters with D>9 km (Fig. 5a) gives the estimate of τ on the order of 220 Ma. This estimate is an average value for various geologic regions of continents. Its value should vary from region to region. However, even this simple estimate shows that the oceanic floor, permanently renovated by spreading and subduction with a time scale of 50–150 Ma, is too

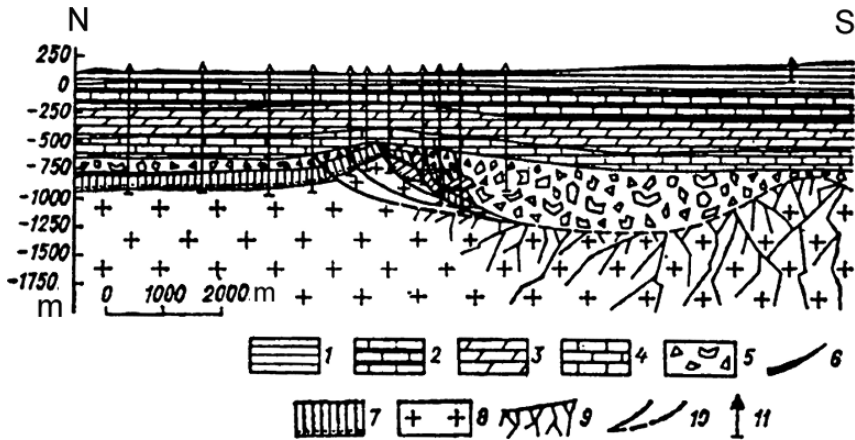


Figure 4. A buried crater in the Russian platform model with the radial cross-section of the Kursk impact crater (Masaitis et al. 1980). 1 to 4—sedimentary rocks, 5—redeposited allogenic breccia, 6—Middle Devon rocks, 7—Vend limestone, 8—crystalline basement (granite, gneiss, shist), 9—fracturing zone (autogenic breccia), 10—faults and thrusts, 11—drill holes. According to drilling data the elevated crater structural rim is still preserved under ~700 m of sedimentary overburden. Adapted from Masaitis et al. (1980) with permission from Nedra Press

young at any given moment to accumulate more impact craters than survive in an average continental environment. In addition, the water layer of oceans successfully shields the floor, effectively destroying asteroids before they reach the sea floor.

Impact crater morphology varies with size from a simple morphology for small craters to a complex morphology for large craters (Melosh 1989). Simple craters are similar to explosion craters created by surface and shallow detonations of high explosive and nuclear charges. Experimental data about simple craters, accumulated in the field and laboratory conditions, furnish decisive knowledge about simple crater formation. Complex craters on Earth are formed when the crater diameter is >3–4 km, the scale range unavailable for direct experimental modeling. The understanding of complex impact crater formation needs a combination of geological investigations, comparative study of impact craters in different planets, and thorough numerical modeling.

The aim of this chapter is to illustrate the approach to complex crater formation study by comparison of geologic data, collected in the field and laboratory, with results of numerical modeling. Terrestrial impact craters are discussed with the well-investigated Russian craters Puchezh-Katunki and Popigai, and the largest known craters Chicxulub (Mexico) and Vredefort (South Africa). A short comparison is also presented for the Sudbury structure (Canada), possibly similar to Vredefort in original size. All impact structures described in the following have been modified by postimpact endogenic processes such as tectonic deformation, erosion, and sedimentation. Consequently, data for various craters should be used for a comparative

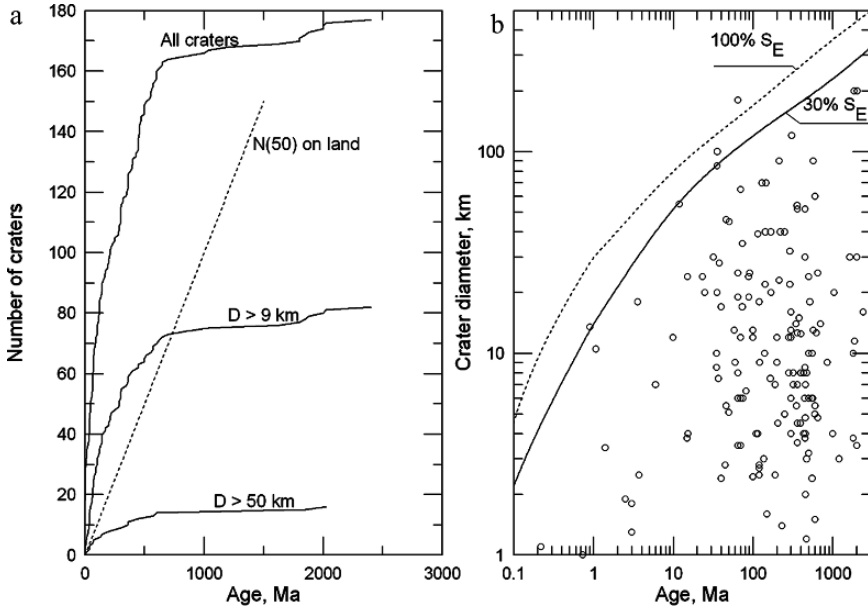


Figure 5. Age–frequency (a) and size–age (b) distributions of known terrestrial impact craters. (a) Cumulative number of craters younger the given age. For craters with diameters $D > 50$ km the production rate estimated in Chap. 2 (dotted line) is shown for total modern continental surface area (\sim one-third of the total surface area of the Earth). The balance of crater formation and obliteration results in accumulation of the observed number of 15–16 craters for the total surface of continents. (b) Scattered diagram of impact crater diameters versus ages of craters. The lunar chronology, recalculated to terrestrial conditions (see Chap. 2) allows one to estimate the cratering rate depending on the crater diameter. (Small craters form more often than large craters.) Solid and dashed curved lines show the estimated average time interval between impacts, created craters of different diameters, for the total surface area of the globe (oceans plus continents), S_T , and for land area only (\sim one-third S_T)

study of variously modified craters before one can arrive at a picture of the largest terrestrial crater formation.

2 NUMERICAL MODELING OF IMPACT CRATERING

Numerical modeling of impact crater formation technically includes solution of standard hydrodynamic equations of the continuous media motion expressing fundamental conservation laws for mass, momentum, and energy. These equations approximated by finite differences are solved with special computer codes, often called hydrocodes. Parameters of the material motion, such as density, velocity, pressure, and energy, are defined in nodes of the computational grid of computational cells. The present chapter uses the hydrocode SALEB. The basic version SALE-2D was published by the Los Alamos National Laboratory, New Mexico (Amsden et al. 1980), as the code for solution of equations, describing motion of

a viscous compressible liquid “at all speeds.” Later Melosh et al. (1992) enhanced the basic code by addition of the elastic stress description with a treatment of the tensile and shear plastic failure. The author of the present chapter (BAI) made further code improvements implementing mixed material cells to the Eulerian option of the hydrocode. The technique allows one to advect mixed-material parameters through the computational grid, including deviatoric stresses. In addition, the elastic–plastic material model (Ivanov et al. 1997) and the acoustic fluidization (AF) model (Melosh and Ivanov 1999) have been incorporated into the code (see Wünnemann and Ivanov 2003; Collins et al. 2004 for details). A manual for the current SALEB version is now under preparation. A Lagrangian variant of the multimaterial code named SALES-2 is supported by Melosh and Collins at the web site http://www.lpl.arizona.edu/tekton/sales_2.html (December 2006).

The SALE hydrocode is a two-dimensional (2D) code. This means that the code can solve planar and spatial problems with axial symmetry (the main case is the vertical impact). The computational grid is rectangular in shape. Boundary conditions for the later case are defined as: left boundary is the axis of cylindrical symmetry, right and bottom are rigid nonpenetrating walls, and the top boundary may be a rigid or unidirectional penetrating boundary (allowing outflux of material beyond the computational area). To suppress stress waves reflected from boundaries SALEB uses a nonuniform grid. The central zone of the main interest is covered with fine cells, whereas beyond this zone cell sizes gradually increase to the grid periphery, to put rigid boundaries as far as possible from the point of impact. In the typical impact cratering run the central zone is covered with 200–300 cells in horizontal directions. An additional 50–100 nonuniform cells around the central zone delay the arrival of reflected waves and decrease their amplitude to a level that does not change dramatically the crater formation process in the central zone. In physical units, for example, in the case of the final crater radius of ~50 km, the central zone has a size slightly larger than the final crater rim radius, whereas grid boundaries are moved to a distance of 400–500 km away from the point of impact.

Equation of state (EOS) is the next essential component of the impact cratering numerical model. These equations, individual for each type of target material and projectile, close the system of equations of the material motion, relating density, pressure, and the specific internal energy (or temperature) of materials in each computational cell at each time step of the model run. In the case of asteroid and comet impacts on terrestrial planets, the EOS should describe factors of 3–5 material compressions to reproduce maximum pressures of 100–500 GPa, and the material decompression to ambient pressure, where compressed materials may convert to melt or vapors. Basic models are well known for each of the three main states of a material (solid, liquid, or vapor), and are verified with experimental data (see the classic books by Landau and Lifshits 1958; Zel’dovitch and Raiser 1967; Zharkov and Kalinin 1968). The numerical modeling needs to use all of these models, and in addition, it needs to have a smooth interpolation between phase space areas described by basic models. In the set of modeling presented in the following the

computer code ANEOS (ANalytical Equation Of State) (Thompson and Lauson 1972) is used to compute a wide range tables for owing use in computations. ANEOS proposes a set of options for calculations of pressure, temperature, and entropy using Mie-Gruneisen and Debye models in a solid-state phase region with a smooth transition to the Thomas-Fermi model at extremely large compressions, and to the ideal atomic gas in the phase region of the material vaporization.

The presented modeling uses ANEOS-based tables, constructed by the author for granite, quartzite, and dunite to model rocks of the Earth crust and upper mantle. Input parameters for granite have been published by Pierazzo et al. (1997); for quartzite and dunite input as preliminary data have been reported by Melosh (see details in Melosh 2000). In the original form ANEOS has severe limitations in the ability to compute simultaneously solid–solid phase transitions, material melting, and vaporization for an individual material. These restrictions may be bypassed by computation of each individual phase as a separate material with the specific input set of parameters with the following computation of proper phase boundaries. This work is still in progress (see preliminary results in Ivanov 2003b, 2004b; Ivanov et al. 2004).

3 NUMERICAL MODELING OF LARGEST TERRESTRIAL IMPACT CRATERS

For insight into processes of large terrestrial crater formation, the authors use numerical modeling of impact cratering events. The authors numerically compute vertical crater-forming impacts for two- and three-layer targets that reproduced the sedimentary cover, terrestrial crust, and upper mantle or two-layer terrestrial crust and upper mantle. Since the resolution of the computational grid (the cell size in the central region) was 200–350 m, a layering thinner than 1–3 km could not be resolved as individual layers. Such a resolution allows one to model a spherical projectile with about 40 cells for the projectile diameter. This is believed to be enough to reproduce, for example, the volume of melted rocks with an accuracy of about 25% compared with computations in which projectiles are represented with twice as many computational cells (Pierazzo et al. 1997). The chosen compromise between the accuracy of shock compression description and the overall size of the computational grid allowed the computations to be performed on a grid with a constant cell size (without usual grid resizing at late computational stages). The formation of a crater was computed up to a physical time of 400–800 s, which in general, was enough for the final crater shape to be formed. The initial guess for the projectile diameter was made with published scaling laws (Schmidt and Housen 1987). Subsequently, the authors chose the projectile diameter (and more rarely, the impact velocity) by trial and error and then varied the model parameters for which no reliable experimental data were available (mainly the AF model parameters). From 10 to 30 computations were performed for each of the craters considered in the following, which allowed the authors to estimate the logic of results to variations in model parameters. These results require a detailed discussion that is

beyond the scope of this chapter. Here the main objective is to demonstrate the approach to comparing numerical models and observational data. Therefore, as a rule, this chapter presents the results of the “best” computations that, in the authors’ opinion, are most useful for further improvement. Computational results for the four largest craters found to date on the Earth are discussed in the following. For the unity of this discussion, the target properties will be given for each crater as well as references to special literature containing the geological and geophysical data on each impact structure known to date.

The Puchezh-Katunki impact crater (age 170 Ma) is located on the left bank of modern Volga river north of Nizhnii Novgorod city (Masaitis et al. 1980). Morphologic elements of the structure include a circular depression (outer diameter of 40 km), with a central uplift (Vorotilovo uprise). The shallow zone of near-surface disrupted target rocks (100–200 m thickness) around the crater has a diameter of 80 km, which is twice larger than the estimated pre-erosional rim crater diameter of 40 km. The target cross-section (top to bottom) consists of ~2 km of sedimentary rocks over the crystalline (gneiss, amphibolite) basement. The well-known Vorotilovo deep drill hole (sampled the central uplift to a depth of 5,374 m) presents unique data on the shocked rocks under the large impact terrestrial crater (Puchezh-Katunki 1999). Scientists of the Institute for Dynamics of Geospheres were invited to participate in data acquisition, modeling, and interpretation (Ivanov 1992; Ivanov et al. 1996b; Puchezh-Katunki 1999; Ivanov 2002). In addition to drilling data analysis, a special study was published on horizontal flow out of crater ejecta after deposition (Ivanov 1996). This study confirmed the hypothesis of Masaitis about the origin of the shallow disturbed zone around the central depression as the zone of ballistic erosion of a surface by landing and moving ejecta. Recently some details of similar ejecta-related near-surface deformations were analyzed and modeled for the Ries crater in Germany (Kenkmann and Ivanov 2006).

Figure 6 compares the morphology of the Puchezh-Katunki impact crater (postimpact sediments are removed) and the similar-size impact crater Sascia on Venus. Both craters have a flat floor with a central mound (uplift). The continued ejecta deposits around the Venusian crater may cover a similar shallow disturbed zone of the original target surface, as was found around the Puchezh-Katunki impact crater.

Numerical modeling of the Puchezh-Katunki impact crater was conducted (after a set of trial model runs) for the vertical impact of an asteroid of 2 km in diameter with a velocity of $15 \text{ km}\cdot\text{s}^{-1}$. Variations in model parameters included projectile size and target rock strength. The fit was controlled with the final crater size and morphology, as well as the final position of rocks shocked to various shock pressures. The latter problem is very sensitive to variation in model parameters as the “stratigraphic column” of rocks just under the point of impact experiences extremely complex deformation and dislocation during crater formation. At the early stage the column experiences strong shock compression, and deformation (squeezing) during the transient crater growth. At this stage the squeezed (shortened and widened) “column” moves well below the initial stratigraphic level. During the

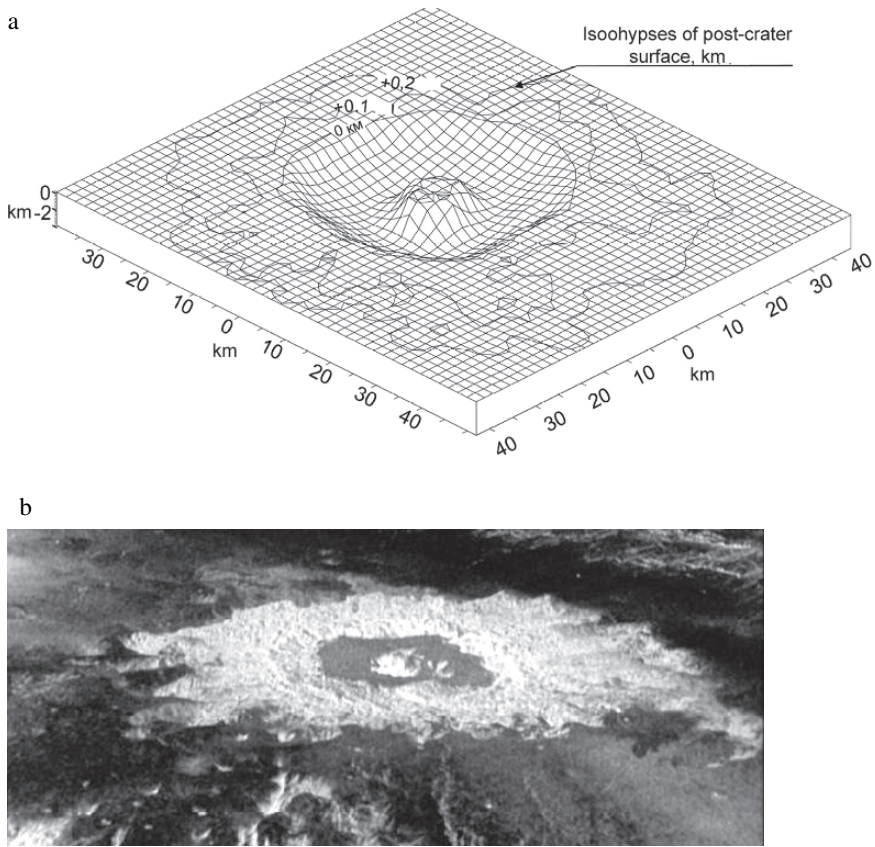


Figure 6. Morphology of the true floor of the Puchezh-Katunki impact crater (top) and the similar size Venusian crater Saskia (bottom). Figure 5.6a is adapted from *Deep Drilling in the Impact Structure: Puchezh-Katunki (1999)* with permission from Vsegei

transient crater collapse the central “column” is uplifted to the observed position (above the initial stratigraphic position) with partial restoration of the initial length. Consequently the apparent variation of the recorded shock pressure along the drilled core is a robust test for the general model of impact cratering.

The cross-section of the Puchezh-Katunki impact crater along one of radial directions is shown in Fig. 7. They demonstrate that the crater depression extends 17–20 km, ensuring that the apparent crater diameter is <40 km. The numerical modeling of crater formation (Ivanov 2002) allows one to reproduce main structural features of the crater (Fig. 7c)—the central uplift and circular crater with a diameter of 40 km. The model estimates that rocks at the end of the Vorotilovo drill hole (5,374 m below the modern surface) originally had been situated at depths of 8–9 km (stippled layer in Fig. 7c).

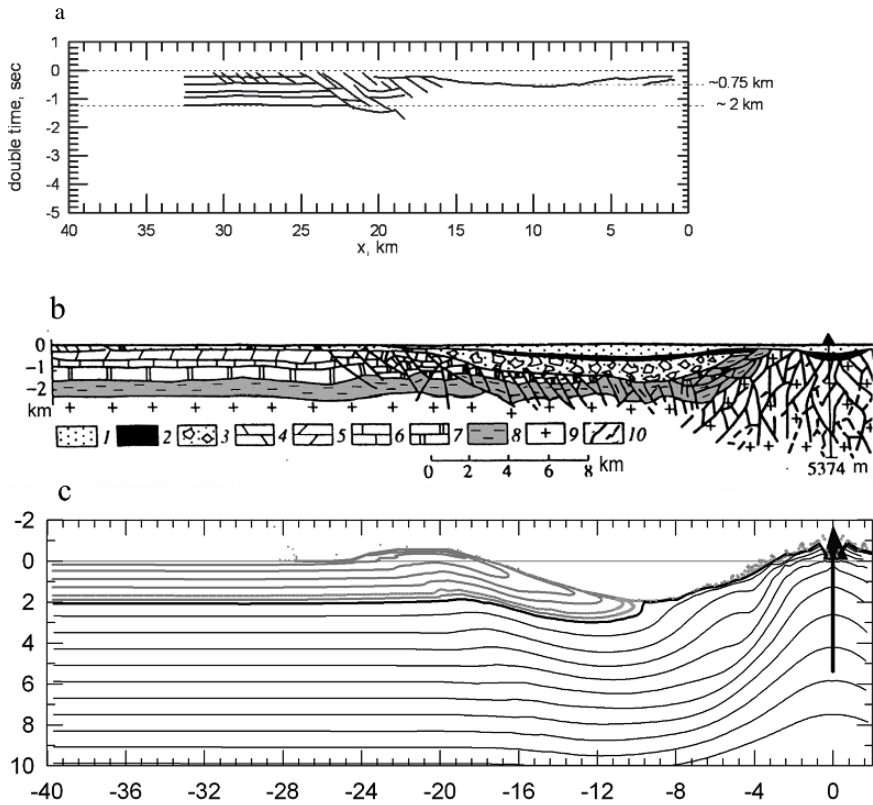


Figure 7. The Puchezh-Katunki impact crater radial cross-section presented through geophysical interpretation of seismic sounding: (a) geologic data (b) and the numerical modeling (c) 1—postimpact ("young") sediments, 2—suevites, 3—allogenic breccia, 4 to 8—sedimentary rocks of various ages, 9—crystalline basement. The lower panel presents results of one model run. Here gray and black curves show displacement of initially flat layers of tracers. The layer stippled with small crosses shows rocks initially buried at the depth interval of 8–9 km, uplifted to the level of the end of the drill hole (vertical black line with the triangle at the top). Vertical and horizontal scales in km

Although the accuracy of the currently available numerical models does not yet allow researchers to reproduce all cratering processes equally exactly, the model results allows them to estimate most parameters, difficult to measure in the field. For example, the throughput cratering model automatically includes the shock wave decay computation. Recording the maximum shock pressure with the Lagrangian tracers one can follow their displacement as the crater grows and collapses, and plot the final position of variously shocked rocks under the final crater. The data offered by core samples from various depths of the Vorotilovo drill hole allow the critical comparison of measured and computed shock level in rocks under the crater (Fig. 8).

The model well fits results of observations, which means that both model and observations show that basement rocks reached by the Vorotilovo drill hole experienced the net structural uplift from depths of 5–9 km into the present position. The model fit in found in this case is used to make the first guess in the modeling of other terrestrial impact craters.

Popigai impact crater was formed by the impact of a rock asteroid (Masaitis and Raikhlin 1986) ~36 Myr ago (Bottomley et al. 1997) near the northern boundary of the Anabar shield (Rosen et al. 1991, 1994). The Anabar shield is an area of the (strongly modified) ancient continental crust consolidated ~3.7–3.8 Gyr ago (Moralev, 1986). The complex structure of the northern part of the shield can be roughly represented as a sequence of increasingly dense crustal rocks overlying the crust–mantle interface at a depth of ~40 km.

The apparent structure of the impact site target the layers of Archean gneiss covered with an inhomogeneous sedimentary and meta-sedimentary cover whose thickness seems to increase from zero in the southeastern part of the future crater to ~1 km near the future northeastern crater wall (Masaitis et al. 1975; Masaitis 1994). A brief history of the structure discovery and a description of its geology are presented by Deutsch et al. (2000). The sedimentary rock's thickness at the impact site is assumed to be <400 m, which is much less than the presumed projectile diameter ($D_{pr} \sim 8$ km at the impact velocity of $15 \text{ km}\cdot\text{s}^{-1}$). Although the presence of sedimentary rocks is crucial to understand conditions at the impact site and the

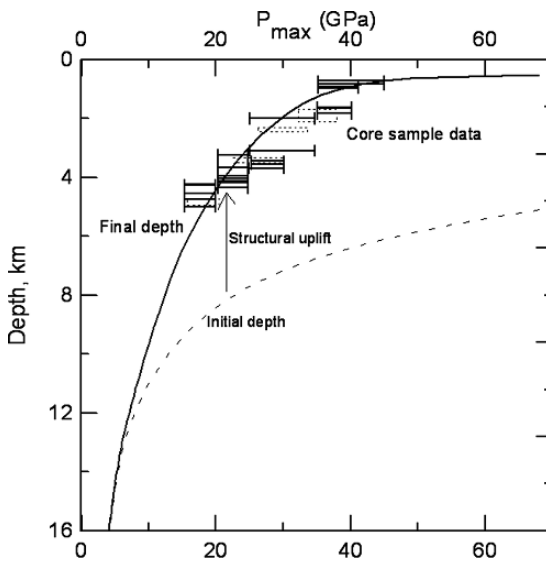


Figure 8. The comparison of modeled and observed shock pressure estimates made on different depths of the Vorotilovo core. Horizontal error-bars are for petrographic estimates by Masaitis and his team, solid and dashed curves are results of the presented numerical modeling (Puchezh-Katunki 1999) presenting maximum pressure in tracers versus initial and final depth under the crater center

origin of the unique shock-metamorphosed rocks, a layer of such thickness could not significantly affect the overall picture of complex crater formation. Therefore, in the computations described here, the authors adopted a two-layer (a granite crust overlying a dunite mantle) or three-layer (an upper crust, a lower crust, and a mantle) target structure.

At present, Popigai is a round depression in which the following are embedded:

- A central depression bounded by a ring uplift of crystalline basement rocks. The ring uplift (inner ring) has a diameter of $D_{IR} \sim 45$ km (Fig. 9)
- An annular trough with an axis diameter of $D_{AT} \sim 60$ km and an outer diameter of 72–75 km
- An outer visible boundary of the crater depression whose diameter can be estimated to be $D_{OV} \sim 90$ km

In addition, a partly preserved ejecta blanket in the form of allogenic breccia patches located within and outside the outer diameter D_{OV} belongs to the structure. The rim crest diameter l immediately after its formation is estimated as 100 km (Masaitis et al. 2003).

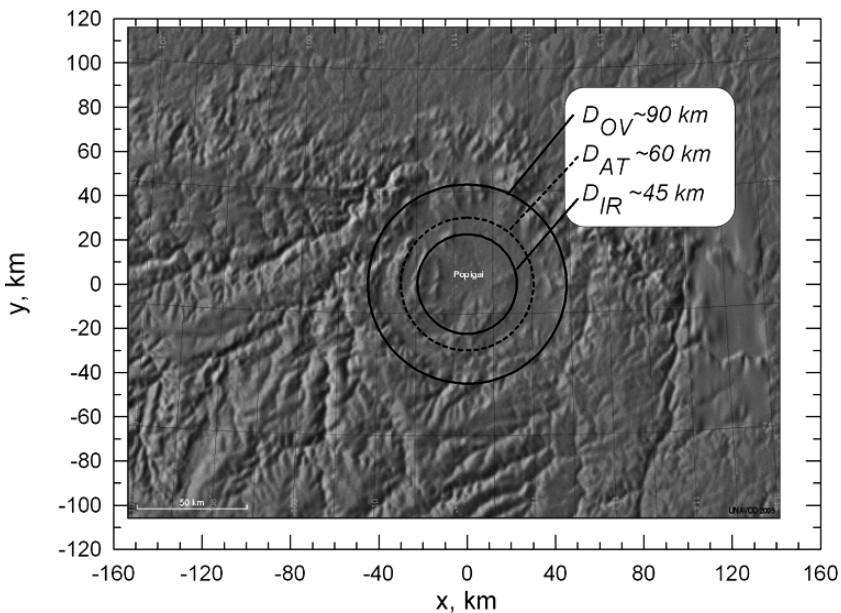


Figure 9. Shadow relief map of the Popigai impact crater (constructed with the web service accessible at <http://jules.unavco.org>, UNAVCO Boulder Facility and the Jules Map server home page web site). *Black circles* correspond to the main morphologic features of the crater drawn using a geological map and a map of gravity anomalies (Masaitis 1998; Masaitis 1998). D_{OV} is the outer visible diameter (slightly smaller than the initial rim crest diameter), D_{AT} is the diameter of the axis of the annular trough, and D_{IR} is the inner rim crest that roughly corresponds to the ring uplift. Reprinted from Ivanov (2005) with permission from Pleiades Publishing Inc.

Geophysical data estimate the burial depth of the crystalline rocks at the center of the crater as 2–2.5 km (Masaitis 1998). Allogenic breccia mixed on various scales with the impact melt overlie the crystalline rocks (the authigenic breccia of the central uplift) almost up to the visible surface in the central depression. Breccia mixed with the solidified melt cover an area of $\sim 5,000 \text{ km}^2$, representing a series of rocks from tagamites (a clast-poor melt) to suavities (a clastic material with a large content of solidified melt fragments). An extensive program of drilling bore holes with a depth as large as 1.5 km was performed to explore the impact of diamond deposits (Masaitis 1998) allowing researchers to estimate the overall volume of the melt (minus clasts) preserved in the crater as $\sim 1,750 \text{ km}^3$ (Masaitis et al. 1980). This value was repeatedly used to calibrate the theoretical relationships between the impact melt volume and the crater diameter and to test impact scaling laws (Grieve and Cintala 1992, 1997; Pierazzo et al. 1997).

The parameters of the computational model for the Popigai crater were chosen to obtain a model crater with the observed morphology and a volume of the impact melt close to the one observed. Varying the parameters of the computational schemes yielded acceptable (at a computational cell size of $\sim 200 \text{ m}$) agreement between the model and the observations for the vertical impact of a spherical body with a density of $2,630 \text{ kg m}^{-3}$ (the granite equation of state) and a diameter of $\sim 8 \text{ km}$ at an assumed impact velocity of 15 km s^{-1} . The impact energy was $8 \times 10^{22} \text{ J}$, and the total volume of the impact melt (for dry granite) was $\sim 2,600 \text{ km}^3$. The model resolution is certainly too low to accurately describe the motion of the melt as the crater grows. Rough volume estimations for the melt remaining in the crater yield the following values:

$\sim 13\%$ within 20 km of the center

$\sim 30\%$ within 30 km of the center

$\sim 85\%$ within 40 km of the center

The melt transport can differ greatly from the computed case for an oblique impact on a wet target under typical conditions of the surrounding atmosphere (i.e., the factors that are disregarded in these computations of a vertical impact on a dry target). With this simplification, the volume of 2,000 to $2,200 \text{ km}^3$ of the melt remaining in the central part of the crater looks close to the observational estimate of $1,750 \text{ km}^3$. The typical effective thickness estimate for the melt sheet at the crater floor (at a density equal to the initial granite density) is:

$\sim 150 \text{ m}$ within 20 km of the center

$\sim 200 \text{ m}$ in the ring with radii from 20–30 km

$\sim 250 \text{ m}$ in a ring with radii from 30–40 km

Interestingly, for a purely ballistic motion of the material in the model (there is neither air drag nor gas acceleration by water vapor), most of the impact melt accumulates in the periphery of the crater depression. In the actual crater, the melt lies in the form of separated bodies immersed in allogenic breccia.

Figure 10 shows the radial surface profile obtained in one of model runs and the final positions of tracers from the impact melt zone. Much of the melt (more

precisely, melt tracers) is buried in the annular trough at depths as large as 4 km. To clarify this transport of the melt, the overall sequence of the crater formation in the model is described briefly (Fig. 11).

Figure 11 shows six time frames illustrated the crater formation process. The crater cavity reaches its maximum depth (~ 18 km) in about 20 s and begins to collapse immediately after that. The collapse of the crater rim results in the crater floor above the original surface level (a maximum “overshooting” of ~ 6 km) about 90 s after the maximum depth is reached (and 115 s after the impact). At this moment, the cavity floor is curved upward. Thus, the crater floor covered with a melt sheet becomes the surface of a slowly collapsing dome; in this case, downward flows of still hot melt in a mixture with rock debris are possible. By 200 s, the collapse of the domal generates an annular wave of material that spreads over the crater floor. This surface flow of material leads to the burial of a part of the melt beneath the crater floor in the annular peripheral depression, as shown in Fig. 10. The high temperature and low strength of the fragmented material facilitate flows on the surface of the collapsing dome. Analysis of the model data shows that 200-m computational grid resolution is not enough to see all the details of material displacement. Hence the results should be treated as preliminary and requiring a special high-resolution modeling, near the surface.

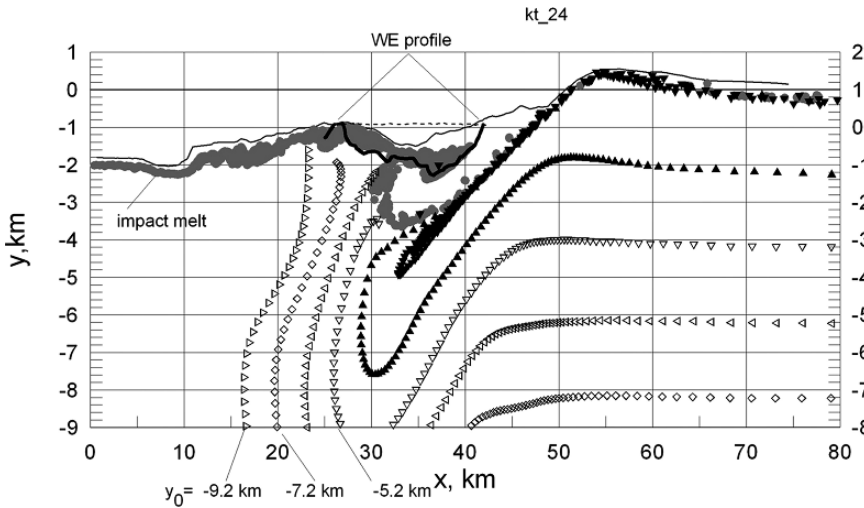


Figure 10. Vertically exaggerated model cross-section of the Popigai crater. Curved sets of various symbols correspond to rock layers, initially located at the same depth for each set. In the area of the transient cavity collapse the original target surface is displaced downward to depths of 5 km at the radial distance of ~ 33 km from the center. The gray shading depicts zones of the final position of impact melted rocks experienced shock pressure > 50 GPa. WE profile of the crystalline basement as deciphered from geophysical survey (black curve) is from Masaitis (1998). Adapted from Ivanov (2005) with permission from Pleiades Publishing Inc.

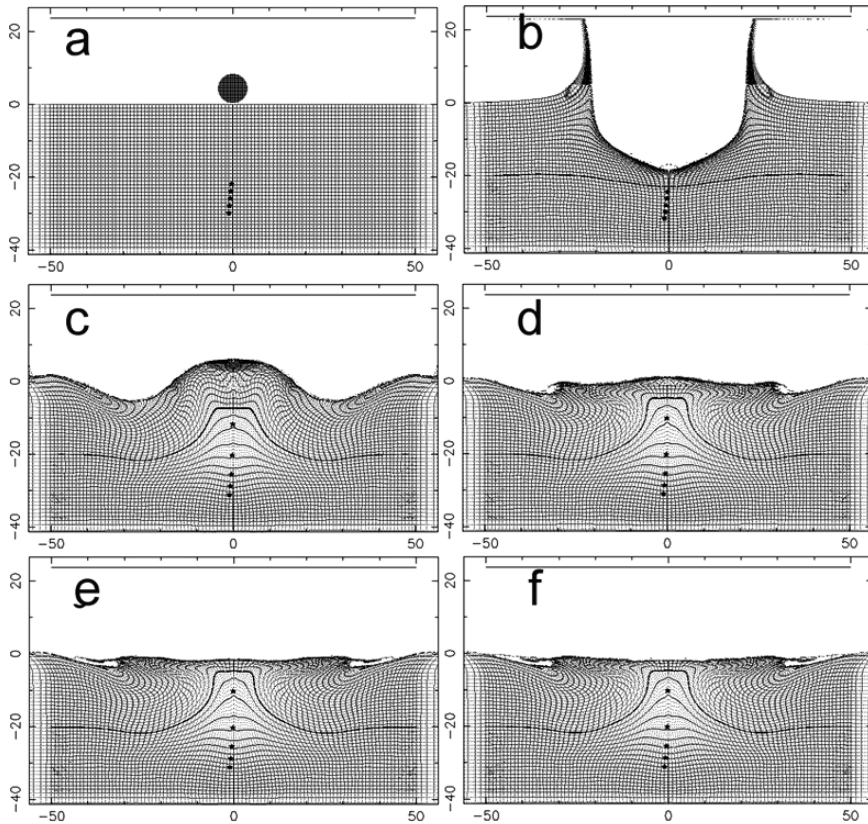


Figure 11. Selected time frames of the Popigai crater formation process. (a) the initial geometry of the target and the spherical projectile; (b) 22 seconds after impact the transient cavity grows to the maximum depth of ~ 19 km; (c) 115 seconds after impact: the continuing collapse of the transient cavity, upward motion of the crater floor with a subsidence of the crater margins; (d) 200 seconds after impact: the transient “dome” is collapsing in the gravity field, while rock motion under the surface is arrested by the internal friction. The velocity of near surface hot rocks moving out of the center is about 200 ms^{-1} ; (e) 300 seconds (5 minutes) after impact: the velocity of material motion is decreased $< 100 \text{ ms}^{-1}$; (f) 400 seconds after impact: the final model crater cross-section. Adapted from Ivanov (2005) with permission from Pleiades Publishing Inc.

In the presented model, the ring (“inner”) uplift at the crater floor morphologically arises from the collapse of the dynamic dome. However, it should be noted that the collapse of the transient crater cavity itself, which gives rise to the domal, results from a large structural uplift of the floor of the growing crater that accompanies the uplift of the crustal layers initially buried at a depth of ~ 18 – 20 km. According to the geophysical model for the northern edge of the Anabar shield (Structure of the Terrestrial Crust of the Anabar Shield, 1986, Fig. 48), the denser rocks of the lower crustal layer with a density of $\sim 3 \text{ g cm}^{-3}$ lie below this level; therefore, it is

unlikely that the center crater uplift can be noticed easily in the gravity anomaly field measured above the crater. Besides, the deep rock uplift is accompanied by fracturing and bulking.

The maximum crater depth of ~ 2 km in these computations most likely corresponds to the depth of the cover of authigenic breccia at the center of the structure, since the computations were performed without including the atmospheric effect; the ejecta deceleration in the atmosphere produces a flow of material returned to the crater through the settling from a gas–dust cloud.

Thus, in the authors' numerical computations, a model crater was obtained that is qualitatively (and, in many parameters, quantitatively) similar to the Popigai meteorite crater.

The Chicxulub impact crater was formed ~ 65 Myr ago by an asteroid impact. The global deposition of projectile material traces associated with this impact event (iridium anomaly) and a fine fraction of ejecta (shocked quartz) and the crater age close to the age of mass extinction at the Cretaceous-Tertiary (K/T) boundary formed the basis for the hypothesis about the K/T boundary as the result of a giant impact (Alvarez et al. 1980). Interestingly, initially global traces of the impact event were found and the impact scale was estimated, and only several years later was the Chicxulub impact crater discovered at the north coast of the Yucatan Peninsula (Mexico) (Hildebrand et al. 1991).

Morphologically, the Chicxulub impact structure is a crater with a ring central uplift (diameter of ~ 90 km) and the apparent outer diameter of the crater depression of ~ 180 km, approximately twice as large as that of Popigai. Consequently, the asteroid that produced Chicxulub during its impact was also twice as large as that for Popigai. Typical asteroid size estimates lie within the range of 10–14 km (Hildebrand et al. 1991; Swisher et al. 1992; Ivanov et al. 1996a).

The currently observed complex crater structure was formed through the collapse of a transient cavity with diameter of 90–120 km (Ivanov et al. 1996a; Pierazzo et al. 1998; Pierazzo and Melosh 1999; Morgan et al. 2000).

Seismic sounding, geophysical modeling, and drilling revealed general structural features of the crater that is now buried beneath a layer of younger sediments ~ 1 km in thickness. To all appearances, many structural features of the crater that were destroyed in other structures have been preserved under these young sediments. For example, a continuous ejecta deposit was partly preserved south of the crater (Pope et al. 1994, 1997).

According to geological and geophysical data (Morgan et al. 1997), the authors simplified the target structure for their numerical computations to three layers: a 3-km-thick upper sedimentary layer (the equation of state for calcite), the crystalline basement (the equation of state for granite), and a mantle below the depth of 33 km (the equation of state for dunite). As in the preceding, the interaction between the atmosphere and the ejecta was not computed—the flight of the ejecta and vapor cloud expansion took place in a vacuum. Previously, the authors published preliminary results of numerical modeling of the crater in a two-layer (crust–mantle) target (Stöffler et al. 2004).

The model parameters were chosen initially (Ivanov 2003a) by a wide variation of projectile parameters. Figure 12a shows the model crater profiles for the vertical impact energy of a spherical projectile varied from 2.2×10^{22} to 7.4×10^{22} J (the projectile diameter varies from 14 to 19 km; the impact velocity varies from 12 to 15 km s^{-1}).

Since the mechanical effects at a high-velocity impact are determined by the specific combination of projectile diameter and impact velocity (for the same ratio of the projectile and target densities), the so-called coupling parameter was chosen in the following form (Dienes and Walsh 1970):

$$L = D_{\text{pr}} v^{0.58} \quad (3)$$

where D_{pr} is the projectile diameter, and v is the impact velocity. Figure 12b shows how the crater diameter increases with coupling parameter. As the crater diameter increases from ~ 150 to 250 km, the ratio of the apparent (at the original surface level) diameter of the crater to its rim crest diameter remains almost constant (Fig. 12b). The depth of the final crater also increases very slowly, roughly in the same way as for all complex craters on Mercury, Venus, and Mars (Pike 1980).

The overall picture of the material motion is similar to that shown in Fig. 11 for the Popigai crater: the growth of a deep transient cavity, its collapse, the uplift of the crater floor, its evolution into a dynamic dome raised above the surface, and the collapse of the dome to produce a low relief (in these computations) concentric central ring. However, in the case of Chicxulub, the proximity of the mantle surface as a contrast density boundary prevents the uplift of the crustal rock layers immediately beneath the crater center—the transient cavity collapses, capturing part of the impact melt at vertical stock at the symmetry axis. This leads to a distortion of the initially flat layers on the symmetry axis at a depth of < 20 km (Fig. 13).

An additional difference with Popigai is the presence of a large amount of vapors expanding in the upper half-space: a result of the “early” vaporization at a temperature of $\sim 1,500$ K imitating the long-discussed possibility of thermal decomposition of calcite and anhydrite behind a strong shock wave included in the equation of state for limestone (for a discussion see Ivanov et al. 1996a, 2004; Pierazzo et al. 1998; Gupta et al. 1999; Langenhorst et al. 2003). According to the fairly popular model by Pope et al. (1994, 1997), the enormous amount of sulfur dioxide thrown into the stratosphere during the impact and the anhydrite decomposition in the sedimentary cover could be responsible for the biota mass extinction as a result of the formation of the Chicxulub crater. A recent paper by Pierazzo et al. (2003) discusses the problem of the climate change due to Chicxulub impact.

The model for the internal structure of the crater (Morgan et al. 1997; Pilkington and Hildebrand 2000; Christeson et al. 2001; Ebbing et al. 2001) based on seismic survey data and geophysical field anomalies allows the direct comparison between

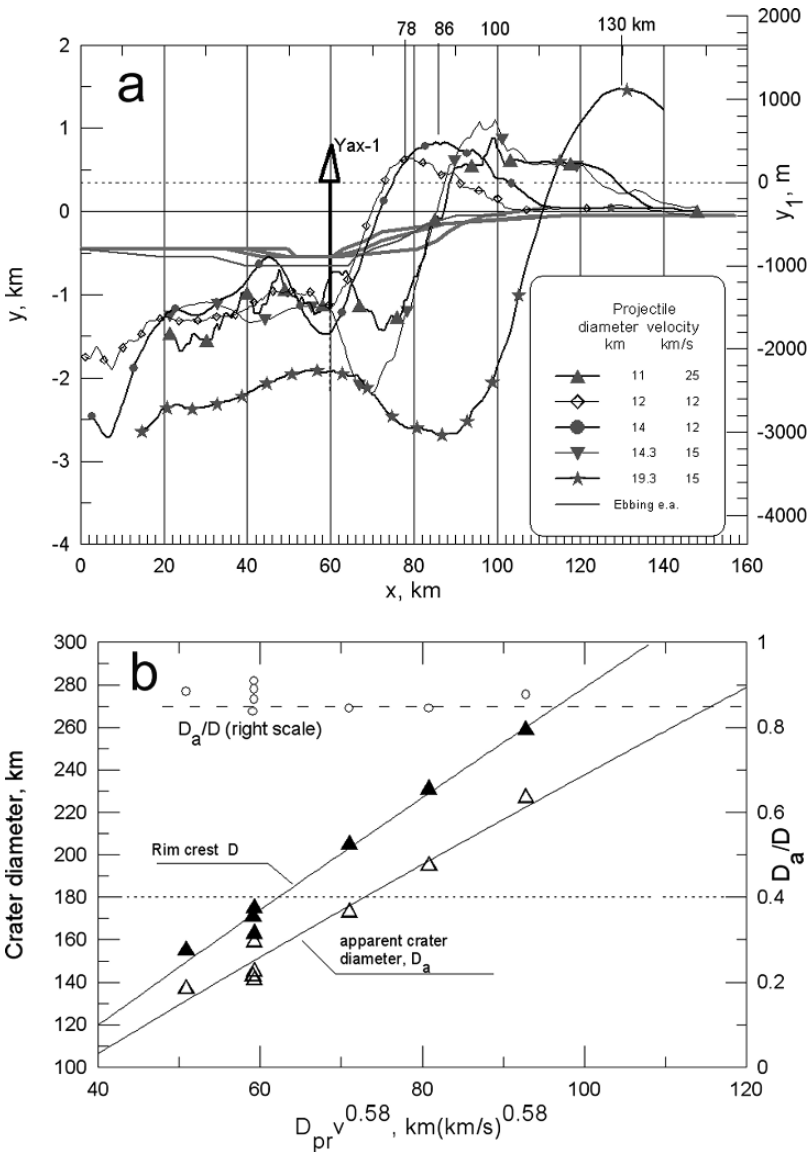


Figure 12. (a) Radial profiles of a set of models used to fit model parameters to reproduce the Chicxulub crater. Rim crest radii vary from 78 to 130 km (correspondingly, rim crest diameters vary from ~160 to 260 km). The Yax-1 drill hole position is shown for comparison. Gray curves without signs are observed crater profiles after removing of overburden sediments, estimated in various azimuthal directions (Ebbing et al. 2001). The horizontal dotted line shows the most often-cited Chicxulub crater diameter of 180 km. (b) The relation between computed rim crest (black triangles) and apparent (open triangles) diameters and the effective impact coupling parameter (Equation 3); left vertical axis. Open circles (and right vertical axis) show the approximately constant ratio of the apparent diameter and rim-crest diameter, D_a/D_{rim} . For all computed variants this ratio is close to 0.82. Adapted from Ivanov (2005) with permission from Pleiades Publishing Inc.

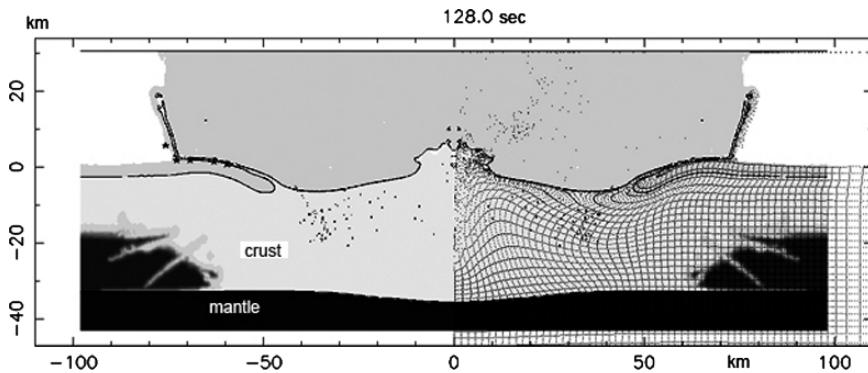


Figure 13. The model cross-section of the growing Chicxulub crater 128 seconds after impact. The dark gray zone $< \sim 33$ km is the mantle material, modeled with dunite. The light gray cloud above the original surface is the vapor plume of thermally decomposed limestone, which model the upper sedimentary layer. The gray shading in the area of the Earth crust, modeled as granite, shows fractured (light gray) and still elastic (nonfractured) zones. The expansion of the vapor plume at this moment is still restricted by the dense ejecta curtain. Reprinted from Ivanov (2005) with permission from Pleiades Publishing Inc.

the model and the observations. Such a comparison makes it possible to find the best set (among those tested to date) of model parameters ensuring that the model is plausible when compared with the observations.

The geometry and relative sizes of the asteroid (just before the impact), the impact melt zone, and the zone of ejecta are schematically shown in Fig. 14a. One sees that a part of the melt zone is located in the sedimentary layer; this is the zone in which the melting and thermal decomposition of calcite and anhydrite are possible. In 2002, the International Continental Drilling Project (ICDP) Yaxcopoil-1 (Yax-1) bore hole was drilled at a distance of 60 km from the Chicxulub center. The computations partly described here were performed to analyze the drilling results. This analysis was published by Stöffler et al. (2004). Figure 14a shows the initial position and trajectories of particles that deposited at distances between 55 and 65 km from the crater center (± 5 km from the nominal distance of the Yax-1 bore hole). Also shown here is the subsidence of the layer of sediments and its overturning near the boundary of the zone of ejecta. In the sense of the sedimentary layer subsidence the presented model run has the closest (of all tested to date) fit to the geophysical data on the crater structure (Fig. 14b). The sedimentary layer during the collapse of the transient cavity subsides to a depth of ~ 10 km at the radial distance of ~ 40 km from the crater center. Geophysics draws approximately the same picture based on seismic sounding data and analysis of the gravity and magnetic anomalies beneath the crater. Figure 14 shows the central column of melt squeezed between the walls of the collapsing cavity (in reality, this must be a zone of rock debris mixed with melt). However, the central basin of impact melt extending to a distance of ~ 40 km from the crater center constitutes more than half of the impact melt of the crystalline basement material in the model. Unfortunately, the model presented here does not reproduce the faults and upthrusts created during the

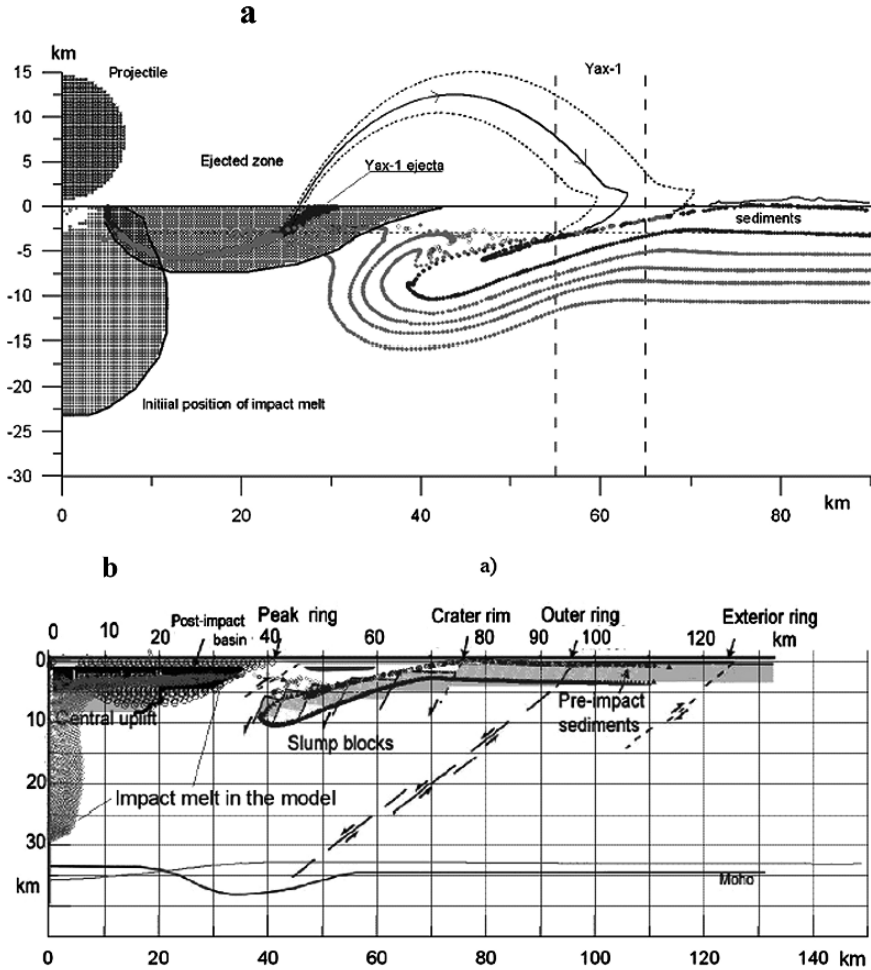


Figure 14. Cross section of the modeled Chicxulub crater. (a) The arrangement of the impact melt zone and ejecta zone. The spherical projectile producing the crater is shown for comparison. The deformation of initially horizontal target layers is shown below the surface level. Trajectories of selected tracers deposited near the Yaxopol-1 bore hole (at radial distance 60 ± 5 km indicated by vertical dotted lines) are close to the ballistic parabolas with a complicated horizontal motion at the end of the modification stage. The gray shading within the ejecta zone highlights all of the tracers deposited near Yax-1. (b) The model crater cross section superimposed on the crater structure reconstruction from geophysical data, including seismic sounding (Morgan et al. 1997, 2000). The melt zone in the model crater consists of the melt layer at the crater floor and the stock of melted rocks gripped near the symmetry axis during the collapse of the transient cavity bounded by the crust–mantle boundary. The deformation of selected initially horizontal crustal layers (curves of almost merging dark symbols) is shown. Solid curves <30 km depict the crust–mantle boundary in the computation and on the geophysical profiles. Adapted from Ivanov (2005) with permission from Pleiades Publishing Inc.

crater collapse. These results should be tested in the future using three-dimensional (3D) modeling in which there are no conditions for the anomalous motion of matter near the symmetry axis.

No diamonds have been found in the shocked rocks in Chicxulub so far. However, even in this case, the formation of a giant (by terrestrial standards) crater gave rise to a mineral deposit. The Chicxulub crater was formed at the carbonate platform that steeply terminates at distances of ~ 300 km from the crater center. (The platform edge is known as the Campeche bench.) The seismic action of the impact is believed to have resulted in the mass underwater collapse of the bench. The dolomitization of limestones on the surface of the underwater landslide formed a sealing under which an oil–gas field was formed (Bralower et al. 1998; Grajales-Nishimura et al. 2000; Ricoy 2003). At present, it provides about two-thirds of the entire oil production of Mexico, bringing ~ 16 billion dollars per year into the country from the territory in which the Chicxulub crater was formed (Donofrio 1998).

To verify the possibility of catastrophic collapse of the underwater slope at such a distance from the impact site (the arrangement is schematically shown in Fig. 15), the authors performed computations using the same SALEB program

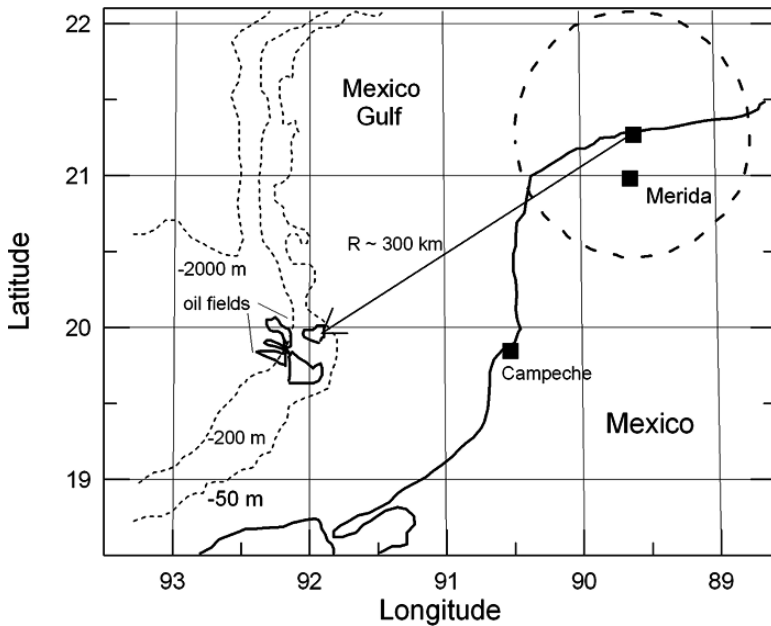


Figure 15. Map of an area near the Yucatan peninsula coast shows the relative location of the Chicxulub crater (dashed circle) and the oil fields near the Campeche underwater bench limiting the carbonate platform. Selected isobaths illustrate the transition from the continental shelf to the deep floor of the Gulf of Mexico. The submarine landslides in which oil fields was formed are believed to have been initiated by a seismic shaking from the crater-forming impact (Bralower et al. 1998). Adapted from Ivanov (2005) with permission from Pleiades Publishing Inc.

on a coarser grid (with a cell size of 0.5 and 1 km). This allowed the authors to reproduce the seismic shaking at a distance of 300 km within the first 100 seconds after the impact (Fig. 16). Later, the general pattern of ground oscillations is still reliable, but the elastic waves reflected from the boundary of the computational region already began to be visible. The ground velocity in a seismic wave at a distance of 300 km is $\sim 10 \text{ m s}^{-1}$ and displacements of $\sim 70\text{--}80 \text{ m}$. Such vibrations seem to be strong enough to destabilize the underwater slope, although this question deserves special analysis. Here, a simple estimate will suffice. Based on the standard formulas for comparing the explosion and earthquake seismic energies (see, e.g., Dahlman and Israelson 1977), one can roughly (the amplitudes are too large) compare the vibrations shown in Fig. 16 with earthquake vibrations with a magnitude M_W from 10 to 11. Extrapolating the available data (for earthquakes with maximum recorded magnitudes $M_W \sim < 9.5$) the distances can be estimated where the saturated slope stability can be lost as $\sim 500 \text{ km}$ (Papadopoulos and Plessa 2000; Dutta et al. 2003).

To summarize the attempts to model the formation of the Chicxulub crater, it should be noted that the simplified three-layer model for the target structure cannot reproduce all of the complex phenomena related to the presence of partially watered

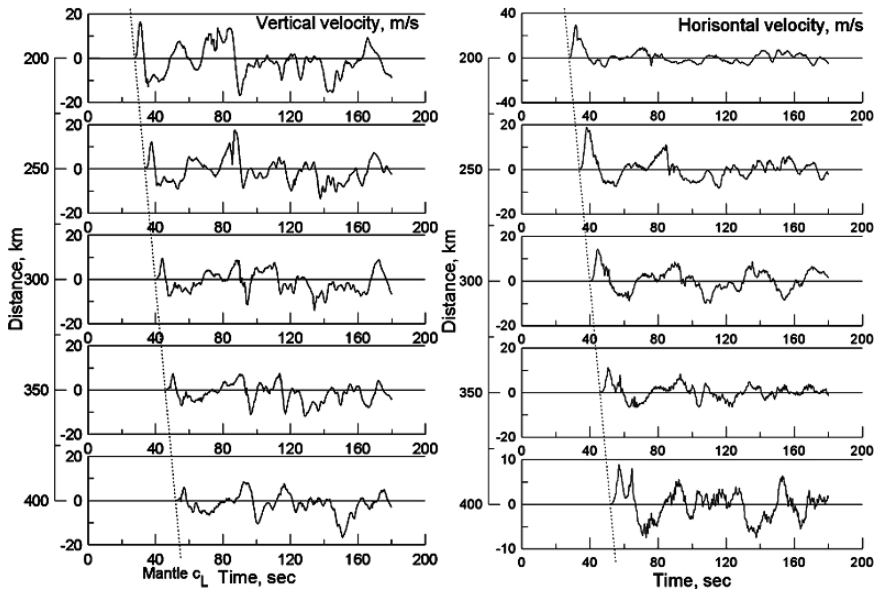


Figure 16. Model seismograms of shaking due to Chicxulub crater formation, recorded in the sedimentary layer at distances from 200 to 400 km. At a distance of 300 km (Fig. 15), the vertical and horizontal vibration velocities reach 10 m s^{-1} or more. The first seismic wave arrival is determined by the longitudinal wave velocity in the mantle, $c_L \sim 8.3 \text{ km s}^{-1}$ (the inclined dotted line). The rock displacements reach 70–100 m in a wave train with a period of 10–20 s. The accelerations reach 1–1.5 g. Adapted from Ivanov (2005) with permission from Pleiades Publishing Inc.

evaporates. The possible thermal decomposition of limestone and anhydrite as well as the water evaporation of shallow lakes significantly changes the pattern of motion of the early ejecta, especially in the case of an oblique impact (Stöffler et al. 2004). However, the relatively low cost of two-dimensional (compared with 3D) computations makes the simple axisymmetric problems attractive for a parametric analysis of existing models and their improvement. In the case of a buried impact crater, such as Chicxulub, numerical computations that ensure the conservation of mass, momentum, and energy in describing the material motion will undoubtedly help construct more realistic solutions of inverse geophysical problems.

The **Vredefort impact structure** is located in South Africa (S 27°0', E 27°30') and is $2,023 \pm 4$ Ma old. The structure has been studied in detail and described in the literature. Recent publications of new observations and geophysical field modeling for the Vredefort structure (Moser et al. 2001; Lana et al. 2003a, 2003b, 2004; Wieland et al. 2003; Wieland et al., 2003) supplement the general reviews (Reimold and Gibson 1996; Grieve and Theriault 2000).

For a brief description of the geological situation in which the crater was formed, the following should be noted. In general, the Vredefort impact structure was formed within a large ancient block of the Archean lithosphere called the Kaapvaal craton. Apart from scientific interest, intensive geophysical studies were associated with the proximity of the economically important Kimberley diamond fields. Here, seismic studies reveal the crust–mantle boundary at a depth from 38 to 40 km (Doucoure et al. 1996; Nguuri et al. 2001). The upper mantle beneath the Kaapvaal craton is characterized by reduced seismic velocities (James et al. 2001). According to these studies, ~ 40 Myr before the formation of the Vredefort crater, the intrusion of igneous rocks of the Bushveld complex ($\sim 2,060$ Myr old) occurred. This could locally produce regions of a high thermal gradient, up to 40 K km^{-1} near the surface (Gibson and Jones 2002). In general, however, the crater formation region had a thermal gradient from 15 to 20 K km^{-1} near the surface and a temperature of ~ 900 K at the crust–mantle boundary at a depth of ~ 40 km (Gibson and Jones 2002).

The geological history of the Kaapvaal craton includes periods of predominance of tensile stresses during which depressions (basins) filled with sedimentary material were formed (de Wit et al. 1992). When the sediments reached a significant thickness (15–20 km), they were subjected to metamorphism, transforming into mechanically strong rocks (metasediments). The Vredefort crater was formed in such a basin (the Witwaterstrand basin), 2.972.1 Gyr ago (see the review by Gibson and Jones 2002 and references therein). Subsequently, the crater region was subjected to significant erosion (to a depth of 5–10 km). Erosion destroyed all of the near-surface features typical for impact craters (the crater rim, the ejecta depositions, etc.), but at the same time exposed the deep structure of the giant meteorite crater. In particular, this is why it is so important to construct a model for the formation of the Vredefort crater. Such a model, on the one hand, can give an insight into the structure of the crater before erosion and, on the other hand, allows the principles of numerical modeling to be tested.

The most characteristic feature of the preserved structure is the so-called Vredefort dome: the central granitoid core surrounded by younger rocks (Fig. 17). Geological and geophysical studies have shown that the granitoid rocks were lifted at least by 10–15 km and are mid-crust rocks (Henkel and Reimold 1998; Reimold and Gibson 1996; Stevens et al. 1999; Lana et al. 2003b, 2004).

Previously, several attempts were made to model the formation of the Vredefort crater (Turtle and Pierazzo 1998; Turtle et al. 2003). In these papers, the numerical modeling of the impact was used to compute the initial impact stage, the shock propagation. The excavation stage of the transient cavity was described analytically using the so-called Z-model. The collapse of a transient crater was computed by a quasistatic finite-element method. Quite plausible estimates of the initial sizes of the crater with a diameter of ~ 180 km were obtained. This chapter presents the throughput computation using a single code, from the impact to the formation of

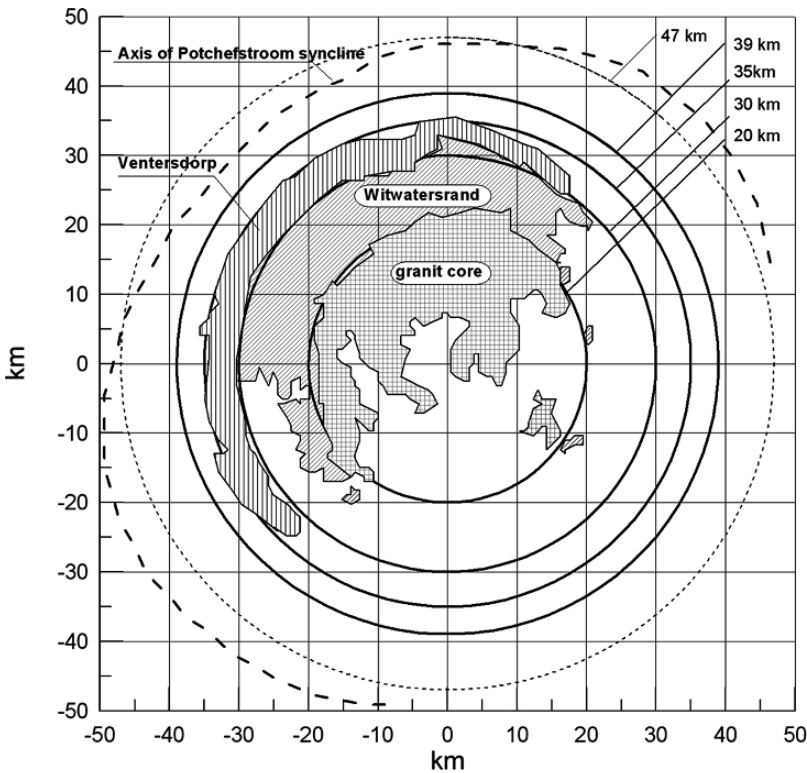


Figure 17. Schematic geological map of the Vredefort dome from published data (Reimold and Gibson 1996; Therriault et al. 1997; Lana et al. 2003a). Rings that roughly correspond to the sequence of crustal rocks at the present erosion surface are shown. Adapted from Ivanov (2005) with permission from Pleiades Publishing Inc.

the final crater, with a spatial resolution comparable to that in the model of the early stage (Turtle and Pierazzo 1998).

For the numerical modeling, the target was represented as three layers: a layer of metasediments, a layer of granitoids, and the underlying mantle. The following triplets of target materials (downward) were used: quartzite/granite/dunite, granite/basalt/dunite, and granite/basalt/dunite. At the available accuracy in the model, no strong effects of various model equations of state describing the crustal material were found; in general, the mechanical properties of these rocks are similar. For this study, after a review of published sources, a thickness of 14 km was chosen for the layer of metasediments and a depth of 45 km for the crust–mantle boundary as the first approximation. Since the erosion depth is uncertain, these values can vary over a wide range.

Trial computations allowed the authors to choose the asteroid projectile diameter (at the model granite density) of about 14 km at the presumed impact velocity of $15 \text{ km}\cdot\text{s}^{-1}$. Figure 18 shows the profile of the model crater for the model run with the best fit to geological data at the erosion level. It should be noted that in this computation, the shape of the crater might not have been achieved by the

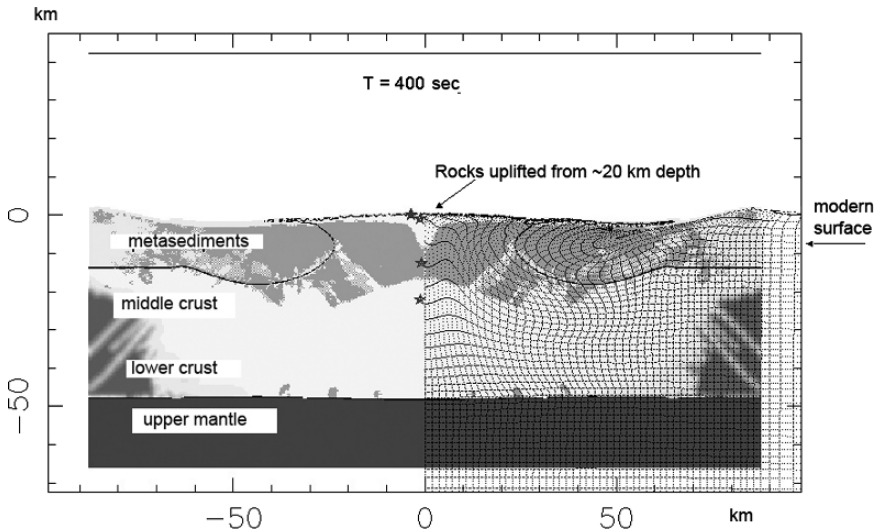


Figure 18. The Vredefort model cross-section 400 s after impact. The dark gray shading near the lower figure edge denotes the mantle rocks; the dark peripheral zones within the crust correspond to the still-elastic rocks with individual cracks. The gray shading at a lighter background near the crater surface corresponds to the computational cells where the internal friction is still reduced due to acoustic fluidization. The curved boundary of the granite crustal layer and the 14-km-thick horizontal layer of metasediments is shown. The deformation of the initially rectangular grid of tracers constructed from the markers located initially in each fifth cell row and in each fifth cell column of the computational grid cells is shown in the right half of the figure. Adapted from Ivanov (2005) with permission from Pleiades Publishing Inc.

time of 400 s when the computation was stopped (in Fig. 18, one can still see the central uplift instead of the central depression). In other computations, the crater was similar to the “model Popigai” and “model Chicxulub” craters.

The diameter of the model crater shown in Fig. 18 is 172 km at the rim crest and 130 km at the original surface level. The computed volume of the impact melt was $\sim 13,000 \text{ km}^3$, with approximately equal fractions of melted metasediments and basement granitoids. At the final computational time, $\sim 25\%$, 50% , and 90% of the impact melt were located closer than 20, 40, and 80 km from the impact site, respectively. The characteristic thickness of the melt sheet within the crater (at the initial rock density) is estimated to be 400–800 m.

The overall scenario for the crater formation through the collapse of the transient cavity and the subsequent collapse of the central dome is generally similar to that described for the Popigai model crater. Figure 19 shows the crater formation scenario with the distribution of the hottest material ($>800 \text{ K}$) highlighted by gray shading.

Figure 20 shows the distributions of basic parameters in the upper 15 km of rocks beneath the formed crater. This range of depths most likely includes the observed

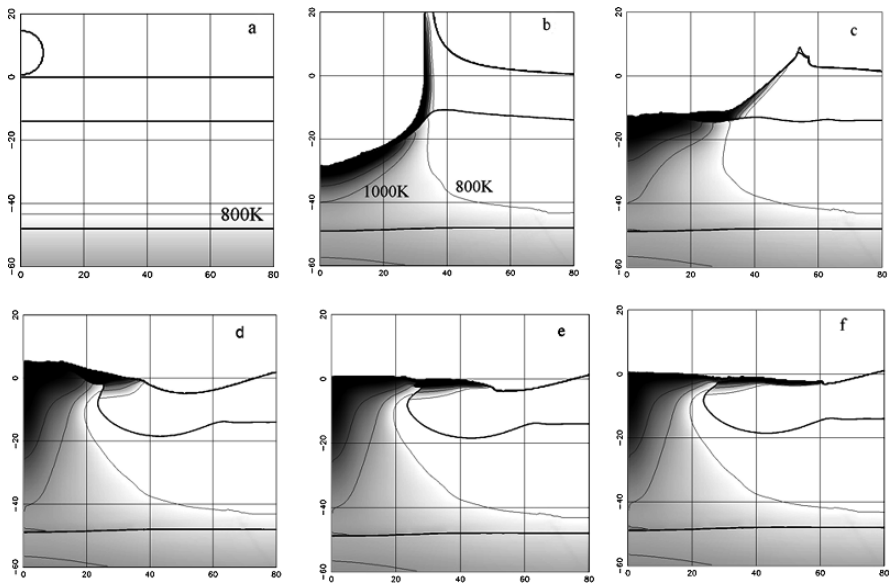


Figure 19. Formation sequence of the model Vredefort crater formation displayed via rock temperature. The gray shading indicates the temperature distribution from 800 K or lower (light shade) to 2,000 K (dark shade). For better perception, the 800, 1,000, and 1,200 K isotherms are shown with curves. Thus, the darkest shade shows the melt distribution in the growing crater: (a) initial position (the 800 K isotherm is horizontal, the incoming spherical projectile is seen above the target); (b) 30 s; (c) 90 s; (d) 240 s; (e) 300 s; (f) 360 s. The left axis is the axis of the cylindrical symmetry. Adapted from Ivanov (2005) with permission from Pleiades Publishing Inc.

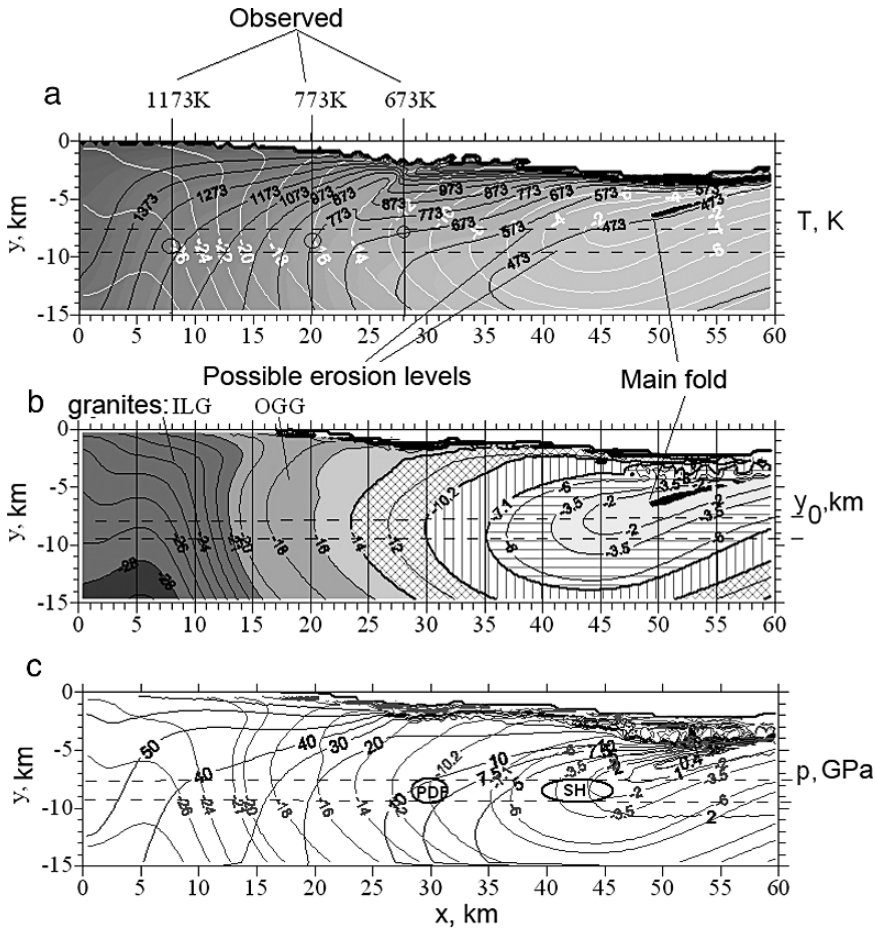


Figure 20. Cross-section of the modeled Vredefort crater illustrated with fields of the various parameters used to compare the model and observations. The horizontal dotted lines at depths of ~ 7.5 and 9.5 km denote the range of expected present erosion cut. The annular main fold, the place where the ejecta curtain falls back to the original target surface, is at a distance of 50 km from the center and a depth of ~ 6.5 km: (a) final rock temperatures. Vertical lines indicate the geological temperature estimates for the postshock rock metamorphism at the present erosion cut. Circles highlight points of intersection between observed and model isotherms. The light tone isolines indicate the initial burial depth of the shown final positions. (b) A detailed representation of the initial rock depth y_0 . (In the computational grid, the y axis is directed downward, and $y = 0$ is at the original surface; therefore, depths have negative values shown at isolines.) Variable gray shading for depths of more than 14 km corresponds to rocks of the granite crustal layer. The presumed boundary between the deeper and ancient rocks (ILG: Inlandsee Leucogranofels), with an age of $3.2\text{--}3.5$ Gyr, and shallower and younger granitoid rocks (OGG: Outer Granite Gneiss), with an age of ~ 3.1 Gyr, are drawn with indication of the original burial depth, 21 km (Reimold and Gibson 1996; Moser et al. 2001). The presumed rocks of the lower crust (in the lower left corner of the figure) are bounded by the initial burial depth of 28 km. The boundaries of the differently designated metasediments originally buried at depths of <14 km are drawn in such a way that their distribution at the present erosion cut corresponds to the observations shown in Figure 5.17. (c) Isobars

erosion level. The depth isolines of rock layers, which are horizontal in the original position, are shown in all panels of Fig. 20*a, b, c*. Since the vertical coordinate in the model increases from the bottom upward, the initial depth is negative. Figure 20*a* shows the residual temperature distribution in the target. The vertical lines indicate temperatures of the postimpact thermal metamorphism observed on the modern visible surface corresponding to the present erosion level estimated from mineralogical data (Gibson et al. 1998; Gibson et al. 1998, 1999a; Foya et al. 1999). The assumption of the erosion level of 7–9 km yields good agreement between the computed and estimated (from geological data) temperatures. A characteristic feature of the model is the “inverted” thermal profile immediately after the crater formation: Hotter rocks are located closer to the surface, as suggested by the flow pattern schematically shown in Fig. 19. The following demonstrates that while cooling down the upper hot layers heat up the rocks at a depth of 7–9 km by 100–150 K above the level indicated in Fig. 20*a*. This late rock heating at the present erosion cut depends on the contribution of the hydrothermal heat flux from several upper kilometers of rocks that could have a significant permeability (Abramov and Kring 2004). Thus, current analysis of the accuracy of the model and the geological temperature estimates can form the basis for the next iteration that would refine the possible crater formation scenarios.

Figure 20*b* shows the uplift–subsidence of the target layers that were originally located at different depths. Assuming, based on the temperature data (Fig. 20*a*), that the depth of the erosion cut is ~8 km, one can trace the model structure of the central uplift along the present surface. Rocks of the lower crust (the initial depth >28 km) in the model are at the present depth of 2–3 km at a distance of ~5 km from the center. It should be noted that the numerical solutions at small distances from the axis are very unstable due to axial symmetry; therefore, the structure of the very central part of the uplift changed over a wide range in various computations. The rocks of the middle granitoid layer (ILG rocks) from depths of more than 20–21 km were lifted to the surface at distances of 12–13 km from the center at the present model surface. Immediately after the crater formation, the temperature in these rocks was ~1,200 K or higher, approaching the melting temperature at the axis. The uplifted rocks in the central zone underwent initial shock compression to pressures of 40–50 GPa (Fig. 20*c*). Since the initial temperature of these rocks (for the geothermal gradient adopted in the model) was ~600 K (in several cases with a slightly larger temperature gradient, ~700 K), the combined effect of the shock and the lifting with a minor adiabatic cooling increased the temperature of these rocks by ~500 K. The surface of the granitoid layer assumed at a depth of



Figure 20. (Continued) of the maximum shock pressure in the rocks drawn for the final tracer positions. The ovals indicate the observed outer boundaries of PDFs in minerals and shatter cones in rocks (SH) at distances of ~30 and 40 to 45 km from the center, respectively. The disordered pattern of isobars near the model crater floor reflects the mixing of tracers that recorded different shock compression levels in these zones. Adapted from Ivanov (2005) with permission from Pleiades Publishing Inc.

15 km approaches almost vertically the level of the presumed erosion surface at a distance of ~ 23 km from the center, which is slightly larger than that observed in the field (~ 20 km, see Fig. 17); this may be considered to be a good coincidence for the fairly crude model used. Since no less deep layers were clearly distinguished in the computation, an inverse approach can be used here. Figure 5.20*b* shows that to roughly reproduce the sequence of rocks in the collar of the Vredefort dome (Fig. 17), one must assume that the rocks of the Witwaterstrand group were originally buried at depths from 7 to 10 km. If the ring fold of the rocks subsided during the crater collapse were identified with the Potchefstroom trough described for Vredefort, then the radii of the model fold (45–50 km, depending on the assumed erosion level) and the observed trough zone (Fig. 17) also would be similar.

According to the model, rocks in the annular trough at the present erosion level must have been located in the original target at a depth of ~ 2 km. The direct comparison with observations is complicated by the fact that the layers of the original actual target were not horizontal (Lana et al. 2003*b*). This gives an expectation that it will be possible to construct more accurate model for comparison with geological data in 3D modeling in the future.

The shock pressure isolines shown in Fig. 20*c* allow the model results to be compared with another series of observations. The planar deformation features (PDFs) in minerals and the shatter cones described in the literature are observed at the present erosion level at distances up to ~ 30 and ~ 40 – 45 km, respectively. For the presumed erosion depth of ~ 8 km, rocks with shock compression levels of 7–10 and 2–3 GPa, respectively, are located at these distances in the model. These values agree with the commonly assumed occurrence levels of PDFs in minerals and shatter cones in rocks (Stöffler and Langenhorst 1994).

For all craters investigated here, the authors estimated the cooling rate of the rocks beneath the crater using a simple heat conduction model (for details, see Ivanov 2004*b*).

Thus, a set of relatively independent parameters (the rock temperature, level of shock metamorphism, and original depth of exposed rocks), the numerical model with the asteroid projectile 14 km in diameter at the impact velocity of 15 km s^{-1} is in good agreement with the geological and geophysical data. A joint analysis of the model and observational data provides a good basis for the necessary next iteration in the description of the Vredefort crater. This analysis is of great interest in discussing the possible relationship to the formation and evolution of the gold fields in the Witwaterstrand basin, which constitute up to 40% of the world's gold reserves (Gibson and Reimold 1999*b*).

The ***Sudbury impact structure*** with an age of 1.85 Ga (Krogh et al. 1984) is now believed to be the erosion remnant of a multiring impact crater (basin) deformed significantly by postimpact tectonic deformations.

A general geological description has been given (see, e.g., Dressler 1984; Deutsch et al. 1995). The Sudbury Igneous Complex (SIC) together with the layer of suavities (the so-called Onaping formation) is interpreted in terms of the hypothesis of the impact origin of the structure as the body of solidified melt (Grieve et al.

1991; Deutsch et al. 1995). The subsequent tectonic deformations of the structure, including the body of solidified melt, led to the thrust of the southern edge of the structure over the northern edge (Shanks and Schwerdtner 1991; Milkereit et al. 1994b). The current (elliptical in a horizontal plane) shape of the erosion remnants of the structure resulted from these processes. According to the Lithoprobe studies, the depth of the preserved bowl-shaped depression filled with the solidified impact melt of target rocks is estimated to be ~ 6 km (Deutsch and Grieve 1994; Milkereit et al. 1994b).

Reconstruction of the original geometry of the structure (Roest and Pilkington 1994) yields an estimate for the initial melt sheet thickness of at least 2.5 km at a diameter of about 60 km. The melt body in the central depression was buried under the layer of allogenic breccia ~ 3 km in thickness (Grieve et al. 1991; Deutsch et al. 1995). The volume of the melted rocks is estimated to be $(1\text{--}2.5) \times 10^4$ km³. The cooling time of such a significant melt volume is long enough for the melt differentiation into more basic quartz gabbro and norites in the floor part and granophyres covering them (Naldrett and Hewins 1984). Recent publications assume the possibility of melt separation just during the short period of vigorous convection in just formed impact melt "lake," buried under suevite cover (Zieg and Marsh 2005). The near-surface geothermal gradient within the Canadian shield ranges from 12 to 15 K km⁻¹, with a temperature at the crust–mantle boundary (at a depth of 40–50 km) of 400–500°C or 700–800 K (Jaupart and Mareschal 1999). At the crater formation epoch, the local geothermal gradient could be larger. In the model presented here, the temperature at the crust–mantle boundary at a depth of 49 km was assumed to be 865 K. The depth of the mantle was estimated from the current value of ~ 44 km (Guillou et al. 1994) with the addition of eroded ~ 5 km of the crust.

Numerical modeling of the Sudbury impact formation and estimates of its cooling history were previously performed by Ivanov and Deutsch (1999). This chapter presents new computations using an updated code and improved equations of state for the materials. Because of the large uncertainty in the structure of the target in the Sudbury region, a simplified two-layer computational model was used, a granite crust over a mantle modeled by the dunite equation of state, for the preliminary analysis.

Trial computations allowed the authors to choose, as the first approximation, the same projectile as that for the Vredefort crater described in the preceding. Consequently, the Vredefort and Sudbury craters are assumed to have similar diameters. The following presents the authors' results for the impact of a spherical projectile 14 km in diameter (granite density) with an impact velocity of 15 km·s⁻¹. The kinetic energy of the projectile is 4.32×10^{23} J. The computed volume of the impact melt (at the initial granite density) is $\sim 12,000$ km³, which is close to the value given in the preceding for the three-layer model of the impact that produced the Vredefort crater. The small difference probably results from small differences in the thermal regimes of the targets and slight modifications of the computational code. These differences are currently being studied. Due to the relatively low

resolution of the projectile, impact melt volumes should be treated as the lowest possible values for the vertical impact.

Since the overall sequence of the Sudbury formation is roughly similar to that for the cases considered in the preceding, for brevity no special illustrations are given here. In the case considered in detail in the following, the crater diameter at the rim crest is ~ 175 km, the diameter at the original surface level is ~ 150 km, the apparent depth under the original surface level is $\sim 1,300$ m, and the rim height is ~ 900 m.

Comparison of the modeled residual rock temperature and the shock compression pressure in the case of Sudbury is complicated due to severe distortions of the original crater shape by tectonic movements and erosion. Here, such comparisons are made with great caution based on the assumptions about the origin of the various observed geologic details.

Based on the interpretation of the seismic sounding together with bore hole drilling results, the following crater evolution scenario was suggested (Dressler 1984; Deutsch and Grieve 1994; Milkereit et al. 1994a, 1994b; Deutsch et al. 1995; Wu et al. 1995). The crater was formed as a two-ring basin with a deep central depression (similar to large Venusian impact craters). A large volume of melt, $\sim 10^4$ km³ (which subsequently formed the main body of igneous rocks, SIC), was in the depression about 60 km in diameter. The melt “lake” surface was immediately covered with a layer of allogenic breccia, stabilized atop of melt through fast cooling and solidification of a fairly thick (several hundred meters) crust of a melt–clast mixture. The bulk of the impact melt covered with a blanket of breccia solidified long enough for the differentiation into a heavy, refractory lower layer of norites and a less dense layer of granophyres (with a possible short time scale of differentiation, as assumed by Zieg and Marsh 2005). The Sudbury region of the Canadian shield was deformed by the front of the Grenville compression (from southeast to northwest) even before the melt completely solidified. The still hot (and, hence, plastic) rocks around the crater formed a giant fold in which the southeastern rim of the crater was thrust onto the collapsed northern rim. The full displacement of the southeastern rim in the form of a giant 30-km thrust created an oval shape in the originally circular crater. The subsequent erosion of rocks to a depth of ~ 5 km resulted in the observed shape to the crater structure remnants. The Sudbury impact origin can still be judged by concentric belts of rocks with PDFs in quartz and plagioclase and shatter cones at distances, respectively, ~ 10 and ~ 20 km from the boundary of the solidified melt body at the present (eroded) surface (Deutsch and Grieve 1994).

This generalized scenario has many “weak” assumptions that need further study. For example, note the unsolved (in the authors’ view) problem of the stability of a kilometer-thick layer of clastic material on the surface of the liquid melt “lake” ~ 60 km in diameter. There are geochemical constraints on the possibility of representing the equilibrium mineral composition of the rock that can give the observed differentials (Ariskin et al. 1999). Solving this problem may require assuming the presence of contrasting (in mineral composition) rocks in the impact

melt zone. Nevertheless, the described scenario makes it possible to formulate a number of useful testable hypotheses.

For example, if one follows the idea of melt differentiation, then one must assume that the boundary between norites (below) and granophyres (above) was initially horizontal, since the differentiation took place in the field of gravity. The revealed tilt of this boundary at the northern margin of the structure, 20–30° to the horizon, should then be attributed to the overall rotation of the block 10–30 km in size (from one-fourth to one-third of the crustal thickness). This picture of the formation of a giant thrust fold was suggested and elaborated by Wu et al. (1995).

Figure 21 compares the numerical model with a sketch of the profile of the structure in the north–south direction constructed from LITHOPROBE data (Milkereit et al. 1994a). In the described approach, the observed profile is rotated through 23° to make the boundary between norites and granophyres almost horizontal. Strictly speaking, this rotation has a meaning only for the region of the northern margin.

In Fig. 21a, the contours of the melt zone were approximately fitted to the location of the computed 1,573 K (1,200°C) isotherm as an approximate estimate of the impact melt location in the central part of the computed crater. This is supported in Fig. 21b by comparison of the observed (rotated) profile with the location of the 50 GPa shock pressure isobar corresponding to the melting of granite after decompression. With this model fit to observations, the base of the melt zone is at a depth of ~4 km relative to the original target level. If the more or less uniformly rotated block of rocks, including the northern margin, extends to another 10–20 km from the northern SIC boundary, then the plane of the present erosion level must go deep into the target with increasing distance from the center, as shown by the inclined dotted line in Fig. 21a. A proper comparison of the rock parameters in the model and on the terrain should then be made along this inclined line.

Figure 21c shows the lines of equal initial rock depth in the model. Comparison of the model with the observations shows that rocks uplifted from depths of 12–16 km are located on the surface behind the SIC margin. Their temperature immediately after the crater formation decreased from the melting temperature (at the boundary of the melt zone) to about 600°C at a distance of ~5 km.

Figure 22 shows the decrease in the shock pressures “recorded” by the tracers whose final locations are within ± 0.5 km of the assumed present target surface with increasing distance from the center. The distance along the lower axis is measured from the intersection of this plane with the original target surface (at a distance of 11 km from the center); the distance along the upper axis is measured from the boundary of the melt zone (a shock pressure of ~50 GPa). This profile can be traced in Fig. 21b. Dots 1 and 2 in Fig. 22 correspond to the 10-km distance from the edge of SIC for a shock pressure of ~10 GPa (appearance of PDF's in quartz and plagioclase) and 20-km distance for a shock pressure of ~5 GPa (appearance of shatter cones in rocks) given in the literature (Deutsch and Grieve 1994; Grieve and Theriault 2000). The model computations are consistent with the few results for the shock pressure estimates in rocks around Sudbury structure up to distances

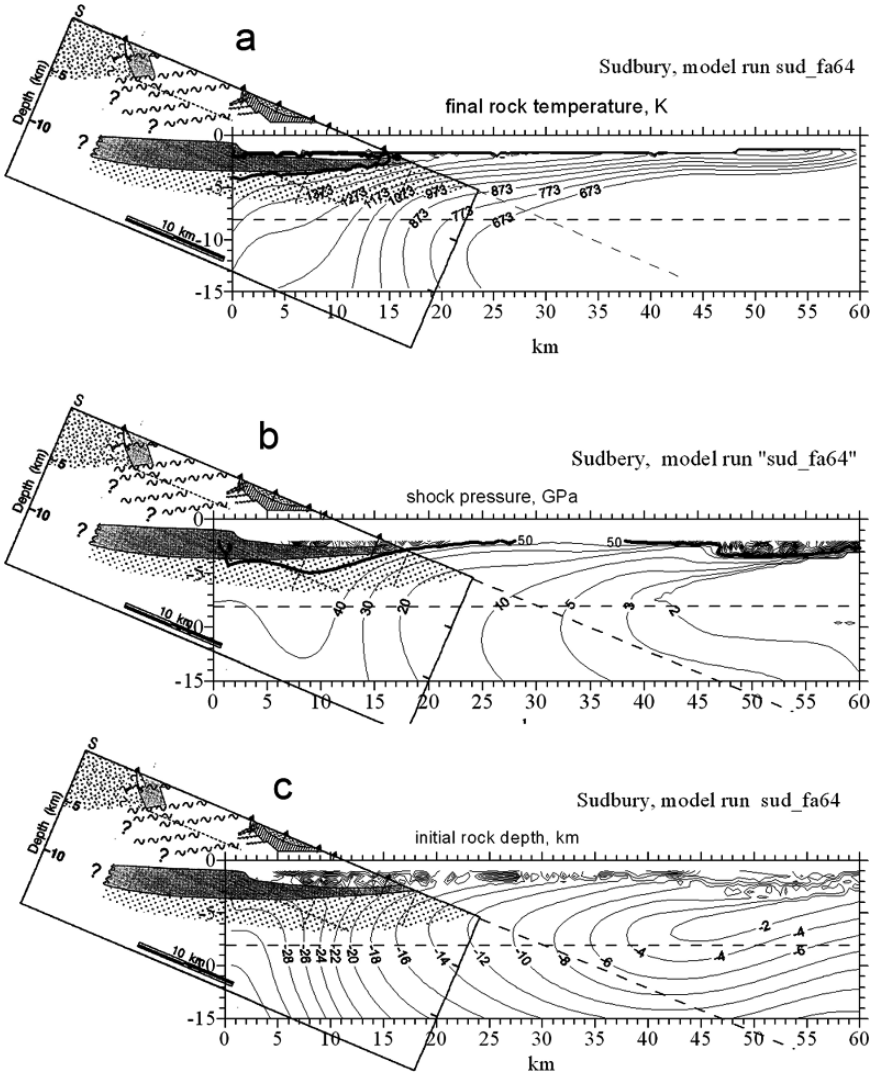


Figure 21. (a) Temperature, (b) shock pressure, and (c) initial rock depth fields for the model Sudbury crater. A portion of the present crater profile constructed from LITHOPROBE data (Milkereit et al. 1994a,b; Wu et al. 1995) was used for comparison with the observations. This portion was rotated through 23° clockwise assuming that the boundary between the heavier and lighter melts (norites and granophyres) was initially horizontal (an equipotential surface in the field of gravity). An approximate alignment with the model profile was made using the 1,500 K isotherm and the 50 GPa isobar that roughly bounds the impact melt zone in the model. The *inclined dotted line* indicates the location of the present surface within the inclined block including the northern edge of the SIC. For comparison, the *horizontal dotted line* indicates an approximate erosion level for Vredefort. Adapted from Ivanov (2005) with permission from Pleiades Publishing Inc.

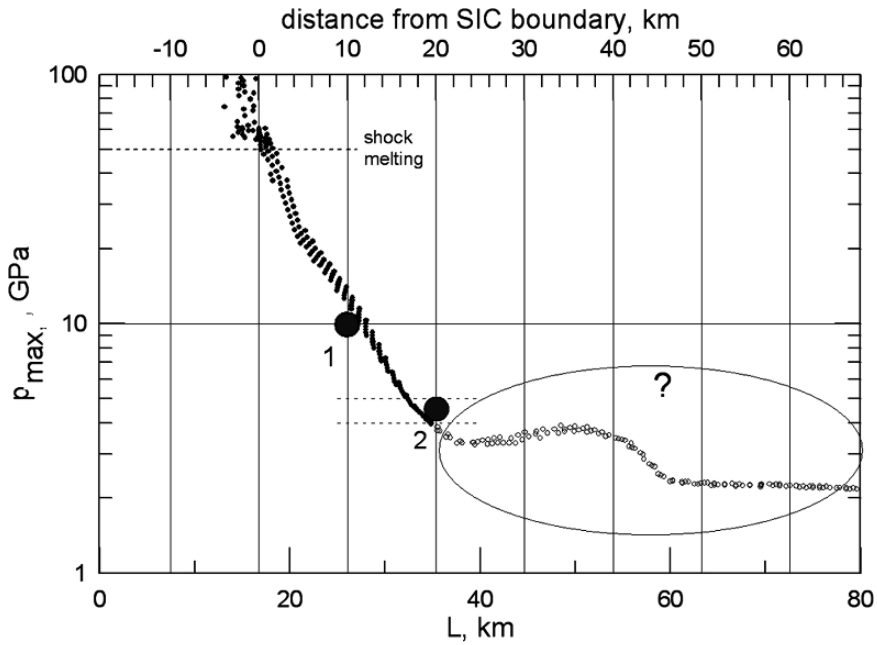


Figure 22. Maximum shock pressure recorded by tracers with the final positions located at ± 500 m from the present erosion surface in the rotated crustal block at the northern edge of SIC (see Fig. 21). The filled black circles show boundaries of PDFs in quartz and plagioclase (1) and shatter cones in rocks (2) observed at the present-day surface. The ellipse with a question mark outlines the extension of the inclined present surface at large distances where the assumption about the rotation of the crustal block as a single body is inapplicable; the next, possibly also inclined block is most likely located at these distances. Adapted from Ivanov (2005) with permission from Pleiades Publishing Inc.

of ~ 20 km from the SIC edge (the boundary of the impact melt zone). Following along the presumed inclined surface too far from the crater could be careless due to the finite sizes of a block rotated as a solid body. If the model described in the preceding is valid, then the transition to the next block is most probably further from the SIC edge. The systems of cracks north of the SIC, which are often interpreted as the ring faults around a multiring structure, the first of which is at a distance of ~ 45 km from the center of the Sudbury basin, can be suspected to be the boundaries of such blocks (Spray et al. 2004)

It should be noted that for the mutual arrangement of the assumed inclined erosion surface and shock pressure isobars shown in Fig. 21b, the position of points in Fig. 22 depend weakly on the horizontal displacement of the observed crater profile rotated at 23° . Note also that the preceding comparison is made for the roughly diametrical profile of the Sudbury basin. The actual 3D basin deformation scheme under the assumed tectonic compression still awaits detailed development.

Summarizing the comparison note that the assumption about the similar <200 km sizes of Sudbury and Vredefort is consistent (for the model of vertical impacts) with the main observations known from published data.

4 DISCUSSION

The authors numerically modeled the formation of the four largest known craters on the Earth. Usage of the same numerical model in all cases to analyze the computational and observational data allows the researchers, on one hand, to check where the model is valid, and on the other hand, form a basis for generalizing the observational data collected for various impact structures variously modified by the endogenic processes of tectonics, erosion, and sedimentation. In general, it can be stated that in all considered cases, the model agrees satisfactorily with the observations for appropriately chosen model parameters.

As follows from the model, the final shape of large impact craters is the result of: (1) growth of a deep transient cavity, (2) its collapse in the field of gravity with the formation of an uplift (a dynamic dome), and (3) the subsequent collapse of the uplift (dome) with intense flow of material over the surface of the forming crater. When the uplift is formed, the floor of the transient cavity, covered with the most strongly fragmented and melted material, becomes the dome surface. When the dome collapses, the hottest surface layers begin to flow down the slopes of the dome as the collapse of the dome itself in the gravity field is going slower due to internal friction in broken, but not melted rocks in the dome body. The inner ring in the model is formed by these near-surface motions of the material.

Such a cratering process is possible only with a temporary friction reduction in the fractured rocks surrounding the growing crater imbedded into the model. The friction reduction can be described in terms of the acoustic fluidization model (Melosh and Ivanov 1999). The true causes of the temporary friction reduction may well be different, but so far the acoustic fluidization model can be considered as a convenient phenomenologic model for the friction coefficient reduction in rocks around the crater to values of 0.05–0.1 followed by an exponential (in time) return of the internal friction coefficient to its normal values of ~ 0.5 (corrected for the friction reduction as the rock melting point is approached). To reproduce the observed shapes of the final flattened craters, one must assume that the characteristic normal friction restoration time (in the time–exponential relation) in rocks beneath the craters is 90–100 s for the Popigai crater and 120–160 s for larger studied craters. These values probably can be used to model large meteorite craters on other planets. More detailed modeling of a wide range of crater diameters suggests that the decay time in the acoustic fluidization model is approximately proportional to the projectile diameter at the same impact velocity in events of different scales (Wünnemann and Ivanov 2003).

The modeling of complex meteorite craters described herein encounter great difficulties in reproducing the observed crater depth. At the excavation phase of the transient cavity, the rocks beneath the impact center are displaced downward by

10–20 km and then, during its collapse, rise up 5–10 km above the original surface layer and, at the end, sink to the final location 1–2 km below the original surface. At vertical displacement amplitude of 30–40 km, it is a difficult problem to find a set of model parameters that would ensure a stop at the position corresponding to the observations. Therefore, one should treat results of the computations for detailed model crater profiles with great caution. One cannot rule out the possibility that introducing better descriptions of the behavior of large fractured rock masses into the model will require researchers to reiterate the basic model parameters.

The spatial resolution of the model is a separate problem. A reliable computation of the shock wave decay in the target requires that the projectile should be covered with at least ~ 40 cells for the projectile diameter. At a projectile diameter of 10–15 km, this implies that the spatial step of the computational grid must be no more than 200–300 m. A finer grid step would lead to a rapid increase in computational time. The commonly used grid remeshing technique after the shock passage through the computational region is inapplicable in the problem under consideration, because at the final formation phase of a flat crater with a diameter of 100–200 km and a depth of ~ 1 km, even cells with a diameter of 100 m are too large to trust the computational results with regard to reproducing the crater floor relief. Further development of the model will probably solve the problem on different grids specially constructed for each phase of the process with a successive reinterpolation. This is particularly necessary for 3D computations in the near future, in which it will be even more difficult to maintain the balance between spatial resolution and computational time.

5 CONCLUSIONS

The results of the present numerical modeling of the formation of the largest terrestrial craters presented here allowed the authors to make a detailed comparison with available geological and geophysical data. Agreement was found in such parameters as crater morphology and depth, impact melt volume, and distribution of shock pressures and temperatures in the rocks beneath the crater. The model parameters for the mechanical behavior of rocks chosen from the conditions for the best agreement between the computations and available observations can be used to study cratering processes on other planets, including the most interesting (for the geological history of the Moon) giant impact basins.

REFERENCES

- Abramov O, Kring DA (2004) Numerical modeling of an impact-induced hydrothermal system at the Sudbury crater. *J Geophys Res (Planets)* 109:E10007
- Alvarez LW, Alvarez W, Asaro F, Michel HV (1980) Extraterrestrial cause for the Cretaceous-Tertiary extinction. *Science* 208(4448):1095–1108
- Amsden AA, Ruppel HM, Hirt CW (1980) SALE: A Simplified ALE computer program for fluid flow at all speeds. Los Alamos Laboratory Report LA-8095, Los Alamos, NM, p 101

- Ariskin AA, Deutsch A, Ostermann M (1999) Sudbury igneous complex: simulating phase equilibria and in situ differentiation for two proposed parental magmas. In: Dressler BO, Sharpton VL (eds) Large meteorite impacts and planetary evolution II. Geological Society of America, Special Paper 339, Boulder, pp 373–387
- Bottomley R, Grieve RAF, York D, Masaitis V (1997) The age of the Popigai impact event and its relation to events at the Eocene/Oligocene boundary. *Nature* 388:365–368
- Bralower TJ, Paull CK, Leckie RM (1998) The cretaceous-tertiary boundary cocktail: Chicxulub impact triggers margin collapse. *Geology* 26(4):331–334
- Christeson GL, Nakamura Y, Buffler RT et al (2001) Deep crustal structure of the Chicxulub impact crater. *J Geophys Res* 106:21751–21770
- Dahlman O, Israelson H (1977) Monitoring underground nuclear explosions. Elsevier Science, New York, p 440
- Deep Drilling in the Impact Structure: Puchezh-Katunki (1999) In: Masaitis VL, Pevzner LA (eds) VSEGEI, St. Petersburg, p 392 (in Russian)
- Deutsch A, Grieve RAF (1994) The Sudbury Structure: constraints on its genesis from Lithoprobe results. *Geophys Res Lett* 21:963–966
- Deutsch A, Grieve RAF, Avermann M et al (1995) The Sudbury Structure (Ontario, Canada): a tectonically deformed multi-ring impact basin. *Geologische Rundschau* 84(4):697–709
- Deutsch A, Masaitis VL, Langenhorst F et al (2000) Popigai, Siberia—well preserved giant impact structure, national treasury, and world's geological heritage. *Episodes* 23(1):3–11
- De Wit MJ, Roering C, Hart RJ et al (1992) Formation of an Archaean continent. *Nature* 357:553–562
- Dienes JK, Walsh JM (1970) Theory of impact: Some general principles and the method of Eulerian codes. In: Kinslow R (ed) High-velocity impact phenomena. Academic Press, New York, pp 46–104
- Donofrio RR (1998) North American impact structures hold giant field potential. *Oil Gas J* 69–83
- Doucoure CM, de Wit MJ, Mushayandebvu MF (1996) Effective elastic thickness of the continental lithosphere in South Africa. *J Geophys Res* 101:11291–11304
- Dressler BO (1984) General geology of the Sudbury area. In: Pye EG, Naldrett AJ, Giblin PE (eds) The geology and ore deposits of the Sudbury structure. Special vol 1. Ontario Geological Survey, Ontario, pp 57–82
- Dutta U, Biswas N, Martirosyan A et al (2003) Estimation of earthquake source parameters and site response in Anchorage, Alaska from strong-motion network data using generalized inversion method. *Physics Earth Planet Inter* 137:13–29
- Ebbing J, Janle P, Koulouris J et al (2001) 3D gravity modelling of the Chicxulub impact structure. *Planet Space Sci* 49:599–609
- Foya SN, Gibson RL, Reimold WU (1999) Impact-related hydrothermal alteration of Witwaterstrand Gold Reefs in the Vredefort Dome and Witwaterstrand Goldfields, South Africa. *Meteoritics Planetary Sci Suppl* 34:A37
- Gibson RL, Jones MQW (2002) Late Archean to Paleoproterozoic geotherms in the Kaapvaal craton, South Africa: constraints on the thermal evolution of the Witwaterstrand Basin. *Basin Res* 14:169–181
- Gibson RL, Reimold WU (1998) Thermal metamorphic signature of an impact event in the Vredefort Dome, South Africa. *Geology* 26(9):787–790
- Gibson RL, Reimold WU (1999a) The metamorphic fingerprint of large impact events: the example of the Vredefort Dome, South Africa. *Meteoritics Planetary Sci Suppl* 34:A42
- Gibson RL, Reimold WU (1999b) The significance of the Vredefort Dome for the thermal and structural evolution of the Witwaterstrand Basin, South Africa. *Mineralogy Petrology* 66:5–23
- Gibson RL, Reimold WU, Stevens G (1998) Impact-related metamorphism in the Vredefort Dome, South Africa. *Lunar Planet Sci XXXIX*. LPSI, Houston, #1360
- Grajales-Nishimura JM, Cedillo-Pardo E, Rosales-Dominguez C et al (2000) Chicxulub impact: the origin of reservoir and seal facies in the southeastern Mexico oil fields. *Geology* 28:307–310
- Grieve RAF, Cintala MJ (1992) An analysis of differential impact melt-crater scaling and implications for the terrestrial impact record. *Meteoritics* 27:526–538
- Grieve RAF, Cintala MJ (1997) Planetary differences in impact melting. *Adv Space Res* 20:1551–1560

- Grieve R, Theriault A (2000) Vredefort, Sudbury, Chicxulub: three of a kind? *Ann Rev Earth Planet Sci* 28:305–338
- Grieve RAF, Stöffler D, Deutsch A (1991) The Sudbury Structure: controversial or misunderstood? *J Geophys Res* 96 (E5), 22,753–22,764
- Guillou L, Mareschal J-C, Jaupart C et al (1994) Heat flow, gravity and structure of the Abitibi belt, Superior Province, Canada: implications for mantle heat flow. *Earth Planet Sci Lett* 122:103–123
- Gupta SC, Ahrens TJ, Yang W (1999) Shock induced vaporization of anhydrite CaSO_4 and Calcite CaCO_3 . APS Meeting. Abstr #P2.01
- Henkel H, Reimold WU (1998) Integrated geophysical modelling of a giant, complex impact structure: anatomy of the Vredefort Structure, South Africa. *Tectonophysics* 287:1–20
- Hildebrand AR, Penfield GT, Kring DA et al (1991) Chicxulub Crater: a possible Cretaceous-Tertiary boundary impact crater on the Yucatan Peninsula. *Geology* 19:867–871
- Ivanov BA (1992) Geomechanical models of impact cratering: Puchezh-Katunki Structure. International Conference on Large Meteorite Impacts and Planetary Evolution. August 31–September 2, 1992. LPI Contribution 790. Sudbury, Ontario, Canada, pp 40
- Ivanov BA (1996) Spread of ejecta from impact craters and the possibility of estimating the volatile content of the Martian crust. *Solar System Res* 30(1):43–48 (in English)
- Ivanov BA (2002) Deep drilling results and numerical modeling: Puchezh-Katunki impact crater, Russia. *Lunar Planet Sci XXXIII*. LPSI, Houston, #1286
- Ivanov BA (2003a) Large impact crater modeling: Chicxulub. Third International Conference on Large Meteorite Impacts. August 5–7, 2003. Nördlingen, Germany, #4067
- Ivanov BA (2003b) Modification of ANEOS for rocks in compression. Impact Cratering: bridging the gap between modeling and observations. February 7–9, 2003. LPI Contribution 1155, Houston, p 40
- Ivanov BA (2004a) Multi-ring basins: modelling terrestrial analogs. 40th Vernadsky/Brown Microsymposium on Comparative Planetology. October 11–13, 2004. Vernadsky Inst, Moscow, Russia. CD ROM, #30
- Ivanov BA (2004b) Heating of the lithosphere during meteorite cratering. *Solar System Res* 38:266–279
- Ivanov BA (2005) Numerical modeling of the largest terrestrial meteorite craters. *Solar System Res* 39(5):381–409
- Ivanov BA, Deutsch A (1999) Sudbury impact event: cratering mechanics and thermal history. In: Dressler B, Sharpton VL (eds) Large meteorite impacts and planetary evolution II. Geological Society of America, Special Paper 339. Boulder, pp 389–397
- Ivanov BA, Petaev MI (1992) Mass and impact velocity of the meteorite formed the Sterlitamak crater in 1990. *Lunar Planet Sci Conf XXIII*. Houston, pp 573–574
- Ivanov BA, Basilevsky AT, Neukum G (1997) Atmospheric entry of large meteoroids: implication to Titan. *Planet Space Sci* 45(8):993–1007
- Ivanov BA, Badukov DD, Yakovlev OI et al (1996a) Degassing of sedimentary rocks due to Chicxulub impact: hydrocode and physical simulations. In: Ryder G, Fastovsky D, Gartner S (eds) The Cretaceous-Tertiary event and other catastrophes. Geological Society of America, Special Paper 307, pp 125–139
- Ivanov BA, Kocharyan GG, Kostuchenko VN et al (1996b) Puchezh-Katunki impact crater: preliminary data on recovered core block structure. *Lunar Planet Sci XXVII*. LPSI, Houston, pp 589–590
- Ivanov BA, Langenhorst F, Deutsch A et al (2004) Anhydrite EOS and phase diagram in relation to shock decomposition. *Lunar Planet Sci XXXV*. LPSI, Houston, #1489
- James DE, Fouch MJ, VanDecar JC et al (2001) Tectospheric structure beneath southern Africa. *Geophys Res Lett* 28(13):2485–2488
- Jaupart C, Mareschal JC (1999) The thermal structure and thickness of continental roots. *Lithos* 48: 93–114
- Kenkmann T, Ivanov B (2006) Target delamination by spallation and ejecta dragging: an example from the Ries crater's periphery. *Earth Planet Sci Lett* 252(1–2):15–29
- Krogh TE, Davis DW, Corfu F (1984) Precise U-Pb Zircon and Baddeleyite ages for the Sudbury area. In: Pye EG, Naldrett AJ, Giblin PE (eds) The geology and ore deposits of the Sudbury structure. Special Volume 1, Ontario Geological Survey, Ontario, pp 431–446

- Lana C, Gibson RL, Reimold WU (2003b) Impact tectonics in the core of the Vredefort dome, South Africa: implications for central uplift formation in very large impact structures. *Meteoritics Planetary Sci* 38:1093–1107
- Lana C, Gibson RL, Kisters AFM et al (2003a) Archean crustal structure of the Kaapvaal craton, South Africa—evidence from the Vredefort dome. *Earth Planet Sci Lett* 206:133–144
- Lana C, Reimold WU, Gibson RL et al (2004) Nature of the Archean midcrust in the core of the Vredefort dome, Central Kaapvaal Craton, South Africa 1. *Geochimica et Cosmochimica Acta* 68:623–642
- Landau LD, Lifshits EM (1958) *Statistical physics*. Pergamon Press, London, p 484
- Langenhorst F, Deutsch A, Hornemann U et al (2003) On the shock behaviour of anhydrite: experimental results and natural observations. *Lunar Planet Sci XXXIV*. LPSI, Houston. #1638
- Masaitis VL (1994) Impactites from Popigai crater. In: Grieve RAF, Sharpton VL, Dressler BO (eds) *Large meteorite impacts and planetary evolution*. Geological Society of America, Special Paper, 293, pp 153–162
- Masaitis VL (1998) Popigai crater: origin and distribution of diamond-bearing impactites. *Meteoritics Planetary Sci* 33:349–359
- Masaitis VL, Raikhlin AI (1986) The Popigai crater formed by the impact of an ordinary chondrite. *Doklady Akademii Nauk SSSR* 286:1476–1478 (in Russian)
- Masaitis VL, Mashchak MS, Naumov MV (2003) Original diameter and depth of erosion of the Popigai impact crater, Russia. *Third International Conference on Large Meteorite Impacts*. August 5–7, 2003. Nördlingen, Germany, #4039
- Masaitis VL, Mikhailov MV, Selivanovskaya TV (1975) The Popigai meteor crater. *Nauka Press, Moscow*, p 124 (in Russian)
- Masaitis VL, Danilin AN, Mashchak MS et al (1980) The geology of astroblemes. *Nedra Press, Leningrad, Russia*, p 231 (in Russian)
- Melosh HJ (1989) *Impact cratering: a geologic process* (Oxford Monographs on Geology and Geophysics, No. 11). Clarendon Press, New York, p 245
- Melosh HJ (2000) A New and improved equation of state for impact studies. *Lunar Planet Sci XXXI*. LPSI, Houston. #1903
- Melosh HJ, Ivanov BA (1999) Impact crater collapse. *Ann Rev Earth Planet Sci* 27:385–415
- Melosh HJ, Ryan EV, Asphaug E (1992) Dynamic fragmentation in impacts—hydrocode simulations of laboratory impact. *J Geophys Res* 97(E9):14,735–14,759
- Milkereit B, White DJ, Green AG (1994b) Towards an improved seismic imaging technique for crustal structures: the Lithoprobe Sudbury experiment. *Geophys Res Lett* 21:927–930
- Milkereit B, Green A, Wu J et al (1994a) Integrated seismic and bore hole geophysical study of the Sudbury Igneous Complex. *Geophys Res Lett* 21:931–934
- Moralev VM (ed) (1986) *Structure of the terrestrial crust of the Anabar Shield*. Nauka, Moscow, p 198 (in Russian)
- Morgan JV, Warner MR, Chicxulub Working Group et al (1997) Size and morphology of the Chicxulub impact crater. *Nature* 390(6659):472–476
- Morgan JV, Warner MR, Collins GS et al (2000) Peak-ring formation in large impact craters: geophysical constraints from Chicxulub. *Earth Planet Sci Lett* 183:347–354
- Moser DE, Flowers RM, Hart RJ (2001) Birth of the Kaapvaal tectosphere 3.08 billion years ago. *Science* 291(5503):465–468
- Naldrett AJ, Hewins RH (1984) The main mass of the Sudbury igneous complex. In: Pye EG, Naldrett AJ, Giblin PE (eds) *The geology and ore deposits of the Sudbury structure*. Special Volume 1, Ontario Geological Survey, Ontario, pp 235–251
- Nguuri TK, Gore J, James DE et al (2001) Crustal structure beneath southern Africa and its implications for the formation and evolution of the Kaapvaal and Zimbabwe cratons. *Geophys Res Lett* 28(13):2502–2504
- Papadopoulos GA, Plessa A (2000) Magnitude-distance relations for earthquake-induced landslides in Greece. *Engineering Geology* 58(3–4):377–386
- Petaev MI, Kisarev Yu.L, Mustafin Sh.A et al (1991) Meteorite Sterlitamak—A new crater-forming fall. *Lunar Planet Sci Conf XXII*. Houston, pp 1059–1060

- Pierazzo E, Hahmann AN, Sloan L (2003) Chicxulub and climate: Radiative perturbations of impact-produced S-bearing gases. *Astrobiology* 3:99–118
- Pierazzo E, Kring DA, Melosh HJ (1998) Hydrocode simulation of the Chicxulub impact event and the production of climatically active gases. *J Geophys Res* 103:28607–28625
- Pierazzo E, Melosh HJ (1999) Hydrocode modeling of Chicxulub as an oblique impact event. *Earth Planet Sci Lett* 165:163–176
- Pierazzo E, Vickery, AM, Melosh HJ (1997) A reevaluation of impact melt production. *Icarus* 127:408–422
- Pike RJ (1980) Control of crater morphology by gravity and target type - Mars, earth, moon. *Lunar Planet Science Conference XI*. Pergamon Press, New York, pp 2159–2189
- Pilkington M, Hildebrand AR (2000) Three-dimensional magnetic imaging of the Chicxulub Crater. *J Geophys Res* 105:23479–23492
- Pope KO, Baines KH, Ocampo AC et al (1994) Impact winter and the Cretaceous/Tertiary extinctions: results of a Chicxulub asteroid impact model. *Earth Planet Sci Lett* 128:719–725
- Pope KO, Baines KH, Ocampo AC, Ivanov BA (1997) Energy, volatile production, and climatic effects of the Chicxulub Cretaceous/Tertiary impact. *J Geophys Res* 102(E9):21645–21664
- Reimold WU, Gibson RL (1996) Geology and evolution of the Vredefort impact structure, South Africa. *J. African Earth Sci* 23(2):125–162
- Ricoy V (2003) The Cantarell Breccia System, Southern Gulf of Mexico: Structural evolution and support for an origin related to the Chicxulub meteorite impact. EGS-AGU-EUG Joint Assembly, abstracts from the meeting held in Nice, France, 6–11 April 2003, #13339
- Roest WR, Pilkington M (1994) Restoring post-impact deformation at Sudbury: a circular argument. *Geophys Res Lett* 21:959–962
- Rosen OM, Bibikova EV, Zhuravlev AB (1991) Early crust of the Anabar Shield: age and formation models. Early Earth's crust: the composition and age. Mergasov GG (ed) Nauka Press, Moscow, pp 199–244 (in Russian)
- Rosen OM, Condie KC, Natapov LM et al (1994) Archean and early Proterozoic evolution of the Siberian craton: a preliminary assessment. *Developments in Precambrian Geology* 11 Windley BF (ed) Elsevier, Amsterdam, pp 411–459
- Schmidt RM, Housen KR (1987) Some recent advances in the scaling of impact and explosion cratering. *Int J Impact Engng* 5:543–560
- Shanks WS, Schwerdtner WM (1991) Crude quantitative estimates of the original northwest-southwest dimension of the Sudbury Structure, south central Canadian shield. *Can J Earth Sci* 28:1677–1686
- Spray JG, Butler RF, Thomson LM (2004) Tectonic influences on the morphometry of the Sudbury impact structure: Implications for terrestrial cratering and modeling. *MAPS* 31(2):287–301
- Stevens G, Armstrong RA, Gibson RL (1999) Pre- and postimpact metamorphism in the core of the Vredefort Dome: clues to crustal response at a massive meteorite strike. *Meteoritics Planetary Sci Suppl* 34:A112
- Stöffler D, Langenhorst F, (1994) Shock metamorphism of quartz in nature and experiment: I. Basic observation and theory. *Meteoritics* 29:155–181
- Stöffler D, Artemieva NA, Ivanov BA et al (2004) Origin and emplacement of the impact formations at Chicxulub, Mexico, as revealed by the ICDP deep drilling at Yaxcopoil-1 and by numerical modeling. *Meteoritics Planetary Sci* 39(7):1035–1067
- Swisher CC, Grajales-Nishimura JM, Montanari A et al (1992) Coeval $^{40}\text{Ar}/^{39}\text{Ar}$ ages of 65.0 million years ago from Chicxulub Crater melt rock and Cretaceous-Tertiary boundary tektites. *Science* 257:954–958
- Therriault AM, Grieve RAF, Reimold WU (1997) Original size of the Vredefort Structure: implications for the geological evolution of the Witwaterstrand Basin. *Meteoritics Planetary Sci* 32:71–77
- Thompson SL, Lauson HS (1972) Improvements in the Chart D radiation-hydrodynamic CODE III: revised analytic equations of state. Report SC-RR-71 0714. Sandia National Laboratory, Albuquerque, p 119
- Turtle EP, Pierazzo E (1998) Constraints on the size of the Vredefort impact crater from numerical modeling. *Meteoritics Planetary Sci* 33:483–490

- Turtle EP, Pierazzo E, O'Brien DP (2003) Numerical modeling of impact heating and cooling of the Vredefort impact structure. *Meteoritics Planetary Sci* 38:293–303
- Wieland F, Reimold WU (2003) Field and laboratory studies on shatter cones in the Vredefort Dome, South Africa, and their genesis. *Meteoritics Planetary Sci Suppl* 38:A5016
- Wieland F, Gibson RL, Reimold WU et al (2003) Structural evolution of the central uplift of the Vredefort Impact Structure, South Africa. *Meteoritics Planetary Sci Suppl* 38:A5027
- Wu J, Milkereit B, Boerner DE (1995) Seismic imaging of the enigmatic Sudbury Structure. *J Geophys Res* 100:4117–4130
- Wünnemann K Ivanov BA (2003) Numerical modelling of the impact crater depth-diameter dependence in an acoustically fluidized target. *Planet Space Sci* 51:831–845
- Zel'dovitch Ya.B, Raiser Yu.P (1967) *Physics of shock waves and high-temperature hydrodynamic phenomena*. Academic Press, New York
- Zharkov VN, Kalinin VA (1971) *Equations of state for solids at high pressures and temperatures*. Consultants Bureau, New York, p 257
- Zieg MJ, Marsh BD (2005) The Sudbury igneous complex: viscous emulsion differentiation of a superheated impact melt sheet. *GSA Bulletin* 117:1427–1450

CHAPTER 6

THERMAL RADIATION AND FIRES AFTER IMPACTS OF COSMIC OBJECTS

VLADIMIR SVETSOV

*Institute for Dynamics of Geospheres, Russian Academy of Sciences, Moscow 119334, Russia
E-mail: svetsov@idg.chph.ras.ru*

1 GEOLOGICAL EVIDENCE FOR IMPACT-RELATED FIRES

After impacts of cosmic bodies their kinetic energy transforms into heat. Materials of an impactor, target, and air are heated to high temperatures; therefore, it seems natural that impacts of cosmic objects are followed by fires. The traces of large fires were first searched for in the layers of sedimentary rocks that approach the periods of biotic mass extinctions in age. There is a widely known hypothesis of Alvarez et al. (1980) about mass extinctions at the Cretaceous-Tertiary (K/T) boundary after the impact of the cosmic object that created the Chicxulub crater. This impact hypothesis is confirmed by high concentrations of iridium and the presence of crater ejecta particles in the global clay layer of an appropriate age (65 million years). Significant amounts of reduced carbon, soot, and charcoal have been discovered in this layer as well; carbon and soot have been found at the K/T boundary over the whole Earth (Wolbach et al. 2003). This clearly points to global fires of that period, which probably caused global atmospheric darkening. Soot could have remained in the atmosphere for months after the impact (Wolbach et al. 1985, 1988, 1990; Anders et al. 1986, 1991; Gilmour et al. 1990; Heymann et al. 1998).

There is no decisive evidence that fires at the K/T boundary were caused directly by the impact. Moreover, there is no decisive evidence that mass extinctions of animals and vegetation 65 million years ago resulted from the impact of a cosmic object. The hypothesis of a global fire at the K/T boundary was disputed in some works (Scott 2000; Scott et al. 2000). One of the arguments is that fires were common at the end of the Cretaceous and beginning of the Tertiary periods. For example, layers of charcoal found at the K/T boundary in New Mexico are quite similar to those found below and above this boundary. In the work of Jones and Lim (2000), charcoal obtained from samples of sedimentary rocks of the K/T

boundary at five different sites in France, Haiti, the United States, Tunisia, and Spain was examined with the use of an electron microscope. Evidence was found that the charcoal was formed from already decomposed plants; about half the studied samples had indications of precharring biodegradation. The authors concluded that some relatively long period of time—months, years, and maybe decades—elapsed between the plant death and fires that turned the vegetation into charcoal. However, as the found soot is mixed with iridium-enriched sediments (Wolbach et al. 1990), even if the fires have not been caused directly by the impact, the time between the impact and the fires was relatively short. It is not possible to recognize the exact reason of the plant death, whether by cosmic object impact or endogenous factors.

The layer at the K/T boundary is unique. No traces of global fires have been found in sedimentary rock layers formed in other times, including the periods of mass extinctions. For example, Herring (1985) studied 186 samples, obtained by deep-water drilling, which had various ages within the last 70 million years. He did not find any peaks in the charcoal content that could serve as evidence of large fires. Wolbach et al. (2003) studied the layers of sedimentary rocks at the Cenomanian-Turonian boundary (C/T, 91 million years ago) and at the Eocene-Oligocene boundary (E/O, 35 million years ago). Iridium anomalies at the both boundaries and microtektites at the E/O boundary show that the extinctions could have resulted from the impacts of large objects. Probably there were several large impacts in the late Eocene epoch (Sanfilippo et al. 1985; Farley et al. 1998; Glass and Koeberl 1999). However, no significant amount of soot has been found either in the layers of the late Eocene or late Cenomanian. This points to the absence of global fires, although the possibility of soot losses due to oxidation cannot be excluded.

The amount of carbon in the layer at the K/T boundary is about $10 \text{ mg}\cdot\text{cm}^{-2}$ in continental areas (Wolbach et al. 1990) and about three times lower in the Central Pacific (Wolbach et al. 2003). However, it should be mentioned that carbon oxidation leads to reduction of its concentration with time. The amount of soot is about the same both over the continents and in the ocean; this adds up to about $2 \text{ mg}\cdot\text{cm}^{-2}$ or 10^{16} g in the whole global layer (Wolbach et al. 1990, 2003). The global precipitation of soot bears witness to global fires and combustion of a large fraction of the biomass of that period; the biomass averaged about $1 \text{ g}\cdot\text{cm}^{-2}$. (The average biomass density is about $0.2 \text{ g}\cdot\text{cm}^{-2}$ in the modern epoch.)

The Chicxulub crater is one of the largest craters discovered on the Earth. Only two of the other craters, Vredefort in South Africa and Sudbury in Canada, have larger diameters. However, both have been formed about two million years ago, in the Proterozoic eon, when fire ignition was impossible. Therefore, it may be suggested that the energy of the Chicxulub impact was above some threshold necessary for ignition of a global fire. Nevertheless, further geological investigations are essential for verification of the hypothesis of global fires at the K/T boundary and connection of these fires with the impact of a cosmic body.

There is no evidence for existence of regional fires after the impacts that created known craters of smaller size. In particular, the Ries crater in Bavaria has been thoroughly studied, but no charcoal has been found in the rock outcrops, quarries,

and vicinities of the crater (Jones and Lim 2000). Not only high temperatures are necessary to set fires, but also the availability of inflammable materials and appropriate conditions for fire development. However, there is one case in which the connection of an impact with fire is well established and studied—the Tunguska impact of 1908 in Central Siberia after which a fire was set in the taiga.

2 FIRE AFTER THE IMPACT OF THE TUNGUSKA METEOROID IN 1908

The fall of the Tunguska cosmic object generated fire over an area that lies within the 2,000 km² area of forest devastation by blast waves. The 200 km² area of initial ignition is in agreement with theoretical models of thermal radiation from the fireball. The fire covered $>\sim 500$ km². Figure 1 shows the region of tree burning at the site of the Tunguska catastrophe (Lvov and Vasilyev 1976). The fire set in this event deserves special attention because these data are unique. Important information is evident from eyewitness reports gathered in the catalog by Vasilyev et al. (1981). The most interesting reports were published earlier by Souslov (1927, 1967). Eyewitnesses who happened to stay about 30 km from ground zero recounted that the fire started simultaneously with the explosion. Dry wood, peat, conifer needles and branches, warehouses, etc. were ignited immediately. The explosion occurred in the morning and the fire began to die out only at night. Some eyewitnesses who lived hundreds of kilometers from the epicenter saw smoke from the fire.

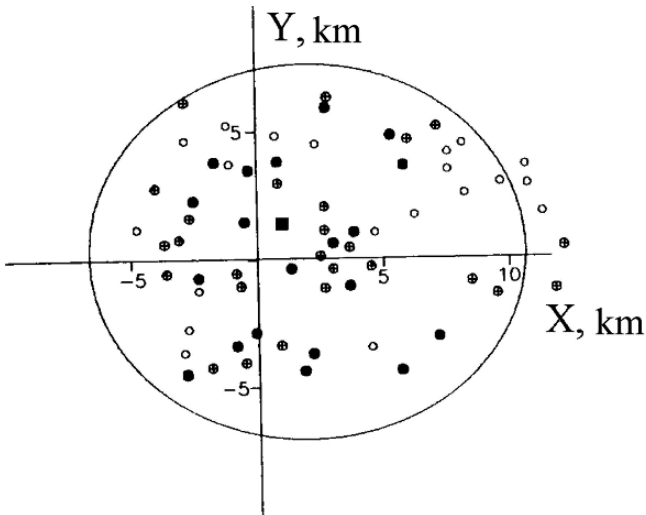


Figure 1. The area of fire generation by thermal radiation from the Tunguska fireball, degree of burning: ○—weak, ⊕—moderate, ●—strong, ■—Kulik's izba (house). Figure is adapted from Adushkin and Nemchinov (1994) and reprinted with the kind permission of the University of Arizona Press

The observational data obtained by the early expeditions of the 1920s and 1930s indicate that a complete burn uniformly covered the trunks of leveled and standing trees for many kilometers, and soils also bore evidence of thermal damage (Astapovich 1933). Although the boundary of an ignition area was not determined, the distance of burn from the epicenter was estimated to be 15–20 km (Kulik 1939, 1976), and >25 km in the southeastern direction (Krinov 1949). Closer examination of the fire of 1908 and several other fires that occurred at the site 150 years before the Tunguska event was not accomplished until the 1960s and 1970s (Berezhnoi and Drapkina 1964; Kurbatsky 1964, 1975; Furyaev, 1975). The area subjected to the 1908 fire has a shape similar to the area of flattened trees and was half its size. The border of the burned area was given by Berezhnoi and Berezhnoi and Drapkina (1964) and has been reprinted in many papers since then (Serra et al. 1994; Vasilyev 1998). The maximum distance of this border from ground zero is about 30 km in the southern direction.

Direct signs of burn from the fireball had already disappeared by the 1960s, but the effects of thermal radiation were studied by thermally affected cambium in the saw cuts of larch tree branches that survived the Tunguska catastrophe (Zenkin and Ilyin 1964; Zhuravlyov 1967; Lvov and Vasilyev 1976; Vorobyov and Demin 1976). It was found that the region of radiation occurrence affected branches as far away as 11–14 km eastward, whereas it extended 8 km to the west, north, and south. This 200 km² area is in general agreement with the theoretical models of fireball radiation (Putiatin 1980; Korobeinikov et al. 1998; Svetsov 1996b). However, the marks of fire have been found farther from the epicenter than the models predict, which suggests that the fire developed beyond the area of initial ignition. Furyaev (1975), using observational data, argued that the forest structure caused propagation of crown fires in the southeastern and northeastern directions, but crown fires in other directions were impossible.

The fire had some specific features that can be summarized as follows (Plekhanov 2000).

1. The fire was ignited over a large area, but was relatively weak, probably due to a high level of ground water at the end of June. Some of the trees at the epicenter survived the catastrophe. The marks of strong fire have been found only on trees that were already dry in 1908.
2. The fire had similar features over a 10–15 km radius area. The same fire marks have been found even on islands surrounded by water or stones. This is evidently a consequence of radiation source location at a height of 5–10 km.
3. The territory was set on fire nonuniformly. Traces of fire were not found at some localities even near the epicenter.

Therefore, the Tunguska fire was not propagated very far from the area of initial ignition. The development of impact-induced fire does not substantially differ from other fires ignited by lightning, for example. A wind generated by the blast shock wave quickly dies down. Crown fires cannot develop within the area of completely flattened trees, but surface and ground fires are not hindered. However, the area of initial ignition by impacts is much larger than in other cases. Fire development

depends on the amount of combustible material, weather, and wind. The weather on 30 June 1908 is very likely to have been fine and quiet. Experiments at the site show that the speed of fire propagation was probably $1\text{--}3\text{ m}\cdot\text{min}^{-1}$ (Kurbatsky 1964). If the wind was stronger, the fire could have covered a larger area. A wildfire could have developed from other conditions.

Tunguska-sized bodies strike the Earth, on the average, once in 300 years (Shoemaker 1983), and probably some of these impactors ignited regional wildfires during the Earth's history. The area of initial ignition depends not only on the impactor size but also on its strength, trajectory, and dispersion of fragments. It is likely that during the Earth's history impacts caused local fires that could have become regional in some cases. However, the rate of fires caused by endogenous factors, not connected with cosmic object impacts, is much higher.

3 DETERMINATION OF HEAT FLUXES ON THE EARTH'S SURFACE—ESTIMATES AND NUMERICAL SIMULATIONS

During the fall of a cosmic object into the atmosphere, air is heated to high temperatures in the shock wave in front of the body. Thermal radiation from the heated air comes to the meteoroid surface and causes melting and vaporization of its material. The meteoroid vapor also gets hot and emits thermal radiation. The radiation from the heated air and vapor in front of the body and in a wake behind it reaches the Earth's surface. The closer the meteoroid comes to the surface, the higher becomes air drag, and a greater amount of energy is released in the atmosphere. The energy release grows both due to the increase in the air density and enlargement of a meteoroid cross-section because of fragmentation. However, if the body has a relatively small size and strongly decelerates, its velocity and air temperature decrease; consequently, the released energy and radiation flux decrease as well. As a result, there is a peak in energy release and radiation. The altitude range of major energy release at the final stage of deceleration typically is relatively narrow; therefore, the process of energy release is similar to explosion. For this reason, energy absorbed by an object located at the Earth's surface may be estimated, as in the case of nuclear tests, in the following way:

$$Q = f \frac{E \cos \alpha}{4\pi r^2} \exp(-r/L), \quad (1)$$

where Q is the energy of thermal radiation coming to the object's surface, E is the explosion energy (meteoroid's kinetic energy), r is the distance from the explosion to the point on the surface, L is the atmospheric visibility, α is the angle between the normal to the irradiated surfaces and the vector directed from the object to the radiation source, and f is the coefficient of explosion energy conversion to that part of thermal radiation that passes through the atmosphere. Typical values of f are from 10 to 30% (Adushkin and Nemchinov 1994; Svetsov 1994; Nemtchinov et al. 1997).

The radiation flux on the surface can be obtained with greater accuracy by calculation of energy release in individual small segments of meteoroid trajectory, using formulas analogous to Equation (1) and integration of the contributions of each segment. The trajectory of a disintegrated meteoroid can be calculated approximately using simple models taking into account the enlargement of a meteoroid cross-section under aerodynamic load (Svetsov et al. 1995). The energy release is determined by drag and heat transfer coefficients. These coefficients, and also f , are functions of altitude, velocity, and size of a body; these variables change during the flight. Special calculations are necessary to obtain exact values of these coefficients. For the Tunguska fall, radiation fluxes on the Earth's surface were calculated in this way (Svetsov 1996a, 1996b, 1998), where the Tunguska cosmic object was treated as a 30-m-radius asteroid that entered the atmosphere with a velocity of $15 \text{ km}\cdot\text{s}^{-1}$ at an angle of 45° to horizon.

Figure 2 shows isolines of energy input to a unit area on the Earth's surface for atmospheric visibilities equal to 40 and 20 km in the assumption that the orientation of an irradiated object provides maximum heat absorption. The value of an energy input necessary for ignition varies from $35 \text{ J}\cdot\text{cm}^{-2}$ for dead leaves to $90 \text{ J}\cdot\text{cm}^{-2}$ for pine needles if the radiation comes from a 20 Mt explosion (Glasstone and Dolan 1977). These values are determined with about 50% accuracy. They strongly depend on moisture content. For a visible tree burn $40\text{--}65 \text{ J}\cdot\text{cm}^{-2}$ is necessary. A 15–20 km radius of tree burning determined by Kulik is in good agreement with the calculated isolines of input energy equal to $65 \text{ J}\cdot\text{cm}^{-2}$ and $35 \text{ J}\cdot\text{cm}^{-2}$ if the visibility is 20–40 km. At a distance of 35 km the light energy per unit area varies from 8 to $13 \text{ J}\cdot\text{cm}^{-2}$ for visibility at 40 km and from 0.8 to $2 \text{ J}\cdot\text{cm}^{-2}$ for visibility at 20 km. This is in reasonable agreement with eyewitness reports.

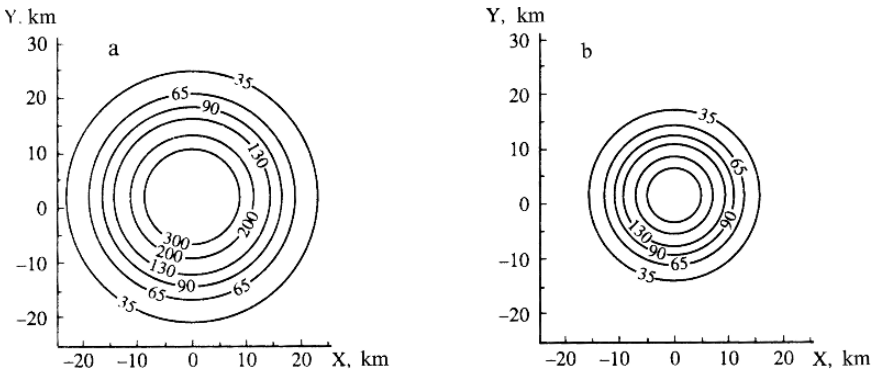


Figure 2. Isolines of radiation energy absorbed by a unit area in $\text{J}\cdot\text{cm}^{-2}$. It is assumed that the irradiated surface is at the sea level and is best oriented to accept the maximum radiation. Results of computations are shown for atmospheric visibility 40 km (a) and 20 km (b). The coordinates start at the epicenter—the Z-axis meets the trajectory at an altitude of 7 km. The Y-axis is a projection of the meteoroid trajectory to the Earth's surface. The figure is adapted from Svetsov (1996b) and reprinted with the kind permission of the Nature Publishing Group

The calculations of thermal effects produced by the Tunguska meteoroid on the Earth's surface were carried out by Korobeinikov et al. (1982, 1991) in which the energy release was approximated as a combination of spherical and cylindrical explosions. The obtained size of the tree burn and ignition area was noticeably smaller despite the fact that light absorption and dispersion in the atmosphere were neglected: isolines 69 and 34 J·cm⁻² confined areas with radial dimensions 7.5–12.5 and 12.5–19 km, respectively. Probably, this results from the smaller energy explosion assumed by the authors; the calculated energy of radiation emitted by the fireball was also smaller, only 12%.

A shock wave can quench a fire if it falls on the place after ignition. Estimates show that in the Tunguska event the shock wave likely extinguished the fire beyond a 10-km radius area (Svetsov 1996a). Inside this area the radiation impulse lasted longer than the time of a shock passage, and if the shock put out the fire there, ignition arose again. Fire generation depends not only on the absorbed energy and time of a light impulse. Grishin and Perminov (1993) studied the process of forest ignition in detail by numerical solution of equations for multiphase multicomponent reactive media.

If a body enters the atmosphere at a very small angle and moves almost horizontally (grazing impact), it can ignite fire in a very long strip on the surface. Such cases were considered in the work of Svetsov (2002) with the use of simplified approaches. However, such situations are very rare. Estimates show that only several grazing impacts of bodies with sizes about 1 km might have occurred during the Phanerozoic epoch. During fine weather these impacts could ignite forests or other inflammable materials (if they existed) covering areas from 1 to 2 million km². The length of the area of fire ignition could range from 1,000 to 3,000 km. With favorable conditions this area of ignition could develop into a wildfire on a continental scale.

If the body is sufficiently large and reaches the Earth's surface, the major part of its energy is released during the surface impact. Vapors of an impactor and a target heated to high temperatures are ejected from a crater upward with high velocities. The vapors and heated air radiate light and heat objects located at significant distances from the impact site. Nemchinov and Svetsov (1991) considered the impact of a comet about 1 km in diameter. Assuming that vapor energies are $2 \cdot 10^{19}$ J (5 Gt TNT) and $2 \cdot 10^{21}$ J (500 Gt), they calculated expansion and radiation of initially spherical vapor volume using a sector approximation (in which an axially symmetrical problem is replaced by a number of one-dimensional problems). They found that intense radiation occurs when an average height of a source (which represents a volume of heated vapor and air) is 15 km for initial vapor energy 5 Gt and 100 km for 500 Gt. In these cases ignition can arise at the distances of direct visibility of a radiation source (to horizon): 440 km from the impact site for 5 Gt and 1,100 km for 500 Gt.

More accurate calculations of gas motion after impacts include numerical solutions of gas dynamic and radiation transfer equations. Nemchinov et al. (1993) made numerical simulations of the impact on the Earth of an icy body with a diameter of 200 m, velocity 50 km·s⁻¹, and kinetic energy equivalent to 1.2 Gt

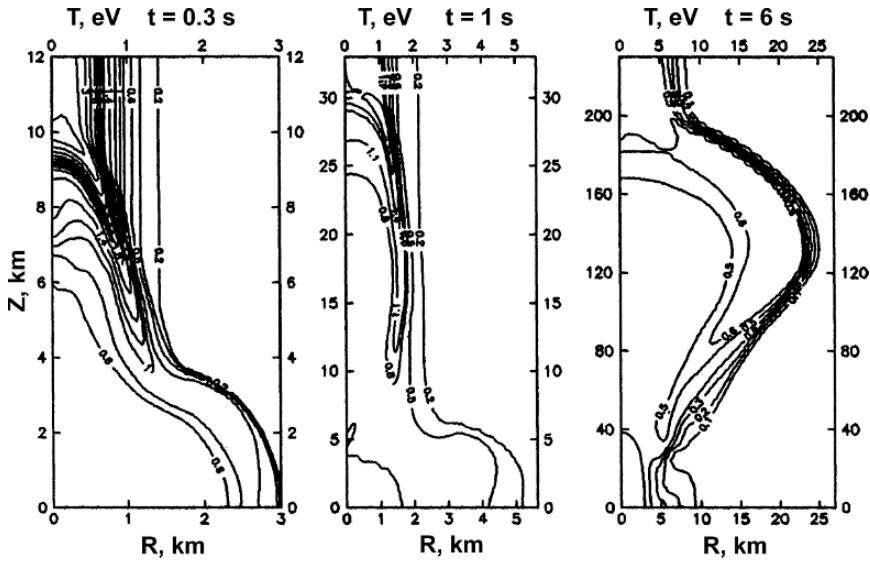


Figure 3. Isotherms in the atmosphere after the vertical impact of a 200-m-diameter body with velocity $50 \text{ km}\cdot\text{s}^{-1}$. The figure is adapted from Adushkin and Nemchinov (1994) and reprinted with the kind permission of the University of Arizona Press

TNT. The results are shown in Fig. 3, in which temperature profiles are plotted for several times. The variation of atmospheric density with altitude and a wake formed during the flight of a body through the atmosphere were taken into account in these calculations.

The speed of a shock wave moving upward along the wake enlarges with altitude and becomes $>40 \text{ km}\cdot\text{s}^{-1}$ in 1 s after the impact. However, the gas in the wake in front of the shock wave also expands upward with relatively high velocities and reduces the amplitude of the shock wave. The thermal radiation transfer also leads to temperature reduction so that the maximum temperatures behind the shock wave are about 2 eV. This is higher than the maximum temperature of a gas near the surface at the same time. The heated gas at high altitudes becomes semitransparent because of both the expansion and the decrease of density of the ambient air. Therefore, the radiation becomes more efficient than in the lower atmospheric layers. However, the wake changes the shape of a fireball so that it becomes elongated rather than spherical. The thermal radiation flux on the Earth's surface shown in Fig. 4 was calculated assuming that the atmospheric visibility was absolute. In 1 s the heat radiation flux exceeds $100 \text{ W}\cdot\text{cm}^{-2}$ at a distance of $\sim 100 \text{ km}$, and in 2.5 s the flux exceeds $200 \text{ W}\cdot\text{cm}^{-2}$.

Shuvalov (2002) numerically modeled a vertical impact of a large 10-km-diameter body commensurate with the Chicxulub crater, including the stages of fall in the atmosphere, crater formation, plume rise, and heat action on the Earth's surface.

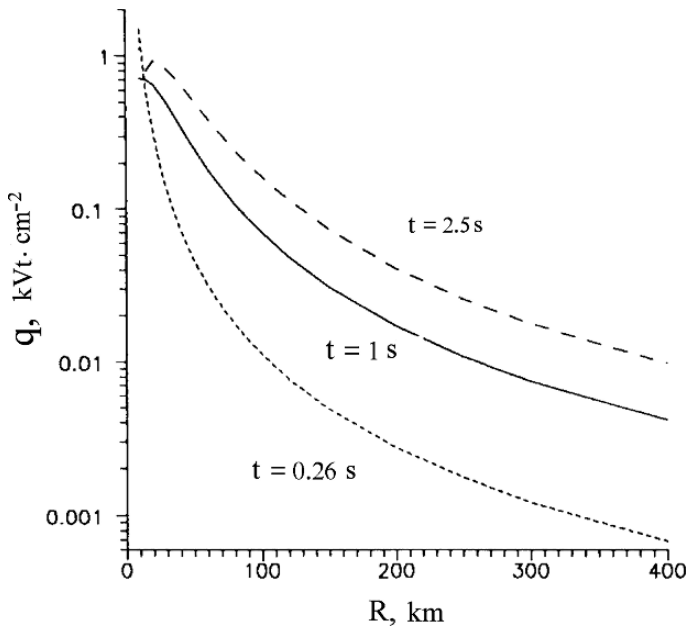


Figure 4. Radiation flux on the Earth's surface as a function of a distance from the site of the impact of a 200-m-diameter icy body with velocity $50 \text{ km}\cdot\text{s}^{-1}$. The figure is adapted from Adushkin and Nemchinov (1994) and reprinted with the kind permission of the University of Arizona Press

The impact velocity was $20 \text{ km}\cdot\text{s}^{-1}$. The equations of gas dynamics were solved numerically and plume cooling was taken into account using the approximation of optically thin volume. Radiation fluxes on the Earth's surface were obtained from the numerical solution of the equation of radiation transfer at separate moments of time. Almost all radiation that comes to the object is emitted by the plume in the infrared range except for a short radiation peak at the beginning of the impact. The spectrum maximum is in the range $0.5\text{--}0.7 \text{ eV}$. This is caused by the fact that condensed material emits a major portion of light. As the calculations show, fire ignition could start at distances from 2,000 to 3,000 km from the impact site. If the impactor size is two times smaller or two times larger, this distance is diminished to 1,500 km or enlarges to 4,000 km, respectively. These distances only insignificantly depend on the impact angle to horizon if it is above 30° .

The direct radiation from the plume after the impact of a 10-km-diameter asteroid can ignite inflammable materials inside the area, which constitutes only 3–5% of the total Earth's surface. This is the maximum value because in the case of the Chicxulub the area of probable ignition was partly covered by sea. Therefore, direct thermal radiation could not cause global fire. However, earlier another mechanism of fire ignition over the whole planet was suggested; this is radiation of high-velocity ejecta from the crater when the ejecta "reaccrete"; that is, enter the atmosphere after

a flight along ballistic trajectories over the Earth (Melosh et al. 1990; Zahnle 1990). It is assumed that the ejecta consists of particles and condensate (with sizes of the order of millimeters and smaller, down to microns) and behaves as a multitude of tiny meteoroids burned in the atmosphere at altitudes ~ 70 km. Estimates of the mass of fallen material based on iridium and spherules (this mass proved to be $1 \text{ g}\cdot\text{cm}^{-2}$) show that the total mass of micrometeoroids was equal to a $5\cdot 10^{18}$ g. Calculations based on a simple model (expansion of a hemispherical volume of particles along ballistic trajectories) show that this mechanism gives a radiation flux that is 50–150 times higher than the solar flux during 1 to several hours. This could cause ignition over the whole planet, or at least strongly act upon living organisms. The estimated flux on the Earth's surface was near the lowest limit. However, it is the authors' opinion that, due to the fluctuations that inevitably existed, fire ignition had to arise with certainty in some places or over the whole Earth. However, the calculations of Shuvalov (2002) show that the mass of ejecta with velocities $>5 \text{ km}\cdot\text{s}^{-1}$ is only a several-percent fraction of the asteroid mass. However, Melosh et al. (1990) believed that this mass is several times greater than the mass of a 10-km-diameter asteroid, which is almost two orders of magnitude greater than the mass obtained in the calculations. It is probable that the asteroid size was larger, about 15–20 km; the impact velocity could also be higher, then the mass of high-velocity ejecta would be significantly greater.

In the relatively simple model of Melosh et al. (1990), the energy of micrometeoroid radiation per unit area depends only on the distance from the impact site. A more realistic model, including the same mechanism of ignition by return of high-velocity ejecta to the atmosphere, was developed in the work of Kring and Durda (2002). This model takes into account the velocity distribution of ejecta particles, the Earth's rotation, and the impact angle. The calculations of radiation fluxes were made for various places on the Earth. In the calculations the mass of high-velocity ejecta varied from 10^{19} g to $2.5\cdot 10^{19}$ g, and the velocity distribution of particles also varied. According to the calculations in this model, about 12% of high-velocity ejecta return to the atmosphere in 2 hours, 55% return no later than in 5 hours, and 85% in 72 hours. About 12% escape from the gravitational field and are lost.

The fallen mass and energy of micrometeoroid radiation (which depends both on the mass and velocity) were found to be distributed over the Earth's surface very nonuniformly. The maximum energy comes to the surface around the impact site, where the direct radiation from the plume is high enough for ignition anyway, and in the area around the antipodal point, which included proto-India and the proto-Indian Ocean 65 million years ago. Nevertheless, the energy input to the surface pulsates—during 3 days three maximums with fading amplitudes were obtained at the antipodal point. It was assumed that the threshold irradiance level necessary for ignition at the surface is $>12.5 \text{ kW}\cdot\text{m}^{-2}$ during 20 minutes. It was found that in both regions, at the impact site and at the antipode, ignition is independent of the velocity distribution of particles, although in other regions of the Earth these distributions played an important role.

As calculated, after a vertical impact fires could be generated in the southern part of North America, southern Africa, India, southern Asia, Australia, and partly in Antarctica. Fires could not arise in Europe. If the meteoroid flew from the northwest and debris was ejected to the southwest of Chicxulub, then fires could have been ignited throughout the equatorial region and the Southern Hemisphere, whereas the Northern Hemisphere would have been left unscathed. These consequences do not depend strongly on the velocity distribution in the expanding vapor plume, although different directions of impacts generate ignition in some parts of the continents and leave other parts free of fire. The direction of the impact that created the Chicxulub is unknown; to determine if ignition occurred in some other place on the Earth, thorough search and study of charcoal at the K/T boundary are necessary. (Soot is insufficient because it could spread over the whole planet even if not all the continents were on fire.)

The threshold irradiance levels for ignition due to the reaccretion of high-velocity ejecta from craters were approximately calculated recently in the work of Durda and Kring (2004). According to their estimates, the threshold ejected plume masses for continent-wide and global fires are 10^{15} and 10^{16} kg, respectively. Global fires with spontaneous ignition of wood are generated after impacts that create craters with final diameters larger than 175–185 km. The continental fires arise if the crater diameters are >105 –145 km. If fires are generated by ignition of foliage, rotten wood, or forest litter, the threshold diameters of final craters diminish to 135–145 km and 85–115 km for global and continental-scale fires, respectively. Impacts in equatorial regions produce fires that are generally limited to the tropics. Impacts in middle latitudes generally produce fires in both the Northern and Southern Hemispheres.

4 LAMB WAVE UPROOTS TREES

It is difficult to set fire to living vegetation. For this reason some hypotheses, distinct from direct ignition by thermal radiation, were suggested to explain the global fire after the Chicxulub impact. It was proposed that trees perished everywhere first and, when a large amount of dry wood was formed, large-scale spreading fires occurred under the action of lightning or other causes (Argyle 1986; Shuvalov 2002). This hypothesis is confirmed by geochemical studies (Jones and Lim 2000), which showed that charcoal was formed in many cases during the burning of already-dead trees. However, the causes of the mass extinction of trees remain unclear. The dust content of the atmosphere was insufficient for the termination of photosynthesis and the extinction of plants (Pope 2002), although a harmful effect on trees could have been created by acid rains (Toon et al. 1997), sulfur aerosols (Pope et al. 1997), emission of toxic gases (Gerasimov 2002), and cooling or other changes in natural conditions. However, it can be suggested that trees on the planet were felled by the intense atmospheric wave induced by an impact.

Kring et al. (2005) estimated that at the impact site and also at the antipodal point (where the atmosphere is heated due to the fall of high-energy crater ejecta)

wind velocities can be as high as 25–50 m·s⁻¹. However, atmospheric acoustic gravity waves can pass the whole Earth's surface. Acoustic gravity waves were repeatedly recorded during volcanic eruptions (Krakatau in 1883), the fall of cosmic objects (including the famous Tunguska meteoroid of 1908), and nuclear explosions with energies up to 2·10¹⁷ J. At distances of thousands of kilometers from these powerful sources of energy, however, atmospheric waves were not so strong as to have a marked effect on the environment, at least on the Earth's surface. The energy released into the atmosphere during impacts of large asteroids and comets onto the Earth can be significantly greater, and such impacts can induce significantly stronger acoustic gravity waves, which can propagate over the Earth's surface as Lamb waves.

The processes of formation and propagation of acoustic gravity waves after the impact of an asteroid commensurate with the size of the Chicxulub crater were studied. The energy of the impact of a cosmic object can be evaluated from the size of the transitional crater by using similarity relations (Schmidt and Housen 1987). Assuming that the diameter of the transitional crater is 100 km (Morgan et al. 1997), one finds that the diameter of the asteroid forming this crater must be ~15 km at a typical velocity of the impact of 15 km·s⁻¹ if the impact is vertical. The kinetic energy of such an object is 5·10²³ J or 3·10⁷ Mt in TNT equivalent.

For the initial data of the problem, take the disturbance of the specific internal energy in the following form:

$$e(r, z) = e_0 \frac{\rho(z)}{\rho_0} \exp\left(-\frac{r^2}{r_0^2}\right), \quad (2)$$

where r is the distance from the point of impact along the Earth's surface, z is the altitude, $\rho(z)$ is the density of the undisturbed atmosphere, ρ_0 is the density at the zero altitude, and r_0 is the horizontal radius of the region of energy release. The values $r = 0$ and $z = 0$ correspond to the point of impact. The constant e_0 is chosen so that the total energy released into the atmosphere amounts to a certain portion α of the asteroid's energy. For an isothermal atmosphere:

$$e_0 = 2\alpha E / (Hr_0^2 \rho_0 \pi^{3/2}), \quad (3)$$

where H is the characteristic height of the uniform atmosphere. When the initial data are chosen in Equation (2), it is suggested that a larger portion of energy is released in denser air layers and heating decreases exponentially with the distance from the point of impact. Disturbances in the density of the atmosphere and its motion were disregarded at the initial time. The second-order accurate numerical code SOVA was used for calculations (Shuvalov et al. 1999; Shuvalov 1999). This code was modified for a spherical geometry of the problem. Several versions of the problem were calculated: for three values of the asteroid's released energy $\alpha = 2.5$, 5, and 10%, and three values of the scale $r_0 = 500$, 1,000, and 2,000 km.

Consider the results of a numerical simulation obtained for the version $\alpha = 5\%$ and $r_0 = 1,000$ km. Under the effect of the pressure gradients caused by heating in

the region of energy release, the air starts to move from the impact point along the Earth's surface and upward. The upward motion leads rather quickly to the ejection of a certain amount of gas to altitudes >100 km and then this gas falls from above onto the atmosphere. In ~ 1 h an internal wave is formed, which propagates from the impact point along the Earth's surface in the lower atmosphere. This is a Lamb wave. In ~ 5 h, the disturbances caused by waves propagating with a higher velocity in the middle atmosphere reach the Earth's surface in the vicinity of the antipodal point. However, these disturbances do not cause significant motions in the lower atmosphere ahead of the front of the Lamb wave moving along the surface. Amplitudes of the waves at the Earth's surface are shown in Fig. 5. The maximum mass velocity in the wave propagating from the site of initial disturbance is $65 \text{ m}\cdot\text{s}^{-1}$ at the moment of time 1 h and decreases to $30 \text{ m}\cdot\text{s}^{-1}$ at the moment of time 10 h. The propagation velocity of the Lamb wave differs insignificantly from the speed of sound. Within the time interval from 1 to 7 h, the maximum pressure point moves with a speed somewhat greater than the speed of sound. Although the front of the wave is rather narrow and looks like a shock wave, this front is not a discontinuity but occupies tens of calculation points and does not narrow with time. The velocity of the wave decreases when it travels a distance of half the meridian, and the wave velocity becomes $<300 \text{ m}\cdot\text{s}^{-1}$ by 10 h. Further, this internal wave decays.

The altitude behavior of the horizontal air velocity is shown in Fig. 6. (The magnitudes of vertical velocities are much lower than those of horizontal velocities.) Up to an altitude of 15 km, the positive mass velocity behind the wave front increases slightly with altitude, and the wave velocity is independent of altitude. At altitudes of 20–25 km, the velocities increase gradually, so that at altitudes >30 km waves propagate with significantly higher velocities. The kinetic energy of waves is concentrated in an altitude range from 0 to 60 km. The volume density of atmospheric kinetic energy as a function of altitude has a maximum near the Earth's surface, then decreases to an altitude of about 15 km because of a decrease in the gas density, and further increases owing to increasing velocities, and has one more maximum at an altitude of ~ 40 km, where its values are only slightly smaller than those near the surface.

This study is primarily interested in the amplitudes of internal waves near the surface. As is well known, if the wind speed is $>20 \text{ m}\cdot\text{s}^{-1}$, branches break from trees, whereas at wind speeds $>25\text{--}30 \text{ m}\cdot\text{s}^{-1}$ (severe storms and hurricanes), trees break and are uprooted. Figure 5 shows that gas speeds no less than $30 \text{ m}\cdot\text{s}^{-1}$ are reached over the whole Earth's surface. Waves with a negative gas velocity are less subject to dispersion (Kshevetskii 1998).

For that reason, despite the decay and amplitude decrease of waves with a positive gas velocity, the maxima of the magnitudes of negative velocities are $>30 \text{ m}\cdot\text{s}^{-1}$ in the range of distances $>13,000$ km. In about 16 h, a packet of internal waves propagating along the surface reaches the antipodal point. After reflection, the wave amplitudes turn out to be sufficiently large. However, their real values may differ from the calculated amplitudes, because the given idealized statement of the problem disregards a number of factors violating its axial symmetry (e.g., the asymmetry of

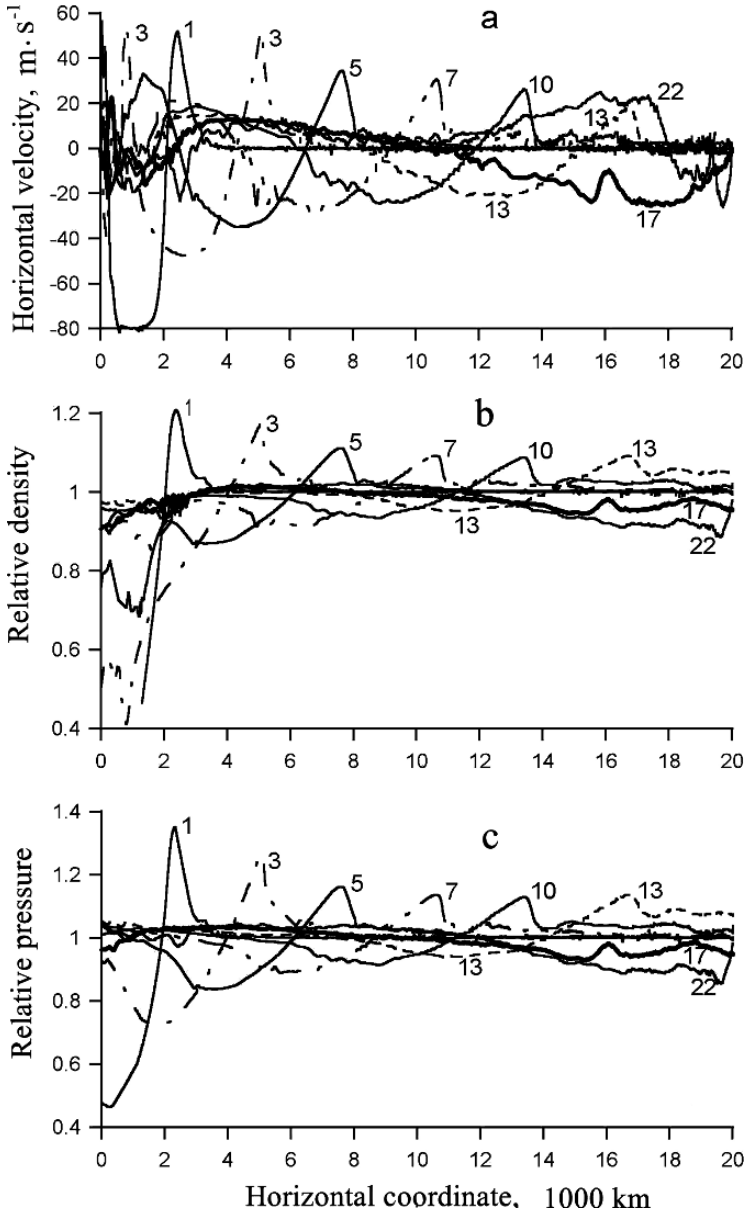


Figure 5. Gas dynamical parameters at the Earth's surface as functions of distance from the impact site. Times in hours are indicated at the curves. *a*—horizontal velocity, *b* and *c*—density and pressure divided by their normal values in the undisturbed atmosphere. The figure is adapted from Svetsov and Shuvalov (2005) and reprinted with the kind permission of Pleiades Publishing Inc.

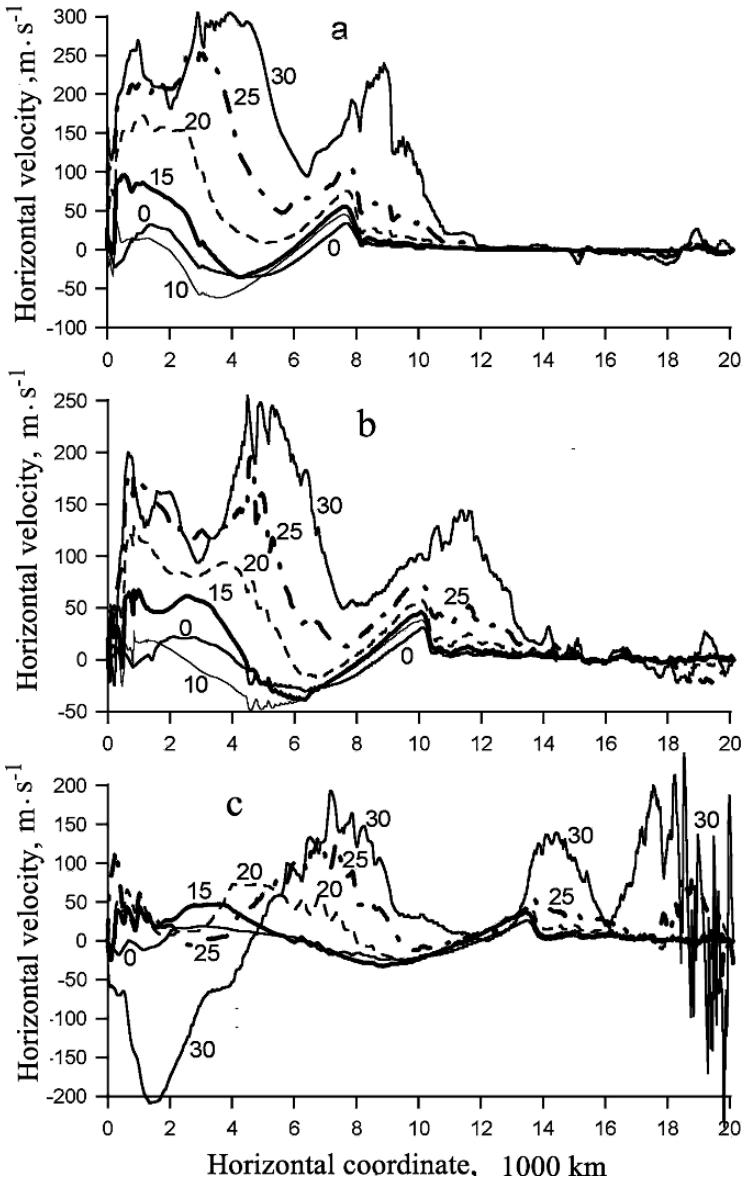


Figure 6. Horizontal components of velocity for altitudes from 0 to 30 km at times 5 hours (a) 7 hours (b) and 10 hours (c). Altitudes in km are indicated at the curves. The figure is adapted from Svetsov and Shuvalov (2005) and reprinted with the kind permission of Pleiades Publishing Inc.

initial energy release during an oblique impact, natural wind, or atmospheric rotation). The total kinetic energy of the atmosphere increases to 3 h and decreases further because of the collision and damping of acoustic gravity waves propagating >30 km. After 16 h from the start of the energy release, the kinetic energy begins to decrease owing to the damping of internal waves propagating near the surface. Atmospheric oscillations and the propagation of smaller-amplitude waves continue for ~ 100 h.

Consider how a change in the initial data affects the results. If $\alpha = 10\%$, then the maximum air velocities at all the points of the Earth's surface reach $45 \text{ m}\cdot\text{s}^{-1}$ or more. If $\alpha = 2.5\%$, then the maximum air velocities amount to about $25\text{--}30 \text{ m}\cdot\text{s}^{-1}$, which corresponds to a storm wind. As the scale r_0 increases, the velocities near the Earth increase. At $r_0 = 2,000$ km, the maximum gas velocities are $>35 \text{ m}\cdot\text{s}^{-1}$ everywhere, whereas at $r_0 = 500$ km, these velocities in the hemisphere opposite to the impact site are no greater than $20 \text{ m}\cdot\text{s}^{-1}$, which is insufficient to fell trees. The decrease in wave amplitudes with increasing concentration of initial energy is due to the fact that, if the concentration is high, a large portion of energy is transferred to waves propagating in the middle atmosphere. For example, at $r_0 = 500$ km, the maximum density of kinetic energy turns out to be at altitudes of $70\text{--}80$ km.

To summarize, when an energy of $0.5\cdot 10^7$ Mt TNT or higher is released in the lower atmosphere on a characteristic horizontal scale of $1,000$ km or larger, a packet of internal gravity waves propagating near the Earth's surface with an air-particle velocity behind the front of $>30 \text{ m}\cdot\text{s}^{-1}$ arises. Such velocities can lead to a significant felling of trees and breaking of their branches over the entire globe. Such an energy release is very likely to occur after the fall of an asteroid with a diameter of 15 km and a typical velocity of $15 \text{ km}\cdot\text{s}^{-1}$ onto the Earth. The size of the object appears to be critical because the fall of smaller objects could not lead to the formation of sufficiently strong internal waves because of both smaller impact energy and smaller scales of the region of initial energy release in the lower atmosphere. The rise in the atmospheric temperature that occurred after the impact of a large cosmic object as a result of both energy transfer by internal waves and high-velocity emissions from the crater into the atmosphere could be responsible by itself for a pulsed violation of global circulation of the atmosphere, intense circulation motions of the atmosphere, and hurricanes persisting for a rather long period of time. In the framework of the impact hypothesis of the global catastrophe at the Cretaceous-Tertiary boundary the global fires can be explained by emergence of a great amount of dead wood due to tree felling by strong internal waves after the impact. Fire ignition could arise afterward due to natural causes, for example, lightning. These atmospheric waves blowing places of initial ignition could increase fires; also they could cause direct injuries to animals, most of all to taller tetrapods.

5 CONCLUSIONS

When cosmic bodies collide with the Earth, thermal radiation emitted by heated air and vapor can generate fire in the vicinity of an impact site. The radius of a region where ignition is possible varies from about 30 km if the meteoroid diameter is

100 m, to 3,000 km if the diameter is 10 km. If the diameter of a body is >15 km, the mechanism of ignition by return of high-velocity ejecta to the atmosphere comes into force. This cardinally enlarges the area of ignition. On the other hand, if the striking body is so large, strong Lamb waves blow the fire set by radiation and break trees, which creates a great amount of dry wood. Thus, an impactor ~15 km in size is the threshold for the generation of global wildfires.

Regional fires that can be caused by the impacts of objects ~1 km in size differ little in essence from standard regional fires; however, they are generated simultaneously over the whole area, which enhances the hazard of damage to people and animals from thermal radiation and suffocation.

Fire generation depends on circumstances that must be favorable for fire development, and coincidence of these circumstances with an impact may be rare. This leads some researchers to believe that the impacts of cosmic objects are not related to fires (Jones and Lim 2000; Jones 2002). This point of view causes quite natural objections based on theoretical estimates and the evidence of forest fire after the Tunguska impact in 1908 (Svetsov 2002). Numerical simulations of thermal effects and highly probable traces of a global fire at the K/T boundary give reasonable arguments for impact-generated fires to be treated as hazardous for humanity. This hazard should be also taken into account in the development of methods for prevention of asteroidal and cometary threat. For example, Artemieva et al. (1997) have shown that the area of thermal damage can become several times larger if a 100-m-diameter meteoroid is broken into fragments but not dispersed over an area >10⁴ m².

There is a general agreement that the problem of fires generated by impacts deserves further theoretical and field, and geological and geochemical investigation, taking into account natural conditions, vegetation species, climate, and weather.

REFERENCES

- Adushkin VV, Nemchinov IV (1994) Consequences of impacts of cosmic bodies on the surface of the Earth. In: Gehrels T (ed) Hazards due to comets and asteroids, University Arizona Press, Tucson, pp 721–778
- Alvarez LW, Alvarez W, Asaro F, Michel HV (1980) Extraterrestrial cause for the Cretaceous-Tertiary extinction. *Science* 208(4448):1095–1108
- Anders E, Wolbach WS, Gilmour I (1991) Major wildfires of the cretaceous/tertiary boundary. In: Levine JS (ed) Global biomass burning. MIT Press, Cambridge, MA, pp 485–492
- Anders E, Wolbach WS, Lewis RS (1986) Cretaceous extinctions and wildfires. *Science* 234:261–264
- Argyle E (1986) Cretaceous extinctions and wildfires. *Science* 234(4774):261
- Artemieva NA, Svetsov VV, Shuvalov VV (1997) An estimate of consequences of the fall of disrupted cosmic object on the Earth. In: Geophysics of strong disturbances. IDG RAS, Moscow, pp 215–226 (in Russian)
- Astapovich IS (1933) Fresh material on the flight of the great meteorite of 30 June 1908 in Central Siberia. *Astronomicheskij Zhurnal* 10:465–486 (in Russian)
- Berezhnoi VG, Drapkina GI (1964) A study of anomalous forest growth at the Tunguska meteorite fall area. *Meteoritika* 24:162–169. Nauka Publishers, Moscow (in Russian)
- Durda DD, Kring DA (2004) Ignition threshold for impact-generated fires. *J Geophys Res* 109:E08004, doi: 10.1029/2004JE002279

- Farley KA, Montanary A, Shoemaker EM, Shoemaker CS (1998) Geochemical evidence for a comet shower in the Late Eocene. *Science* 280:1250–1253
- Furyaev VV (1975) Forest fires in the Tunguska meteorite fall area and their effect on forest formation. In: Sobolev VS (ed) *Problemy Meteoritiki*. Nauka, Novosibirsk, pp 72–87 (in Russian)
- Gerasimov MV (2002) Toxins produced by meteorite impacts and their possible role in a biotic mass extinction. In: Koeberl C, MacLeod KG (eds) *Catastrophic events and mass extinctions: impacts and beyond*. Geological Society of America Special Paper 356, Boulder, CO, pp 705–716
- Gilmour I, Wolbach WS, Anders E (1990) Major wildfires at the Cretaceous/Tertiary boundary. *Catastrophes and evolution*. In: Clube SVM (ed) *Astronomical foundations*. Cambridge University Press, Cambridge, MA, pp 195–213
- Glass BP, Koeberl C (1999) Ocean Drilling Project Hole 689B spherules and upper Eocene microtektite and clinopiroxene-bearing spherule strewn fields. *Meteoritics and Planetary Sci* 34:197–208
- Glasstone S, Dolan PJ (1977) *The effects of nuclear weapons*. US department of defense and US Department of Energy, US Government Printing Office, Washington, DC, p 653
- Grishin AM, Perminov VA (1993) On the forest-tract firing caused by the Tunguska meteorite explosion. *Fiz Goreniya Vzryva* 29(6):8–14
- Herring JR (1985) Charcoal fluxes into sediments of the north Pacific Ocean: the Cenozoic record of burning. In: Sundquist ET, Broecker WS (eds) *The carbon cycle and atmospheric CO₂: natural variations Archen to present*. American Geophysical Union, Washington, DC, pp 419–442
- Heymann D, Yancey TE, Wolbach WS et al (1998) Geochemical markers of the Cretaceous-Tertiary boundary event at Brasos River, Texas, USA. *Geochim Cosmochim Acta* 62:173–181
- Jones TP (2002) Reply “Extraterrestrial impacts and wildfires.” *Palaeogeogr Palaeoclimatol Palaeoecol* 185:407–408
- Jones TP, Lim B (2000) Extraterrestrial impacts and wildfires. *Palaeogeogr Palaeoclimatol Palaeoecol* 164(1–4):57–66
- Korobeinikov VP, Chushkin PI, Shurshalov LV (1982) Interaction between large cosmic bodies and atmosphere. *Acta Astronom* 10(10):641–643
- Korobeinikov VP, Chushkin PI, Shurshalov LV (1991) Combined simulation of the flight and explosion of a meteoroid in the atmosphere. *Solar System Res* 25(3):242–254
- Korobeinikov VP, Shurshalov LV, Vlasov VI, Semenov IV (1998) Complex modelling of the Tunguska Catastrophe. *Planet Space Sci.* 46(2/3): 231–244.
- Kring DA, Durda DD (2002) Trajectories and distribution of material ejected from the Chicxulub impact crater: Implications for postimpact wildfires. *J Geophys Res* 107 (E6), 10.1029/2001JE001532
- Kring DA, Showman AP, Durda DD (2005) Global winds and aerosol updrafts created by the Chicxulub impact event. *Lunar Planet Sci XXXVI*. LPSI, Houston, #1544
- Krinov EL (1949) *The Tunguska Mmeteorite*. Akademiya Nauk SSSR, Moscow, Leningrad (in Russian)
- Kshevetskii SP (1998) Comparison between an analytic model of nonlinear internal waves and the results of numerical experiments. *Izv Atmos Ocean Phys* 34:282–290
- Kulik LA (1939) Data on the Tunguska meteorite up to 1939. *Dokl Akad Nauk SSSR* 22:520–524 (in Russian)
- Kulik LA (1976) The pattern of tree flattening and burn in the Tunguska meteorite fall area. In: Vasilyev NV (ed) *Voprosy Meteoritiki*. Tomsk University Press, Tomsk, pp 15–19 (in Russian)
- Kurbatsky NP (1964) On the forest fire in the 1908 Tunguska fall area. *Meteoritika* 25:168–172, Nauka Publishers. Moscow (in Russian)
- Kurbatsky NP (1975) On the forest fire ignition in the Tunguska meteorite fall area. In: Sobolev VS (ed) *Problemy Meteoritiki*. Nauka, Novosibirsk, pp 69–71 (in Russian)
- Lvov Yu A, Vasilyev NV (1976) Radiation burn of trees in the Tunguska meteorite fall area. In: Vasilyev NV (ed) *Voprosy Meteoritiki* Tomsk University Press, Tomsk, pp 53–57 (in Russian)
- Melosh HJ, Schneider NM, Zahnle KJ, Latham D (1990) Ignition of global wildfires at the Cretaceous/Tertiary boundary. *Nature* 343:251–254
- Morgan JV, Warner MR, Chicxulub Working Group et al (1997) Size and morphology of the Chicxulub impact crater. *Nature* 390(6659):472–476

- Nemchinov IV, Svetsov VV (1991) Global consequences of radiation impulse caused by comet impact. *Adv Space Res* 11(6):(6)95–(6)97
- Nemchinov IV, Popova M, Shubadeeva L et al (1993) Effects of hydrodynamics and thermal radiation in the atmosphere after comet impacts. *Lunar Planet Sci Conf XXIV*. Houston, pp 1067–1068
- Nemchinov IV, Svetsov VV, Kosarev IB et al (1997) Assessment of kinetic energy of meteoroids detected by satellite-based light sensors. *Icarus* 130(2):259–274
- Plekhanov GF (2000) Thoughts about the Nature of the Tunguska Meteorite. Tomsk University Press, Tomsk (in Russian)
- Pope KO (2002) Impact dust not a cause of the Cretaceous-Tertiary mass extinction. *Geology* 30(2): 99–102
- Pope KO, Baines KH, Ocampo AC, Ivanov BA (1997) Energy, volatile production, and climatic effects of the Chicxulub Cretaceous/Tertiary impact. *J Geophys Res* 102(E9):21645–21664
- Putiatin BV (1980) The radiation action on the Earth during the large meteoritic body flight in the atmosphere. *Dokl Akad Nauk SSSR* 252(2):318–320
- Sanfilippo A, Riedel WR, Glass BP, KYTE FT (1985) Late Eocene microtektites and radiolarian extinctions on Barbados. *Nature* 314:613–615
- Schmidt RM, Housen KR (1987) Some recent advances in the scaling of impact and explosion cratering. *Int J Impact Engng* 5:543–560
- Scott AC (2000) The pre-Quaternary history of fire. *Palaeogeogr Palaeoclimatol Palaeoecol* 164:281–389
- Scott AC, Lomax BH, Collinson ME (2000) Fire across the K/T boundary: initial results from the Sugarite coal, New Mexico, USA. *Palaeogeogr Palaeoclimatol Palaeoecol* 164:381–395
- Serra R, Cecchini S, Galli M, Longo G (1994) Experimental hints on the fragmentation of the Tunguska cosmic body. *Planet Space Sci* 42:777–783
- Shoemaker EM (1983) Asteroid and comet bombardment of the Earth. *Ann Rev Earth Planet Sci* 11:461–494
- Shuvalov VV (1999) Multi-dimensional hydrodynamic code SOVA for interfacial flows: application to thermal layer effect. *Shock Waves* 9(6):381–390
- Shuvalov VV (2002) Radiation effect of the Chicxulub impact event. In: Buffetaut E, Koeberl C (eds) *Geological and biological effects of impact events*. Springer-Verlag, Berlin, pp 237–247
- Shuvalov VV, Artem'eva NA, Kosarev IB (1999) 3D hydrodynamic code SOVA for multimaterial flows, application to Shoemaker-Levy 9 Comet impact problem. *Intern J Impact Engng* 23(1):847–858
- Souslov IM (1927) The search for the great meteorite of 1908. *Mirovedenie* 16:13–18 (in Russian)
- Souslov IM (1967) The interrogation of Tunguska catastrophe eyewitnesses in 1926. In: Plekhanov GF (ed) *Problema Tungusskogo Meteorita*. Iss 2 Tomsk University Press, Tomsk, pp 21–30 (in Russian)
- Svetsov VV (1994) Explosions in the lower and middle atmosphere: Spherically symmetric stage. *Fiz Gorennya Vzryva* 30(5):697–707
- Svetsov VV (1996a) Where have the debris of the Tunguska meteoroid gone? *Solar System Res* 30(5):378–390
- Svetsov VV (1996b) Total ablation of the debris from the 1908 Tunguska explosion. *Nature* 383(6602):697–699
- Svetsov VV (1998) Could the Tunguska debris survive the terminal flare? *Planet Space Sci* 46(2/3): 261–268
- Svetsov VV (2002) Grazing meteoroids could ignite continental-scale fires. In: Koeberl C, MacLeod KG (eds) *Catastrophic events and mass extinctions: impacts and beyond*. Geological Society of America Special Paper 356, Boulder, CO, pp 685–694
- Svetsov VV, Shuvalov VV (2005) Strong acoustic gravity waves from impacts of large cosmic objects. *Izvestia, Atmos Ocean Phys* 41(5):545–554
- Svetsov VV, Nemchinov IV, Teterev AV (1995) Disintegration of large meteoroids in Earth's atmosphere: theoretical models. *Icarus* 116:131–153. Errata: *Icarus*. 1996 120(2):443
- Toon OB, Zahnle K, Morrison D et al (1997) Environmental perturbations caused by the impacts of asteroids and comets. *Rev Geophys* 35(1):41–78

- Vasilyev NV (1998) The Tunguska meteorite problem today. *Planet Space Sci* 46(2/3):129–150
- Vasilyev NV, Kovalevskiy AF, Razin SA, Epiktetova LE (1981) Reports of eyewitnesses of the Tunguska fall. VINITI (All Union Institute of Science Information), Deponent No. 5350–81, Moscow (in Russian)
- Vorobyov VA, Demin DV (1976) New results of studies of heat affection on larch trees in the Tunguska meteorite fall area. In: *Problems of Meteoritics (Voprosy Meteoritiki)*. Tomsk University Press, Tomsk, pp 58–63 (in Russian)
- Wolbach WS, Lewis RS, Anders E (1985) Cretaceous extinctions—evidence for wildfires and search for meteoritic material. *Science* 230:167–170
- Wolbach WS, Widicus S, Kyte FT (2003) A search for soot from global wildfires in Central Pacific Cretaceous-Tertiary boundary and other extinction and impact horizon sediments. *Astrobiology* 3(1):91–97
- Wolbach WS, Gilmour I, Anders E et al (1988) Global fire at the Cretaceous Tertiary boundary. *Nature* 334:665–669
- Wolbach WS, Gilmour I, Anders E, Orth CJ (1990) Major wildfires at the Cretaceous/Tertiary boundary. In: Sharpton VL, Ward PD (eds) *Global catastrophes in earth history*. Geological Soc of America Special Paper 247. Boulder, CO, pp 391–400
- Zahnle KJ (1990) Atmospheric chemistry by large impacts. In: Sharpton VL, Ward PD (eds) *Global catastrophes in earth history*. Geological Society of America Special Paper 247. Boulder, CO, pp 271–288
- Zenkin GM Ilyin AG (1964) On radiation burn of trees in the Tunguska meteorite explosion area. *Meteoritika* 24:129–140. Nauka Publishers, Moscow (in Russian)
- Zhuravlyov II (1967) On a possible reason of larch tree branch damage in the Tunguska meteorite fall area. In: Plekhanov GF (ed) *Problema Tungusskogo Meteorita* 2, pp 118–119 Tomsk University Press, Tomsk (in Russian)

CHAPTER 7

TUNGUSKA CATASTROPHE OF 30 JUNE 1908

VLADIMIR SVETSOV AND VALERY SHUVALOV

*Institute for Dynamics of Geospheres, Russian Academy of Sciences, Moscow 119334, Russia
E-mail: svetsov@idg.chph.ras.ru; shuvalov@idg.chph.ras.ru*

1 THE MOST DANGEROUS IMPACT DURING THE LAST MILLENNIUM

The event that happened almost 100 years ago in Siberia, in the basin of the Podkamennaya Tunguska River, continues to attract the attention of researchers and the general public throughout the world. In the press and popular literature, especially those published in Russia, the Tunguska event is described fairly often as a curiously enigmatic phenomenon, and a great deal of exotic hypotheses were invented for the explanation of this event. However, from research performed during recent decades it has been determined that this event was caused by the fall of a cosmic body, asteroid or comet, 50–100 m in size; the body decelerated at altitudes of 5–10 km, and released energy into the air that was equivalent to 10–50 Mt TNT. It was the typical fall of a rather large cosmic body, which essentially differs from frequently observed smaller impacts (bolides) only in the scale.

The fall of quite a few bodies commensurate with the Tunguska cosmic object (TCO) in size occurred during the existence of humanity. According to various estimates, such impacts happen on average from once in 300 years (Shoemaker 1983) to once in 1,000 years (Brown et al. 2002). The latter period seems to be overestimated (see Chap. 4). If one considers that cosmic bodies fall with a higher probability over oceans, seas, and unpopulated areas, it seems quite probable that the Tunguska event is the only large fall humankind has confronted directly. The impacts of cosmic bodies on such a scale, if they happened not very long ago, had to be reflected at least in chronicles and probably in legends. More than once it was suggested that the biblical catastrophes and the destructions of cultures existed in the Bronze Age resulted from impacts of cosmic bodies. Some traces obtained through archaeological research suggest that the impact of a large cosmic body, comparable to the Tunguska cosmic object, took place in the Near East about 4,000 year ago (Courty 1998). Another supposition was made that a circular depression in

southern Iraq, >3 km in diameter, seen on space photographs and topographic maps, is a young impact crater left by a body that caused the catastrophe in the Bronze Age (Master 2001). However, no explicit evidence of such an impact has been found as yet. Moreover, as a matter of fact there are no direct traces to suggest that an impact comparable to the TCO or larger occurred during some thousand years ago somewhere on Earth, except for the 1908 event in the basin of the Podkamennaya Tunguska. However, data on lunar craters and observations of the contemporaneous falls of meteoroids in the atmosphere evidently testify that such events undoubtedly had to take place during such a length of time.

There were attempts to attribute an event that happened on 13 August 1930 in Brazil to an impact of a large cosmic body (Kulik 1931; Bronshten 2000), although serious grounds for such a suggestion were absent. This suggestion about the impact was based on eyewitness reports collected by a Catholic missionary who came to the place some time after the incident (Bailey et al. 1995). The interpretation of these reports was made very arbitrarily, whereas the descriptions of the event are quite similar to a forest fire. After all, according to eyewitnesses, the event began from dustiness and smoke generation in the atmosphere and the fall of ash (the sun turned red, darkness covered everything, reddish dust appeared), which are clear evidence of the beginning of a large fire. Only some time after this were sounds and explosions heard, which could have been caused, for example, by the detonation of a mixture of natural gases and air initiated by the fire, or by electric discharges connected with powerful flows of dusty air supported by the fire. In the Brazilian stories there was not one word about the action of a shock wave. Ash continued to fall and darkness remained for several hours, and the fire lasted several months, as was written in a newspaper report. There is no way to link the impact of a cosmic body with the ash fall and appearance of dust long before the impact. Some attempts to connect a depression found in the region, ~ 1 km in size, with the event, suggesting that the depression is an impact crater formed in 1930, are rather naïve (Bronshten 2000). The impact energy commensurate with a 1-km-diameter crater must be so big that the impact inevitably would register over the whole terrestrial globe. Meanwhile, as is reported in Bronshten (2000) an observatory located only about 1,300 km from the scene of action has not registered any seismic waves that could correspond to the impact event in time and distance from the source.

The falls of cosmic bodies observed and registered in the twentieth century had energies by several orders of magnitude lower than the TCO. Deceleration and energy release (flashes) during such smaller falls with average energy ~ 1 kt TNT usually occur in the atmosphere at altitudes >25 km. (The number of the falls is about 25 per year over the whole Earth's surface.) As a rule, among small objects only iron bodies reach the Earth's surface with a speed sufficient for crater formation. This happened when a relatively small iron meteoroid about 3 m in size produced the Sikhote-Alin meteorite shower on 12 February 1947. The shower left a strewn crater field with a large quantity of holes and craters, the largest of which was ~ 25 m in diameter.

Among approximately 150 well-studied impact craters, there are only about 10 craters with sizes from 100 m to 2 km; they are not older than 50,000 years. These craters were formed after the impacts of bodies from 10 to 100 m in size, which are smaller or somewhat larger than the TCO. It is evident that many craters with such diameters are not found and some of them disappeared because of erosion.

One of the most famous young craters is the Barringer Meteorite Crater, also known as Meteor Crater, in Arizona, United States, 1,200 m in diameter. It was produced 49,000 years ago as a result of the impact of an iron meteorite about 50 m in size with kinetic energy fairly close to that of the TCO. However, in this case, due to the relatively high strength and density of the iron meteoroid, fragments of a broken body hit the surface as a rather compact mass with a size smaller than the diameter of the crater. The diameter of the Barringer Meteorite Crater is close to the diameter of the crater that would be formed by the impact of a very strong solid body (in contrast to the Sikhote-Alin meteorite shower, in which individual craters and holes were much smaller than the size of the strewn crater field). The consequences of shock waves and hurricane winds after the meteorite fall that created the Barringer Meteorite Crater were assessed by Kring (1997). The devastation area due to aerial shock waves after this impact was approximately the same as from the Tunguska air blast. According to Neukum and Ivanov (1994), crater-producing impacts with such energies take place on average once in 1,600 years on the Earth, and once in 6,000 years in continental regions.

Among impact craters younger than the Meteor Crater, the largest is the Macha crater group in western Yakutia, Russia, which consists of five craters from 60 to 300 m in size, and ~7,000 years old. The Henbury crater field in Australia is even younger; it was created ~5,000 years ago after the impact of an iron meteorite. The field consists of about ten craters; the largest crater is <200 m. These craters are likely to have been produced by bodies with somewhat smaller masses and energies than the TCO. Except for these craters, there is no evidence of impacts with energies close to that of the TCO that could have occurred in the last millennia on the Earth.

The Moon experiences fewer impacts of cosmic bodies in comparison with the Earth, in accordance with its smaller size and mass. It is interesting that in 1953 a flash was observed on the Moon's surface, which was likely caused by the impact of a cosmic body. The flash lasted not longer than 8 seconds; however, it was photographed with the help of a ground-based telescope. On photographs of the Moon made from space, a crater 1.5 ± 0.5 km in size is distinguishable in the region of the photographed flash (Buratti and Johnson 2003). Estimates, although rather rough, show that the impact could have been produced by a body close in size to the TCO, but further studies of the lunar crater are necessary to be certain.

The impacts of relatively large meteoroids (comparable with the TCO) undoubtedly happened during the last millennia but did not leave evident traces either on the Earth's surface or history. For this reason, one can say that the Tunguska event is unique. Much has been written and hundreds of papers have been published in the scientific literature about the Tunguska event. The results of

investigations were summarized in a number of reviews (Turco et al. 1982; Vasilyev 1998; Bronshten 2000; Plekhanov 2000; Vasilyev 2004), but many questions related to this event still remain unanswered. This results from both the remoteness of the impact site and the lack of knowledge about such phenomena in the first half of the twentieth century, which did not permit the optimal and timely study of the Tunguska event. This chapter mainly addresses the aspects that are connected with risk and those that are disputable or unclear and need further investigation.

2 EYEWITNESS REPORTS

Typically not all eyewitnesses tell real stories, and most of eyewitness reports were collected decades after the Tunguska event. Nevertheless, these cataloged reports (Vasilyev et al. 1981) contain convincing evidence of the impact of a relatively large cosmic body.

Hundreds of Siberians, who lived at different distances from the epicenter, watched the flight of a glowing body and the consequences of its disintegration in the atmosphere. The place of the explosion detected by the eyewitnesses usually corresponded to the catastrophe epicenter. Some local Evenks turned out to be closer to the epicenter than other people, at distances 25–35 km. Their reports are in accord with the main modern conceptions on the effects of explosions caused by impacts. (The explosion implies a sufficiently fast, about 1-s, deceleration of the body in the atmosphere and transformation of its kinetic energy to the thermal energy of air.) The main effects of such an explosion near the epicenter are radiation of the heated air and meteoroid vapor, arrival of a shock wave and its propagation along the Earth's surface, strong winds generated behind the shock wave, and seismic waves. Intense radiation could last for tens of seconds, which is noticeably longer than the time of the shock wave's arrival to the surface. Light phenomena connected with the motion of heated air and vapor upward along a wake under action of atmospheric pressure gradients, could last for some minutes after the explosion. Electric discharges after the explosion of a cosmic body have not been well investigated but are quite possible effects of such an event (Svetsov 2002). Electric phenomena (lightning) were observed after nuclear tests and volcanic eruptions.

Evenks in the nearest to the epicenter zone were in leather nomadic tents; for this reason they experienced at first the arrival of a shock wave and hurricane wind. They related how tents and people were scattered, and how once out of their shelters they observed the fall of fiery trees, and the burning of dry peat moss, dry grass, and needles. They watched strong luminescence and heard sounds like blows. There were no directly fatal cases, but there were injuries, fractures, and contusions, and the explosion itself produced a strong psychic shock on the local inhabitants. They did not report thermal burns because they were defended from the impulse of thermal and light radiation by the leather walls of their tents. However, closer to the epicenter, flocks of hundreds deer and property kept in special barns burned.

The inhabitants of the trading station Vanavara who were out of their houses at first felt the effects of thermal radiation. This settlement is nearest to the epicenter, at a distance of 65 km to the south-southeast. At this distance the thermal radiation did not cause skin burns; however, it was noticeably strong. The eyewitnesses related “such heat came that one could not rest,” “as though something strongly scorched ears,” “as if a shirt could take just a little fire.” The shock wave came after the radiation impulse and broke window glass and threw an eyewitness from his porch; seismic waves were felt. Another eyewitness, an inhabitant of Katanga, 116 km southeast of the epicenter, also said he felt heat. However, the heat action was substantially weaker at this distance.

Eyewitnesses who were even farther away reported that they watched the body flight and light phenomena, and heard various sounds similar to thunder, shots, and rumbling. The field of event vision stretches to 400 km in a sector limited by azimuths of 130–240 degrees from the epicenter (in a clockwise direction), and the listening distance stretches to 1,000 km in a sector with azimuths from 90 to 290 degrees (Plekhanov 2000). The eyewitnesses described the dimensions and color of the fireball and the direction of the flight in different ways. This is a rather typical situation; eyewitnesses of bolide falls often talk of different directions, and special computer codes are created for determination of bolide trajectories from controversial eyewitness reports. However, in the case of the Tunguska event, eyewitnesses could see not only the meteoroid fall into the atmosphere to the ground but also the rise of a luminous formation, plume, upward along the wake (see the following). Some eyewitnesses at first saw the falling meteoroid and then heard sounds or felt the action of seismic waves, whereas others began to look upward after the arrival of the acoustic or seismic waves and watched the plume luminescence. These two groups of eyewitnesses could have had different perceptions. Analyzing the eyewitness reports, one should keep in mind that eyewitnesses of various events often report inauthentic information and may confuse successions of occurrences even immediately after meteor falls. Also, many eyewitnesses of the 1908 event were not questioned until 50 years after the incident.

On the whole the 1908 eyewitness reports give a picture of a meteoroid explosion that is in many respects similar to a nuclear explosion with certain energy and at a certain altitude, especially in thermal and mechanical effects. This is quite natural because in both cases either the nuclear energy of a charge or the kinetic energy of a meteoroid releases as thermal energy in the air with the formation of a shock wave. Quantitative information also can be derived from eyewitness reports and some attempts to do this have been made.

3 ANALYSIS OF EYEWITNESS REPORTS

About 100 eyewitness reports have been processed by computer to obtain the atmospheric trajectory of the TCO (Zotkin and Chigorin 1988, 1991). Researchers found that the azimuth of the trajectory projection on the ground (measured in a clockwise direction) is equal to $A = 126^\circ$, and the inclination angle of the trajectory

to the horizontal is $\alpha = 20^\circ$ with an accuracy $\pm 12\%$. This result was obtained from the condition of the minimum sum of squared deviations of separate indications from the average.

Simpler methods were used also for determination of the trajectory azimuth. In this way Konenkin (1967) used the reports of eyewitnesses from the Nizhnyaya Tunguska River, which flows approximately north at a distance about 300 km to the east from the epicenter. Using only eyewitness accounts of the bolide's movement to the north or to the south, Konenkin found that $A = 120^\circ$. Bronshten (1999), using the same eyewitness reports from the Nizhnyaya Tunguska River, obtained 54 years and more after the event, came by almost the same method to the conclusion that the TCO trajectory passed over the village of Preobrazhenka, which is located 347 km from the epicenter, or perhaps somewhat to the south of this village. This gave the trajectory azimuth $A = 104^\circ$. The same simple method applied to the reports of eyewitnesses from the Lena River gave an azimuth $A = 120^\circ$ (Epiktetova 1976). The trajectory passed over the Lena at a distance >500 km from the epicenter. It is difficult to judge the accuracy of these trajectory–azimuth determinations obtained from the reports of eyewitnesses who were questioned so many years after the fact.

Attempts were also made to estimate the angle of trajectory inclination to the horizontal α (see Bronshten 2000) using simple methods. The easiest way of estimation is to use the reports of eyewitnesses from Preobrazhenka, who said they watched the glow near the zenith. However, if it is assumed that they saw the bolide fall (which could be sufficiently bright only at altitudes <90 km) and take into account that the distance of Preobrazhenka from the epicenter is 347 km, the inclination angle α becomes $< 12^\circ$; that is, the TCO entered the atmosphere along a very shallow trajectory. On the other hand, eyewitnesses from Kezhma (~ 274 km to the south from the epicenter, at the middle stream of the Angara River) said that they watched some optical phenomena near the sun that, in the morning at the explosion time, stood at an angle of about 28° to the horizon: “the sun rays were intersected by a wide fiery-white strip,” “another sun appeared, a little higher and to the right from the real one” (Vasilyev et al. 1981). However, if the meteoroid passed right over Preobrazhenka, the eyewitnesses from Kezhma could not watch the bolide or its wake against the sun because simple geometric constructions show that the meteoroid would be very high and would not be discernible (Dyomin et al. 1984).

Some estimates were made using the observations from the most distant points. An eyewitness from Bodaibo (775 km from the epicenter) reported that he saw the bolide at an angle height of 9° above the horizon, from which it follows that $\alpha < 23^\circ$ if one assumes that the glow could be distinguishable when the TCO was at altitudes <110 km (Bronshten 2000). From reports of eyewitnesses from the villages of Kamenskoe (600 km from the epicenter) and Malyshevka (795 km from the epicenter), who also saw a glow, it follows that $\alpha > 25^\circ$ if one assumes the appearance of the TCO at the same altitude; otherwise the glow could not be seen above the horizon (Yavnel' 1988, 1992). However, such estimates can include an error resulting from the statement that the eyewitnesses saw the bolide glow. It is

likely that they could see not the bolide, but the plume glowing at altitudes substantially higher than 100 km. Besides, it is necessary to take atmospheric visibility into account at small angles of observation; that is, significant weakening of light from the bolide or plume due to absorption and dispersion by air. Therefore, the results of these estimates are highly unreliable. These methods of α estimations should not be used without appropriate theoretic grounds because the plume develops at first along the wake, which exists along the trajectory, and then moves upward (Boslough and Crawford 1997; Shuvalov and Artemieva 2002). Sytinskaya (1955), using only the reports of those eyewitnesses who saw the trajectory pass through either the sun or zenith, obtained $A = 133^\circ$, $\alpha = 22^\circ$. Bronshten and Boyarkina (1975), using the reports of eyewitnesses from Preobrazhenka, estimated that $\alpha < 15^\circ$. Both of these estimates are dubious for the same reasons. The estimates of A and α , obtained by Zotkin and Chigorin by automatic processing of many eyewitness reports seem to be more reliable.

The estimates of α made using the primitive interpretations of eyewitness reports seem to be equivocal. A stony 60-m-diameter asteroid can be seen from a distance of 100 km as an object with a brightness of -10 magnitude (this corresponds to the brightness of the moon in the first or last quarter phase), if its surface is heated to a melting temperature. Fast meteors are registered at altitudes up to 130 km, but large bodies become heated more slowly. At very high altitudes, where the free paths of molecules are comparable with the size of a body, the energy obtained in collisions with molecules is insufficient for substantial heating of the surface. Convection heat flux to the surface (which decreases with increasing body size) could heat the TCO up to the temperature of melting only at altitudes < 80 km (at moderate velocities $< 40 \text{ km}\cdot\text{s}^{-1}$ and entry angles $> 15^\circ$). Radiation energy flux at the body surface (which vice versa increases with increasing body size) could reach the value necessary for melting at altitudes < 90 km. At this altitude, the air heated in the shock wave is still transparent for visible light, and emits radiation only slightly but lets radiation from the surface pass through it. During the subsequent reduction of altitudes the object brightness grows due to heating of vapors and increasing optical thickness of heated air. In several seconds, at altitudes of 50–70 km the object's brightness reaches a magnitude of -25 (approximately the brightness of the sun). The brightness of an icy body would probably be lower than that of a stony body at high altitudes due to lower vapor temperatures. In order to notice the fall of the Tunguska bolide against a bright sky at altitudes of 80–90 km, when its brightness was about -10 magnitude, an eyewitness had to look at the sky narrowly in the correct direction at exactly right instant. It is more likely that Siberians could observe a bright falling meteoroid only at altitudes < 70 km. However, such low altitude leads to substantial controversy, because the angle α is very small. For this reason those who estimated the altitudes of bolide appearance tried to make this altitude as high as possible.

Tens of seconds after the explosion, as the mass of vapor and heated air rose through the wake, the visible brightness could have grown. Many eyewitnesses paid attention to the phenomenon, heard and felt sound and seismic effects, only a

minute or so after the meteoroid's entry. A plume had to be seen in the atmosphere at this time. Plume glow is determined by the temperature, size, and amount of condensed particles thrown to high altitudes. The eyewitnesses who reported that they observed the object against the sun probably watched not the fall of the meteoroid but the plume at altitudes >100 km or the sun shading by condensed particles. It is likely that the inhabitants of Preobrazhenka also observed the plume glowing near the zenith. It would be interesting to perform calculations of radiation of both the bolide, during its motion in the atmospheric upper layers, and the plume and compare the results with the eyewitness reports.

Except for the determination of A and α , attempts have been made to derive more sophisticated effects connected to the fall of the TCO from the eyewitness reports, which sometimes led to unjustified conclusions. For example, Astapovich (1958), according to a number of reports, believed that the Tunguska event eyewitnesses saw a smoky trail after the bolide fall. Meanwhile no one accentuated the existence of a clear dusty trail (in contrast to the fall of the Sikhote-Alin meteorite, for example), and most eyewitnesses did not mention any trail at all, which creates the feeling that a strong smoky trail was absent after the fall of the TCO (Plekhanov 2000). Despite the uncertainty in the presence of the trail, the authors of these works (Kolesnikov et al. 1999, 2003; Rasmussen et al. 2001) considered, without any theoretical estimates, that the absence of a smoky trail is evidence of the fall of a comet. However, contrary to smaller bolides, intense radiation fluxes in the wake could entirely vaporize particles of a stony TCO (Svetsov 2003).

Some researchers, using eyewitness reports, tried to explain various zigzags of the TCO; that is, changes in the velocity vector and trajectory during the fall in the atmosphere (Bronshen 2000). A feeling arises that, handling the contradictory eyewitness reports at wide discretion, one can discover in the event whatever one likes, right up to a flying saucer; but there is no serious ground for the conclusions about zigzags in the eyewitness reports.

The picture of the TCO's fall and its hazardous consequences emerge from the eyewitness reports, but many attempts to derive quantitative information from these reports leave much to be desired.

4 ANOMALOUS ATMOSPHERIC PHENOMENA

In addition to the reports of eyewitnesses who saw the fireball at distances as far as $\sim 1,000$ km from the epicenter, many reports have been collected about unusual atmospheric phenomena in Europe and Asia (Zotkin 1961, 1969; Vasilyev et al. 1965; Romeiko 1992). These phenomena began on the night of 30 June and continued until 1 July 1908 at a territory encompassing the Yenisei River to the Atlantic, which is restricted from the south by an imaginary line connecting the towns of Tashkent, Stavropol, Sevastopol, and Bordeaux, and by the zone of polar day from the north. People saw unusually light twilights and nights, colorful sunsets and sunrises, solar halos, and Bishop's rings. Unusual positions of the Arago neutral polarization points in the atmosphere were also detected. The optical anomalies

were of a different character and are likely to have been caused by perturbations in the troposphere, stratosphere, and mesosphere.

Reports about the anomalous atmospheric phenomena were received from more than 140 points, although the brightest events were observed in Germany. No unusual atmospheric phenomena were registered in the Southern and Western Hemispheres at all. The sky brightness was noticeably weaker in the night from 1 to 2 July and entirely disappeared on 3 July. Some observers reported that the anomalous optical phenomena were prior to the event, on 25–29 July, but the number of such reports was very small, on 29 July in eight settlements, and earlier there were only single reports. It is worthwhile to mention that the Tunguska event happened just in the period when the annual appearance of noctilucent clouds is at the maximum at the middle latitudes. Moreover, there was strong volcanic activity in 1908: 22 volcanic eruptions have been registered, five of which were extremely strong (Romeiko 1992). For these reasons, the effects caused by the Tunguska event could be confused with atmospheric phenomena resulting from natural terrestrial sources.

Nevertheless the anomalous atmospheric phenomena were unusual in scale and coincided with the Tunguska catastrophe in time. It is quite natural to surmise that the anomalous optical phenomena were caused by dusting of air by microparticles of the Tunguska meteoroid, which spread at various altitudes into the atmosphere. According to estimates (Fesenkov 1949; Turco et al. 1982), the mass of dispersed dust had to be on the order of 1 million tons. For all that, the mechanism of dust spreading had to be very fast because the anomalous phenomena began just after the Tunguska event. Fesenkov (1961, 1969), the author of a hypothesis that was popular some time ago, suggested that the TCO was a comet, and its tail, oriented to the west, entered the atmosphere over Europe. Bronshten (1992) suggested a more sophisticated mechanism of comet-envelope dust spreading as it enters the upper atmospheric layers. Namely, if one assumes that the dust envelope were extensive, several hundred kilometers in size, some part of the dust at large distances from the impact site would enter the atmosphere at very sharp angles to the horizontal, as if slightly grazing the atmosphere. Some particles, being decelerated at high altitudes, would then go into elliptical orbits and would move along these orbits descending from the Yenisei to the British islands. However, these particles entering the atmosphere had to fall in a very narrow interval of altitudes with a width of not more than 10 km. Another suggestion was made: that the Earth came through a cloud of cosmic dust with the TCO inside it (Vasilyev et al. 1965), or that the TCO was itself a cloud of dust (Plekhanov 2000). However, given such explanations, many details remain dubious or unclear. First, nobody observed such dust clouds as well as comets of such small size as the TCO. Second, the mass of dust that could cause atmospheric anomalies must be on the same order of magnitude as the estimated mass of the TCO, ~1 Mt. As only a small part of the entire dust envelope can fall in the narrow range of altitudes and come into an elliptical orbit, the question arises why there was a dust envelope around the core of a compact cosmic body (perhaps an icy nucleus of a comet) much more massive than the core.

The explosion was local, and such a massive envelope had to release huge energy and strongly influence the atmosphere and the surface over a much larger area than was observed. How was this cosmic object arranged? How did it form and exist prior to its collision with the Earth? These hypotheses leave much freedom for various fantasies.

It is simpler and more natural to explain the unusual atmospheric phenomena by penetration of dust or condensate produced from the vaporized TCO material to far distances. This reason for the anomalous atmospheric brightness, along with the possibility of noctilucent cloud formation from water entrained in the explosion cloud and chemical reactions of nitrogen oxides with oxygen, was suggested in the work of Turco et al. (1982). Chyba et al. (1993), using the analogy with nuclear explosions, estimated that the altitude of lifting of the TCO explosion cloud had to be ~ 40 km, and an amount of water sufficient for the production of noctilucent clouds could be cast to this altitude. However, at a latitude of 60° stratospheric winds in summer blow more often from the west, and they are not strong enough for the speedy transportation of material. Therefore it is doubtful that the material could reach western Europe so rapidly. Ivanov (1967) suggested that the TCO material reached higher altitudes and was picked up by ionospheric winds.

Only recently it became clear that the lifting of meteoroid material occurs not like the vertical rise of the cloud from a nuclear explosion, but along a slanting rarefied wake in which the gas is accelerated due to pressure gradients. This is confirmed by an analogy with the fall of fragments of comet Shoemaker-Levy 9 onto Jupiter, in which this phenomenon was observed, and also by simulations of the Tunguska event (Boslough and Crawford 1997). Material of the vaporized meteoroid mixed with troposphere air is ejected inside the plume to altitudes up to several hundred kilometers, and in 10–15 minutes after the explosion falls back to the mesosphere to the southeast or east (depending on the trajectory azimuth A) at a distance of 2,000 km from the epicenter. In the mesosphere and lower thermosphere, in the Northern Hemisphere in summer, primarily easterly winds blow with average velocities of tens of meters per second. This can cause propagation of microparticles westward to a distance of 6,000 km over ~ 10 hours. According to computations, the maximum velocity of plume ejection along the wake is $4.5 \text{ km}\cdot\text{s}^{-1}$. It is likely that a small part of meteoroid material is accelerated to even higher velocities. Then this part of the material could fly around the Earth from the west to east along ballistic trajectories and land in Europe much earlier than with the mesospheric winds, already in the night from 29 to 30 July in western European time. However, more accurate gas dynamic computations of the wake and plume formations are necessary to test this supposition.

Romeiko (1992) suggested that the optical anomalies of 1908 were caused by intense formation of noctilucent clouds due to acoustic gravity waves propagated from the Tunguska explosion during the period when the atmosphere was dusted by volcanoes. However, proper investigations are necessary to prove the connection of noctilucent clouds with acoustic gravity waves. As a whole, anomalous atmospheric phenomena, which are possible after large meteoroids fall, are imperfectly

understood. The study of such phenomena should be made along with a simulation of the Tunguska event, which presents a problem in itself.

5 REGISTRATION OF THE TUNGUSKA EXPLOSION

The Tunguska explosion has been recorded in many points. Seismic waves have been registered in Irkutsk (965 km from the epicenter), Tashkent, Tiflis, and Jena. These seismic waves were initiated by an aerial shock wave struck the ground around the epicenter; the magnitude of the earthquake was 4.5–5. The instant of the Tunguska explosion has been determined from the time of the shock wave arrival to Irkutsk. This instant is 0:14:30 Universal Time (Pasechnik 1986). Probably this instant could be determined more precisely using new data on seismic wave propagation. However, it should be kept in mind that the explosion itself (i.e., the deceleration of the body at the late stage of its flight) is extended over a time interval on the order of 10 s.

Barographs of many Siberian and European meteorological stations have registered the arrival of aerial waves initiated by the explosion. It is possible to estimate the instant of the event, using these data, too; however, the accuracy is poorer than from seismograms of the Irkutsk observatory. If data of different meteorological stations are used, the estimated time instant varies within 30 minutes. Six meteorological stations in London and its vicinity have registered microbarograms of air oscillations connected with the Tunguska event. The moment of the explosion calculated from the difference in arrivals of a direct aerial wave and a wave propagating over the globe and coming from the opposite side proved to be 0:23:30 Universal Time. The accuracy of this estimate is likely to be lower than from the seismograms. Trinitrotoluol equivalent of the Tunguska explosion has been estimated from the aerial and seismic waves by Ben-Menachem (1975) as from 9.5 to 12.5 Mt TNT. Pasechnik (1976) estimated this trinitrotoluol equivalent to be from 20 to 50 Mt. The altitude of the explosion was estimated as 8.5 km (Ben-Menachem 1975) and from 2.5 to 9 km (Pasechnik 1976).

A magnetograph in the Irkutsk observatory has registered a geomagnetic effect—variations of the magnetic field constituents up to several tens of nanoteslas; the peak variation was about 70 nT (Ivanov 1961; Plekhanov et al. 1961). The anomalous variation of the geomagnetic field began at 0:20:30 UT, that is, 6 minutes after the explosion (according to Pasechnik 1986), and lasted for more than 4 hours. Any other of meteorological stations in which the geomagnetic record was checked did not register the geomagnetic effect. All the other stations were substantially farther from the epicenter (Ekaterinburg, Pavlovsk). The variations of the geomagnetic field recorded in Irkutsk were similar to those caused by high-altitude nuclear explosions.

Various mechanisms that could cause the geomagnetic effect registered in Irkutsk were suggested, as listed in Bronshten's paper (2002). Nevertheless quantitative models have not been developed. It is most likely that the current system responsible for this effect is a local perturbation of regular daily solar currents (Ivanov 2002). As the correlation between variations of terrestrial magnetic field and current systems

in the ionosphere is established, such an approach seems to be quite justified. The effect of anomalous geomagnetic field variations could be explained by heating the air at high altitudes during the motion of a shock wave and the rise of a fireball and explosion cloud, subsequent changes in conductivity and a current system, and propagation of this perturbation in the ionosphere (Ivanov 1961, 1964, 1967). However, the lifting of meteoroid substance occurs along the wake and a huge mass with rather high velocity reaches the ionosphere. The perturbation of the ionosphere seems to be the strongest just in this process, because both the shock wave and wake carry much less energy. Unfortunately, only the main features of the models have been suggested, and no accurate calculations have been performed.

Any model of the geomagnetic effect must take into account the delay time of the beginning of the geomagnetic effect in Irkutsk relative to the determined time of the explosion. Nemchinov et al. (1999) suggested that the ionosphere perturbation was caused by the fall of the plume back to the ionosphere after the flight of the material along the ballistic trajectories. The time between the ejection and the fall of the air and vapor, according to calculations of Boslough and Crawford (1997), is about several minutes. As a first approximation, this agrees with the determined 6-minute delay time of the beginning of magnetic field variations. However, as there is no detailed model of the geomagnetic effect, what caused this delay remains unclear: development of the gas dynamic flow, ejection and fall of the plume, or development of perturbations in the ionospheric current system. Geomagnetic variations are also registered after rocket launchings. After launchings from the Baikonur cosmodrome, long-wave perturbations were registered at a station situated at a distance of ~ 800 km from a rocket trajectory only in 10–15 min after the start (Sokolova et al. 2003). It is possible that the delay was caused by the same effect in the both cases; however, this effect has not yet been studied.

Magnetodynamic disturbances propagating from the ionosphere to the magnetosphere can cause precipitation of fast particles from the radiation belts and lead to auroral phenomena, i.e., additional ionization. Regional and even global abnormalities in radio communications resulting from meteoroid impacts can present a particular hazard and deserve detailed investigation. Magnetic field variations caused by the impact of bodies several times larger than the TCO are studied in Chap. 10. It is worthwhile to continue the study of the geomagnetic effect caused by the Tunguska event for which there are unique data of registrations.

6 FIELD STUDIES

6.1 Tree Fall

Trees were felled after the Tunguska event over a 2,150 km² area. Today almost no noticeable marks of the explosion remain. However, the area of the tree fall has been thoroughly studied, the number of felled trees and directions of their trunks were measured, and the results were statistically processed (Fast 1967). The area of tree fall represents a sufficiently symmetric figure, a triangle with rounded corners

or a butterfly, with an axis of symmetry stretched along the azimuth 115–295°. The average direction of felled trees is radial, and there is a center to which roots of felled trees are directed. The coordinates of this epicenter are 60°53'09" N and 101°53'40" E. In a central part of the tree-fall area, at a distance 2–3 km from the epicenter, a substantial amount of dry trees with broken off branches remained, and everywhere, especially in surface folds, there were separate trees that survived the catastrophe.

The main picture of the tree fall was of the same type; however, there are some specific features. There were axially symmetric deviations from the radial direction in the eastern and western parts of the fall. In the central part, there was a zone of chaos, where stripped fall on one part did not fit in direction to the fall on another part. Some researchers perceived in this chaotic pattern of the tree fall several localized areas, which could have been produced by shock waves from separate small explosions at the surface (Serra et al. 1994; Goldine 1998). However, it is clear that the tree fall resulted from powerful air flows behind the shock wave front rather than from the action of the shock wave itself. It is likely that vortices are formed in the air flows, which can cause a complex pattern of tree fall.

Qualitatively, these specific features can be explained by nonsphericity of the explosion at the late stage of body deceleration, vortex motions of air at the surface, influence of relief, and heterogeneity of the forest. Probably, it will be possible to perform detailed numerical simulations to determine these tree fall features in the future. For now more general problems concerning the area of the fall are still incompletely understood. A butterfly shape is typical for large meteoroid impacts at some angle to the horizontal; this has been reproduced in numerous simulations (Korobeinikov et al. 1991, 1998; Boslough and Crawford 1997) and laboratory modeling experiments (Zotkin and Tsikulin 1966b). In these experiments the energy release during the fall was modeled by detonation of a long explosive fuse, and the energy release at the late stage of meteoroid deceleration—by detonation of a concentrated charge. Interaction of the shock waves from both sources with trees at the surface led to their fall within an area similar in shape to a butterfly. The action of a shock wave on the surface, when a meteoroid flies up to it, are seen in photographs of Venus as dark and light areas often similar to a butterfly (Takata et al. 1995). Thus, the butterfly of the tree fall is a typical pattern caused by the action of air shock waves on the surface after oblique impacts. Nevertheless, atmospheric winds also could substantially change the shape of the shock wave and make the area of tree fall to be that observed.

Korotkov and Kozin (2000) studied (calculated) the action of atmospheric winds on the shock wave produced by a concentrated charge with an energy of 10 Mt at an altitude of 7 km. The profile of the wind, from zero at the ground to 40–50 km·s⁻¹ at altitudes 4–7 km, was taken from reference data and was close to typical maximum values. The area of the tree fall would be a circle in the absence of any wind, but an area obtained in the calculations in the presence of an eastward wind was very similar to the butterfly-shaped area at the Tunguska site. Undoubtedly the wind could also substantially change the shape of the luminous volume (fireball),

which itself could be very asymmetric. Certainly, an oblique impact produces a butterfly-shaped tree fall pattern without any wind; however, the wind, if it had a component perpendicular to the meteoroid motion, could disturb the symmetry, and if it blew along the trajectory, could flatten the butterfly or make it more circular, depending on its direction. Korobeinikov et al. (1991), using calculations based on the concept of an explosion at the end of the trajectory, concluded that the angle of the trajectory inclination to the horizontal was 40° , because this value gave better conformity with the shape of the area of tree fall and tree burn. However, we can change the result and enlarge or diminish the angle, assuming that a wind blew to one or another direction. The discrepancy between the 40° and the estimates of the entry angle based on eyewitness reports (which are often very questionable) led some researchers think that the meteoroid substantially changed the direction of its motion in flight (Bronshen 2000). This is absolutely false. Detailed investigations are necessary to determine the trajectory angles at which the observed tree fall butterfly could have formed.

It is worth noting that the explosion energy can be determined with some accuracy, using the data on the tree fall. The estimates of different authors give energy values from 10 to 50 Mt.

Trees in the central area of the fall presumably had marks of thermal burn, but the first expeditions to the impact site did not study these characteristic features of the event; their main efforts were applied to the search of meteorites. However, many larch trees that survived after the catastrophe remained in the central area. In the 1960s, most of them had ribbon damage at the tops of trunks and branches dated to 1908. Most likely this is a result of thermal burn (Zhuravlyov 1967). However, a part of such damage is dated to other years, and about half the damage dated to 1908 is directed to the sides and downward (Plekhanov 2000). For this reason doubts have arisen that the damage was caused by the direct action of light and thermal radiation from the fireball. It is not improbable that those are marks of a fire caused by the radiation flux, or even represent mechanical damage caused by the shock wave. Certain patterns of damage distribution were found from studies of 120 larch trees. The shape of the area with these trees resembles an irregularly shaped ellipse (or egg), with a major axis oriented along an azimuth of $95\text{--}275^\circ$ (Vorobyov and Dyomin 1976). The transverse size of the ellipse is ~ 12 km, the southern boundary is 13 km from the tree-fall center, and the western boundary is at 5 km—the total area is ~ 200 km². The ellipse boundary has grooves in which trees with damage have not been found. Because of doubts about the cause of ribbon damage, these data should be used with constraint in simulation results, and only with proper care.

The area of the 1908 fire has been studied sufficiently well, and the characteristic features of the fire have been revealed. The fire was weak but arose over a large area, ~ 500 km². It was spotty, but was of the same type up to 10–15 km from the epicenter. The fire and probably the ribbon damage of larch trees resulted from thermal radiation from vapor and air heated behind the shock wave during the

meteoroid's motion into the atmosphere. The estimates of radiation fluxes correlate well with field studies of fire traces and ignition zone.

6.2 Search for Matter

Neither the first nor the following expeditions to the catastrophe area found any meteorites. The area around the epicenter was thoroughly studied due to the efforts of numerous participants of complex amateur expeditions. The chance of finding meteorites in the epicenter area may be considered to be very small. Maybe it seems strange, but amateur groups attempted to find meteorites west or northwest from the epicenter along the course of the probable trajectory projection. Conceivably these searches resulted from the thought that a part of the body decelerated in the atmosphere and another part deflected from its line upward and managed to fly farther. In principle this might have happened, but is most improbable. In fact a descending meteoroid flies into the atmosphere along a trajectory close to a straight line and does not "know" where it flies. Evidently the TCO was broken up into many fragments, and if the strongest of them deflect for some reason from the line and begin to fly at an angle to the trajectory in some direction, it is very likely that other fragments will fly at the same angles to the trajectory in all other directions. Most important, fragments would fall still in the vicinity of the epicenter, where they have not been found.

If the TCO was stony (or cometary with inclusions of stony fragments), meteorites could have fallen in a narrow strip along the trajectory projection to the east from the epicenter. This could have occurred during the flight at some altitude, when the body broke up, but the radiation fluxes were not high enough for full vaporization of the fragments and the fragments were still large (Svetsov 1996b, 1998). However, the mechanism of fragment separation from the parent body and fragment deceleration in the atmosphere needs special substantiation. It is not impossible that the fragments could acquire the necessary lateral velocity during breakup and collisions among themselves, during propagation of elastic waves over the meteoroid material, or under action of vapor pressure, formed inside the broken body due to friction. In any case there is a chance of finding the remnants of the TCO in less investigated areas to the east or southeast of the epicenter at distances of some tens of kilometers. However, this territory to the east did not attract the special attention of enthusiasts searching for meteorites.

With time the search for TCO material began to be directed more toward microparticles. A large number of microspherules, mainly magnetite and silicate, were found in the 1960s during the study of numerous soil samples from the epicenter area. The spherules were no different from similar microspherules found in other regions, and it remained unclear if there was any connection between them and the Tunguska event. A collection of microspherules from the area of the fall of the TCO is kept in the Meteorite Committee (Vernadsky Institute of Geochemistry and Analytical Chemistry) of Russian Academy of Sciences. These spherules can be studied using modern techniques.

Two methods of searching for microparticles in natural traps—in resin of survived conifers and in peat layers—gave positive or at least not negative results. If material of a vaporized and condensed TCO precipitated, it could be captured by tree resin or peat moss. It is rather easy to date annual tree rings and it is likely that any substance found in tree rings from 1908 is connected with this event. Indeed, a great number of microparticles of various composition have been found in resin rings of trees studied around the epicenter; the concentration of the particles had a considerable peak in the rings formed about 1908 (Longo et al. 1994; Serra et al. 1994). It is conceivable that these particles (or a part of them) are the products of the meteoroid material; however, their cosmic origin has not been proved. Possible terrestrial origin is not excluded. They could be remnants of ground dust lifted by the shock wave, tree fall, or fire. Even more so, it is difficult to derive the composition of the TCO from these particles. If they are made from the meteoroid material, they were produced after its substantial processing by melting, vaporization, and condensation. Trees with higher concentrations of microparticles were located closer to the center of tree fall, but only six trees have been studied.

Sphagnum moss, which absorbs aerosols from air and forms annual layers in peat bogs, could preserve atmospheric admixtures caused by explosion-like vaporization of the cosmic body. There are many peat bogs in the area of the Tunguska event. Therefore chemical analyses of peat layers, including those of 1908, have been carried out. Anomalies of a number of elements and isotopes have been discovered in the layers close in time of formation to 1908 in samples extracted from bogs in the vicinity of the epicenter (Kolesnikov et al. 1995, 1996, 1998a, 1998b, 1999, 2000, 2003; Hou et al. 2000, 2004). These anomalies are treated as being formed by the substance of the TCO after its explosion; at least there are no other reasonable explanations. The peat layers with anomalous concentrations are located at depths from 35 to 60 cm, depending on peat bog locations, but in all cases these layers are below the permafrost boundary. The presence of iridium in the peat layers (Nazarov et al. 1990; Hou et al. 1998; Rasmussen et al. 1999) is a very compelling argument in favor of TCO material precipitation around the epicenter; evidently not all the cosmic substance was ejected upward and dispersed.

Basing on chemical analyses of peat samples from two columns cut at the Northern Swamp (2 km from the epicenter) Hou et al. (1998, 2000, 2004), concluded that the TCO material or its dust component, if it was a comet, had to be close in composition to carbonaceous chondrites CI. This result followed from comparison of ratios of platinum group elements and rare-earth elements in the anomalous peat layers, normal peat layers, and cosmic objects. A rough estimate of the TCO mass, based on concentration of palladium and rare-earth elements in the peat and comparison with the composition of carbonaceous chondrites show that if the material fell homogeneously over the area of the tree fall, the mass of the TCO, if it was carbonaceous, could be from 10 kt to 1 Mt.

Even stronger conclusions regarding the TCO composition have been made (Kolesnikov et al. 1999; Rasmussen et al. 1999). The authors analyzed composition of samples—five peat columns taken from different peat bogs located close

(not >6 km) to the epicenter (Bublik, Nothern, Southern, and Prikhushminskiy) and also from other distant peat bogs in the surroundings of Tomsk and Vanavara to check the results. The authors found increased concentrations of carbon isotope ^{13}C in the peat layers of samples from the vicinity of the epicenter; they explained the ^{13}C increase by the fall of TCO cosmic material. They also found iridium in the layers at the same depths; the ratio of carbon to iridium in the anomalous samples proved to be much higher than in carbonaceous chondrites (by four orders of magnitude) and in achondrites as well (Kolesnikov et al. 1999). Rasmussen et al. (1999) found that there is a deficit of carbon isotope ^{14}C at depths corresponding to the iridium maximum (~ 55 cm). Some portion of the isotope ^{14}C usually is included in terrestrial aerosols, and ^{14}C is absent in the interiors of cosmic bodies. It is possible to explain the ^{14}C deficit, assuming that at least for 2 days the sphagnum fed on aerosols with high concentrations of carbon ^{13}C (Rasmussen et al. 2001). Assuming that the moss constantly absorbs the same amount of carbon, and calculating an increase of ^{13}C from the decrease of ^{14}C , the authors find that the mass ratio of carbon to iridium was very high, on the order of 10^9 . At the same time it seems that the natural losses of carbon could only be bigger than those of iridium. The authors conclude that the TCO was a comet, the concentration of dust (close in composition to carbonaceous chondrites) in this comet was extremely low, and the major part of the comet mass was constituted from volatile materials with a carbon high content. According to observational data on comets, the most prevalent of such materials are CN, CN_2 , and carbohydrates.

Such a conclusion disagrees with common notions about cometary bodies formed during studies of several comets. According to these notions, comets contain large amounts of water and their dust content is in the tens of percents. For this reason the obtained results have been criticized. Doroshin (2002) noted that the carbon isotope shifts could result from natural variations, but there are a number of arguments in favor of cosmic origin of the isotope ^{13}C found in peat (Kolesnikov 2002). Jull et al. (2001), in their comment, prejudiced the correctness of dating peat layers with a ^{14}C deficit in the work of Rasmussen et al. (2001). Indeed, it is difficult to count out the 1908 layer and determine the age of the layer with the minimum of ^{14}C because peat layers have no distinct boundaries. Depths from 43 to 63 cm, in which the deficit of ^{14}C was found, correspond to depths of the 1908 layer determined in other works. However, the layer with the deficit of ^{14}C has no marks (which might be attributed to the catastrophe), and no marks of fire also. It was only determined that the depth of 80 cm corresponds to the first half of the seventeenth century or an earlier period. Also note that the studies of ^{14}C variations in annual rings of a fir tree from the epicenter (Yonenobu and Takenaka 1998) did not reveal any anomalies of this carbon isotope. Nonetheless, the minimum of ^{14}C correlate with the maximum of ^{13}C and iridium in peat depths (Rasmussen et al. 2001). Besides, the ^{13}C maximum coincides with a detected minimum of deuterium (Kolesnikov et al. 1999). These specific features could not be explained by any terrestrial causes (e.g., precipitation of terrestrial dust and soot, change of local climate, change in the environment, volcanic eruptions). In addition, anomalous concentrations are absent

in examined peat samples taken far from the epicenter; therefore, it is most probable that the anomalies in the peat layers from the epicenter vicinity are caused by the fall of TCO matter.

Another two peat columns from the Northern Swamp (2 km from the epicenter) and peat bog Raketka (8 km) were studied in the recent work of Kolesnikov et al. (2003). Dating in this work has been made more accurately, by count out of annual peat growth. An anomaly in concentration of nitrogen isotope ^{15}N was studied. Increased concentrations of the heavy nitrogen isotope were connected with the TCO material and with acid rains caused by chemical reactions between nitrogen and oxygen in the atmosphere heated during the fall and explosion of the cosmic body. According to estimates of Kolesnikov et al. (2003), about 200,000 tons of nitrogen fell in the area of felled trees. Increased concentrations of ^{13}C in the column from the peat bog Raketka have been found both in the layers corresponding to 1908 at a depth of ~ 45 cm and also at depths of 60–63 cm, which correspond to the permafrost boundary of 1908. However, in the latter case, in contrast to the 1908 layer, the peak of ^{13}C coincided with the peak of the total concentration of carbon. The authors confirmed their conclusion that the high concentration of ^{13}C is the evidence of cometary origin of the TCO with a composition substantially different from the studied comets. (Only three of them were studied in space missions: Halley, Borrelly, and Wild 2.) At the same time they admit that the TCO could be similar to (C type) asteroid 253 Mathilde or a core of comet Borrelly, despite the fact that both objects have not been adequately studied.

In the conclusions of these works, it is implicitly assumed that the vaporized meteoroid material, condensed or in a gaseous state, precipitated or was captured by terrestrial dust and precipitated, and then was absorbed by moss or washed down to moss, and correspondingly to elemental composition of the objects fallen to the Earth. However, the processes of vaporization, condensation, mixing of carbonaceous gases with air, interaction with dust, and chemical reactions following the TCO explosion remain unstudied. The mechanisms of carbon penetration to peat from the comet after its explosion are also unclear. The carbon could settle down with dust; however, it is not known what is captured by dust and settles more easily—cosmic carbon included in gases or microparticles of iridium condensate. The proportion of iridium in aerosols absorbed by sphagnum moss is far from clear. Microparticles containing iridium could simply not be assimilated by sphagnum. Many questions arise in the various scenarios about the TCO explosion and carbon and iridium settling down, which are associated with the formation of the peak concentrations in peat. Without the answers to these questions there is no assurance that the measured element ratios in the anomalous peat layers reflect the real composition of the TCO.

On the other hand, the method of search of TCO material using anomalies in peat seems to be not quite accurate. The anomalous concentrations in peat layers are small, and background values that could change in the epicenter area are not known. Selection of samples and analyses demand much expenditure; therefore, there are no measurements over a large area, which are necessary to make certain that the

results are stable. The work becomes complicated because the effect of increased concentrations is not expressed quite certainly. The anomalies have been found only in seven peat columns from a total of 21 columns studied. At that, “empty” columns can be situated near those that have peak concentrations of elements and isotopes. (It is likely that this is a natural effect of heterogeneity of processes that accompanies the meteoroid explosion.) One of the disadvantages in the analysis of peat layers is that the dating of layers with anomalous concentrations is inaccurate; that is, there is no exact determination of the layer that corresponds to the catastrophe. Only peat samples with certain thickness, about several centimeters, were analyzed; however, such thickness of peat can contain layers formed during many years both before and after the catastrophe.

6.3 Other Anomalies

Investigations of thermoluminescence have been made in rock samples (including plagioclase, calcite, and quartz), mineral fraction of soils (including feldspar and quartz), and pure quartz extracted from soils. The samples were taken around the epicenter and at far distances from it. Statistical processing of data obtained from more than 400 soil samples and 200 rock samples show that there is an anomalous area in which the samples have either an increased or reduced level of thermoluminescence (Vasilyev et al. 1976; Bidyukov 1988, 1997; Bidyukov et al. 1990). On average, the level of thermoluminescence is diminished within a radius of 6 km and increased within radii from 6 to 15 km. For a certain radius, angle distribution is heterogeneous; samples with increased thermoluminescence are found more often in a strip going from the east to the west through the epicenter. The main supposition about the cause of the reduced level of thermoluminescence is annealing of minerals under action of thermal radiation from the Tunguska explosion (Bidyukov et al. 1990; Bidyukov 1997; Vasilyev 1998). The cause of increased thermoluminescence could be radiation of air and vapor after the meteoroid explosion in an ultraviolet band with quantum energies 4–6.5 eV (Svetsov 2002), except it should be noted that additional data about the radiation spectrum of the fireball in the Tunguska event and further studies of ultraviolet radiation influence on thermoluminescence are necessary for adequate determination of the causes of the thermoluminescence anomaly. Statistics over samples are insufficient and need improvement for definitive conclusions about the anomaly’s existence.

The magnetic properties of soil were studied and residual magnetization and magnetic susceptibility were measured from 1969 to 1976 in an area of 15,000 km² around the Tunguska explosion (Boyarkina and Sidoras 1974; Sidoras and Boyarkina 1976; Boyarkina et al. 1980). The results were statistically averaged because the vector of residual magnetization changed from one sample to another by a wide range. The authors obtained an anomalous deviation of the averaged values from the background in some area located within the tree fall area. Deviations in magnetic inclination, declination, and magnetic susceptibility were determined. They tried to explain the result by precipitation of ferromagnetic material, but

geochemical analyses of samples were not carried out; consequently, the kind of material remained unknown. Such effect can also arise from displacement of dust lifted by the shock wave and precipitation of terrestrial ferromagnetic particles settling along the geomagnetic field, which was somewhat different in 1908 (Svetsov 2002). Later on, it was revealed that the samples substantially changed their properties during maintenance and transportation. Because of this, studies of the magnetic anomaly were stopped and doubts were cast on the anomalies' existence. Measurements of magnetic susceptibility and residual magnetization of soil samples from the tree-fall area made by Lind (1997) show that the magnetization vectors are distributed chaotically and there is no magnetization reversal.

Since the early 1960s biological studies were performed in the catastrophe region with the purpose of revealing any anomalies in plants or animals that could be caused by the action of the Tunguska explosion. It turned out that at distances up to 20 km from the epicenter pine trees often have an increased amount of three-needle tufts (Plekhanov et al. 1968; Dragavtsev et al. 1975; Plekhanova et al. 1984). It was also established that in the area of tree fall trees grow faster than in the surrounding taiga (Nekrasov 1962; Vasilyev and Batisheva 1976). Experts conclude that similar morphometric anomalies with three-needle tufts are observed in pine trees growing on old fire sites or forest clearings. The rapid growth of trees can be well explained by increased light in the tree-fall area, better soil heating, and also by the additional fertilization of soil by the products of fires (Plekhanov 2000). This effect is observed on fire sites and forest clearings as well. In addition to the pine tree anomalies, morphologic anomalies in ants have been found (Vasilyev et al. 1980), but there is no evidence that those are mutative changes. They might result from ecological conditions in this territory.

7 SIMULATIONS OF THE TUNGUSKA IMPACT

7.1 Simple Models

Numerical simulations of the Tunguska impact were performed to understand its characteristic features: the release of energy 10–50 Mt at altitudes 5–10 km, thermal effect, and distinctive features of the tree-fall area.

The motion of a body in the atmosphere can be derived from simple differential equations (Bronshen 1981):

$$m \frac{dV}{dt} = -\frac{1}{2} C_d \rho S V^2 \quad (1)$$

$$Q \frac{dm}{dt} = -\frac{1}{2} C_h \rho S V^3 \quad (2)$$

$$\frac{dh}{dt} = -V \sin \alpha, \quad (3)$$

where m is the meteoroid mass, V is the meteoroid velocity, t is time, ρ is the density of air at the flight altitude h , S is the cross-sectional area of the body, C_d is the drag coefficient, and C_h the heat transfer coefficient.

If the body does not break up, and hence does not change its shape and size, the ablation of such a large object as the TCO may be neglected to a first approximation and the object mass may be considered as constant. Then only Equations (1) and (3) remain; they have a simple analytical solution for isothermal atmosphere with the exponential altitude dependence of density:

$$\rho = \rho_0 \exp(-h/H), \quad (4)$$

where ρ_0 is the air density at a zero altitude, and H is the atmospheric scale height ($H \approx 8$ km if $h < 100$ km). This solution is:

$$V = V_0 \exp\left(-\frac{C_d S H \rho_0}{2m \sin \alpha} \exp\left(-\frac{h}{H}\right)\right), \quad (5)$$

where V_0 is the meteoroid entry velocity.

Let the initial energy of the TCO, equal to $mV_0^2/2$, be known. If the body velocity is given, its mass will be determined and the body size will depend on its density ρ_m . It turns out that only a very porous body with a proper mass and unlikely low density can be decelerated at altitudes of 5–10 km (Petrov and Stulov 1975).

Many meteorites have very low strength. Undoubtedly the strength of the TCO was low and the body broke up into a large number of fragments during its flight in dense layers of the atmosphere. The broken mass enlarges its cross-section under action of air pressure at its face—the body behaves as if it is flattened and it is decelerated stronger. Several approximate models have been suggested for calculations of the cross-sectional size of a crushed body during its flight in air (Grigoryan 1979; Zahnle 1992; Chyba et al. 1993; Hills and Goda 1993; Klein et al. 1994; Field and Ferrara 1995). All the models are based on the principle that the air pressure at the center of the leading face is about ρV^2 and is negligibly small at side surfaces; therefore, a force perpendicular to the body velocity acts on the fragments. With the aid of various argumentations one can obtain a fairly simple formula for enlargement of the body's cross-sectional size r (Grigoryan 1979; Hills and Goda 1993).

$$\frac{dr}{dt} = V \sqrt{\frac{\rho}{\rho_m}}. \quad (6)$$

As these calculations show, this and other formulas of semianalytical models of flattening meteoroid give rather close results with an accuracy, at least as good as that in this rather rough model of flattening.

It is necessary to take ablation into account for a fragmented body; that is, to include Equation (2) into the set of equations. The set of Equations (1)–(4) can be easily solved numerically with the help of a computer, using the simplest finite-difference schemes. The following values: V_0 , r_0 (the initial body size), ρ_m , and α

are taken as initial data. The altitude of explosion can be defined as the value of h , which corresponds to the maximum loss of the body's kinetic energy. However, the added complication is that the values of C_H are not known with sufficient accuracy. The calculation of this coefficient presents a problem, and estimates of C_H for a large fragmented body are unreliable. The results obtained for smaller bodies cannot be used for the TCO because there is no similarity if radiation plays a role. Chyba et al. (1993), using evidently overestimated values of C_H , obtained that the hypothetical TCO could be only stony with sufficiently high density, because both a comet and a carbonaceous chondrite would decelerate too high. Lyne and Tauber (1995) and Lyne et al. (1996, 1998) used estimates that gave lower values of C_H and came to the conclusion that the density of carbonaceous chondrites suits the TCO best, although both a comet and an ordinary chondrite cannot be excluded. Grigoryan (1998), neglecting ablation completely, obtained that a comet with a density of $1\text{--}2\text{ g}\cdot\text{cm}^{-3}$ will decelerate at altitudes about 10 km or below. He concluded that only bodies of cometary density can be decelerated at necessary altitudes and stony bodies release their energy too low.

Thus, the modeling with the use of simple semianalytical models of flattening body explain in principle the TCO deceleration at altitudes of 5–10 km, but based on these models on cannot obtain constraints on such TCO parameters as its density, velocity, or entry angle. Modeling a fragmented body's motion by means of numerical solutions of gas dynamic equations has been carried out in a number of works. The body was treated as a volume of fluid with a certain equation of state, flowed around by gas. Meteoroid motion in dense layers of the terrestrial, Venusian, and Jovian atmospheres was simulated (Svetsov 1995; Svetsov et al. 1995; Koricansky et al. 2000, 2002; Koricansky and Zahnle 2003). It has been shown that a crushed body not only is flattened in flight but also unpredictably distorts its shape due to development of hydrodynamic instabilities at its boundary. The behavior of a crushed body depends on its shape. Therefore, the usage of simple approaches does not allow researchers to take into account important features of the process of meteoroid deceleration and explosion. Nevertheless, one can hope to construct adequate models that would describe the change in body mass and momentum with acceptable accuracy in the future, when serial numerical simulations are made. Some steps toward this goal have been taken by Koricansky and Zahnle (2003), who have shown that in the absence of radiation the mass of a crushed and flattened meteoroid diminishes due to material blowoff and can be described with good accuracy by the following:

$$\frac{dm}{dt} = -C_A \rho V S, \quad (7)$$

where C_A is some constant. Nevertheless, it still remains unclear how to construct a model of the combined motion of blowoff material and the remaining crushed mass. The need to take into account radiation transfer presents a severe problem for construction of models.

7.2 Numerical Modeling

Modeling of the Tunguska event, using gas dynamic computations, began in the 1970s and 1980s (Korobeinikov et al. 1991, 1998). However, substantial simplifications of the problem were made because of the limitations of numerical schemes and insufficient computer resources. The stages of a body's flight with a constant size and the explosion at the end point of a trajectory were considered separately. For the first stage the set of Equations (1)–(3) was solved. The explosion was treated as a gas dynamic flow with the following initial data: A uniform sphere of compressed air with some radius is located at some altitude, the air has a velocity close to the entry velocity of a cosmic body and has some thermal energy, the sum of thermal and kinetic energies conforms to the estimated energy of the Tunguska event. The air density in the sphere depends on its radius. Thus, three fitting parameters are preset: the initial altitude of the gaseous volume, its radius, and thermal energy, apart from the fact that the entry velocity, entry angle, and body density are free parameters of the problem. The gas flow was simulated by numerical solution of the gas dynamic equations, and the altitude of gas deceleration and energy release in the atmosphere were obtained. The gas contained in the sphere decelerated at a distance about 1 km from the initial altitude; that is, in fact the choice of the initial altitude of the gaseous volume determined the end point of the explosion, which took place very quickly. The motion of shock waves in air and their amplitudes at the Earth's surface were approximately calculated using the energy-release at the stage of flight, which can be treated as a cylindrical explosion, and at the stage of deceleration of the gaseous sphere. The area in which a horizontal component of air velocity after reflection of the shock wave from the ground exceeded $25 \text{ m}\cdot\text{s}^{-1}$ was compared with the area of tree fall.

Radiation fluxes were also calculated in the framework of this simplified model of two explosions, approximately cylindrical and spherical. Using some approximate approach (diffusive approximation for angle distribution of radiation, 10 groups for quantum energies, neglect of vapor radiation), it was obtained that about 12% of the initial energy is emanated by radiation (Shurshalov 1980). The radiation fluxes on the ground also were calculated (Putiatin 1980). As a consequence of these computations, Korobeinikov et al. (1998) came to the conclusion that the following parameters give the best fit to the observational data on the tree-fall and tree-burn areas: the angle of the trajectory inclination to the horizontal $\alpha = 40^\circ$, the energy of the TCO is 20 Mt, the TCO density is either $0.5 \text{ g}\cdot\text{cm}^{-3}$ and then $V_0 = 35 \text{ km}\cdot\text{s}^{-1}$ (which corresponds to a comet) or $2 \text{ g}\cdot\text{cm}^{-3}$ and then $V_0 = 26 \text{ km}\cdot\text{s}^{-1}$ (which corresponds to a carbonaceous chondrite). However, because of undue model simplifications, it is unlikely that the resulted figures exactly correspond to the real parameters of the TCO. Nevertheless, this model of two explosions qualitatively describes rather well the main features of the propagation of shock waves in the motionless atmosphere after a meteoroid explosion.

Boslough and Crawford (1997) carried out three-dimensional computations of the shock waves produced by the energy release obtained from the model of a flattening body. A stony asteroid with a kinetic energy of 12.5 Mt, velocity $V_0 = 20 \text{ km}\cdot\text{s}^{-1}$

and $\alpha = 35^\circ$ gave a good fit to the boundary of tree fall. Svetsov (1996a, 1996b), using a similar model of flattening, calculated the radiation fluxes and obtained that the radiation effects on the ground produced by a stony 60-m-diameter asteroid with $V_0 = 15 \text{ km}\cdot\text{s}^{-1}$ and $\alpha = 45^\circ$ fit the observational data well.

Now numerical gas dynamical methods have been developed that allow researchers to take into account the interfaces between air and body material and simulate the motion and disintegration of meteoroids in the atmosphere. The closest to the Tunguska event variant was simulated using modern methods in the work (Shuvalov and Artemieva 2002). They simulated a vertical impact of a body with properties appropriate to comets (density of $1 \text{ g}\cdot\text{cm}^{-3}$, latent heat of vaporization $2 \text{ kJ}\cdot\text{g}^{-1}$, equation of state of ice). It was assumed that the body begins to move down vertically with a velocity of $30 \text{ km}\cdot\text{s}^{-1}$ at an altitude of 32 km; a rarefied wake formed behind the body was taken into account. In the process of numerical simulations the equations of radiation transfer were also solved in the approximation of radiation thermal conductivity. This allowed them to take vaporization into account. Tabulated values of averaged radiation free paths for vapors and air were used.

Here are some figures from the work of Shuvalov and Artemieva (2002). Figure 1a shows the initial stage of the fall when a body leading face is compressed and the body slightly enlarges its cross section. The leading face is somewhat distorted because of development of hydrodynamic Rayleigh-Taylor and Kelvin-Helmholtz instabilities. When the body descends, its deformation grows and, as Fig. 1b shows, at an altitude of 17 km the body is flattened, its cross-section is increased four times, and the body boundary is so distorted that it is on the verge of disintegration.

Already at an altitude of 15 km the meteoroid changes into a jet of debris that falls to smaller and smaller pieces and flies surrounded by heated air and vapor. The motion and deceleration of this jet are shown in Fig. 2.

At this stage, at altitudes $>10 \text{ km}$, the body loses the major part of its kinetic energy, but vapors continue to move down and reach an altitude of 4 km. At the jet stage the model of the flattening meteoroid fails because the process changes. The jet stretches, the largest fragments move ahead, and smaller ones move in a rarified wake behind them, decelerating to a lesser extent. Then the larger fragments break up, drag and move back, and the largest fragments from those flying in the wake move forward and replace them. So all the fragments have different velocities and mix in the jet. The process progressively continues to the point of full vaporization of all the fragments.

After total deceleration of vapor at an altitude of about 4 km, the jet remains rarefied with a density 1–2 orders of magnitude lower than the air density around, and the temperature of the vapor–air mixture is several thousand degrees. As Fig. 2 shows, vortex structures develop in the vapor–air jet at the final stage of deceleration. Ten minutes after deceleration, the heated gas begins to lift along the wake. Formation of a plume is shown in Fig. 3. The heated gas is ejected to altitudes $>200 \text{ km}$ 1 minute after deceleration.

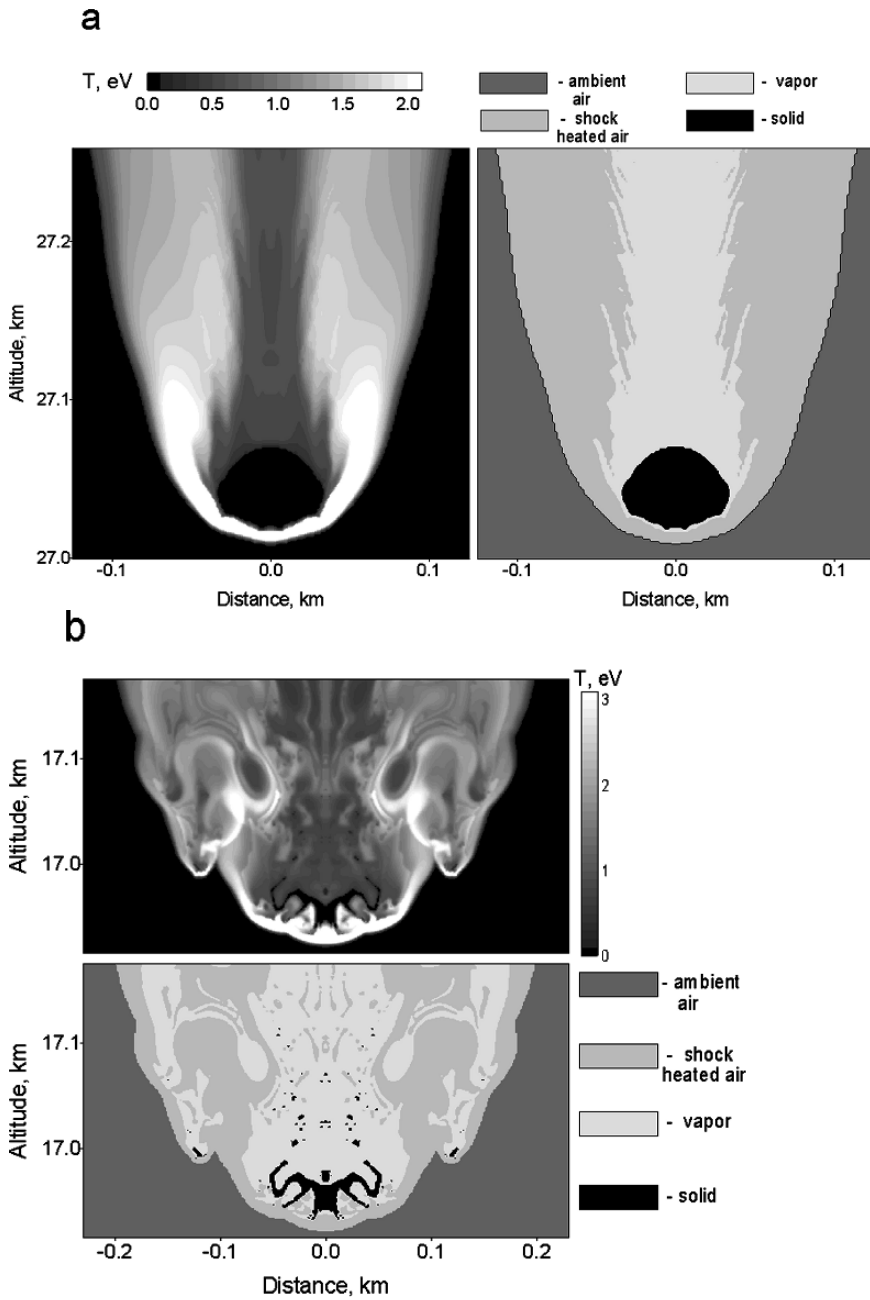


Figure 1. Temperature and material distribution around a cometary meteoroid, 30 m in radius, moving at 30 km·s⁻¹ at altitudes of 27 km (a) and 17 km (b). The figure is adapted from Shuvalov and Artemieva (2002) and reprinted with the kind permission of Elsevier

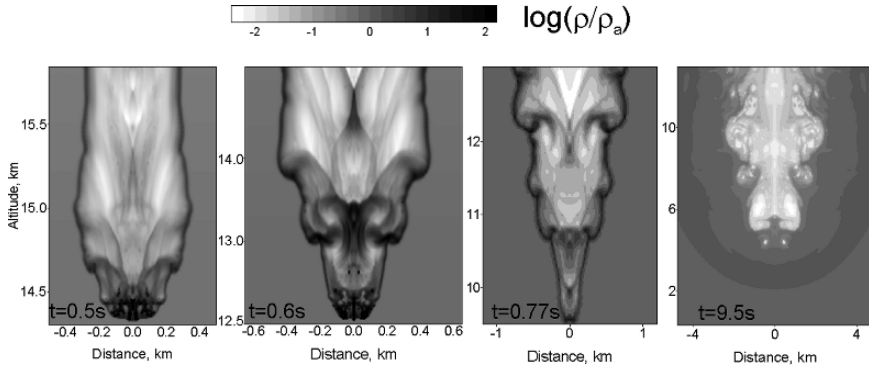


Figure 2. Debris jet, formed after disintegration of the meteoroid shown in Fig. 1. The figure is adapted from Shuvalov and Artemieva (2002) and reprinted with the kind permission of Elsevier

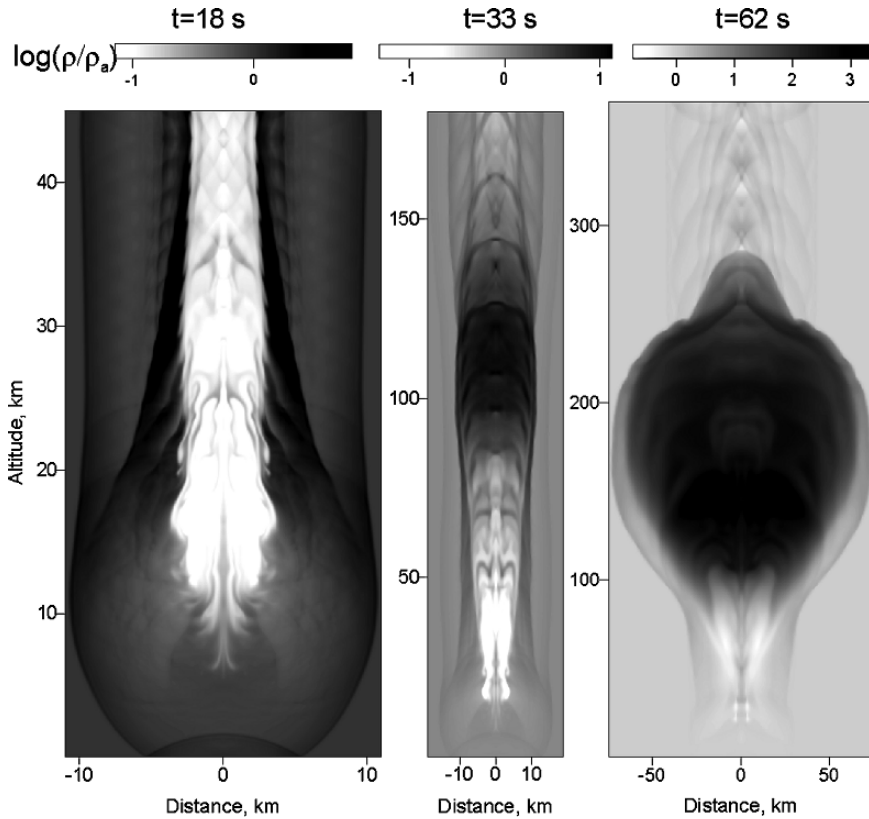


Figure 3. Distribution of relative density at the initial stage of plume formation. The figure is adapted from Shuvalov and Artemieva (2002) and reprinted with the kind permission of Elsevier

The simulation results correlate well with the main features of the Tunguska impact; the body entirely vaporizes and decelerates at altitudes 5–10 km, generating a shock wave. The instabilities developed during meteoroid disintegration and such body's parameters as shape, velocity, and entry angle can play a more important role in the explosion process than the difference in physical properties of hypothetical comets and asteroids. Therefore, it is doubtful that the results of simulations can give the answer to the question about the composition of the TCO, although it is probable that the difference between cometary and stony TCOs will be found, gradually making more accurate computations and enriching our knowledge about comets.

One can see from the obtained results that the body cannot noticeably change its trajectory at all stages of its fall into the atmosphere. A typical large stony body must begin to break up at altitudes >50 km, and comets have quite inconsequential strength. The crushed body changes its shape, enlarges the cross-section, and falls to pieces at altitudes of 20–30 km, and the body acquires an unpredictable shape due to instabilities at its surface. The drag force and velocity change are insignificant at these altitudes; therefore, the body shape cannot influence its trajectory in the atmosphere >20 km. In the following, when the swarm of debris flies at altitudes of 10–20 km and the fragments move alternately ahead or behind, the trajectory could be changed if at least one of the leading fragments were very strong and had a shape that could provide a significant lifting force. This could occur at a certain stage of the fall of the Sikhote-Alin meteorite. However, in the case of the Tunguska body, which evidently had low strength and broke up into small debris, such strong leading fragments could hardly arise. When the body entirely vaporizes, the changes in its trajectory due to aerodynamic forces are obviously impossible; but the influence of gravity is insignificant. Therefore, a noticeable change in the direction of the TCO's movement is highly improbable and could be only in the imagination of an eyewitness.

Both a comet and a stony body break up into fragments that, after the full disintegration of the body, fly into the atmosphere as a swarm of separate particles embraced by a shock wave. When the body was assumed to consist of finite number of particles in numerical simulations, the TCO ultimately disintegrated to this number of particles, as Fig. 4 shows.

Svetsov (1996a) and Svetsov (1996b, 1998), using an approximate approach, calculated radiation fluxes inside and beyond the swarm of debris. Inside the fireball, these fluxes are sufficiently high for vaporization of stony fragments not larger than 10 cm in size. If there are no large fragments, the whole swarm of stones can be entirely vaporized. Figure 5 schematically shows the flight of the TCO in the atmosphere and a zone of possible fragment fall on the ground if they get detached from the main swarm at sufficiently high altitudes.

The numerical simulations of the Tunguska impact clarified its main features. However, the vertical impact is a simplified two-dimensional axially symmetrical problem, whereas the fall of the TCO occurred at some angle to the horizontal. As computer resources improve we will probably be able to perform similar three-

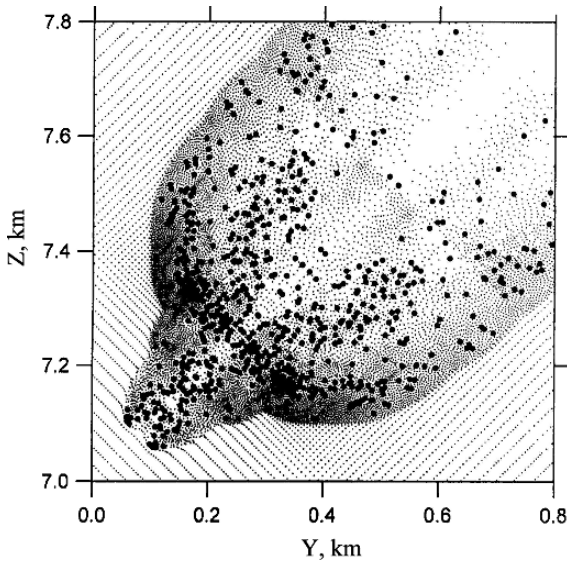


Figure 4. A swarm of debris of a Tunguska meteoroid at a stage of its full disintegration. Z is the altitude, Y is the horizontal coordinate. The meteoroid particles are shown by the *black solid circles*; atmospheric particles are shown by the *points*. The particles are regularly distributed in the undisturbed atmosphere. In the computations a hypothetical stony 58-m-diameter meteoroid consisted of 650 particles, 340 of them remain in the area embraced by the figure. By this time the swarm of debris has an average velocity of $10 \text{ km}\cdot\text{s}^{-1}$, whereas the entry velocity was assumed to be $15 \text{ km}\cdot\text{s}^{-1}$. More massive particles move ahead of the swarm. The figure is adapted from Svetsov (1996b) and reprinted with the kind permission of the Nature Publishing Group

dimensional computations for oblique trajectories, including winds, and compare them with the data on the tree fall and thermal effect of the explosion. Many details remain to be clarified by numerical simulations in the future; for example, interactions of the shock wave with a real relief, vortice and turbulent flows on the ground, deviations from the radial directions of felled trees, and lack of concurrence in the axes of symmetries of the tree-fall and tree-burn areas. Also, it would be interesting to make simulations to determine what eyewitnesses observing the event from different points could see and hear, the possible brightness of a bolide and plume, whether or not a visible smoky trail forms, and how acoustic and acoustic-gravity waves propagate after such an event. The authors hope that interest in the problem of hazards due to comets and asteroids will stimulate further studies of this unique Tunguska event.

8 PLUME

Effects associated with the energy release at the final stage of deceleration of a large meteoroid differ little in essence from altitude nuclear explosions, beginning

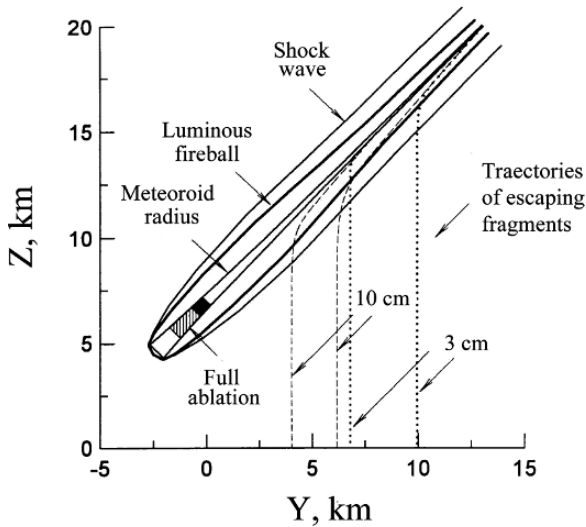


Figure 5. The shape of a shock wave and a luminous volume of the Tunguska meteoroid at an altitude of 5 km. The meteoroid velocity dropped to $3 \text{ km}\cdot\text{s}^{-1}$. In the hatched area of full ablation stony fragments with sizes up to 10 cm are entirely vaporized. If fragments, 3–10 cm in size, due to collisions and gaining an additional lateral velocity, lose contact with the fireball at altitudes 10–15 km, they can survive and fall onto the ground, as is shown in the figure. The figure is adapted from Svetsov (1996b) and reprinted with the kind permission of the Nature Publishing Group

from the moment of shock wave separation from a fireball. However, the late stages are different—the fireball of a nuclear explosion floats vertically upward, whereas the heated volume of gas after the meteoroid explosion is accelerated along the wake. As mentioned, the development of a plume is a very important phenomenon, and its investigation illuminated some aspects of the Tunguska event: the eyewitness reports, the anomalous atmospheric phenomena, and the geomagnetic storm. Formation of plumes became apparent during observation of the impacts of comet Shoemaker-Levy 9 fragments on Jupiter from 16 July to 22 July 1994, when plumes were ejected to $>1,000 \text{ km}$. The role of a wake and formation of plumes during these impacts have been studied (Crawford et al. 1994; Zahnle and McLow 1994). In light of these studies it became clear that the plume had to be formed during the Tunguska event too; this was also shown in the computations of Boslough and Crawford (1997).

After the meteoroid flies down to the Earth and is decelerated, a wake containing gas heated in the shock wave stretches upward at some angle to the horizontal over the region where the major part of the energy is released (the fireball). This wake expands until the pressure inside it becomes equal to the pressure of ambient air. In a rough approximation the wake has a cylindrical shape, and its diameter is about an order of magnitude larger than the meteoroid size. The gas density inside the wake is lower than the density in the ambient air ρ ; that

is, the wake represents a rarefied channel. A degree of rarefaction as well as temperature in the wake depend on the body velocity, processes of radiation and vaporization, and amount of vapor and condensate. However, parameters of the wake have not been calculated for the case of the Tunguska event, which is an evident gap in its investigation. Rough estimates show that the density in the wake is 1–2 orders of magnitude lower than the air density ρ in the ambient atmosphere. After leveling the pressure inside the channel, the pressure gradient becomes the same as the pressure gradient in the ambient atmosphere, that is, equal to ρg , where g is the gravitational acceleration, but this gradient substantially exceeds a value $\rho_w g$, where ρ_w is the gas density in the wake; therefore, the hydrostatic equilibrium is violated and gas begins to move upward inside the wake.

Velocity of some mass of gas in the channel obeys, to a first approximation:

$$\frac{du}{dt} = -\frac{1}{\rho_w} \frac{dp}{dh} - g, \quad (8)$$

where p is the atmospheric pressure. On the assumption that the gas, lifting along the wake, expands adiabatically and that the pressure varies exponentially with altitude, Equation (8) can be transformed to the form (Shuvalov 1999):

$$\frac{du}{dt} = g\beta \exp\left(-\frac{\gamma-1}{\gamma H} h\right) - g, \quad (9)$$

where β is the ratio of the atmospheric density to the gas density in the wake at the beginning of the motion, and γ is the gas effective adiabatic exponent that depends on the gas temperature and density ($\gamma \approx 1, 2$ can be taken for estimates).

Integrating Equation (9) one finds the gas velocity in the wake and the altitude of ejection. At first, the gas is accelerated under action of the pressure gradient, and then, beginning from some altitude, flies along a ballistic trajectory. This model explains the plume formation qualitatively but has only rough accuracy. A real wake is heterogeneous and the motion in different parts of the channel begins at different times; this can be taken into account only by means of numerical modeling using the gas dynamical equations.

An important feature of the wake is that it is turbulent and the heated gas gets mixed up with cold air inside it. Then the rarified channel ceases to exist. When the gas moves upward inside the wake, hydrodynamic instabilities develop at the boundary of the rarefied channel; the smaller is the wake diameter, the faster is the instability growth. Because of this, as shown in the work of Shuvalov (1999b), meteoroids <1–3 m in radius do not produce ballistic plumes, but bodies 10–30 m in radius and larger can create plumes. Modeling of these plumes demands special efforts aimed at fine spatial resolution of a long and relatively thin wake and adequate calculation of the mixing process at the boundary.

Plume modeling for the Tunguska event has been performed (Boslough and Crawford 1997; Shuvalov and Artemieva 2002). Figure 6 shows modeling results,

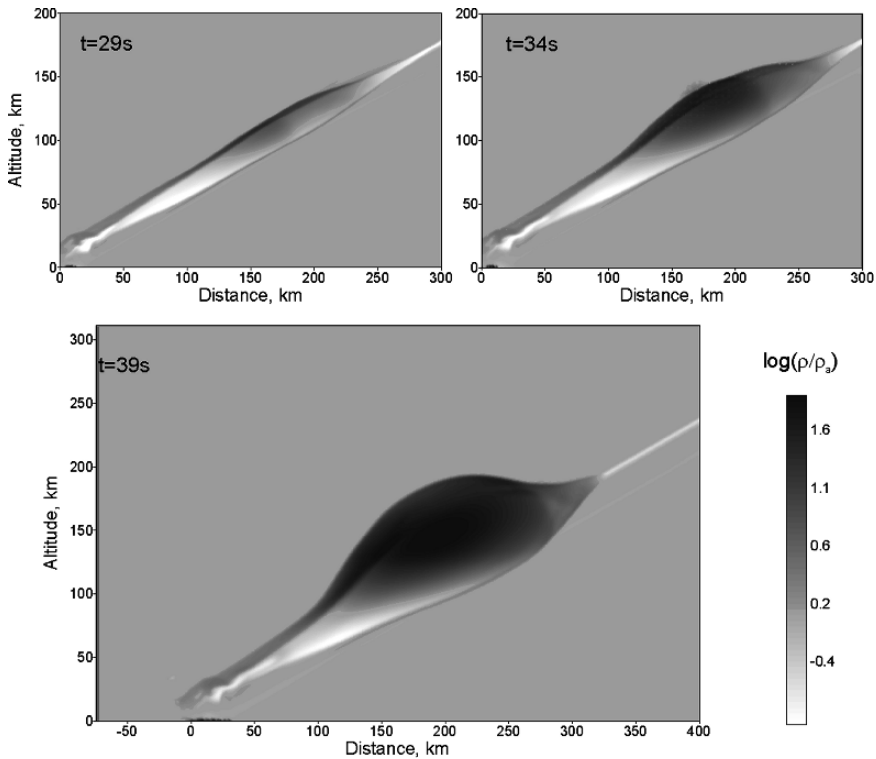


Figure 6. Evolution of a slant wake. Distribution of relative density $\rho/\rho_0(h)$

obtained by the work of Shuvalov and Artemieva (2002) for the inclination angle of the trajectory to the horizontal $\alpha = 30^\circ$.

Substantial simplifications were made in the modeling—the rarefied wake was set as a cylinder with a radius of 1 km at altitudes >10 km and radius 10 km at altitudes from 5 to 10 km. Vapor was not taken into account in these three-dimensional computations. A distinct plume forms 40 s after the explosion that reaches an altitude of 200 km. Later the plume expanded ballistically (the pressure stops to play a substantial role) and in 80 s the disturbed region stretches in the atmosphere from 100 to 600 km. Then the plume falls down and the major mass is braked at altitudes ~ 100 km.

Boslough and Crawford (1997) simulated the plume for a TCO entering the atmosphere at an angle of 45° to the horizontal. It turned out that a great mass of air is ejected from the troposphere to high altitudes ~ 100 km, and the maximum velocity of the leading edge of the plume is $4.5 \text{ km}\cdot\text{s}^{-1}$. Unfortunately, Boslough and Crawford (1997) and Shuvalov and Artemieva (2002) did not take into account the meteoroid material and did not calculate plume brightness. Because of this, it is difficult to compare the results with the eyewitness reports and infer to what

altitudes and in what state the TCO material was ejected. If all the material in the plume consists of 10- μm -diameter droplets that radiate light with a brightness temperature $\sim 2,000$ K, the brightness of such objects will be quite comparable with the sun. The particles of condensate can shade the sun and the whole plume can refract its rays.

At which minimal angle of trajectory inclination the ballistic plume can be formed also remains unknown. After a very powerful energy release in the lower atmosphere, even in the absence of a wake, oscillations of the upper atmosphere arise. For example, after the nuclear explosion with an energy of 58 Mt detonated in 1961 at an altitude of 3.6 km over Novaya Zemlya, the shock wave first attenuated and then, beginning from an altitude ~ 30 km, gained strength because it moved in a medium with diminishing density. As the calculations show (Adushkin and Nemchinov 1994), the shock wave acceleration after the explosion led to formation of a powerful ascending motion. The air flow directed upward began to decelerate by the gravitational force, and then a flow directed downward was formed. The descending gas collided with dense layers, decelerated, and caused heating and pressure rise, which led to formation of an air flow coming from the opposite direction. Because of this, shock waves arose (at altitudes about 100 km and higher) and large-scale nonlinear oscillations of the atmosphere were generated, which by 15 and 25 minutes covered a region with radii 700 and 1,200 km, respectively (with density disturbances as high as 50–100% and velocities 0.5–1 $\text{km}\cdot\text{s}^{-1}$). Certainly, if there are a wake and a plume, such oscillations are generated more easily. If the impact is oblique, the ballistic plume causes oscillations far from the impact site when it falls back.

9 THE NATURE OF THE TUNGUSKA METEOROID

There are no data that could allow one to conclude with certainty what cosmic body caused the Tunguska catastrophe. In the meantime, many researchers have their own opinions about this question, most of whom can be divided to two groups: adherents of the hypothesis that a comet impacted the Earth in the basin of the Podkamennaya Tunguska River, and supporters of the hypothesis of a stony body, a small asteroid. An iron body, as is now evident, would reach the ground and therefore has been excluded from consideration. A comet is implied, as a rule, to be a body made of a substantial amount of ice, because a dead comet seems very similar to stony bodies. A number of arguments have been expressed for and against both hypotheses in the course of numerous discussions; very questionable arguments are advanced quite often.

A typical argument of the cometary hypothesis partisans is: If it were a stony asteroid, where did its mass, on the order of a million tons, go? Meteorites had to have fallen, but they have not been found (Bronshen 2000). However, the theory and observations show that stony bodies some hundred of tons in mass, which yearly enter the atmosphere and are observed as bolides, often entirely vaporize, or as they say, burn down, in the atmosphere at altitudes >25 –30 km. Larger bodies

penetrate deeper into the atmosphere, and being subjected to higher pressures they break up into smaller debris; energy release per unit mass of the body grows at a distance equal to its size. Therefore, larger meteoroids have a better chance to be crushed and entirely vaporized. The necessary condition of full ablation is a sufficiently small size for fragments: for the Tunguska body the size must be about 10 cm and smaller, as estimates show (Svetsov 1996a). This is caused by the fact that the fragment vaporization needs time. Breakup of a hypothetical stony TCO into fragments of such size is very likely for typical strengths of stony meteorites and aerodynamic loads of hundreds of bars. The radiation fluxes at the fragment surfaces are sufficient for their vaporization because at the jet stage the debris disperse and get mixed with hot air. The full energy of a typical stony asteroid is sufficient for vaporization of at least ten such bodies. Thus, the answer to the posed question is that the TCO has been totally vaporized, and the vapor has been lifted inside the plume, condensed, dispersed, and carried away with the wind to Europe.

The supporters of the asteroidal hypothesis ask the following question (Zahnle 1996). Let an icy body, after the entry at some angle, maybe rather acute, be decelerated at an altitude of about 5 km. Then a stony body with the same kinetic energy, more compact, strong, and heat resistant, having on average lower velocity and subjected to smaller drag force, falls at a 45° angle to the horizontal (this is the most probable angle of impacts of cosmic bodies on planets), reaches the ground, and forms a crater. There are more stony bodies in space, and those with energies on the order of the TCO energy, falling on average every 300–1,000 years, would produce a lot of impact craters during a short (geological) time. Where are these craters? The answer to this question is unclear.

The TCO entry velocity V and the angle of trajectory inclination α are unknown; therefore, its orbit is also unknown. In the meantime some researchers, estimating α and V from some other considerations, calculated these orbits. Sometimes the orbits proved to be close to orbits typical for asteroids (Sekanina 1983, 1998; Farinella et al. 2001), sometimes for comets (Bronshen 1999); but definite conclusions about the nature of the TCO could not be derived from such calculations, even if α and V were known with good accuracy. The fact is that asteroids and comets moving in the Solar System change their orbits under the action of perturbations. For this reason an asteroid can have an orbit completely typical for a comet and vice versa (Yeomans 2000).

More than one attempt has been made to determine the nature of the TCO by means of comparison of results obtained using some other numerical scheme with the observational data. They debated about the adequateness of various models. However, sufficiently accurate models have not yet been created, and it is unclear in general whether the conclusions about the TCO's nature can be drawn in this way.

Last, an argument was put that the eyewitnesses did not definitely describe a smoky trail after the flight of the TCO (Kolesnikov et al. 1999; Rasmussen et al. 2001; Kolesnikov et al. 2003). Smoky trails are typical phenomena that can be observed minutes and even hours after the falls of stony and iron bodies (Astapovich

1958). The authors do not know if the trails can be observed after the falls of comets as well. The partisans of the cometary hypothesis ask the following question: If the TCO was an asteroid, why did eyewitnesses not watch a smoky trail? This incorrect question includes an implicit assumption about the similarity of meteoroid falls with different scales; however, such similarity does not exist. Bodies of some meters in size and smaller do not form a plume, and a body of the Tunguska scale does form a plume. Therefore, a smoky trail similar to those observed after the impacts of small meteors can exist after the impact of a stony TCO only within a very short time between the fall and plume development. However, it is likely that a smoky trail cannot form at this time interval as well because the ionized wake behind the TCO is much larger and brighter, optical thickness is bigger and, therefore, on the one hand, the wake screens dust and, on the other hand, the radiation fluxes are higher and dust blown off the meteoroid surface is intensely vaporized in the wake. And ablation of a 60-m-diameter stony body goes somewhat differently than in meteoroids of much smaller size at the same altitudes. A quantity of melted material per unit area of a body surface is determined by the thermal conductivity of meteoroid material and is approximately of the same order of magnitude for bodies of various sizes, but vaporization of a large body is more intense due to higher radiation flux density at the surface, which increases with the size. Therefore, a large body produces fewer melted particles per unit area of a surface. Second, the melt is blown off the surface of a large body at lower altitudes because the velocity of melt motion along the surface depends mainly on altitude and meteoroid velocity, and to escape the body the melt must travel a distance on the order of a meteoroid size. Third, melt droplets, which nevertheless get to the wake, are subjected to more intense radiation fluxes. Because of this, the wake after the TCO fall at altitudes 40–80 km probably could contain only condensed particles, but the air in the wake continues to radiate as long as the plume develops contrary to smaller bodies with a wake that rapidly cools, mixing with cold air. However, these considerations are only qualitative, and more precise estimates or calculations in support of (or against) formation of a smoky trail after the fall of a hypothetical TCO should be made by those researchers who put forward this argument.

The chemical analyses of found microparticles and microspherules provided contradictory opinions about the nature of the TCO. Analysis of microspherules found in soil has not given a chance to establish their connection with TCO. Microparticles found in annual tree rings were interpreted as vestiges of a stony body (Longo et al. 1994; Serra et al. 1994); however, this has not been proved. Only recently a sufficiently serious argument appeared. It is the result of geochemical analyses of peat, which count in favor of the hypothesis of an impact of a comet, at that, probably a comet with a composition different from those studied so far, that is a comet with a very high content of carbon, low content of dust, and, probably low content of water. But it still lies ahead to adjust these results to the entire picture of the Tunguska event and trace the evolution of the TCO material from the entry of an icy body to the atmosphere to the final underground state of a cometary carbon

and other components in permafrost layers. This is a very intricate problem, if one does not restrict the considerations to the general ideas. The question about the existence of icy comets with a high content of carbon and low content of mineral dust can probably only be solved in the future, when observational data on the comet compositions will be gained.

10 CONCLUSIONS

This chapter has considered many aspects of the Tunguska event problem. Owing to the efforts of many researchers the general picture of the event has become more or less clear, to the first rough approximation; however, many unanswered questions remain. The answers would allow researchers first, to develop a more accurate model of this phenomenon; second, to understand better the physical and chemical processes that accompany the falls of large meteoroids; and third, perhaps to find new effects that are still unknown. The history of the Tunguska event investigations shows how understanding the main processes gradually advanced from an idea of pioneering research about a “simple” fall of an iron meteorite, to the concept of a fragmented flattening meteoroid, which developed at the end of the 1970s, and at last, to the electromagnetic effects, which still remain largely unknown. The most hazardous impact with which humankind has been confronted is worthy of further investigation and appropriate efforts.

The threshold of meteoroid sizes that determines when the asteroid and comet hazards become appreciable lies in the range of 30–100 m. The chance is good that impacts of such bodies will occur in the not very distant future. The probability that our contemporaries will observe them is several percents and the consequences of such impacts can be very substantial. An impact such as that of TCO is undoubtedly very perilous. In mechanical and thermal effects, it is similar to the most powerful of all nuclear charges, detonated at an altitude that gives maximum devastation. A large city could be demolished after the fall of a body with energy equal to the Tunguska event.

Some effects, such as the ejection of plume or electromagnetic disturbances, were not clearly apparent in the Tunguska event and remained poorly understood. Today these effects greatly increase the danger. Tunguses had no electricity, radio communication, any important instruments, storages of explosive or inflammable materials, or radioactive materials. The 1908 impact took place over a sparsely populated area in which the population density remains the lowest on Earth even today. Because of this the damage was minimal. Nobody knows where and when the next such impact will happen and what the damage will be. However, it is clear that with the growth of population density on the Earth and the increase in the number of vulnerable objects the damage and disaster will be appreciably greater.

It is doubtful whether it is possible to discover in proper time a body of the same class as the TCO: a very small comet with a velocity that can be higher than typical asteroid velocities and an unpredictable orbit. Therefore, should this threatening object be discovered, mitigation measures must be undertaken immediately. The evident effective technique of defense in such a situation is meteoroid destruction

by a nuclear explosion. However, this has an important disadvantage—a nuclear weapon arsenal must be maintained on the Earth and new special nuclear devices must be created. The matter is also complicated by the fact that the properties of bodies like the TCO are poorly understood. The composition and structure of a great majority of comets can be judged only by the few that have been studied; and the TCO (if it was a comet) could possibly be different from them. For the present, it is not known how multifarious the comets can be. Further investigations of the Tunguska event could contribute significantly to knowledge about the properties of perilous bodies and the struggle against the hazards caused by comets and asteroids.

REFERENCES

- Adushkin VV, Nemchinov IV (1994) Consequences of impacts of cosmic bodies on the surface of the Earth. In: Gehrels T (ed) Hazards due to comets and asteroids University Arizona Press, Tucson, pp 721–778
- Astapovich IS (1958) Meteoric phenomena in the Earth atmosphere. Fizmatgiz, Moscow, (in Russian), p 640
- Bailey ME, Markham DJ, Massai S, Scriven JE (1995) The 1930 August 13 ‘Brazilian Tunguska’ event. *Observatory* 115(1128):250–253
- Ben-Menachem A (1975) Source parameters of the Siberian explosion of June 30, 1908, from analysis and synthesis of seismic signals at four stations. *Phys Earth Planet Intern* 11:1–35
- Bidyukov BF (1988) Thermoluminescent analysis of soils of the Tunguska fall area. *Nauka, Siberian Branch, Novosibirsk*, pp 96–104 (in Russian)
- Bidyukov BF (1997) Thermoluminescent anomalies in a zone of the Tunguska phenomenon influence. *Tungusskiy Vestnik KSE (in Russian)* 5:26–33
- Bidyukov BF, Krasavchikov VO, Razum VA (1990) Thermoluminescent anomalies of soils of the Tunguska fall area. *Nauka, Siberian Branch, Novosibirsk*, pp 88–108 (in Russian)
- Boslough MB, Crawford DA (1997) Shoemaker-Levy 9 and plume-forming collisions on Earth. In: Remo JL (ed) Near Earth objects. *Ann NY Acad Sci* 822:236–282
- Boyarkina AP, Sidoras SD (1974) Paleomagnetic studies in the area of Tungusian meteorite falling. *Geologiya i Geofizika (in Russian)* 3:79–84
- Boyarkina AP, Goldine VD, Sidoras SD (1980) About territorial structure of the remnant magnetization vector of soils in the area of the Tunguska meteorite fall. *Nauka, Siberian Branch, Novosibirsk*, pp 163–168 (in Russian)
- Bronshten VA (1981) Physics of meteoric phenomena. *Nauka, Moscow*
- Bronshten VA (1992) Nature of the anomalous sky luminescence connected with the Tungus event. *Solar System Res* 25(4):69–80
- Bronshten VA (1999) Trajectory and orbit of the Tunguska meteorite revisited. *Meteoritics and Planetary Sci* 34:A137–A143
- Bronshten VA (2000) Tunguska meteorite: history of investigation. A.D. Selyanov, Moscow, p 312 (in Russian)
- Bronshten VA (2002) Magnetic effect of the Tungus meteorite. *Geomagnetism and Aeronomy* 42(6): 816–818
- Bronshten VA, Boyarkina AP (1975) Calculation of air waves of the Tunguska meteorite. In: Problems of meteoritics. *Nauka Publishers, Siberian Branch, Novosibirsk*, pp 47–53 (in Russian)
- Brown PG, Spalding RE, ReVelle DO et al (2002) The flux of small near-Earth objects colliding with the Earth. *Nature* 420(6913):294–296
- Buratti BJ, Johnson LL (2003) Identification of the lunar flash of 1953 with a fresh crater on the Moon’s surface. *Icarus* 161:192–197
- Chyba CF, Thomas PJ, Zahnle KJ (1993) The 1908 Tunguska explosion: atmospheric disruption of a stony asteroid. *Nature* 361(6407):40–44

- Courty M-A (1998) Causes and effects of the 2350 BC Middle East anomaly evidenced by micro-debris fallout, surface combustion and soil explosion. In: Peiser BJ, Palmer T, Bailey ME (eds) Natural catastrophes during bronze age civilisation: archaeological, geological, astronomical and cultural perspectives. British Archaeological Reports—S728. Archaeopress, Oxford, pp 93–108
- Crawford DA, Boslough MB, Trucano TG, Robinson AC (1994) The impact of comet Shoemaker-Levy 9 on Jupiter. *Shock Waves* 4:47–50
- Doroshin IK (2002) About interpretation of data on carbon isotopy in peat from the region of the fall of Tunguska meteorite. *Tungusskiy Vestnik KSE* 15:29–30 (in Russian)
- Dragavtsev VA, Lavrova LA, Plekhanova LG (1975) Environmental analysis of linear growth of *Pinus silvestris* at the area of 1908 Tunguska event. In: Problems of meteoritics. Nauka. Siberian Branch, Novosibirsk, pp 132–141(in Russian)
- Dyomin DV, Dmitriev AN, Zhuravlyov VK (1984) Informational aspect of studies of Tunguska phenomenon of 1908. In: Meteoritic studies in Siberia. Nauka, Novosibirsk, pp 30–48 (in Russian)
- Epiktetova LE (1976) New reports of eyewitnesses of the fall of Tunguska meteorite. In: Problems of meteoritics. Tomsk University Press, Tomsk, pp 20–34 (in Russian)
- Farinella P, Foschini L, Froeschle Ch et al(2001) Probable asteroidal origin of the Tunguska cosmic body. *Astronom Astrophys* 377:1081–1097
- Fast VG (1967) Statistical analysis of the Tunguska flattened area. Tomsk University Press, Tomsk, vol 2, pp 40–61 (in Russian)
- Fesenkov VG (1949) Atmosphere dimness caused by fall of Tunguska meteorite on June 30, 1908. *Meteoritika* 6:8–12. Nauka Publishers, Moscow (in Russian)
- Fesenkov VG (1961) The cometary nature of the Tunguska meteorite. *Astronom J* 38(4):577–592
- Fesenkov VG (1969) Nature of comets and the Tunguska phenomenon. *Solar System Res* 3:177–179
- Field GB, Ferrara A (1995) The behaviour of fragments of Comet Shoemaker-Levy 9 in the atmosphere of Jupiter. *Astrophys J* 438:957–967
- Goldine VD (1998) Search for local centres of the Tunguska explosions. *Planet Space Sci* 46(2/3):151–154
- Grigoryan SS (1979) On the motion and disruption of meteorites in planetary atmospheres. *Kosm Issled* 17(6):875–893
- Grigoryan SS (1998) The cometary nature of the Tunguska meteorite: on the predictive possibilities of mathematical models. *Planet Space Sci* 46(2/3):213–217
- Hills JG, Goda MP (1993) The fragmentation of small asteroids in the atmosphere. *Astronom J* 105(3):1114–1144
- Hou QL, Ma PX, Kolesnikov EM (1998) Discovery of iridium and other element anomalies near the 1908 Tunguska explosion site (1908). *Planet Space Sci* 46(2/3):179–188
- Hou QL, Kolesnikov EM, Xie LW et al(2000) Discovery of probable Tunguska cosmic body material: anomalies of platinum group elements in peat near the Explosion Site (1908). *Planet Space Sci* 48:1447–1455
- Hou QL, Kolesnikov EM, Xie LW et al(2004) Platinum group element abundance in a peat layer associated with the Tunguska event, further evidence for a cosmic origin. *Planet Space Sci* 52(4): 331–340. Erratum: *Planet Space Sci* 2004 52(8):773
- Ivanov KG (1961) Geomagnetic phenomena observed at Irkutsk magnetic observatory after explosion of the Tunguska meteorite. *Meteoritika* 21:46–48. Nauka Publishers. Moscow (in Russian)
- Ivanov KG (1964) Geomagnetic effect of Tunguska catastrophe. *Meteoritika* 24:141–151. Nauka Publishers. Moscow (in Russian)
- Ivanov KG (1967) On the nature of the Tunguska fall influence on the upper ionosphere, geomagnetic field and night glows. *Geomagnetism Aeronomy* 7:1031–1035 (in Russian)
- Ivanov KG (2002) Once again on the problem of modeling the geomagnetic effect of the Tungus impact. *Geomagnetism and Aeronomy* 42(6), 819–820
- Jull AJT, Burr GS, Kring DA (2001) Comment on “Evidence for a very high carbon/iridium ratio in the Tunguska impactor”. *Meteoritics Planetary Sci* 36(7):999–1001
- Klein RI, McKee CF, Colella P (1994) On the hydrodynamic interaction of shock waves with interstellar clouds. I. Nonradiative shocks in small clouds. *Astrophys J* 420 (1):Pt.1, 213–236

- Kolesnikov EM (2002) Isotopic and geochemical data prove presence of cosmic material in the region of Tunguska catastrophe. In: *Tungusskiy Vestnik KSE* 15, pp 4–8. Tomsk University Press, Tomsk (in Russian)
- Kolesnikov EM, Boettger T, Kolesnikova NV (1995) Isotopic composition of carbon and hydrogen in peat from 1908 Tunguska space body explosion site. *Doklady RAS* 343(5):669–672
- Kolesnikov EM, Boettger T, Kolesnikova NV (1999) Finding of probable Tunguska cosmic body material: isotopic anomalies of carbon and hydrogen in peat. *Planet Space Sci* 47:905–916
- Kolesnikov EM, Kolesnikova NV, Boettger T (1998b) Isotopic anomaly in peat nitrogen is a probable trace of acid rains caused by 1908 Tunguska bolide. *Planet Space Sci* 46:163–167
- Kolesnikov EM, Longo J, Boettger T et al (2003) Isotopic-geochemical study of nitrogen and carbon in peat from the Tunguska Cosmic Body explosion site. *Icarus* 161(2):235–243
- Kolesnikov EM, Stepanov AI, Gorid'ko EA et al (2000) Traces of comet material in peat from the site of explosion of Tunguska cosmic body. In: *Tungusskiy Vestnik KSE* 11, pp 27–35. Tomsk University Press, Tomsk (in Russian)
- Kolesnikov EM, Boettger T, Kolesnikova NV, Younger F (1996) Anomalies in isotopic composition of carbon and nitrogen of peat from the region of 1908 explosion of Tunguska cosmic body. *Geochemistry (Geokhimija)* 347(3):378–382 (in Russian)
- Kolesnikov EM, Stepanov AI, Gorid'ko EA, Kolesnikova NV (1998a) Discovery of probable traces of Tunguska comet of 1908—Element anomalies in peat. *Doklady RAS* 363(4):531–535 (in Russian)
- Konenkin VG (1967) Eyewitness reports about Tunguska meteorite of 1908. In: *Problem of Tunguska meteorite*. Vol 2, pp 31–35 Tomsk University Press, Tomsk (in Russian)
- Koricansky DG, Zahnle KJ (2003) High-resolution simulations of the impacts of asteroids into the Venusian atmosphere III: further 3D models. *Icarus* 161(2):244–261
- Koricansky DG, Zahnle KJ, Mac Low M-M (2000) High-resolution simulations of the impacts of asteroids into the Venusian atmosphere. *Icarus* 146:387–403
- Koricansky DG, Zahnle KJ, Mac Low M-M (2002) High-resolution simulations of the impacts of asteroids into the Venusian atmosphere II: 3D models. *Icarus* 157:1–23
- Korobeinikov VP, Chushkin PI, Shurshalov LV (1991) Combined simulation of the flight and explosion of a meteoroid in the atmosphere. *Solar System Res* 25(3):242–254
- Korobeinikov VP, Shurshalov LV, Vlasov VI, Semenov IV (1998) Complex modelling of the Tunguska catastrophe. *Planet Space Sci* 46(2/3):231–244
- Korotkov PF, Kozin VN (2000) The Tunguska meteorite explosion and flattened wood origin. *Solar System Res* 34(4):326–332 (in Russian)
- Kring DA (1997) Air blast produced by the Meteor Crater impact event and a reconstruction of the affected environment. *Meteoritics Planetary Sci* 32:517–530
- Kulik LA (1931) Brazilian double of Tunguska meteorite. *Priroda i Lyudi* 13–14, 6–11 (in Russian)
- Lind EN (1997) Magnetic properties of soils in the region of Tunguska catastrophe of 1908. *Geophysical research in Middle Siberia*. KNIIGiMS, Krasnojarsk, pp 306–312
- Longo G, Serra R, Secchini, S, Galli M (1994) Search for microremnants of the Tunguska cosmic body. *Planet Space Sci* 42:163–177
- Lyne JE, Tauber ME (1995) An analysis of the Tunguska event. *Nature* 375(6533):638–639
- Lyne JE, Tauber M, Fought R (1996) An analytical model of the atmospheric entry of the large meteors and its application to the Tunguska event. *J Geophys Res* 101(E10):23,207–23,212
- Lyne JE, Tauber ME, Fought RM (1998) A computer model of the atmospheric entry of the Tunguska object. *Planet Space Sci* 46(2/3):245–252
- Master S (2001) A possible Holocene impact structure in the Al'Amarah Marshes, near the Tigris-Euphrates confluence, southern Iraq. *Meteoritics and Planetary Sci Suppl* 36(9):A124
- Nazarov MA, Korina MI, Barsukova LD et al (1990) Material traces of the Tunguska bolide. *Geokhimiya* 5:627–639 (in Russian)
- Nekrasov VI (1962) Study of forest growth on the region of the fall of Tunguska meteorite. *Lesnoje Khozjajstvo* 1:22–24 (in Russian)
- Nemchinov IV, Losseva TV, Merkin VG (1999) Estimate of geomagnetic effect at a falling of Tunguska meteoroid. In: *Physical processes in geospheres: their developments and interacting (Geophysics of the strong disturbances)*. Trans. Inst. Dynamics Geospheres RAS. Moscow, pp 324–338 (in Russian)

- Neukum G, Ivanov BA (1994) Crater size distributions and impact probabilities on Earth from Lunar, terrestrial-planet, and asteroid cratering data. In: Gehrels T (ed) Hazards due to Comets and Asteroids. University of Arizona Press, Tucson, pp 359–416
- Pasechnik IP (1976) Evaluation of parameters of the Tunguska meteorite explosion by seismic and microbarographic data. In: Space matter in the Earth. Nauka Publishers, Siberian Branch, Novosibirsk, pp 25–54 (in Russian)
- Pasechnik IP (1986) Refinement of time of the 30 June 1908 Tunguska explosion using seismic data. Nauka Publishers, Siberian Branch, Novosibirsk, pp 62–69 (in Russian)
- Petrov GI, Stulov VP (1975) Motion of large bodies in planetary atmospheres. *Kosm Issled* 13(4): 587–594
- Plekhanov GF (2000) Thoughts about nature of Tunguska meteorite. Tomsk University Press, Tomsk, p 68 (in Russian)
- Plekhanov GF, Plekhanova LG, Privalov GF (1968) On mutational consequences of Tunguska explosion of 1908. *Izvestiya Sibirskogo Otdeleniya Akademii Nauk SSSR. Ser Biolog Med Nauk* 5(1):44–48 (in Russian)
- Plekhanov GF, Kovalevskiy AF, Zhuravlyov VK, Vasilyev NV (1961) On effect of the Tunguska meteorite explosion on the geomagnetic field. *Geologiya i Geofizika* No.6:94–96 (in Russian)
- Plekhanova LG, Dragavtsev VA, Plekhanov GF (1984) Effect of some environmental factors upon genetic consequences of 1908 Tunguska catastrophe. In: Meteoritic studies in Siberia. Nauka Publishers, Siberian Branch, Novosibirsk, pp 94–98 (in Russian)
- Putiatin BV (1980) The radiation action on the Earth during the large meteoritic body flight in the atmosphere. *Dokl Akad Nauk SSSR* 252(2):318–320
- Rasmussen KL, Olsen HJF, Gvozdz R, Kolesnikov EM (1999) Evidence for a very high carbon/iridium ratio in the Tunguska impactor. *Meteoritics Planetary Sci* 34:891–895
- Rasmussen KL, Olsen HJF, Gwozdz R, Kolesnikov EM (2001) Reply to comment by Jull AJT, Burr GS, Kring DA *Meteoritics Planetary Sci* 36(7):1001–1006
- Romeiko VA (1992) Nature of the optical anomalies of summer of 1908. *Solar System Res* 25(4): 362–368
- Sekanina Z (1983) The Tunguska event: no cometary signature in evidence. *Astronom J*, 88:1382–1414. Erratum *Astronom J* 1984 89:185 (Paper 1)
- Sekanina Z (1988) Evidence for asteroidal origin of the Tunguska object. *Planet Space Sci* 46(2/3): 191–204
- Serra R, Cecchini S, Galli M, Longo G (1994) Experimental hints on the fragmentation of the Tunguska cosmic body. *Planet Space Sci* 42:777–783
- Shoemaker EM (1983) Asteroid and comet bombardment of the Earth. *Ann Rev Earth Planet Sci* 11:461–494
- Shurshalov LV (1980) On taking into account of radiation in calculation of explosion in nonuniform atmosphere. *Izvestiya Akademii Nauk SSSR. Ser Fluid Dynamics* 3:105–112 (in Russian)
- Shuvalov VV (1999) Atmospheric plumes created by meteoroids impacting the Earth. *J Geophys Res* 104(E3):5877–5889
- Shuvalov VV, Artemieva NA (2002) Numerical modeling of Tunguska-like impacts. *Planet Space Sci* 50:181–192
- Sidoras SD, Boyarkina AP (1976) About results of paleomagnetic studies in the area of the Tunguska meteorite fall. In: Problems of Meteoritics. Tomsk University Press, Tomsk, pp 64–73 (in Russian)
- Sokolova OI, Krasnov VM, Nikolaevskii NF (2003) Changes in the geomagnetic field under the effect of rocket launches from the Baikonur spaceport. *Geomagnetism and Aeronomy* 43(4):525–529
- Svetsov VV (1995) A comet fall into the Jovian atmosphere. *Solar System Res* 29(4):287–294
- Svetsov VV (1996a) Where have the debris of the Tunguska meteoroid gone? *Solar System Res* 30(5):378–390
- Svetsov VV (1996b) Total ablation of the debris from the 1908 Tunguska explosion. *Nature* 383(6602):697–699
- Svetsov VV (1998) Could the Tunguska debris survive the terminal flare? *Planet Space Sci* 46(2/3): 261–268
- Svetsov VV (2002) Petrophysics hints at unexplored impact physics. In: Buffetaut E, Koeberl C (eds) Geological and biological effects of impact events. Springer-Verlag, Berlin, pp 265–295

- Svetsov VV (2003) What eyewitnesses of Tunguska event could see. Jubilee Scientific Conference 95 Years of Tunguska Problem. Abstr. Moscow State University, Moscow, pp 72–75 (in Russian)
- Svetsov VV, Nemtchinov IV, Teterev AV (1995) Disintegration of large meteoroids in Earth's atmosphere: theoretical models. *Icarus* 116:131–153. Errata: *Icarus*. 1996 120(2):443
- Sytinskaya NN (1955) To the problem of trajectory of the Tunguska meteorite. *Meteoritika* 13:86–91. Nauka Publishers, Moscow (in Russian)
- Takata T, Ahrens TJ, Phillips RJ (1995) Atmospheric effects on cratering on Venus. *J Geophys Res* 100(E11):23,329–323,348
- Turco RP, Toon OB, Park C et al (1982) An analysis of the physical, chemical, optical and historical impacts of the 1908 Tunguska meteor fall. *Icarus* 50:1–52
- Vasilyev NV (1998) The Tunguska meteorite problem today. *Planet Space Sci* 46(2/3):129–150
- Vasilyev NV (2004) Tunguska “meteorite”. Cosmic phenomenon of 1908 summer. *Russkaya Panorama*, Moscow, p 360 (in Russian)
- Vasilyev NV, Batisheva AI (1976) On connection of increased forest renewal with trajectory of Tunguska meteorite. In: *Problems of meteoritics*. Tomsk University Press, Tomsk, pp 149–160 (in Russian)
- Vasilyev NV, Dmitrienko VK, Fedorova OP (1980) On biologic consequences of Tunguska explosion. In: *Interaction of meteoritic matter with Earth*. Nauka, Novosibirsk, pp 188–195 (in Russian)
- Vasilyev NV, Kovalevskiy AF, Razin SA, Epiketova LE (1981) Reports of eyewitnesses of the Tunguska fall. VINITI (All Union Institute of Science Information), Deponent No. 5350–81, Moscow (in Russian)
- Vasilyev NV, Zhuravlyov VK, Dyomin DV, Ammosov AD, Batisheva AI (1976) On some anomalous effects associated with the Tunguska meteorite fall. *Nauka, Siberian Branch, Novosibirsk*, pp 71–87 (in Russian)
- Vasilyev NV, Zhuravlyov VK, Zhuravlyova RK, Kovalevsky AF, Plekhanov GF (1965) Noctilucent clouds and optical anomalies connected to the Tunguska meteorite fall. *Nauka, Moscow* (in Russian)
- Vorobyov VA, Dyomin DV (1976) New results of studies of heat affection on larch trees in the Tunguska meteorite fall area. In: *Problems of meteoritics*. Tomsk University Press, Tomsk, pp 58–63 (in Russian)
- Yavnel' AA (1988) On the moment of flight and trajectory of the Tunguska bolide on June 30, 1908 as observed by witnessess. In: *Actual problems of Meteoritics in Siberia*. Nauka Publishers, Siberian Branch, Novosibirsk, pp 75–85 (in Russian)
- Yavnel' AA (1992) Time of transit and trajectory of the Tungus meteorite, from data collected in 1908. *Solar System Res* 25(4):381
- Yeomans D (2000) Small bodies of the Solar System. *Nature* 404:829–832
- Yonenobu H, Takenaka C (1998) The Tunguska event as recorded in a tree trunk. *Radiocarbon* 40(1–2):367–371
- Zahnle K (1992) Airburst origin of dark shadows on Venus. *J Geophys Res* 97(E8):10243–10255
- Zahnle K (1996) Leaving no stone unburned. *Nature* 383:674–675
- Zahnle K, McLow M.-M (1994) The collision of Jupiter and Comet Shoemaker-Levy 9. *Icarus* 108(1): 1–17
- Zhuravlyov VK (1967) On the estimate of the light energy of the Tunguska explosion. In: Plekhanov GF (ed) *The Tunguska meteorite problem*. 2 edn, pp 120–122 Tomsk. University Press, Tomsk
- Zotkin IT (1961) On anomalous optical effects in atmosphere related to the Tunguska meteorite fall. *Meteoritika* 20:40–53. Nauka Publishers, Moscow (in Russian)
- Zotkin IT (1969) Anomalous twilights related to the Tunguska meteorite. *Meteoritika* 29:170–176 Nauka Publishers, Moscow (in Russian)
- Zotkin IT, Chigorin AN (1988) Determination of radiant of Tunguska meteorite from visual observations of eyewitnesses. *Actual problems of meteoritics in Siberia*. Nauka, Novosibirsk, pp 85–95 (in Russian)
- Zotkin IT, Chigorin AN (1991) Radiant of the Tunguska meteorite from visual observations. *Solar System Res* 25:459–464
- Zotkin IT, Tsikulin MA (1966) Modelling of the Tunguska meteorite explosion. *Dokl Akad Nauk SSSR* 167(1):59–62

CHAPTER 8

HIGH-VELOCITY IMPACT EJECTA: TEKTITES AND MARTIAN METEORITES

NATALIA ARTEMIEVA

Institute for Dynamics of Geospheres, Russian Academy of Sciences, Moscow 119334, Russia
E-mail: artemeva@psi.edu

When you have excluded the impossible, whatever remains,
however improbable, must be the truth

Arthur Conan Doyle

1 INTRODUCTION

Earth retains the poorest record of impact craters through geologic time. Important clues of the occurrence of large impact events through Earth's geologic history come from the presence of preserved distal ejecta layers. Distal ejecta comprise a small but essential fraction of material ejected in impacts; it was crucial in the recognition of the end-Cretaceous impact event (Alvarez et al. 1980). This chapter discusses specific types of distal ejecta, which are characterized by substantial shock compression, and high ejection velocity, and are best represented by the enigmatic tektites and Martian–lunar meteorites.

Tektites are naturally occurring glasses, generally a few centimeters in diameter, currently found in four distinct strewn fields (Table 1).

Microtektites (<1 mm in diameter) have been found in deep-sea cores of three of the four strewn fields (Glass 1972). Tektites of a given strewn field are related to each other by their chemistry, age, and petrologic and physical characteristics (see reviews by Glass 1990; Koeberl 1990, 1994). There is numerous evidence that tektites were used by ancient civilizations. However, their scientific study began with Charles Darwin's description of Australites in *Geology of the Voyage of the Beagle* (1851). Early hypotheses of their origin (volcanic glass, impact of glassy asteroid, ablation of high-velocity cosmic body in the Earth's atmosphere, and

Table 1. Characteristics of the four strewn fields (based on Koeberl, 1994; Montanari and Koeberl 2000). Table is adapted from Artemieva (2002) and reprinted with kind permission of Springer Science and Business Media

	North American	Central European	Ivory Coast	Australasian
Age, Ma	35.4	15	1.1	0.77
Area, 10 ⁶ km	10–30	0.3	4	50
Total mass, 10 ⁶ t	300–42 000	5?	20	2000?
Source crater	Chesapeake Bay	Ries	Bosumtwi	
Source crater diameter, km	85	24	10.5	
Distance from source crater, km	>1300	250–420	300–1000	

even artifacts of ancient glass-makers) are clearly unrealistic. The first celestial mechanics deduction was that tektites must come from some source no farther than the Moon (Urey 1955). The result was confirmed by the small amounts of cosmogenic isotopes (²⁶Al and ¹⁰Be) in Australian-Asian tektites (Viste and Anders 1962). At the same time the huge extent of some of the known strewn fields implies a powerful launch mechanism: the only two in nature are volcanism and impact. By the mid-1960s, four hypotheses emerged: high-velocity impacts on Earth or the Moon, and volcanic activity on these bodies. Terrestrial volcanic glasses (obsidians) are similar to tektites in many aspects. On the other hand, typical ejection velocities during a volcanic eruption never exceeds 700 m·s⁻¹, which is not enough to create a large tektite strewn field similar to the Australian-Asian. The extremely young age of all tektites (<35 Myr) is in disagreement with lunar chronology and the early extinction of lunar volcanism. Geochemical studies of Apollo lunar samples demonstrated that the silica content of lunar rocks is not >50%, whereas tektites usually have >60% silica. It is worth mentioning that the first real samples of lunar rocks reaching the Earth, lunar meteorites, were identified on Earth only toward the end of the 1980s (Eugster 1989). A very interesting historical description of tektite exploration can be found in O’Keefe 1976. This chapter concentrates on the latest hypothesis: Tektites are high-velocity molten ejecta originating in terrestrial craters.

1.1 Martian Meteorites

The hypothesis of a Martian origin for nine achondrites was suggested more than 20 years ago (Nyquist et al. 1979; Walker et al. 1979; Wasson and Wetherill 1979; McSween and Stolper 1980; Wood and Ashwal 1981) and is now widely accepted (Nyquist et al. 2001). They were called the SNC meteorites (Shergotty, Nakhla, and Chassigny) for a long time; however, this abbreviation is not valid anymore, as ALH84001 is not SNC. The term Martian meteorites (MM) is used here. Although understanding of the mineralogy and geochemistry of MM has made significant progress, the physics of the phenomenon is still not totally clear. Initially, the impossibility of producing high-velocity solid ejecta was based on simple estimates of shock compression: The stress level of shergottite meteorites

(30 GPa) corresponds to a maximum ejection velocity of $3.2 \text{ km}\cdot\text{s}^{-1}$ (well below escape velocity for Mars), whereas a shock stress level of 57 GPa (well above incipient melting for basaltic materials) is required to produce escape. Various ideas to accelerate solid material to escape velocities have been suggested since then: additional acceleration of the materials at near-tangential incidence—ricochet (Nyquist 1982; Swift and Clark 1983); turbulent mixing with material shocked to higher stresses (Swift 1983); and acceleration by shock vaporized buried ice (Wasson and Wetherill 1979; Wood and Ashwal 1981; O’Keefe and Ahrens 1983) or by high-density impact vapor plume (O’Keefe and Ahrens 1986). However, the most consistent hypothesis of MM origin is acceleration of solid material in a spallation zone, where the pressure gradient, not the absolute shock pressure, is extremely high (Melosh 1984). The growing family of Martian meteorites together with the lack of appropriate large craters points to a “small impact” scenario of ejection—a few moderate impacts (four to eight on the basis of geochemical data and cosmic ray exposure [CRE] age) and ejection of rather small, 10s-cm-sized particles. Head et al. (2002) found that craters as small as $\sim 3 \text{ km}$ can eject cm-sized particles from Mars after a vertical impact, but did not address the process of the atmospheric deceleration of these particles. Later, Artemieva and Ivanov (2004) showed that oblique impacts are much more efficient in producing high-velocity ejecta, and fragments $>30 \text{ cm}$ in size could escape Mars.

2 HYDROCODE MODELING OF HIGH-VELOCITY EJECTA

2.1 SOVA Hydrocode

Oblique impacts are simulated with a three-dimensional (3D) version of the SOVA code (Shuvalov 1999), coupled to ANEOS-derived (Thompson and Lauson 1972) equation of state (EOS) tables for the materials in use. The code allows the modeling of multidimensional, multimaterial, large deformation, and strong shock wave flows. The initial stage of an impact is described in the frame of Eulerian equations of motion for a continuous medium without any constitutive models. At this stage shock pressure is high and allows for a simplified hydrodynamic description, neglecting material strength. To include some Lagrangian features into the model the authors use a tracer particle technique (Pierazzo et al. 1997). Tracers are massless particles, which move with local flow velocity and allow reconstructing dynamic (trajectories, velocities), thermodynamic (pressure, temperature), and even disruption (strain, strain rate) histories in any part of the flow. The authors have up to a few million tracers to define maximum shock compression (which defines melting) and maximum velocity (which defines escape) values, and write a full history for up to 1,000 tracers.

2.2 Particles in the Flow

The late stage of ejecta motion in an impact-disturbed atmosphere is described by multiphase hydrodynamics (Valentine and Wohletz 1989). Material disruption is

assumed to occur when the density of the solid or molten material drops below the normal density for a given temperature within a single computational cell (i.e., the material is subject to tension). Each particle that is not a massless tracer is characterized by its individual parameters (mass, density, position, and velocity) and exchanges momentum and energy with a surrounding vapor–air mixture. The particle's initial position within the cell is randomly defined and the hydrodynamic velocity gives its initial velocity. All particles are treated as spherical, although the shape may differ substantially. Nevertheless, strongly asymmetric fragments rotate quickly and may be presented, on average, as spheres.

After disruption, each particle is subject to drag and gravity forces. In the absence of gas flow, the balance of Stokes drag and gravity defines the precipitation velocity of the particle that depends on the particle's density, diameter, and gas viscosity. Its value varies from a few $\text{cm}\cdot\text{s}^{-1}$ for small, mm-sized particles to tens of $\text{m}\cdot\text{s}^{-1}$ for m-sized fragments. Thus, ballistic motion, which takes into account only gravity and is widely used in ejecta deposition estimates (Melosh 1989), is a simplified example of particle motion in a post-impact flow. As the authors consider simultaneously all particles within a given computational cell, they describe both the individual and the collective behavior of these particles (e.g., the presence of a high-velocity large fragment allows the smaller neighbors to move in its hydrodynamic shadow). Direct collisions between particles are not considered. This assumption is valid if the volume of solid particles is less than the volume of a computational cell. To save computational time and computer memory the representative particles approach (Teterev 1999) is used, i.e., each particle describes the motion of a large number of real fragments (up to a billion) having approximately the same parameters and trajectories.

The size distribution of the fragments is a crucial issue for particles' motion in an ejecta plume. The diameter of molten particles is taken in a range from 0.01 to 3 cm (Stöffler et al. 2002), in agreement with Melosh and Vickery's (1991) estimates and the size of terrestrial tektites (O'Keefe 1976). The size distribution of solid fragments in high-velocity impacts or high-energy explosions is a much more complex problem. It has been studied experimentally (Nakamura and Fujiwara 1991; Cintala et al. 1999), and numerically (Grady and Kipp 1980; Melosh et al. 1992), and has been derived from the lunar and terrestrial crater observations (Gault et al. 1963; Ivanov and Basilevsky 1983; Vickery 1986). This fragment's size distribution is a consequence of the whole cratering process, i.e., it represents the sum of individual ejection events taking place through time and space. The size of fragments ejected at a given point and at a given time depends on the material properties and the process itself, i.e., maximum compression, ejection velocity, strain, strain rate, etc. (Grady and Kipp 1980; Melosh et al. 1992; Asphaug and Melosh 1993; Head et al. 2002; Artemieva and Ivanov 2004). An average fragment size can be also related to ejection velocity (Melosh 1984) or, alternatively, one can use the standard cumulative distribution of fragments $N = CM^{-b}$ (Melosh 1989) with the maximum size defined by the value of maximum compression (Shuvalov 2002). Comparison of all three methods may be found in Artemieva and Ivanov (2004).

2.3 Initial Conditions on Mars and on the Earth

Oblique impacts of asteroids (granite EOS) or comets (ice EOS) into both a dry (granite EOS) and wet (granite plus 20% of water) surface have been modeled. The surface is treated as intact and nonporous as all known meteorites are intact solid fragments from terrains of volcanic origin (with probably a few exceptions, such as ALH84001 and one of the Yamatos, which are shocked monomict breccia). Average asteroid impact velocity on Mars is around $10 \text{ km}\cdot\text{s}^{-1}$, whereas comet impact velocity is substantially higher, up to $35 \text{ km}\cdot\text{s}^{-1}$. These values are typical for the modern flux of impactors on Mars (Steel 1998). Impact angle varies from 15° to 90° . Neglecting gravity and strength in the initial stage of the impact one can rewrite all hydrodynamic equations in a dimensionless form, where the projectile size is not important and all spatial values may be measured in projectile units. (The radius of the projectile is used throughout this chapter.) For late-stage modeling the projectile diameter is 200 m, producing a final crater diameter of $\sim 3 \text{ km}$, according to scaling laws for oblique impacts (Chapman and McKinnon 1986; Schmidt and Housen 1987).

Initial conditions on the Earth have been chosen from the known stratigraphy of the Ries and Bosumtwi craters with reasonable simplifications (Stöffler et al. 2002; Artemieva et al. 2004). Spatial resolution has been optimized to best reflect the target lithology, and varied from 10 m, to resolve the thin surface layers, to 60 m at the depth of $\sim 1 \text{ km}$.

3 TEKTITES' ORIGIN

3.1 Geochemical and Geophysical Constraints

Compositional data (chemical and isotopic) strongly suggest that tektites are formed as a result of melting of terrestrial sedimentary rocks during the impact cratering process. The European and Ivory Coast strewn fields are located several hundred kilometers away from their probable source craters, Ries and Bosumtwi, respectively. The North American strewn field has been linked to the Chesapeake Bay impact structure (Poag et al. 1994; Koeberl et al. 1996). The parent crater for the Australasian tektites has not yet been found, but variations in microtektite concentrations (Glass and Pizzuto 1994) and ^{10}Be contents (Tera et al. 1983; Blum et al. 1992) point strongly toward a location in Indochina. The meteoritical component in tektites is very low (with maximum of about 0.06 wt% for Ivory Coast tektites) (Koeberl and Shirey 1993). At the same time tektites differ from all other types of natural glasses, such as obsidians and impact melts, by having very low water contents of 0.002–0.02 wt% (Gilchrist et al. 1969; Koeberl and Beran 1988) compared with several percent for normal impact glasses. A high degree of chemical homogeneity for regions $>0.1 \text{ mm}$ in size (Glass 1990; Koeberl 1990) and physical homogeneity (density, refractive index) (Friedman 1963) are also typical for tektites. These facts, as well as petrographic properties (Chao 1963) indicate that tektites originate from a high-temperature melt. The only exception is the group of Muong Nong-type

tektites, which are found within the Australasian strewn field and differ from regular tektites by being of larger size, being heterogeneous in composition, and having a layered structure (Chapman and Scheiber 1969; Schnetzler 1992). The noble gas contents (Matsuda et al. 1993) and low ferric to ferrous iron ratios (Fudali et al. 1987; Jakes et al. 1992) indicate tektite solidification in the upper Earth atmosphere with low oxygen fugacity. The study of cosmogenic radionuclides (^{10}Be and ^{26}Al) provides further proof of the terrestrial origin of tektites (Pal et al. 1982). If tektites were exposed to cosmic radiation in space, then the $^{26}\text{Al}/^{10}\text{Be}$ ratio must be between 2.7 and 5.4, but Middleton and Klein (1987) found that it is ~ 0.07 in only one sample and even lower in others. This means that the ^{10}Be in the tektites has been introduced from sediments that have absorbed ^{10}Be that was produced in the terrestrial upper atmosphere. Moreover, the concentration of ^{10}Be in the environment is a strict function of the depth from the surface; most of it is concentrated in the upper 20 m (Valette-Silver et al. 1983). This limit may vary as a function of different rock types, rainfall rates, and porosity, but probably by less than a factor of 10. It means that tektites were formed exclusively of the top few hundred meters of the target.

One more fact should be mentioned. All the strewn fields are on one side of the known (or inferred) location of the parent crater, but this direction changes for different strewn fields. The European strewn field is to the east from the Ries crater, the Ivory Coast field is to the west from the Bosumtwi, the North American field is to the south of the Chesapeake Bay, and all the Australasian tektites are to the south of Indochina. This position of the strewn fields indicates that tektites formed after oblique impacts; otherwise, the ejecta deposition would have been more or less symmetric.

Geochemical and geophysical studies provide important data, but do not answer two principal and closely linked questions: (1) How do tektites form during the impact and are then transported for hundreds of kilometers? and (2) Are they really rare or are they a normal type of distal ejecta? Numerical modeling, based on analysis of the available geochemical data summarized shortly may be a useful tool to investigate the tektite origin and discuss their rarity.

3.2 Modeling Results

Summarizing geochemical data and EOS-based estimates, one can conclude that the target region no deeper than 50 m and compressed up to 100–300 GPa during the impact should be considered as the main source of tektites. For brevity, material from this region is referred to as the “tektite” material. It is not identical to real tektites, but it is an appropriate material for tektite production.

Early modeling attempts (Artemieva 2002) have shown that the most suitable conditions for the origin of tektites arises in the case of a high-velocity impact ($>20 \text{ km}\cdot\text{s}^{-1}$) with the impact angle ranging from 30° to 60° . It is important to note that a very oblique impact is not needed to produce tektites (Vickery 1993; Artemieva 2002). Approximately 30% of NEOs (Near-Earth Objects) have

velocities $>20 \text{ km}\cdot\text{s}^{-1}$ (Ivanov et al. 2001) and $\sim 50\%$ of the impacts have impact angles in the desirable interval (Gilbert 1893; Shoemaker 1962). This means that $\sim 15\%$ of the Earth's craters should have tektite-strewn fields. The percent might be smaller, because in addition to high-impact-velocity and specific (but not far from average) impact angle one needs a rather large projectile (to produce a crater of at least 10 km) and silica-rich target (but silica is a very abundant material on the Earth's surface). The percent might also be higher, because lower-velocity impacts (but still not far from the average impact velocity on the Earth of $\sim 18 \text{ km}\cdot\text{s}^{-1}$) also produce and eject tektite material (melt production is roughly proportional to V^2 ; see Pierazzo et al. 1997).

3.3 Ries Crater and Moldavites

Using detailed geological, petrographic, geochemical, and geographical constraints, numerical modeling studies have been performed (Stöffler et al. 2002) that relate the Steinheim crater (apparent diameter $D_a = 3.8 \text{ km}$), the Ries crater ($D_a = 24 \text{ km}$) in Southern Germany, and the moldavite (tektite) strewn field in Bohemia and Moravia (Czech Republic), Lusatia (East Germany), and Lower Austria. The moldavite strewn field extends from about 200 to 450 km from the center of the Ries to the ENE, forming a fan with an angle of about 57° . An oblique impact of a binary asteroid from the WSW direction appears to explain the locations of the craters and the formation and distribution of the moldavites. The impactor must have been a binary asteroid with two widely separated components (some 1.5 and 0.15 km in diameter, respectively).

The simulations in a wide range of impact angles and velocities (Stöffler et al. 2002) combined with previous results (Artemieva 2002) suggest that a 30° , $20 \text{ km}\cdot\text{s}^{-1}$ impact is the most favorable for tektite-type melt production. Special long-term simulations of this impact have been carried out to investigate the formation and distribution of tektites formed in the Ries impact event. Molten particle diameters are in the range of 1 ("hot" melt) to 3 cm ("cold" melt), whereas particle size drops to 0.01 cm if particles are produced by condensation from a two-phase mixture (Zel'dovitch 1967).

The modeling of the motion of impact-produced tektite-type particles through the atmosphere allows one to address mainly the "mechanical" component of the complex tektite problem; that is, the possibility of ballistically transporting particles hundreds of kilometers away from the parent crater. At this point, the "geochemical" component of the problem cannot be addressed in detail, although the calculated P-T conditions (low dynamic pressure, high temperature, and slow cooling) are consistent with some tektites' characteristics, such as low water content, homogeneity, and scarcity of vesicles of tektites. A simulation of a Ries-sized impactor at 30° and $20 \text{ km}\cdot\text{s}^{-1}$ produces a relatively narrow-angle distribution of tektite-type material down range, in agreement with that observed for the moldavites strewn field (Fig. 1). Although the modeled particle distribution extends over a continuous radial range, somewhat different from the known distribution of the

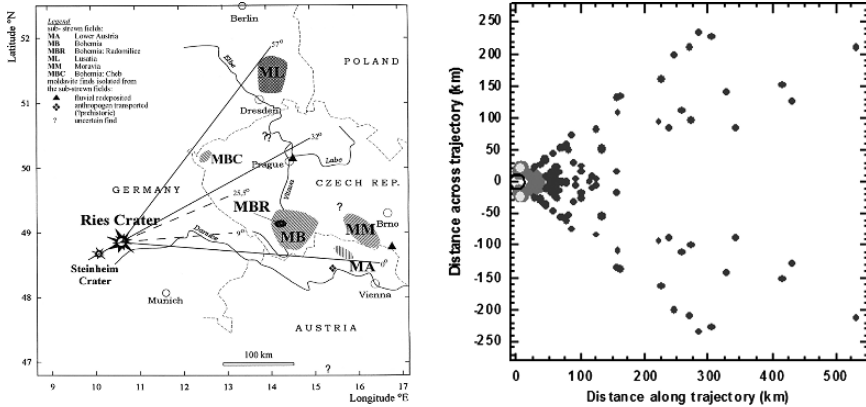


Figure 1. On the left—map of the moldavite strewn field with the sub-strewnfields hatched and explained in the legend. On the right—modeled deposition of tektites-like particles. Colors represent mass of material deposited at a given location: *dark gray*—0.01–0.1 Mt; *light gray*—0.1–1.0 Mt. The *open circle* roughly corresponds to the rim of the Ries crater. The figure is adapted from Stöfler et al. (2002) and reprinted with the kind permission of the University of Arizona/Geosciences Department

moldavites, these results represent an important step toward a better understanding of the moldavite strewn field. The lack of tektites at ranges up to 200 km is easily explained by the lack of 15-My-old host sediments that would be contemporaneous with the Ries event in the entire region between the Ries and the western border region of the Czech Republic. Several other factors could have influenced the final distribution of the moldavites. Besides projectile-related factors, such as projectile size, impact angle and impact velocity, target characteristics affect the final distribution of the moldavites, such as local variations in the stratigraphy, a discontinuous distribution of the upper layer of Tertiary sands in the Ries, and the size distribution of the melt particles. The 57° fan where the moldavites are found today may have been slightly modified from the original distribution because of mechanisms such as erosion and surface transport of tektites since their formation. Therefore, the estimated MBR 75° fan is considered to be in good agreement with the observed distribution.

3.4 Bosumtwi and Ivory Coast Tektites

The 1 Ma Bosumtwi Crater in Ghana (06°32'N, 01°25'W) is a complex impact structure with a rim-to-rim diameter of 10.5 km. The crater is associated with the Ivory Coast tektite strewn field (Barnes 1961; Jones et al. 1981; Koeberl et al. 1997, 1998, and references therein), an expansive region of distal, molten ejecta deposition to the SW of Bosumtwi. The crater is almost completely filled by Lake Bosumtwi, which measures 8 km in diameter and has a current maximum depth of about 80 meters. The crater rim rises about 250–300 m above lake level. It

is the youngest and best preserved of the ~95 terrestrial impact structures with diameter >6 km formed in a crystalline target. Because the impacting body struck a subaerial site in the continental interior, rather than a submerged continental shelf, no profound backwash effects distorted the structure following the impact. Also, no postimpact tectonic deformation of the structure has been observed.

Ivory Coast tektites were first reported in 1934. The tektites were found in a region with a radius of about 40 km around the town of Qualle. Additional collections were made later, but the total number collected remains small (~200). Age data, isotope studies, and compositional data (Jones 1985) confirm the tektites' origin from the Bosumtwi crater. Glass spherules and microtektites were found in deep sea deposits from the equatorial Atlantic in 1967 (Glass et al. 1991 and references therein). The strewn field does not extend below 12°S and north of 9°N, the eastern and western limits are not well defined. In total, the strewn field lies in the quadrant SW of the crater, showing preferable direction of the impact from ENE. Additional cores from the Atlantic must be studied before the shape and extent of the strewn field can be determined with any confidence.

Tektite-producing processes in the Ries and the Bosumtwi may be different, as the Bosumtwi crater is half the size of the Ries and a substantial volatile-rich layer is not expected at the impact site. In the current modeling of the Ivory Coast tektites the authors consider two types of targets: a simple granite target, and a granite basement covered by a 40-m thick sand layer. In the latter case the total melt production is a bit (2–3%) higher, because of the lower melting pressure value for the porous sand (20–30 GPa in comparison with 50–60 GPa for solid quartz). The difference in the melt volumes ejected outside the crater is much more profound: 0.54 km³ (13% of the total melt) and 1 km³ (25%), respectively. This may be explained by preferential melt ejection from the uppermost, low-density target layer in the two-layer case.

One second after the impact, almost all of the molten and solid high-velocity material is ejected and broken into particles, whereas intensive ejection of either molten or solid material from deeper layers continues for much longer. The initial ejection velocities of material are high, up to 10 km·s⁻¹, which is close to the velocity of the expanding gas. As a result, the particles are not subjected to high dynamic pressures that otherwise would disrupt them into a fine dust immediately after ejection. The temperature of the entraining gas is rather high, in the range of 1,000–2,000 K, so the particles do not cool quickly during the flight, allowing enough time for them to be aerodynamically shaped (which is typical for tektites), and lose volatiles (e.g., water).

The Bosumtwi structure is not large enough to create worldwide ejecta: All of the ejected material is decelerated in the atmosphere and deposited on the surface at distances up to 2,000 km from the crater. The majority of this material (80–85%), however, is deposited in the vicinity of the crater (probably as a molten component of suevite). The rest may be identified as a tektite-strewn field. The total mass of deposited tektites (molten particles 1–3-cm in diameter) is about 170–280 Mt (higher values are for the porous sandy layer); the calculated mass of

microtektites is in the range 80–100 Mt. These values are an order of magnitude higher than the total mass of 20 Mt, derived from geological estimates (Koeberl, 1994). Also, the maximum concentration of microtektites at the drill core V19-297 (see Glass et al. 1991 for details) corresponds to the lowest modeled limit of deposited tektite concentration ($2,000 \text{ kg}\cdot\text{km}^{-2}$). The reasons for this discrepancy should be investigated in the future: Is it lower impact velocity, another impact angle, or another mechanism of tektite production? Probably, the geological data are still incomplete.

On the basis of the authors' numerical model (Artemieva et al. 2004) two possible directions of the impact are suggested. The first one is from the north to the south. This scenario correlates with known asymmetry in the crater morphology (Karp et al. 2002) and magnetic signatures (Plado et al. 2000). The Ivory Coast strewn field may be connected in this case with modeled deposit in the direction perpendicular to the trajectory. However, an absence of microtektites in the southeast direction is not clear. The second possibility is the impact from the northeast to the southwest. It correlates better with the microtektites' deposit and allows the connection of the Ivory Coast strewn field with the modeled deposition at the 45° angle to the trajectory.

4 METEORITES: MODELING RESULTS

4.1 Meteorites Ejection

The initial stage of impact has a short duration, comparable with the duration of the projectile's shock compression, and is characterized by extremely high shock pressures. These two facts allow one to neglect gravity and strength. In the case of a homogeneous target, all spatial variables can be expressed in terms of the projectile radius R and the volume of high-velocity solid material (MM material or MMM) in terms of projectile volume.

The ejection process after an oblique impact differs from that for a vertical or near vertical impact: It starts immediately after contact, and is clearly asymmetric, mainly in a downrange direction. Molten projectile and molten or solid target material are ejected with velocities comparable with impact velocity, or even slightly higher (similar to tektite ejection). Figure 2 shows pressure and ejecta velocity distributions with respect to the initial position of the target material, reconstructed with the tracers. Target material near the impact point ($x/R < 2$) is molten, and target material far from the impact point ($x/R > 4$) is ejected with velocity below escape. The area bound by pressure contours of 50 GPa and velocity contours of $5 \text{ km}\cdot\text{s}^{-1}$ represents MM material. In addition to being laterally restricted, the MMM region is also very thin. This result is in qualitative agreement with the "spallation theory" for the SNC-origin (Melosh 1984): High-velocity solid ejecta are produced in a thin layer near the surface due to interference of the direct compressive wave with the reflected rarefaction wave from the planetary surface. In this layer shock pressure drops extremely quickly and near-surface material can be ejected at high velocities without experiencing high compressive shock pressures.

The ratio of MMM volume to projectile volume for different impact angles (but for a constant impact velocity of $10 \text{ km}\cdot\text{s}^{-1}$) is presented in Table 2. It is typically

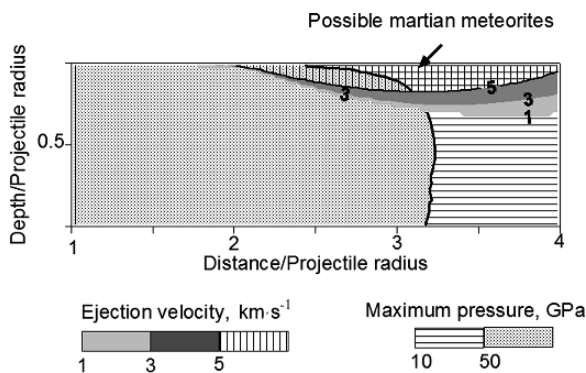


Figure 2. Hydrodynamic flow after a 45° asteroid impact at 10 km·s⁻¹. Maximum pressure and ejection velocity distributions in the central cross-section are shown. Overlapping of pressure contours P < 50 GPa (partial melting of basalts) and ejection velocity contours V > 5 km·s⁻¹ (escape velocity on Mars) shows the spallation zone and the Martian meteorites launch site

about 2–10%, with a maximum at the 30°-impact. These values change by <0.1%, with spatial resolution increase by a factor of two. In vertical or near-vertical impacts the amount of escaping material is extremely small, about 0.1%, in the authors' calculations. A lower impact velocity of 7 km·s⁻¹ (45°-impact) results in a 1.5-times lower fraction of high-velocity solid ejecta. Surprisingly, high-velocity cometary impact produces practically the same volume of MMM. The spallation zone in a cometary impact is even thinner than in an asteroid impact. This may be qualitatively explained by a smaller penetration depth for comets, which is proportional to the projectile:target density ratio (ρ_p/ρ_t)^{0.5} (Melosh 1989).

4.2 Atmospheric Effects

First, make some simple estimates of the particle size needed to penetrate through the Martian atmosphere, while maintaining escape velocity. For undisturbed atmosphere the problem is opposite to the meteoroid entry problem: During passage through the

Table 2. The ratio of the SNC-volume to the projectile volume

Impact angle	Asteroid impact, 10 km·s ⁻¹	Comet impact, 35 km·s ⁻¹
90	0.001	0.01
75	0.004	
60	0.024	0.052
45	0.088 (0.058*)	0.076
30	0.105	0.12
15	0.035	

*Lower impact velocity of 7 km·s⁻¹

atmosphere the particle accelerates gas within the tube with the same cross-section and length equal to a trajectory length. Under this assumption, one derives an estimate for a particle radius r large enough to maintain escape velocity:

$$r = \frac{3P_a(1 + V_{esc}/V_{ej})}{8\rho_t g \sin \alpha (1 - V_{esc}/V_{ej})},$$

where P_a is atmospheric pressure near the surface, 640 Pa, $\rho_t = 2.7 \text{ g}\cdot\text{cm}^{-3}$ is the particle density (target density in this case), $g = 3.72 \text{ m}\cdot\text{s}^{-2}$ is gravity, α and V_{ej} are ejection velocity and angle, and $V_{esc} = 5 \text{ km}\cdot\text{s}^{-1}$ is the escape velocity. For a preliminary estimate a value of ejection velocity equal to the impact velocity, and ejection angle equal to the impact angle may be used. This is certainly an overestimate, as the results from 3D modeling show (on average) lower ejection velocities and ejection angles. However, even these optimistic estimates give a critical value $>33 \text{ cm}$ for particle size. Thus, only rather large m-sized fragments, ejected with high velocity, can maintain the velocity required to escape from Mars. A more serious problem is that these particles are subjected to a high aerodynamic loading $P = \rho_a V_{ej}^2$, immediately after ejection into a supposed “undisturbed” atmosphere and may be disrupted into smaller particles, which are decelerated even more efficiently.

In reality, the postimpact atmosphere is strongly disturbed by high-velocity ejecta from the growing crater, consisting of vaporized and molten projectile and target materials. Hence, hydrodynamic modeling of ejecta plume is needed for accurate estimates of atmospheric effects. The initial size distribution of particles (Fig. 3, at $t = 0.1$) reflects a typical Grady-Kipp distribution: The difference between the smallest and the largest particles is 2 orders of magnitude, and the most probable particle to be ejected is approximately three times smaller than the largest one. The particles do not have a continuous size distribution, but are divided into discrete groups with the ratio of sizes $10^{0.25} = 1.78$ (not all modeled groups are shown in the figure). The authors make full-scale two-phase hydrodynamic simulations, which run to 15 s after the impact, and then use a ballistic approach for the surviving particles until they reach an altitude of 500 km. Atmospheric losses are substantial in the case of the “small impact” (3-km-diameter final crater): All 10-cm and smaller particles are decelerated (the smaller the particle, the quicker its deceleration). However, $\sim 20\text{--}40\%$ of the largest fragments (14 cm and larger) survive and escape Mars. Fragment survivability depends on the fragment size non-monotonically, as one would expect: The highest survivability (37–39%) is for the largest fragments of 75 cm and for the most probable fragment of 24 cm, whereas for a 40-cm fragment it is only 26%. This effect can be explained by the “collective” behavior of particles in the postimpact flow: Compact groups of smaller particles have more chance of escaping than large but isolated pieces.

Atmospheric permeability for high-velocity ejecta depends on two factors: fragment size and scale of the impact event. In the case of a large event the atmosphere is not a substantial obstacle even for cm-sized particles, whereas ejection in a small-scale event is equivalent to ejection in an undisturbed atmosphere. As the maximum fragment size decreases (roughly linearly) with projectile size, a rather

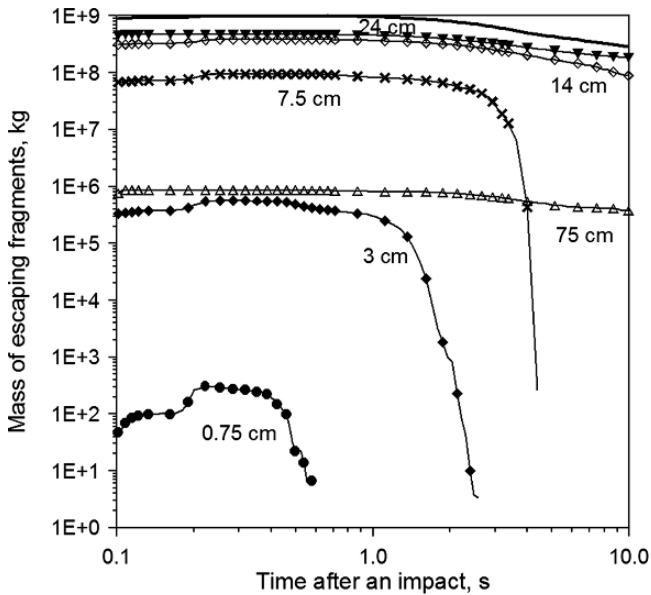


Figure 3. Survivability of escaping material in the Martian atmosphere for the “small impact” with maximum fragment size of 75 cm. Initial distribution (at $t = 0.1$) corresponds to Grady–Kipp distribution immediately after disruption. Thick solid line shows the total amount of ejecta with escape velocity. The smallest fragments are decelerated in the atmosphere, whereas a substantial part of the fragments >14 cm leave the Martian gravity field. The figure is adapted from Artemieva and Ivanov (2004) and reprinted with the kind permission of Elsevier

abrupt boundary between MM-productive and nonproductive craters should exist. More modeling is needed to clarify this point; however, to a first approximation one can consider 2–3 km diameter craters as defining this boundary.

5 METEORITES: COMPARISON WITH AVAILABLE DATA

5.1 Shock Metamorphism in Martian Meteorites

An important observation is that all MM are moderately to strongly shock metamorphosed (Nyquist et al. 2001 and references therein). New shock wave barometry data by Fritz et al. (2005) clearly show that all known MM are shocked in the range of 10–45 GPa. There may be a correlation between petrologic type and peak shock pressure, with the group of clinopyroxenites (Nakhlites) being most weakly shocked (10–20 GPa), the basalts (basaltic shergottites) clustering at 28–31 and 42–45 GPa, and the lherzolitic rocks (lherzolitic shergottites) at 43–45 GPa. These shock effects can be attributed to one specific event in each case (with the single exception of ALH84001 indicating at least two, and probably for some lherzolitic meteorites, Yamato 793605), which is, most probably,

the ejection event. It is not yet clear whether this is a result of “random” choice, probably from a huge but yet undiscovered family of meteorites from Mars, or whether it is a real “launch window” for the Martian escaping ejecta? On the other hand, the observed shock pressure range, i.e., the lowest shock compression above 10 GPa, is essentially confirmed by the authors’ computer code calculations.

5.2 Burial Depth of the Meteorites’ Parent Rocks

The complete lack of $2\text{-}\pi$ cosmic ray exposure (with the single possible exception for Yamato 980459, which also exhibits extremely high cooling rate and quenching; Greshake et al. 2003) argues that the Martian meteorites came from some depth in the crust, at least 1 m (Warren 1994). Furthermore, the regolith on the young Martian terrains is no less than 1 m-thick (Hartmann 1999). Thus, the finest computational mesh in the authors’ modeling of 1 m is consistent with the available data and with common sense.

On the other hand, mineralogical and petrological studies of the MMs microstructures clarifies their formation conditions and cooling rate, and hence, one may derive the maximum burial depth in a parent magma chamber. The first comparison of Nakhla with terrestrial igneous rocks (Treiman 1987) argued that this meteorite originated from thick lava flows (>125 m, but <1 km) somewhere in the Tharsis region. Friedman et al. (1994) estimated a magma body at least 11–26 m thick. A recent study by Mikouchi et al. (2003) revealed a relative burial depth for all Nakhilites from 30-m-thick lava, with the shallowest depth of 0.5–2 m for NWA817 and Y000593, Lafayette at the bottom of this layer, and Nakhla and Governador Valadares somewhere in the middle of the section. The majority of Shergottites also indicate rapid cooling near the Martian surface, with a burial depth of <3 m (Mikouchi et al. 2001). A rather low cooling rate in Shergotty (Müller 1993) and Zagami (Brearly 1991) does not necessarily mean a substantially deeper magma structure, but may be explained by the late (after partial cooling) intrusion of a dyke.

5.3 Preatmospheric Size

As is known from terrestrial craters, the size of displaced shocked rock fragments is, on average, inversely proportional to the shock intensity (Pohl et al. 1977). Crystalline rock fragments in polymict breccia of the Ries structure, shocked to 30–45 GPa, do not exceed 0.5 m, and most sizes are 0.1–10 cm. As discussed, the size of high-velocity particles may be a factor of 2 larger. The size distribution of distal ejecta in the authors’ “small impact” simulations (a Martian crater ten times smaller than the Ries) is consistent with these data, with a maximum size of 75 cm and a minimum size of ~ 0.1 cm. The smallest fragments are decelerated in the Martian atmosphere quickly, and do not produce MM.

Recently, Eugster et al. (2002) measured the Kr isotopic composition and observed effects induced by secondary cosmic rays produced epithermal neutrons with an energy of 30–300 eV in a few MM (Los Angeles, Queen Alexandra Range 94201, Shergotty, Zagami, Nakhla, Chassigny, and ALH84001). The neutron capture took place in free space during the Mars–Earth transfer of the meteoroids. Calculated epithermal neutron fluxes allow an estimate of the minimum preatmospheric radius, which is in the range of 22–25 cm, corresponding to a minimum mass of 150–220 kg. Zagami is the largest single individual Martian meteorite ever found, with a mass of 18 kg. Nakhla was disrupted during atmospheric entry into ~40 stones, with total mass of ~10 kg. Standard estimates of the mass loss (ablation and fragmentation) during atmospheric passage (Ceplecha et al. 1993; Bland and Artemieva 2003) show that stony meteorites entering the atmosphere with a velocity of 18 km·s⁻¹ lose ~90% of their initial mass. This value strongly depends on the preatmospheric velocity, mass, trajectory, and individual properties of a meteorite. Dynamic modeling by Gladman (1997) showed that MM arriving within the first 4 Myr after ejection seldom have atmospheric entry velocities greater than the relatively low value of 13 km·s⁻¹, which will result in ablative mass losses of 40–60%. Nonetheless, the preatmospheric mass of the largest meteorites was well above 100 kg.

Thus, the results of the authors' numerical model, revealing survivability of high-velocity fragments larger than 14–20 cm, are consistent with estimates based on the terrestrial crater records, isotopic composition of Martian meteorites, and mass loss in the Earth's atmosphere.

5.4 A Possible Parent Crater for Martian Meteorites

Recently a large 10-km-diameter rayed crater, called Zunil, was discovered in the young volcanic plains at the southwest of Elysium Planitia (McEwen et al. 2005). Its rays, extending >800 km, are associated with millions of secondary craters ranging from 15 to 100 m in diameter. Dating of the young surface is rather uncertain (within a factor of 30) because the secondary craters are highly clustered in space and time. Most probably, it is the youngest crater on Mars in this size class, with an age < 1 Myr old. MM with ejection ages < 1 Myr (EET79001) could have originated from this crater, but many more rocks from this crater should arrive at the Earth over the next 15–20 Myr, keeping the meteorite flux from Mars constant in time.

5.5 Temperature Estimates

The authors attempted to make more accurate temperature estimates based on experimentally determined EOS for geological materials (Stöffler 1982; Trunin et al. 2001). Details of these calculations can be found in Fritz et al. (2005). Dunite and pyroxenite have the smallest postshock temperatures. Dunite is at 22–130° above the initial level after compression to 20–40 GPa, typical for Chassigny (Nyquist et al. 2001). ALH84001 (orthopyroxenite) was compressed at ~35–40 GPa (Nyquist

et al. 2001) and would then have a maximum temperature increase during the shock of ~ 112 – 231 degrees (for $P = 30$ and 40 GPa, respectively) and a long-lasting postshock temperature increase of about ~ 94 – 122° . Taking into account the initial subsurface temperature on Mars, maximum temperatures of 32 – 151°C and postshock temperatures of 14 – 42°C are obtained. Weiss et al. (2000), analyzing remnant magnetization, argued that this meteorite was never heated $>40^\circ\text{C}$, which means that the value of shock compression (poorly defined for this sample) was close to its lower limit. In summary, the highest postshock temperature increase ($>350^\circ$) for basaltic and lherzolithic shergottites (shock compression up to 45 GPa), and the lowest increase (probably a few degrees) for nakhlites (shock pressure 9.5 – 17 GPa) can be expected.

6 DISCUSSION

6.1 Are Tektites Rare?

The preliminary modeling described in the preceding shows that no special conditions are needed to produce tektite material: The impact velocity should be slightly above average impact velocity for the Earth ($\sim 18 \text{ km}\cdot\text{s}^{-1}$), impact angle should be close to the most probable impact angle of 45° (probability of an impact angle between 30 and 60° is 50%). Certainly, the influence of target and projectile material is not yet clear, but the simulations show that tektites should not be a rare phenomenon in impact cratering. What are the reasons for tektites “deficiency” on the Earth? The first one is obvious: Only craters exceeded a certain diameter may produce distal ejecta. The estimate for this critical size ranges from 3 to ~ 10 km (Melosh 1989). Excluding small craters from the impact structure list (<http://solarviews.com/eng/crater.htm>) the number of possible parent craters can be reduced three times, from 150 to 49 . The second restriction is crater age. Small glass bodies break down to clays rather quickly. It is impossible to estimate the exact critical age for tektites and it should undoubtedly depend on the environmental conditions and tektite chemical composition, but the oldest tektite-strewn field is ~ 35 Ma and most impact glasses are much younger (Montanari and Koeberl 2000). If now old craters are excluded from the crater list (say, older than 50 Ma), only 13 craters remain that, in principle, may be connected with tektites (Table 3). Three of these 13 craters are actually parent craters for tektites (Bosumtwi, Ries, and Chesapeake Bay). Remembering that a high-velocity oblique impact is needed, it can be concluded that indeed there are enough tektites. Certainly, these estimates are rather crude (probabilities really apply only to really large numbers, >150) and the list of known impact structures on the Earth is not complete (e.g., the parent crater for the Australasian tektites has not yet been identified). Nevertheless, the widely accepted theory of the rarity of tektites is not quite correct and should be revised.

Table 3. Possible parent craters for tektites. Table is adapted from Artemieva (2002) and reprinted with kind permission of Springer Science and Business Media

Name	Diameter, km	Age, Ma	Method	References
Bosumtwi, Ghana	10.5	1.07 ± 0.05	^{40}Ar - ^{39}Ar	Koeberl et al. 1997
Chesapeake Bay, United States	85	35.3 ± 0.2	stratigraphy	Poag and Aubry 1995
El'Gygytgyn, Russia	18	3.58 ± 0.04	^{40}Ar - ^{39}Ar	Layer 2000
Haughton, Canada	20.5	23.4 ± 1.0	^{40}Ar - ^{39}Ar	Jessberger 1988
Kara-Kul, Tajikistan	52	<25	stratigraphy	Gurov et al. 1993
Karla, Russia	12	10	stratigraphy	Masaitis 1999
Logancha, Russia	20	25 ± 20	stratigraphy	Feldman et al. 1985
Logoisk, Belarus	17	40 ± 5	stratigraphy	Masaitis 1999
Mistastin, Canada	28	38 ± 4	^{40}Ar - ^{39}Ar	Mak et al. 1976
Montagnais, Canada	45	50.5 ± 0.8	^{40}Ar - ^{39}Ar	Bottomley and York 1988
Popigai, Russia	100	35.7 ± 0.2	^{40}Ar - ^{39}Ar	Bottomley et al. 1997
Ries, Germany	24	15.1 ± 1.0	^{40}Ar - ^{39}Ar	Staudacher et al. 1982
Zhamanshin, Kazakhstan	13.5	0.9 ± 0.1	^{40}Ar - ^{39}Ar	Deino and Becker 1990

6.2 Martian Meteorites versus Lunar Meteorites

The total number of meteorites from the Moon (http://meteorites.wustl.edu/lunar/moon_meteorites_list_alumina.htm) and Mars (<http://www.jpl.nasa.gov/snc/index.html>) are comparable, although one can assume that lunar meteorites should be much more common than MM because of a lower escape velocity on the Moon, absence of atmosphere, and easier delivery process. This creates an apparent paradox.

The numerical methods to model lunar meteorite ejection are identical to those described in the preceding. Nevertheless, at least four principal points should be taken into account: The average impact velocity on the Moon ($\sim 18 \text{ km}\cdot\text{s}^{-1}$, twice higher than on Mars), lower escape velocity ($\sim 2.4 \text{ km}\cdot\text{s}^{-1}$), absence of atmosphere on the Moon, and important difference in the target properties. The lunar surface sampled by all known lunar meteorites is not an intact volcanic terrain, but a highly porous, inhomogeneous regolith (Warren 1994). The thickness of the lunar regolith layer (e.g., Shoemaker et al. 1969; Oberbeck et al. 1973) varies from 3 to 23 m. There are no water or other volatiles in the target. If the projectile is large enough to excavate high-velocity material from below the regolith layer, then there should be a certain fraction of lunar meteorites with the lunar crust composition. The lack of this sort of lunar meteorite means that the majority of impactors were small, probably with diameters <10 times thickness of the regolith layer (on the basis of the authors' Mars modeling). Crater counts for the Moon (Neukum et al., 2001) combined with CRE-age of the lunar meteorites (half of them spent <0.1 Myr in space; Warren 1994) are also in favor of the "small impact" scenario. Similar to the authors' discussion of parent crater sizes for the meteorites from Mars, it estimates that the maximum possible size of a lunar parent crater is 0.6–1 km. This means that the projectile size is not larger than 10–30 m, depending on impact

conditions. This value is comparable with the thickness of a regolith layer. On the basis of MM modeling, it can be concluded that all lunar meteorites should be produced from the regolith layer. The maximum burial depth should be $<1\text{--}3$ meters in agreement with their 2π -exposure depth (Warren 1994).

Preliminary modeling assuming a regolith thickness of 15 m and a projectile diameter of 30 m (maximum size from the authors' estimates) shows that maximum excavation depth for lunar meteorites is ~ 4 m, and there are no meteorites from the subregolith basement. The volume of escaping solid material is substantially higher than on Mars: Up to half of the projectile volume. According to the authors' calculations, the average value of maximum shock pressure for the total escaping unmolten mass is 22.5 GPa, assuming melting pressure for highly porous rocks at 32 GPa (Stöffler 1984).

The total number of meteorites, delivered to the Earth from Mars or the Moon after the largest statistically probable single impact (3 km-diameter crater on Mars and 1 km-diameter crater on the Moon) is equal to the projectile volume ($\sim 0.004 \text{ km}^3$ for Mars and $\sim 1.4 \cdot 10^{-5} \text{ km}^3$ for the Moon), multiplied by the ejection efficiency (0.05 and 0.5), atmospheric permeability (0.3 and 1), and delivery efficiency (0.1 and 0.3). Thus, the final numbers ($6.0 \cdot 10^{-6}$ and $2.1 \cdot 10^{-6} \text{ km}^3$) differ by a factor of 3. Smaller-scale Martian impacts cannot produce meteorites because of substantial atmospheric deceleration. Hence, the total volume of the meteorites delivered from Mars to the Earth is roughly equal to the mass delivered during one impact multiplied by the number of sampling events (4–8), i.e. $\sim (2.5\text{--}5) \cdot 10^{-5} \text{ km}^3$. On the Moon, smaller (and therefore much more frequent) events may also produce escaping ejecta. Then, the total volume of lunar meteorites delivered to Earth during the last 0.1 Myr, V_{lunar} , may be defined by integration over all crater sizes smaller than statistical maximum. The results depend on the slope of the SFD curve (3.55 or 3.82 for Neukum's and Hartmann's approximations, respectively; see Neukum et al. 2001) and vary in the range $2.5 \cdot 10^{-5}$ to $4 \cdot 10^{-4} \text{ km}^3$. This value is comparable with the total volume of Martian meteorites. Hence, there is no lunar–MM paradox.

6.3 Microbes Transfer

The values of shock and postshock temperatures are of crucial importance for assessing whether viable microorganism transfer can occur between the two planets. A recent publication by Mileikowsky et al. (2000) assumed unrealistically low compression at ejection (~ 1 GPa), to allow organic molecules' survival of MM ejection and the following transfer from Mars to Earth. The authors' modeling shows that, although for MM it is impossible to eject material with escape velocity without substantial (> 10 GPa) shock compression, on the other hand, a temperature increase in meteorites with composition similar to pyroxenite (Nakhla ALH84001) or dunite (Chassigny) may be well below 100° . Thus, if microbes can survive the shock, they would not be overheated in Nakhrites or Chassignites. To confirm (or reject) the idea of microbes transfer (or to reject it) much more investigations are needed, including numerical modeling (Pierazzo and Chyba 1999) and experiments (Horneck et al. 2001).

REFERENCES

- Alvarez LW, Alvarez W, Asaro F, Michel HV (1980) Extraterrestrial cause for the Cretaceous-Tertiary extinction. *Science* 208(4448):1095–1108
- Artemieva NA (2002) Tektite origin in oblique impacts: Numerical modeling of the initial stage. In: Plado J, Pesonen LJ (eds) *Impacts in pre-Cambrian shields*. Impact Studies. Springer-Verlag, Berlin, 257–276
- Artemieva NA, Ivanov BA (2004) Launch of Martian meteorites in oblique impacts. *Icarus* 171:84–101
- Artemieva N, Karp T, Milkereit B (2004) Investigating the Lake Bosumtwi impact structure: insight from numerical modelling. *Geochem Geophys Geosyst* 5, Q11016: doi:10.1029/2004GC000733
- Asphaug E, Melosh HJ (1993) The Stickney impact of Phobos: a dynamical model. *Icarus* 101, 144–164
- Barnes VE (1961) Tektites. *Sci Am* 205:58–65
- Bland PA, Artemieva NA (2003) Efficient disruption of small asteroids by Earth's atmosphere. *Nature* 424:288–291
- Blum JD, Papanastassiou DA, Koeberl C, Wassenberg GJ (1992) Nd and Sr isotopic study of Australian tektites: new constraints on the provenance and age of target materials. *Geochimica et Cosmochimica Acta* 56:483–492
- Bottomley R, York D (1988) Age measurement of the submarine Montagnais impact crater. *Geophys Res Lett* 15:1409–1412
- Bottomley R, Grieve RAF, York D, Masaitis V (1997) The age of the Popigai impact event and its relation to events at the Eocene/Oligocene boundary. *Nature* 388:365–368
- Brearily AJ (1991) Subsolidus microstructure and cooling history of pyroxenes in the Zagami shergottite. *LPSC XXII*, pp 135–136
- Ceplecha Z, Spurný P, Borovička J, Kecklíková J (1993) Atmospheric fragmentation of meteoroids. *Astronom Astrophys* 279(2):615–626
- Chao ECT (1963) The petrographic and chemical characteristics of tektites. In: O'Keefe JA (ed) *Tektites*. University of Chicago Press, Chicago, pp 51–94
- Chapman CR, McKinnon WB (1986) Cratering of planetary satellites. In: Burns JA, Matthews MS (eds) *Satellites*. University of Arizona Press, Tucson, pp 492–580
- Chapman DR, Scheiber LC (1969) Chemical investigation of Australasian tektites. *J Geophys Res* 74:6737–6776
- Cintala MJ, Berthoud L, Hörz F (1999) Ejection-velocity distribution from impacts into coarse-grained sand. *Meteoritics Planetary Sci* 34:605–623
- Darwin C (1851) *Geology of the Voyage of the Beagle*. Vol. 2. Smith, Elder & Co, London, pp 38–39
- Deino AL, Becker TA (1990) Laser-fusion $^{40}\text{Ar}/^{39}\text{Ar}$ ages of acid Zhamanshinite. *Lunar Planet Scientific Conference XXI*. Houston, pp 271–272 (abstr)
- Eugster O (1989) History of meteorites from the Moon collected in Antarctica. *Science* 245:1197–1202
- Eugster O, Busemann H, Lorenzetti S, Terribilini D (2002) Ejection ages from krypton-81-krypton-83 dating and pre-atmospheric sizes of Martian meteorites. *Meteoritics Planetary Sci* 37:1345–1360
- Feldman VI, Mironov YuV, Melikhov BA, Ivanov BA, Basilevsky AT (1985) Astroblemes on trap rock: structural features and differences from impact structures on other targets. *Meteoritika, Nauka Publishers, Moscow*. 44:139–145 (in Russian)
- Friedman RC, McCoy TJ, Taylor GJ (1994) Constraints on the physical details of Nakhlite formation. *LPSC XXV*, pp 391–392
- Fritz J, Artemieva N, Greshake A (2005) Ejection of Martian meteorites: petrological data and numerical modeling. *Meteoritics Planetary Sci* 40 1393–1411
- Fudali RF, Dyar MD, Griscom DL, Schreiber HD (1987) The oxidation state of iron in tektite glass. *Geochimica et Cosmochimica Acta* 51:2749–2756
- Gault DE, Shoemaker EM, Moore HJ (1963) Spray ejected from the lunar surface by meteoroid impact. NASA, TND-1767
- Gilbert GK (1893) The moon's face, a study of the origin of its features. *Bulletin of the Philosophical Society, Washington, DC* 12:241–292

- Gilchrist J, Thorpe AN, Senftle FE (1969) Infrared analysis of water in tektites and other glasses. *J Geophys Res* 74:1475–1483
- Gladman B (1997) Destination: Earth. Martian meteorite delivery. *Icarus* 130:228–246
- Glass BP (1972) Bottle green microtektites. *J Geophys Res* 77:7057–7064
- Glass BP (1990) Tektites and microtektites: key facts and inferences. *Tectonophysics* 171:393–404
- Glass BP, Pizzuto JE (1994) Geographic variation in Australasian microtektite concentrations: implications concerning the location and size of the source crater. *J Geophys Res* 99:19075–19081
- Glass BP, Kent DV, Schneider DA, Tauxe L (1991) Ivory Coast microtektite strewn field: description and relation to the Jaramillo geomagnetic event. *Earth Planet Sci Lett* 107:182–196
- Grady DE, Kipp ME (1980) Continuum modeling of explosive fracture in oil shale. *Int J Rock Mech Min Sci Geomech* 17:147–157
- Greshake A, Fritz J, Stöffler D (2003) Petrography and shock metamorphism of the unique shergottite Yamato 980459. International symposium on Evolution of Solar System Materials: A New Perspective from Antarctic Meteorites. September 3–5, 2003. National Institute of Polar Research, Tokyo, pp 29–30
- Gurov EP, Gurova EP, Rakitskaya RB, Yamnichenko A Yu (1993) The Karakul depression in Pamirs: the first impact structure in central Asia. *Lunar Planet Science Conference XXIV*. Houston, pp 591–592
- Hartmann WK (1999) Martian cratering VI: Crater count isochrones and evidence for recent volcanism from Mars Global Surveyor. *Meteoritics Planetary Sci* 34:167–177
- Head JN, Melosh HJ, Ivanov BA (2002) Martian meteorites launch: high-speed ejecta from small craters. *Science* 298:1752–1756
- Horneck G, Stöffler D, Eschweiler U, Hornemann U (2001) Bacterial spores survive simulated meteorite impact. *Icarus* 149:285–290
- Ivanov BA, Basilevsky AT (1983) On the fragment-size distribution of ejecta of impact craters. *LPSC XIV*, pp 345–346
- Ivanov BA, Neukum G, Wagner R (2001) Size-frequency distribution of planetary impact craters and asteroids. Collisional processes in the solar system. Marov MY, Rickman H (eds). *Astrophys Space Sci Library* 261. Kluwer Academic Publishers, Dordrecht, pp 1–34
- Jakes P, Sen S, Matsuishi K, Reid AM, King EA, Casaniva I (1992) Silicate melts at super liquidus temperatures: reduction and volatilization. *Lunar Planetary Science Conference XXIII*. Houston, pp 599–600
- Jessberger EK (1988) ^{40}Ar – ^{39}Ar dating of the Haughton impact structure. *Meteoritics* 23:233–234
- Jones WB (1985) Chemical analyses of Bosumtwi crater target rocks compared with Ivory Coast tektites. *Geochimica et Cosmochimica Acta* 49:2569–2576
- Jones WB, Bacon M, Hastings DA (1981) The Lake Bosumtwi impact crater, Ghana. *Geol Soc Am Bull* 92:342–349
- Karp T, Milkereit B, Janle P, Danurob SK, Pohl J., Berckhemerd H, Scholz CA (2002) Seismic investigation of the Lake Bosumtwi impact crater: preliminary results. *Planetary and Space Science* 50:735–743.
- Koerberl C (1990) The geochemistry of tektites: an overview. *Tectonophysics* 171:405–422
- Koerberl C (1994) Tektite origin by hypervelocity asteroidal or cometary impact: target rocks, source craters, and mechanisms. In: Dressler BO, Grieve RAF, Sharpton VL (eds) *Large meteorite impacts and planetary evolution*. Geological Society of America Special Paper 293, pp 133–151
- Koerberl C, Beran A (1988) Water content of tektites and impact glasses and related chemical studies. *Lunar Planetary Science Conference XVIII*. Houston, pp 403–408
- Koerberl C, Shirey SB (1993) Detection of a meteoritic component in Ivory Coast tektites with rhenium-osmium isotopes. *Science* 261:595–598
- Koerberl C, Bottomley R, Glass BP, Storzer D (1997) Geochemistry and age of Ivory Coast tektites and microtektites. *Geochimica et Cosmochimica Acta* 61:1745–1772
- Koerberl C, Poag CW, Reimold WU, Brandt D (1996) Impact origin of the Chesapeake Bay structure and the source of the North American tektites. *Science* 271:1263–1266

- Koeberl C, Reimold WU, Blum JD, Chamberlain CP (1998) Petrology and geochemistry rocks from the Bosumtwi impact structure, Ghana, and comparison with Ivory Coast tektites. *Geochimica et Cosmochimica Acta* 62:2179–2196
- Layer PW (2000) Argon-40/argon-39 age of the El'gygytgyn impact event, Chukotka, Russia. *Meteoritics Planetary Sci* 35:91–99
- Mak EK, York D, Grieve RAF, Dence MR (1976) The age of the Mistastin Lake crater, Labrador, Canada. *Earth Planet Sci Lett* 31:51–57
- Masaitis VL (1999) Impact structures of northeastern Eurasia: the territories of Russian and adjacent countries. *Meteoritics Planetary Sci* 34:691–711
- Matsuda JI, Matsubara K, Koeberl C (1993) Origin of tektites: constraints from heavy noble gas concentrations. *Meteoritics* 28:586–589
- McEwen AS, Preblich BS, Turtle EP, Artemieva N, Golombek MP, Hurst M, Kirk RL, Burr DM, Christensen PR (2005) The rayed crater zunil and interpretations of small impact craters on mars. *Icarus* 176:351–381
- McSween HY, Stolper E (1980) Basaltic meteorites. *Sci Am* 242:54–63
- Melosh HJ (1984) Impact ejection, spallation and the origin of meteorites. *Icarus* 59:234–260
- Melosh HJ (1989) Impact cratering: a geologic process (Oxford Monographs on Geology and Geophysics, No. 11). Clarendon Press, New York, p 245
- Melosh HJ, Vickery AM (1991) Melt droplet formation in energetic impact events. *Nature* 350:494–497
- Melosh HJ, Ryan EV, Asphaug E (1992) Dynamic fragmentation in impacts: hydrocode simulations of laboratory impact. *J Geophys Res* 97(E9):14,735–14,759
- Middleton R, Klein J (1987) ²⁶Al: measurement and applications. *Philosophical Transactions of the Royal Society. London*, A323:121–143
- Mikouchi T, Miyamoto M, McKay GA (2001) Mineralogy and petrology of the Dar and Gani 476 Martian meteorites: implications for its cooling history and relationship to other shergottites. *Meteoritics Planetary Sci* 36:531–548
- Mikouchi T, Koizumi E, Monkawa A, Ueda Y, Miyamoto M (2003) Mineralogical comparison of Y000593 with other Nakhilites: implications for relative burial depths of Nakhilites. *LPSC XXXIV [abstr] #1883*
- Mileikowsky C, Cucinotta FA, Wilson JW, Gladman B, Horneck G, Lindgren N, Melosh HJ, Rickman H, Valtonen M, Zheng JQ (2000) Natural transfer of viable microbes in space. 1. From Mars to Earth and Earth to Mars. *Icarus* 145:391–427
- Montanari A, Koeberl C (2000) Impact stratigraphy: the Italian record. *Lecture Notes in Earth Sci* 93. Springer-Verlag, Berlin, p 364
- Müller WF (1993) Thermal and deformation history of the Shergotty meteorite deduced from clinopyroxene microstructure. *Geochimica et Cosmochimica Acta* 57:4311–4322
- Nakamura A, Fujiwara A (1991) Velocity distribution of fragments formed in a simulated collisional disruption. *Icarus* 92:132–146
- Neukum G, Ivanov BA, Hartmann W (2001) Cratering records in the inner Solar System in relation to the lunar reference system. *Space Sci Rev* 96(1/4):55–86
- Nyquist LE (1982) Do oblique impacts produce Martian meteorites? *LPSC XIII*, pp 602–603
- Nyquist LE, Bogard DD, Shin C.-Y., Greshake A, Stöffler D, Eugster O (2001) Ages and geological histories of Martian meteorites. *Space Sci Rev* 96(1/4):105–164
- Nyquist LE, Bogard DD, Wooden JL, Wiesmann H, Shin C.-Y., Bansaë BM, McKay G (1979) Early differentiation, late magmatism, and recent bombardment on the shergottite parent planet. *Meteoritics* 14:502
- Oberbeck VR, Quaide WL, Mahan M, Paulson J (1973) Monte Carlo calculations of lunar regolith thickness distributions. *Icarus* 19:87–107
- O'Keefe JA (1976) Tektites and their origin. Elsevier, Amsterdam, p 254
- O'Keefe JD, Ahrens TJ (1983) Constraints on the impact-on-Mars origin of SNC meteorites. *LPSC XIV*, pp 578–579
- O'Keefe JD, Ahrens TJ (1986) Oblique impact: a process for obtaining meteorite samples from other planets. *Science* 234:346–349

- Pal DK, Tuniz C, Moniot RK, Kruse TH, Herzog GF (1982) Berillium-10 in Australasian tektites: evidence for a sedimentary precursor. *Science* 218:787–789
- Pierazzo E, Vickery AM, Melosh HJ (1997) A reevaluation of impact melt production. *Icarus* 127:408–422
- Pierazzo E, Chyba CF (1999) Amino acid survival in large cometary impacts. *Meteoritics Planetary Sci* 34:909–918
- Plado J, Personen LJ, Koeberl C, Elo S (2000) The Bosumtwi meteorite impact structure, Ghana: a magnetic model. *Meteoritics Planetary Sci* 35:723–732
- Poag CW, Aubry M.-P (1995) Upper Eocene impactites of the U.S. East Coast: depositional origins, biostratigraphic framework, and correlations. *Palaios* 10:16–43
- Poag CW, Powars DS, Poppe L, Mixon RB (1994) Meteoroid mayhem in Ole Virginny: source of the North American tektite strewn field. *Geology* 22:691–694
- Pohl J, Stöffler D, Gall H, Ernst K (1977) The Ries impact crater. In: Roddy DH, Pepin RO, Merill RB (eds) *Impact and explosion cratering*. Pergamon Press, New York, pp 343–404
- Schmidt RM, Housen KR (1987) Some recent advances in the scaling of impact and explosion cratering. *Int J Impact Engng* 5:543–560
- Schnetzler CC (1992) Mechanism of Muong Nong-type tektite formation and speculation on the source of Australasian tektites. *Meteoritics* 27:154–165
- Shoemaker EM (1962) Interpretation of lunar craters. In: Kapal Z (ed), *Physics and astronomy of the Moon*. Academic Press, Orlando FL, pp 283–359
- Shoemaker EM, Batson RM, Holt HE, Morris EC, Rennison JJ, Whitaker EA (1969) Observations of the lunar regolith and the earth from the television camera on Surveyor 7. *J Geophys Res* 74:6081–6119
- Shuvalov VV (1999) Multi-dimensional hydrodynamic code SOVA for interfacial flows: application to thermal layer effect. *Shock Waves* 9(6):381–390
- Shuvalov VV (2002) Displacement of target material due to impact. *LPSC XXXIII*. #1259
- Staudacher T, Jessberger EK, Dominik B, Kirsten T, Schaeffer OA (1982) ^{40}Ar – ^{39}Ar ages of rocks and glasses from the Nordlinger Ries crater and the temperature history of impact breccias. *J Geophys* 51:1–11
- Steel D (1998) Distributions and moments of asteroid and comet impact speeds upon the Earth and Mars. *Planet Space Sci* 46:473–478
- Stöffler D (1982) Density of minerals and rocks under shock compression. In: Angenheister A (ed) *Physical properties of rocks 1a*. Springer-Verlag, Berlin, pp 120–183
- Stöffler D (1984) Glasses formed by hypervelocity impact. *J Non-Cryst Solids* 67:465–502
- Stöffler D, Artemieva NA, Pierazzo E (2002) Modeling the Ries-Steinheim impact event and the formation of the Moldavite strewn field. *Meteoritics Planetary Sci* 37:1893–1908
- Swift HF, Clark BC (1983) Mechanism for crater debris escape from planetary-sized bodies. *LPSC XIV*, pp 765–766
- Tera F, Middleton R, Klein J, Brown L (1983) Berillium-10 in tektites. *EOS Trans. AGU*. 64:284
- Teterev AV (1999) Cratering model of asteroid and comet impact on a planetary surface. *Intern J Impact Engng* 23:921–932
- Thompson SL, Lauson HS (1972) Improvements in the Chart D radiation-hydrodynamic CODE III: Revised analytic equations of state. Report SC-RR-71 0714. Sandia National Laboratory, Albuquerque, p 119
- Treiman AH (1987) Geology of Nakhilite meteorites: cumulate rocks from flows and shallow intrusions. *LPSC XVIII*, pp 1022–1023
- Trunin RF, Gudarenko LF, Zhernokletov MV, Simakov GV (2001) Experimental data on shock compression and adiabatic expansion of condensed matter. *RFNC-VNIIEF, Sarov*, p 446
- Urey HC (1955) On the origin of tektites. *Proc Natl Acad Sci* 41:27–31
- Valentine GA, Wohletz KH (1989) Numerical models of Plinian eruption columns and pyroclastic flows. *J Geophys Res* 94:1867–1887
- Valette-Silver N, Brown L, Klein J, Middleton R, Pavic MJ, Tera F (1983) Berillium-10: vertical distribution in solis and sediments. In: *Yearbook of the Carnegie Institution '82*, Carnegie Institution, Washington, DC, pp 462–463

- Vickery AM (1986) Size-velocity distribution of large ejecta fragments. *Icarus* 67:224–236
- Vickery AM (1993) The theory of jetting: application to the origin of tektites. *Icarus* 105:441–453
- Viste E, Anders E (1962) Cosmic-ray exposure history of tektites. *J Geophys Res* 67:2913
- Walker D, Stolper EM, Hays JF (1979) Basaltic volcanism: the importance of planet size. *Lunar Planetary Science Conference X*, pp 1995–2015
- Warren P (1994) Lunar and Martian meteorites delivery services. *Icarus* 111:338–363
- Wasson JT, Wetherill GW (1979) Dynamical chemical and isotopic evidence regarding the formation locations of asteroids and meteorites. In: Gehrels T (ed) *Asteroids*. University of Arizona Press, Tucson, pp 926–974
- Weiss BP, Kirschvink JL, Baudenbacher FJ, Vali H, Peters NT, Macdonald FA (2000) A low temperature transfer of ALH84001 from Mars to Earth. *Science* 290:791–795
- Wood CA, Ashwal LD (1981) Meteorites from Mars: prospects, problems and implications. *LPSC XXII*, pp 1197–1199
- Zel'dovitch Ya B, Raiser Yu P (1967) *Physics of shock waves and high-temperature hydrodynamic phenomena*. Academic Press, New York

CHAPTER 9

MARINE TARGET IMPACTS

VALERY SHUVALOV, IRINA TRUBETSKAYA
AND NATALIA ARTEMIEVA

*Institute for Dynamics of Geospheres, Russian Academy of Sciences, Moscow 119334, Russia
E-mail: shuvalov@idg.chph.ras.ru; trub@idg.chph.ras.ru; artemeva@psi.edu*

Most cosmic bodies impacting the Earth fall into seas and oceans, which cover more than two-thirds of the Earth's surface. However, among more than 150 craters discovered on the Earth, only 15–20 found recently were formed as a result of marine target impacts (Ormö and Lindström 2000). The deficit of underwater craters is explained by the relative youth of a typical ocean floor (<150–180 Ma), insufficient exploration of the sea/ocean floor, and specific features of the underwater cratering process. Most of the known underwater craters were formed in shallow seas, where the water depth is comparable with an impactor size. Eltanin (Gersonde et al. 1997) is the only presently known impact structure formed due to impact into a deep (~4 km) ocean.

The process of cratering of marine target impacts has been poorly investigated; however, relations obtained for continental craters are commonly used to estimate the parameters of underwater craters. A small number of numerical simulations were performed for the first stage of marine impacts of very large projectiles (~10 km), which are of interest from the viewpoint of impact-induced mass extinctions of biota (O'Keefe and Ahrens 1982b; Roddy et al. 1987). However, these simulations gave neither the shape of a final crater nor the parameters of generated tsunami waves. Laboratory experiments (Gault and Sonnet 1982) and detailed numerical simulations (Artemieva and Shuvalov 2002) made it possible to determine the critical sea depth at which an underwater crater is formed at the sea floor and where shock-modified material can be found. A number of works (Adushkin and Nemchinov 1994; Hills et al. 1994; Nemtchinov et al. 1996) used the estimates based on nuclear explosion data and the numerical modeling of the impact initial phase to study tsunami generation caused by the impact of a comet into an ocean 4 km in depth.

Ormö and Lindström (2000) presented a hypothesis that marine impacts can generate concentric craters with a relatively small depression on the top of a solid crystalline basement, which is located in the center of a larger shallow crater formed in low-strength sedimentary rocks. Such structures are observed, for example, on the Moon (Quaide and Oberbeck 1968), where solid rocks are covered with a layer of regolith. The diameter ratio for the outer and inner craters can reach 5:10. However, preliminary calculations (Shuvalov 2000) have shown that this ratio cannot exceed 2:3 for the fall of cosmic bodies into terrestrial seas, and it is likely that the real ratio is even less.

One more characteristic feature of underwater craters is radial channels (gullies) around the central depression. Such channels (up to 100 m in depth, 1 km in width, and several kilometers in length) are clearly seen around the crater Lockne (Ormö and Lindström 2000) and Kamensk (Movshovich and Milyavskii 1990). The formation of gullies is accounted for by erosion of the crater floor while water is filling the crater (Dalwigk and Ormö 2001). A theoretical model of this process has not yet been developed. It is not clear how the expected effect depends on the ocean depth and why well-pronounced gullies have not been found around other underwater craters. The morphology of underwater craters has hardly been studied so far.

The fall of an asteroid into a water basin is a typical example of a high-velocity impact into a stratified target. At least three layers can be distinguished here: water, low-strength sedimentary rocks, and a crystalline basement. A qualitative description of crater formation in the stratified target was given by Quaide and Oberbeck (1968). They investigated experimentally the impact (at a speed of $1\text{--}7\text{ km}\cdot\text{s}^{-1}$) of cylindrical and spherical bodies (glass, lexan, aluminum), 4–8 mm in size, into a target composed of a sand layer covering a stronger material (sand glued with epoxide resin). Various craters (parabolic, flat-bottomed, and concentric) were generated at different ratios between the impactor diameter and the sand layer thickness. However, these results can not be used quite correctly to explain the mechanism of formation of underwater craters on the Earth, since Quaide and Oberbeck (1968) investigated small strength-dominated craters with morphology and relative sizes differing from those for large gravitational craters (Melosh 1989).

The existing results of experimental and theoretical studies show that the cratering process is largely determined by parameter d/H , where d is the impactor diameter and H is the sea depth. When $d/H < 0.1$, no underwater crater is formed at all (Gault and Sonnet 1982; Artemieva and Shuvalov 2002). When $0.2 < d/H < 2$, a water layer significantly influences the cratering process, sizes, and morphology of the resulting crater (Shuvalov 2000). Finally, when $d > 2H$, the water column has almost no effect on the crater-forming flow (Shuvalov 2000). However, even in this case the structure and morphology of the resulting crater can differ from those of similar craters on land. This difference is explained by the different petrophysical properties of the target as well as by the erosion of the surface of the crater while it is being filled with water (Ormö and Lindström 2000).

This chapter describes a physical and mathematical model of marine target impacts and presents results of numerical simulations of three terrestrial underwater impact structures: Eltanin, Lockne, and Mjølnir. These impact structures have been chosen because they have been relatively well studied and they represent the typical regimes of crater formation at different projectile diameter to water depth ratios: $d/H = 0.25$ for Eltanin, $d/H = 4$ for Mjølnir, $d/H = 1$ for Lockne.

1 NUMERICAL MODEL

The SOVA multi-material multi-dimensional hydrocode (Shuvalov 1999a; Shuvalov et al. 1999) was used to simulate all the stages of the impact (the impactor penetration into the target, crater-forming flow, filling of the crater with water, generation of tsunami waves). The main feature of the code is an explicit definition of the boundaries between the areas occupied by different materials or materials in different states of aggregation (e.g., soil, water, air, vapor, etc.). To build the boundaries the method described by McGlaun et al. (1990) is used. To calculate the thermodynamic parameters of involved materials the tabular equation of state for air (Kuznetsov 1965), the Tillotson equation of state (Tillotson 1962) for water, and the tables obtained by the ANEOS code (Thompson and Lauson 1972) for target rocks are employed. The SOVA code is close in its characteristics to the CTH code (McGlaun et al. 1990) which is widely used in the United States. In order to simulate the crater modification stage, a subroutine taking into account the influence of strength on the soil motion was added into the SOVA code. The authors used the approach developed by Melosh and Ivanov (1999) and O'Keefe and Ahrens (1999), which is based on the rigid-plastic model (Dienes and Walsh 1970).

2 MJØLNIR

According to estimates (Tsikalas et al. 1998a), the 40-km-diameter Mjølnir crater in the Barents Sea was a result of an asteroidal impact that occurred 142 Ma ago. The estimated projectile diameter is 1–3 km, a probable water depth is 300–500 m. The seismic sounding made it possible to find the size of a disturbed zone in the underwater soil, which is interpreted as a transient crater (Tsikalas et al. 1998a). At the time of the impact the crystalline basement was covered with a thick (4–5 km) layer of Mesozoic sediments. Due to low strength of the sedimentary rocks the process of crater collapse under gravity (modification) was more intensive than in similar continental impacts. As a result the final crater is wider and shallower than continental counterparts (Tsikalas et al. 1998a).

On the basis of previous estimates a vertical impact of a 1,600-m-diameter asteroid into a 400-m-deep sea was considered. A set of runs with different cohesion Y_0 and dry friction coefficient k dependencies on depth were performed. The best fit to observational data was obtained for $Y_0 = 10^6$ Pa and a composite target strength structure: very low strength for the upper 3 km of sedimentary rocks (described by

the Tillotson equation of state for wet tuff) and a gradual strength increase from 3 to 6.5 km depth up to values typical for granitic rocks (Melosh 1989) at greater depths. This friction–depth dependence corresponds to the geological structure of the Barents Sea floor at the impact site (Tsikalas et al. 1998b).

The initial stage of the impact is shown in Fig. 1. The asteroid with a chosen diameter reaches the solid surface without noticeable deformation and deceleration. A shock wave generated in the target induces a crater-forming flow, and a growing cavity appears. Ten seconds after the impact the transient crater reaches its maximum depth (~6 km). The crater diameter continues to grow due to excavation. Within approximately 30 s the excavation terminates, but the crater diameter continues to grow due to the collapse of crater walls under gravity (modification stage). At the same time the temporal fluidization induces the uplift of the crater floor and the formation of a central hill, which are typical for complex craters (Melosh 1989). However, the intensive collapse of crater walls (which is more intensive than that for continental craters because of the low strength of sedimentary rocks) continuously “buries” the growing central hill. Slumping flows moving inwards collide at the symmetry point, forming a high temporal pike. The shape of the crater is close to the final one 150 s after the impact.

The increase in the strength of sedimentary rocks in the calculations requires a larger (2,000-m) impactor for formation of the crater of the same size. In this

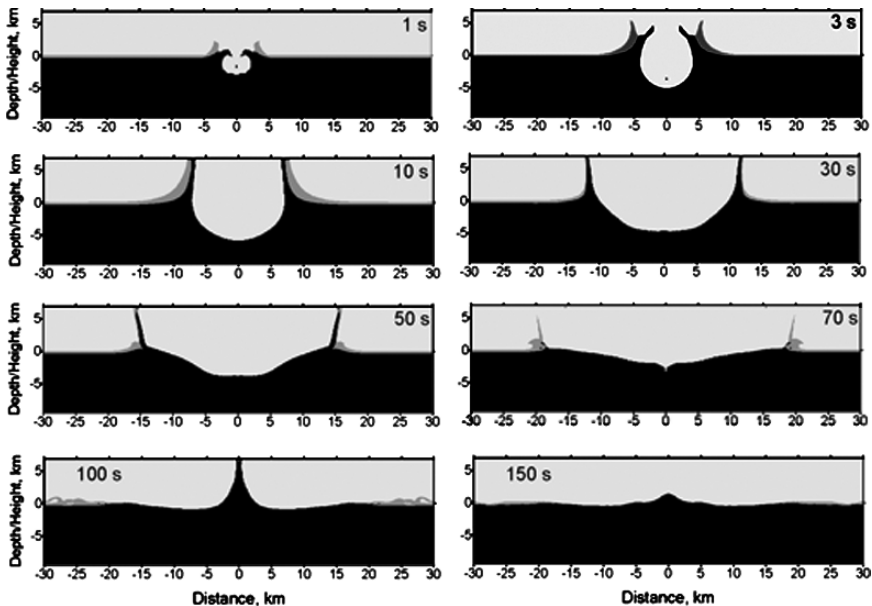


Figure 1. Cratering flow after the impact of a 1,600-m-diameter stony asteroid into a sea 400 m in depth (Mjølnir). Water is shown in gray, soil in black. The figure is adapted from Shuvalov et al. (2002) and reprinted with the kind permission of the American Geophysical Union

case, the depth of the transient crater is ~ 8 km, which contradicts the seismic data. The rim of the growing crater pushes sea water outward and upward, thereby generating a water surge. The surge moves from the center ahead of the crater wall and the ejecta curtain. The height of the water surge increases first, and then the surge collapses, breaking down into several waves. Interaction between these waves results in a tsunami (Fig. 2). It should be noted that all the images in Fig. 2 are stretched vertically by a factor of 10 for visualization. The last distribution in Fig. 1 coincides with the first one in Fig. 2. A tsunami wave with amplitude of ~ 200 m is formed approximately 300 s after the impact at a distance of 50 km from the crater center. Until this moment, the water flow is considerably heterogeneous: The layers at different depths move at different velocities (and sometimes even in different directions).

Typically, it takes 30 min for the crater to be filled with water and the stationary sea level to be restored. The initial velocity of the water flow directed to the crater center reaches $50\text{--}70\text{ m}\cdot\text{s}^{-1}$ (Fig. 3) and remains at a rather high level ($\sim 20\text{ m}\cdot\text{s}^{-1}$) for 20–30 min. Such a high speed flow can significantly influence the ejecta sedimentation and erode the crater floor. Falling particles with sizes of ~ 1 cm or less can be transported by the water flow for long distances comparable to the crater size.

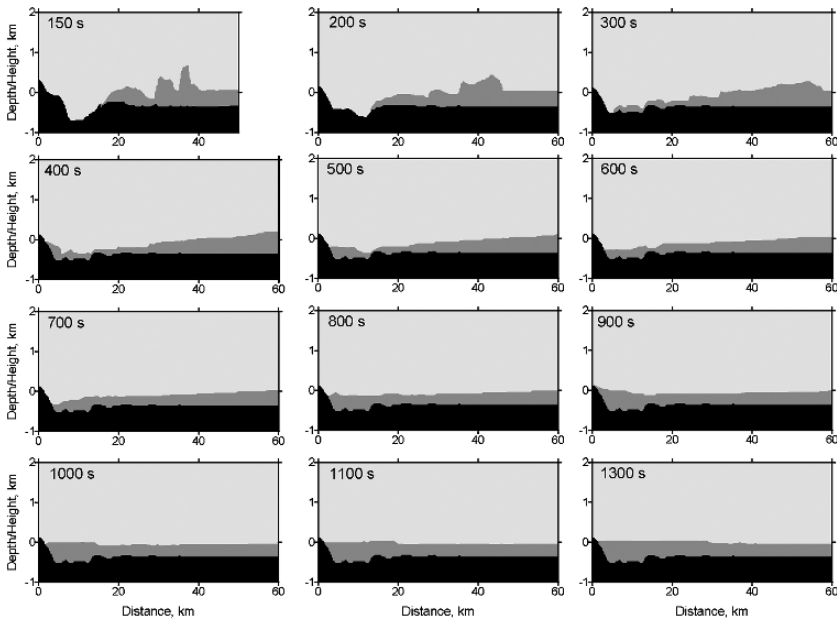


Figure 2. Filling of the crater Mjølknir with water and generation of the tsunami wave. All images are stretched in the vertical direction by a factor of 10. Water is shown in gray, soil in black. The figure is adapted from Shuvalov et al. (2002) and reprinted with the kind permission of the American Geophysical Union

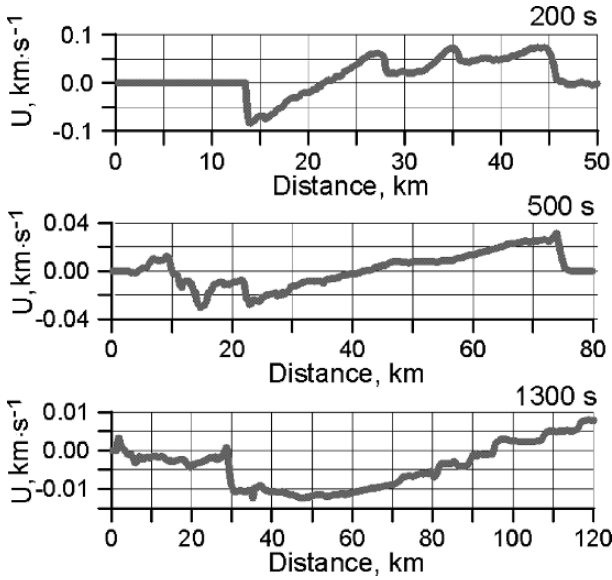


Figure 3. Velocity distributions in resurge flow (during filling of the crater with water). Values of horizontal velocity averaged over the stream depth are shown. The figure is adapted from Shuvalov et al. (2002) and reprinted with the kind permission of the American Geophysical Union

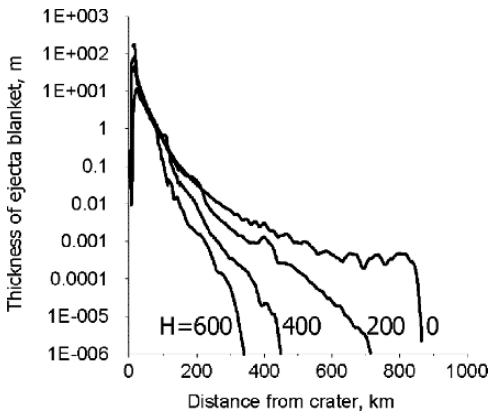


Figure 4. Thickness of ejecta blanket versus distance from the crater center for different water depth H (in meters). The figure is adapted from Shuvalov and Dypvik (2004) and reprinted with the kind permission of the University of Arizona/Geosciences Department

Since the tsunami amplitude is inversely proportional to the distance from the source, its height must reach 20 m at a distance of 500 km from the crater and 4 m at 2,000 km. When the wave approaches a shore, the wave height increases sharply.

The results described in the preceding show that 400 m water layer very slightly influences the cratering flow and parameters of the transient crater. However, even such shallow water can considerably affect the distribution of distal ejecta. It follows from numerical simulations that the fastest (and, consequently, farthest reaching) ejecta are thrown out from the uppermost target layer. In the marine impact the upper target layer consists of water. Hence, the water ejecta have the highest velocities, and solid ejecta (being ejected from deeper target layers) are characterized by lower velocities and, consequently travel smaller distances than in the case of similar subaerial (land) impacts. Figure 4 shows that the area of ejecta deposition strongly decreases as water depth increases.

It is known that most craters (even those resulting from oblique impacts) are nearly circular. However, the impact angle can strongly influence ejecta deposition as shown in Pierazzo and Melosh (2000) and references therein. This effect for subaerial impact craters was first demonstrated in experiments by Gault and Wedekind (1978). They found that ejecta deposits remained near circular for impact angles down to 45° , with only a slight downrange shift from the center. As the impact angle decreases $< 45^\circ$, ejecta deposits become strongly asymmetrical, and the so-called “forbidden” azimuthal zones appear first uprange and then downrange of the crater. Recent experiments by Schultz (1999) show that high-velocity ejecta move preferably in the downrange direction, whereas low-velocity ejecta are distributed more symmetrically. To estimate the influence of impact angles on the Mjølfnir ejecta distribution the 3D numerical simulations were performed for 30° and 45° oblique impacts (Shuvalov and Dypvik 2004).

The initial stage of the oblique impact (Fig. 5) is strongly asymmetrical and produces an asymmetrical ejecta cone. The projectile decelerates on the downrange crater wall, gradually moves downrange and upward, and in 5 s after the impact most projectile material escapes from the crater. The crater itself becomes almost symmetrical, although its center is shifted downrange by about 3 km.

Figure 6 shows the distributions of ejecta deposits for different impact angles, without water and into the sea 400 m in depth. The ejecta blanket area strongly increases as the impact angle decreases from vertical to 45° .

This increase of ejecta blanket is the result of a significant increase in the downrange ejecta velocity. In the land impact the central part of ejecta deposits (at a distance of a few crater radii) looks very similar to experimental data of Gault and Wedekind (1978). “Forbidden” azimuthal zones do not appear, although a region of relatively lower thickness of ejecta deposits can be seen at distances $> 1,000$ km or 25 crater radii (Fig. 6*b*). Overall, the decrease in impact angle strongly increases the area of ejecta deposits and makes it strongly asymmetrical, although close ejecta are almost symmetrical.

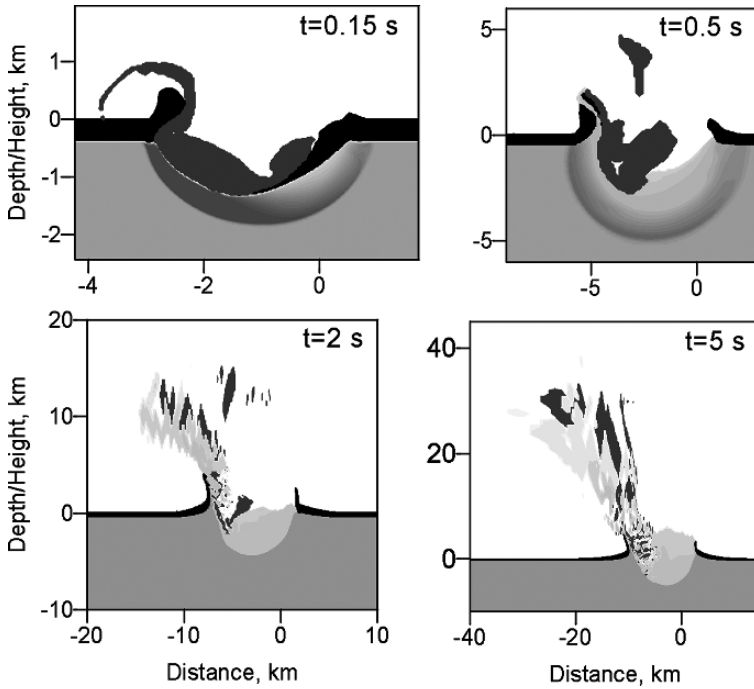


Figure 5. Initial stage of the cratering flow after the oblique 45° impact of a 1,600-m-diameter asteroid into the sea 400 m in depth. Water is shown by black, projectile material is shown by dark gray shading, solid target material is shown by light gray shading. The figure is adapted from Shuvalov and Dypvik (2004) and reprinted with the kind permission of the University of Arizona/Geosciences Department

The ejecta distributions for impacts into the 400 m layer of water at different angles demonstrate both tendencies: a decrease of ejecta blanket in the presence of water layer and an increase of ejecta deposit area with a decrease in impact angle (Figs. 6c–e). In the vertical impact into the 400-m sea an area of ejecta deposits is restricted to a distance approximately 600 km from the crater. A decrease of impact angle leads to an increase of this area up to 3,000–4,000 km in the downrange direction. The area of ejecta deposits becomes even more anisotropic than in an equivalent subaerial case. The structure of this downrange zone of deposits probably depends on both water depth and a projectile shape. However, these particular distributions illustrate where to find the deposits: downrange, in the cone with angle 60° at a distance $<3,000\text{--}4,000$ km. The projectile ejecta for a 45° oblique impact into the sea (Fig. 6f) have a larger velocity and are even more asymmetrical (move in a narrower angle) than the target ejecta.

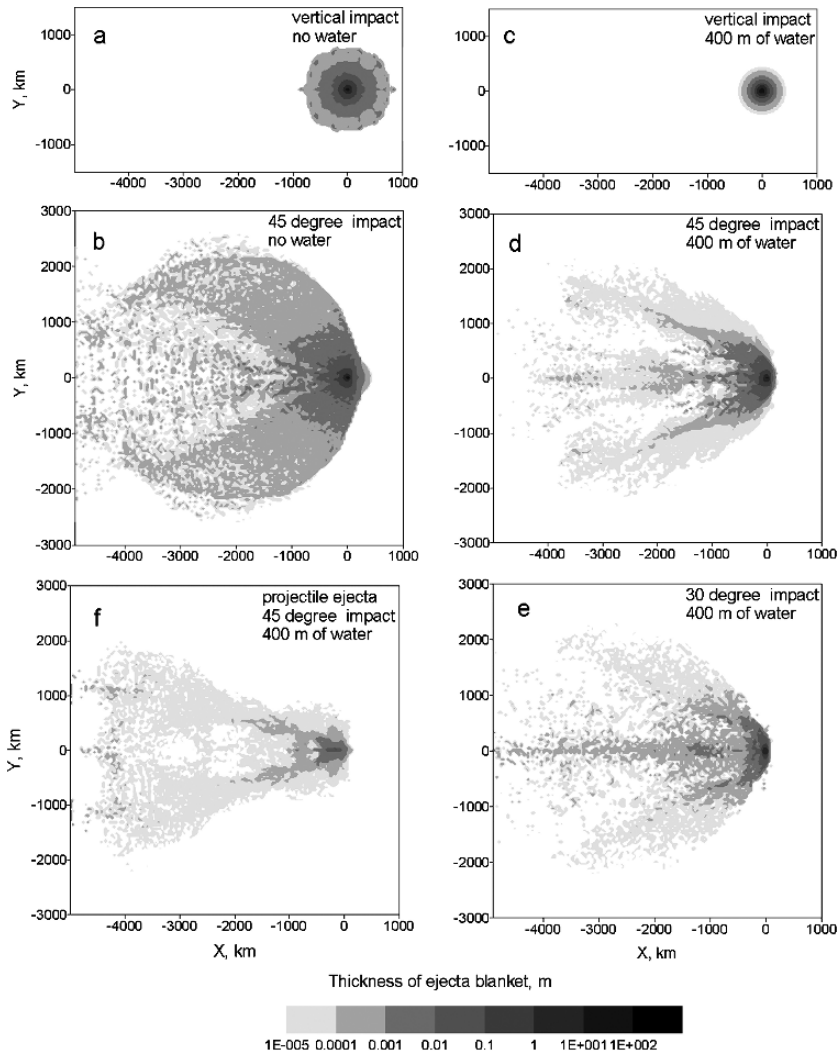


Figure 6. Distributions of basement ejecta deposits after the vertical impact without water (a) 45° oblique impact without water (b) vertical impact into 400 m deep sea (c) 45° (d) and 30° (e) oblique impact. Plate f shows distribution of projectile material after the 45° oblique impact into the sea 400 m deep. Impact direction is from right to left. The figure is adapted from Shuvalov and Dypvik (2004) and reprinted with the kind permission of the University of Arizona/Geosciences Department

3 LOCKNE

The age of the underwater crater Lockne located in Sweden is estimated to be ~450 Myr (Ormö and Lindström 2000). Presumably, the crater is a result of an asteroidal impact into the sea with a depth ranging from 200 to 1000 m. The morphology of

the Lockne crater differs noticeably from that of continental craters of the same size. There is an inner crater in the center of the impact structure; its diameter is ~ 7.5 km, and its depth is ~ 500 m. The inner crater formed in the crystalline basement is surrounded by an outer shallower crater in 80-m-thick sedimentary rocks; its diameter is estimated to be 12–25 km. The upper layer of crystalline rocks is strongly fractured at a distance of 2–3 km from the inner crater; dikes and chaotically located breccia areas are observed. A characteristic feature of the Lockne crater is the radial gullies up to 3 km in length; they are up to 100 m deep and 1 km wide. At least four such gullies have been clearly identified.

Ormö and Lindström (2000) supposed that the origin of the concentric impact structure is similar to that of lunar craters, the forming mechanism of which was reproduced experimentally by Quaide and Oberbeck (1968). Ormö and Lindström also suggested that all or at least most of the underwater impact structures have inner and outer craters.

The first attempt to numerically check the possibility of concentric crater formation due to a marine target impact was made by Shuvalov (2000). The impacts of 100-m-radius asteroids and comets into a water basin of depth 100–500 m were considered. Most of the calculations did not take the layer of sedimentary rocks into account, but the evolution of the water crater and the formation of the depression in the crystalline basement were considered in detail. It was assumed that the outer crater (in sedimentary rocks) could not be larger than the maximum transient water crater, because the water strength is zero and water density is less than that of sedimentary rocks. The calculations showed that, at different ratios of impactor diameter d to water depth H , the ratio between the radii of water craters and inner craters does not exceed 2–2.5. One of the variants considered a 100-m layer of sedimentary rocks at a depth of 300 m. The size of an outer crater in sedimentary rocks obtained in the simulations was noticeably less than the maximum radius of a water transient crater. However, the work of Shuvalov (2000) used a very rough strength model, did not describe the modification stage, and studied craters that are considerably smaller than the Lockne crater.

More accurate simulations of asteroidal impacts occurring at a speed of $20 \text{ km}\cdot\text{s}^{-1}$ into a sea 200, 500, and 1,000 m deep were described in Shuvalov and Trubetskaya (2002) and Ormö *et al.* (2002). The diameter of a spherical impactor (600 m) was chosen so that the crater size in crystalline rocks (for which the granite equation of state was used) corresponds to the geologic survey data on the Lockne crater. Some results of these calculations are shown in Figs. 7 and 8. Two seconds after the impact into a sea 1,000 m in depth, a pronounced hemispherical bottom crater appears inside a cylindrical water cavity (Fig. 7). About 10 s after the impact, the water cavity reaches its maximum diameter of ~ 10 km. At this moment, the crater in crystalline rocks is approximately twice as less, but its diameter continues to increase due to the collapse of crater walls (crater modification).

The collapse results in a decrease in the crater depth and the formation of a central high. The modification of the crater ends before water begins to fill it. The finally

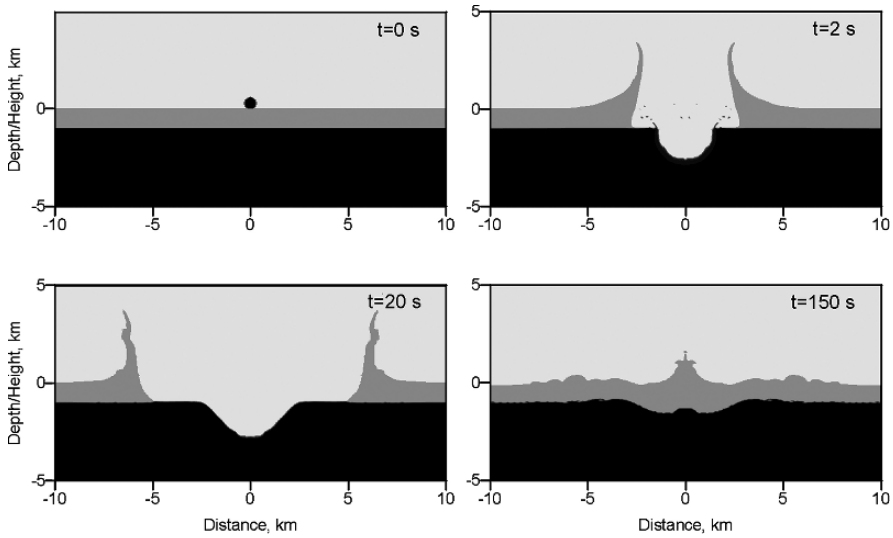


Figure 7. Formation of the crater (Lockne) after impact of a 600-m-diameter asteroid into a sea 1,000 m in depth. Water is shown in gray, the impactor and solid target in black. The figure is adapted from Shuvalov and Trubetskaya (2002) and reprinted with the kind permission of Pleiades Publishing Inc.

formed central crater is filled with water 150 s after the impact. Its diameter is 6–7 km; i.e., it is less than the maximum size of the transient water crater by only a factor of 1.5.

If the sea depth is 500 m, the flow pattern changes slightly (Fig. 8). One second after the impact, a bottom crater and a water crater are formed separately, as in the case of the 1-km depth. However, the water cavity stops growing earlier than in the previous case, and the crater in the rocks grows faster. As a result, ~ 10 s after the impact intensive interaction between the ejecta from the basement crater and the walls of the water cavity begins. The excavated soil pushes water out and mixes with it. After 100 s, water begins to fill the crater. The shape of the final crater is almost the same as in the previous case; the diameter is somewhat larger (~ 8 km).

The growth of the water cavity is determined by the propagation of the cylindrical compression wave, which induces the outward directed motion of water. The increase of the size of the water crater ends when the dynamic pressure behind the wave front $\rho_w u^2$ becomes equal to the hydrostatic pressure $\rho_w g H$. Here, u is the horizontal velocity of water, ρ_w is the water density, and H is the water depth. When the depth H is small, the amplitude of the compression wave (i.e., dynamic pressure) rapidly falls because of the lateral release behind the front (i.e., due to the upward ejection of water). This causes a decrease in the water cavity diameter as the depth decreases. Note that if the depth is very large, the cavity diameter can decrease due to the increase in the hydrostatic pressure $\rho_w g H$, but this occurs at a depth comparable to the crater depth in deep water.

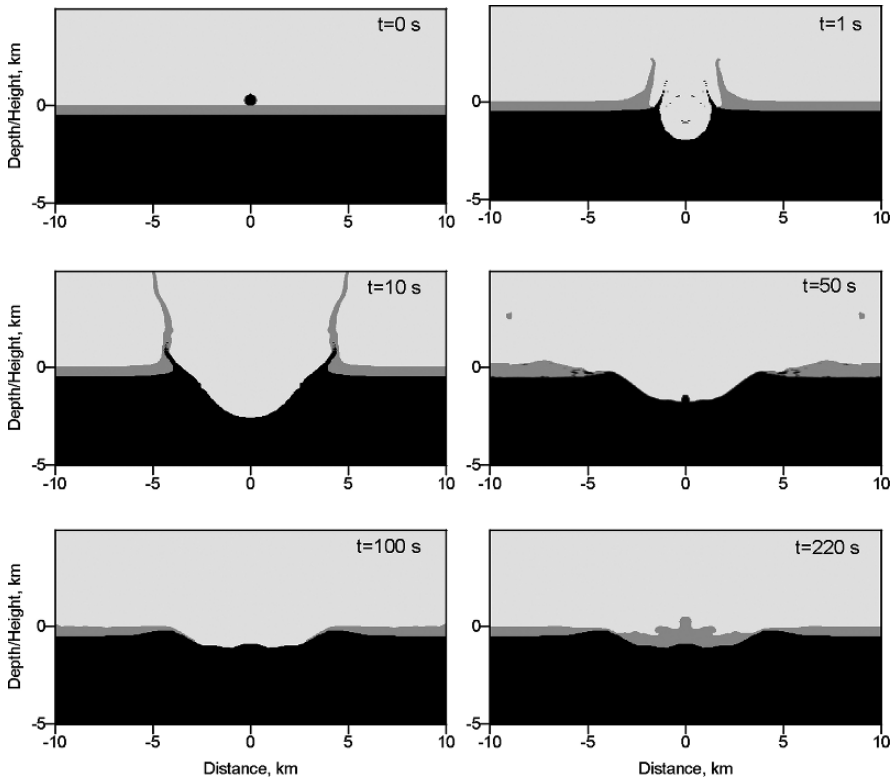


Figure 8. Formation of the crater (Lockne) after impact of a 600-m-diameter asteroid into a sea 500 m in depth. Water is shown in gray, the impactor and solid target in black. The figure is adapted from Shuvalov and Trubetskaya (2002) and reprinted with the kind permission of Pleiades Publishing Inc.

When the sea depth is as low as 200 m, a detached water crater practically does not appear. The water layer behaves like a thin skin whose motion is governed by soil displacement. In this process water only slightly influences the cratering flow in soil. The crater diameter reaches 9 km. (It would be the same if there were no water at all.) It remains unknown whether the crater is filled with water or not, since a crater-wall height is comparable to the sea depth. The accuracy of the model, resolution of the computational grid, and approximate data on the soil properties used in the calculations do not allow investigating such effects.

Numerical simulations of the vertical impact of a 600-m-diameter asteroid on a three-layered target (a crystalline basement, 100 m of sedimentary rocks, and 800 m of water) were described in (Shuvalov et al. 2005). The strength of the sedimentary rocks was considered to be very small (zero friction and 10^7 Pa cohesion). Some results are shown in Fig. 9.

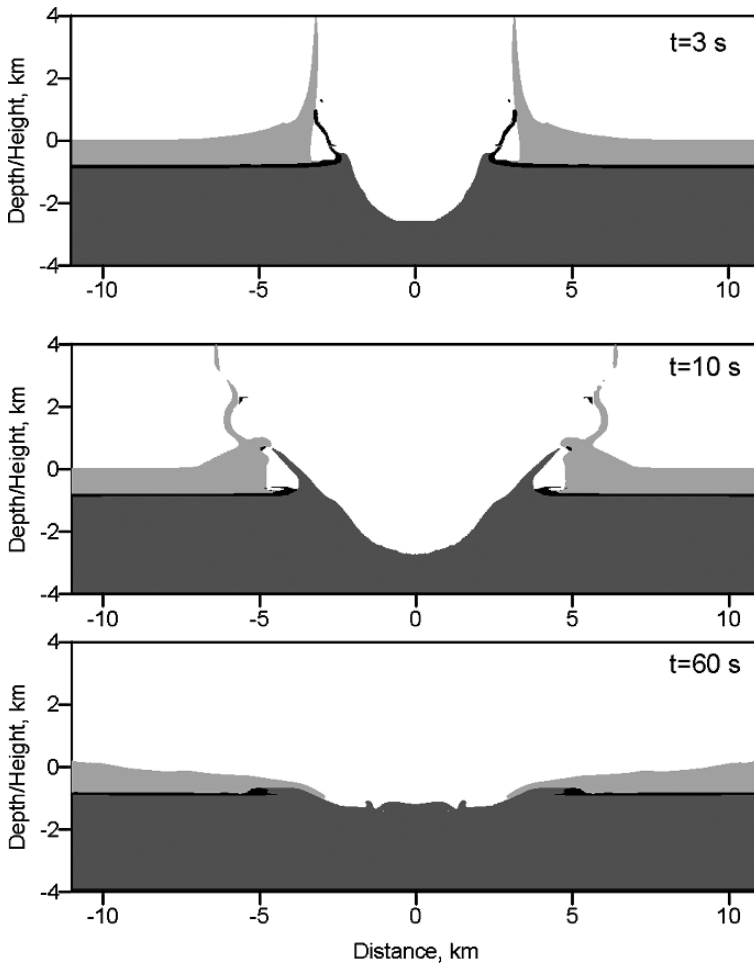


Figure 9. Cratering flow at various times after the vertical impact of a 300-m-radius granitic asteroid into a 800 m deep sea. Black is sediments, light gray is water, dark gray is basement material. Atmospheric gas, projectile material, and ejecta with low bulk density are not shown. The figure is adapted from (Shuvalov et al. 2005, Fig. 1) and reprinted with the kind permission of Springer Science and Business Media

At the beginning the ejecta curtain consists of sedimentary fragments only. Later, more powerful basement ejecta curtains form. A considerable difference between water and sediments behaviors can be seen. The difference is explained by the higher density and strength (small though it is) of sediments. One more reason is the small thickness of the sediment layer. In an analogy with water, it could be said that there is an impact into “shallow sediments.” As a result there is no detached cavity in sediments (similar to a detached water cavity). However, moving outward,

the rim of the basement crater pushes off low-strength sediments (like a bulldozer). As a result, an area cleared from sediments appears outside the basement crater rim; its width reaches 1–1.5 km.

The area cleared from sediments can increase due to water erosion (at the stage of water cavity growth). Dense, shock compressed water moves outside at a velocity of about $100 \text{ m}\cdot\text{s}^{-1}$ and can strongly erode a sedimentary surface disturbed by shock wave and spallation. The erosion mechanism also can explain the wide range of available estimates of the outer crater diameter (from 12 to 24 km). The flow velocity continuously decreases with distance from the central crater, and the erosion ceases.

As mentioned, one of the results of the floor erosion produced by the water stream is radial gullies around the central crater, which are clearly observed for the Lockne crater. Moreover, the presence of such gullies is likely to be an indicator that the crater was created due to a marine target impact (Ormö and Lindström 2000). However, well-pronounced gullies have been found only around two craters: Lockne (Dalwigk and Ormö 2001) and Kamensk (Movshovich and Milyavskii 1990). The reason remains unclear why such gullies have not been found around ~15 other known hydroblems, as well as the mechanism of formation of radial channels. The general claim is that the gullies are formed by erosion of the upper destroyed layer of crystalline rocks produced by a strongly turbulent water stream containing a large amount of soil particles of different size (Dalwigk and Ormö 2001). The radial orientation of gullies can be accounted for either by the specific nature of the disruption of the crystalline basement (e.g., by the disruption along large radial fractures) or the development of some instability leading to an increase (deepening) in radial irregularities. The first estimates of different possible mechanisms of gullies formation are discussed in Shuvalov and Trubetskaya (2002). Investigation of these mechanisms is important for identification of marine impact craters on the Earth and other planets.

4 ELTANIN

Eltanin (Gersonde *et al.* 1997) is the only presently known impact structure formed during the fall of a cosmic body into a deep (4–5 km) oceanic basin. The evidence for the impact origin of the structure is the discovery in 1981 of an iridium anomaly in the bottom deposits (Kyte *et al.* 1981). Subsequent studies showed that meteoritic material is presented in three sedimentary rocks spaced at 500 km. The maximum concentration of iridium was found in vesicular fragments that were formed by melting of the impactor. Unmelted fragments of the impactor with sizes <2 cm were also found. Traces of heavy erosion of the oceanic floor and secondary sedimentation of the eroded material were discovered. According to the estimates by Gersonde and Kyte (2001), the Eltanin impact structure was formed after the impact of an asteroid 0.5–2 km in size that occurred 1.1 Myr ago. No traces of the bottom crater have been bound.

The results of numerical simulations of the initial stage (first 10 s) of the vertical impact of a 1.5-km-diameter asteroid at $20 \text{ km}\cdot\text{s}^{-1}$ velocity into a 4-km-deep ocean (Shuvalov 2003b; Shuvalov and Trubetskaya 2004b) show that a clearly pronounced crater about 2 km in depth is formed. The mass of melted rocks is about six times the impactor mass. These results disagree with the observational data; therefore, the mass of the impactor was less, at least if the impact was close to vertical. The impact of a smaller, 1-km-diameter projectile results only in a weak deformation of the sedimentary rocks, which was probably accompanied by strong erosion of the oceanic floor all around.

While penetrating a water layer, the asteroid decelerates, undergoes fragmentation, and transmits most of its energy to the water. Some portion of the impactor material can evaporate. However, contrary to the case of continental impacts, a considerable portion of impactor material (from 25% for velocity $20 \text{ km}\cdot\text{s}^{-1}$ and a vertical impact to 100% for velocity $15 \text{ km}\cdot\text{s}^{-1}$ and a 30° oblique impact) remains unmelted. This result is important from the viewpoint of possibly bringing organic material to the Earth by comets and asteroids (Pierazzo and Chyba 1999). Some amino acids can survive shock heating during asteroidal impacts into a deep ocean. After fragmentation and deceleration a portion of the projectile material (both melted and unmelted) is ejected at a velocity of $1\text{--}3 \text{ km}\cdot\text{s}^{-1}$ (together with water) to high altitudes and then falls into the ocean at distances as large as 100–1,000 km from the impact point. Another part is caught up by the water flow and disperses around the impact point. About 2 s after the impact, the growing water crater reaches the ocean floor. After 10 s, the water cavity takes on an almost cylindrical shape with a diameter of $\sim 15 \text{ km}$. The collapse of the water cavity starts approximately 30–40 s after the impact; near the outer surface the velocity of the water flow is directed away from the center; near the bottom the water velocity is directed to the center. The upward ejection of the water ends 60 s after the impact, and a head wave forms. In 100 s, the center-directed water flows collide and form a water column at the symmetry center. The collapse of this column results in generation of a second water wave, which is clearly seen in the last panel of Fig. 10.

The development of instability at the boundary between the moving water and the resting sediments leads to excavation of solid particles, and they are drawn into the water flow. However, the roughness of the model in use and insufficient spatial resolution do not allow modeling the floor erosion with sufficient accuracy. These results (concerning involvement of soil particles in the water flow) are completely illustrative.

The time dependence of water-level altitudes at distances of 20, 30, 50, and 70 km are shown in Fig. 11. The amplitude of the head wave reaches 1,200, 800, 450, and 300 m, respectively. A period of the wave is about 150 s. If it is assumed that the wave amplitude is inversely proportional to the distance from the source, the tsunami amplitude at the nearest point of South America must reach 20 m (without taking into account the change of the ocean depth in the near-shore zone). Such a powerful wave could induce catastrophic consequences through a large coastal area of the Pacific Ocean.

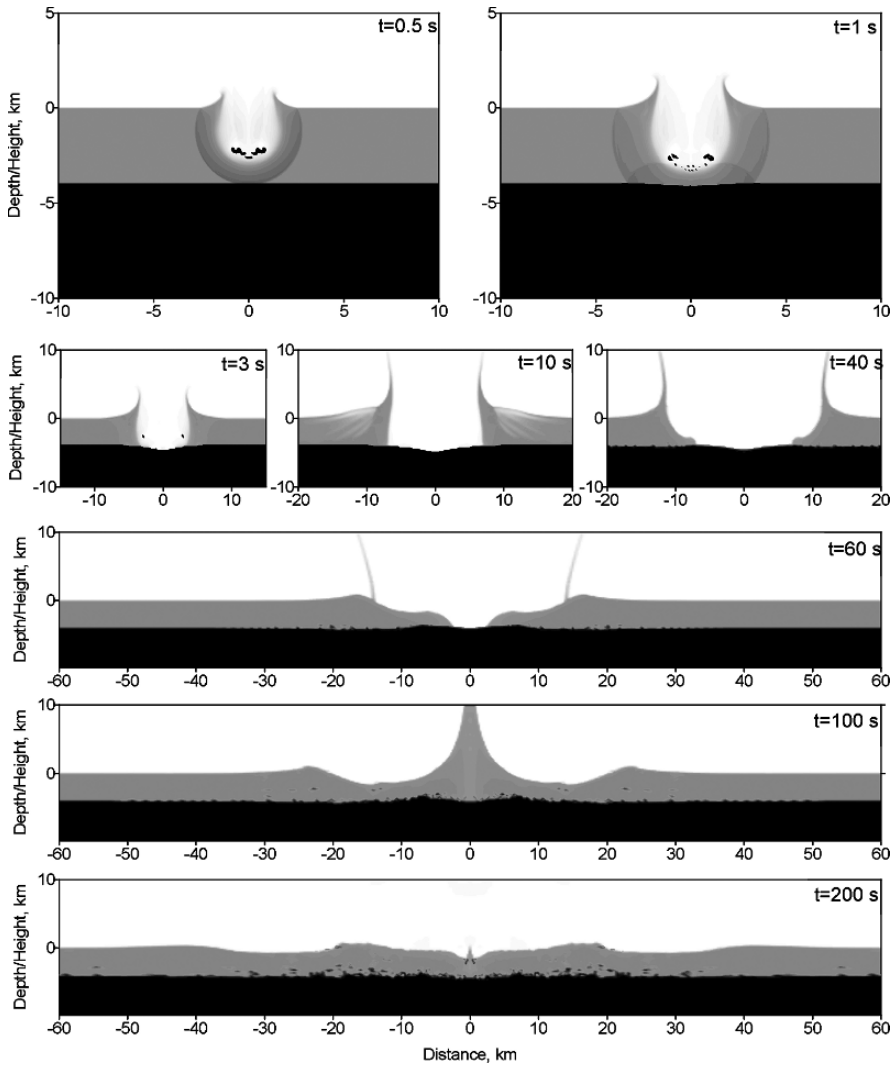


Figure 10. Evolution of water transient cavity and tsunami generation after impact of a 1-km-diameter asteroid into the ocean 4 km in depth. Water is shown in gray, projectile and solid surface are shown in black. The figure is adapted from Shuvalov and Trubetskaya (2002) and reprinted with the kind permission of Pleiades Publishing Inc.

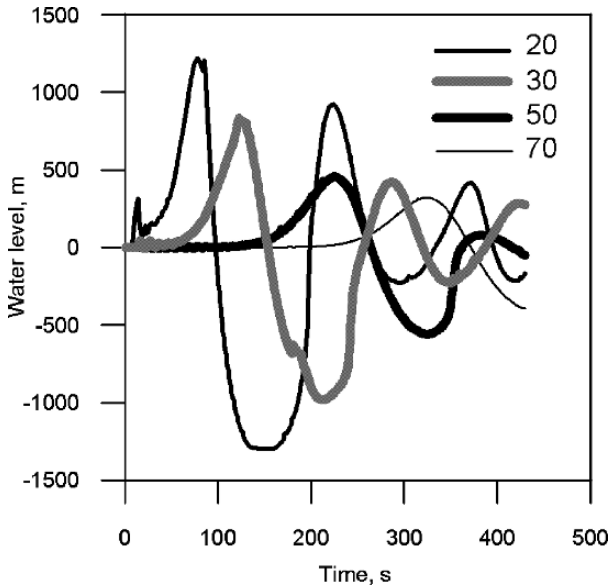


Figure 11. Oscillations of water level (induced by passing the tsunami wave) at distances 20, 30, 50, and 70 km from impact point. The figure is adapted from Shuvalov and Trubetskaya (2002) and reprinted with the kind permission of Pleiades Publishing Inc.

5 TSUNAMI: A COMPARISON WITH NUCLEAR-EXPLOSION DATA

At present, tsunami waves are considered as one of the main shock factors in the problem of asteroidal hazards (Adushkin and Nemchinov 1994). In the analysis of consequences of tsunami produced by marine target impacts, the following formula is commonly used (Glasstone and Dolan 1977):

$$h = 45 \frac{H}{L} (Y)^{0.25}, \quad (1)$$

Here, H is the water basin depth, h is the wave amplitude in meters, L is the distance from the source in kilometers, and Y is the released energy in kt TNT equivalent. This formula was derived from the analysis of data obtained during the Baker nuclear explosion in the 60-m deep lagoon on Bikini atoll; its energy was 20 kt (Glasstone and Dolan 1977).

For the impact of a 1-km-diameter asteroid (which is presumably responsible for the formation of the Eltanin impact structure), Equation (1) gives the wave amplitudes 850, 570, 340, and 240 m at distances 20, 30, 50, and 70 km from the impact site. The numerical simulations give, respectively, 1,200, 800, 450, and 320 m. The agreement is satisfactory: The difference does not exceed 30%. For the energy 2.5×10^8 kt released for the formation of the Mjølner crater,

Equation (1) gives amplitude of about 40 m at a distance 60 km from the center. This amplitude is significantly lower than that obtained in the simulations described in the preceding (~ 200 m). The energy of the impact under consideration is seven orders of magnitude higher than that released at the explosion on Bikini; consequently, the equivalent depth of the basin (according to hydrodynamic similarity) must be 200 times higher than the lagoon depth at the nuclear explosion site; i.e., it must be 12 km. From the viewpoint of cratering mechanics, a 12-km depth is deep water for the 1.6-km-diameter projectile: No underwater crater in bottom is formed, and tsunami results from the collapse of water transient cavity. In other words, Equation (1) was derived for the case of qualitatively different (from Mjøltnir case) mechanism of tsunami generation. When a 1.6-km-diameter projectile impacts a sea 400 m in depth, the tsunami is generated as a result of the expulsion water by the growing crater rim and the uplift of the sea bottom in the process of cratering flow. At the same time, a 12-km depth can be considered as “shallow water” in terms of the propagation of the tsunami wave, the length of which reaches tens of kilometers. Because of this, Glasstone and Dolan (1977) use Equation (1) for the case of shallow water.

To check these speculations and the obtained results, special simulations of an impact of a stony asteroid (with a diameter of 7.4 m and a velocity of $20 \text{ km}\cdot\text{s}^{-1}$) into a sea 60 m in depth have been performed. The energy of such an impact completely corresponds to that of the Baker explosion. This impact is purely hypothetical, since stony bodies of this size are fragmented in the Earth’s atmosphere and their fragments totally ablate in the atmosphere (Nemtchinov et al. 1997c). The maximum values of the wave height at different distances from the impact site obtained in calculations and measured on Bikini (Glasstone and Dolan 1977) are listed in Table 1. The difference between the calculated and measured results does not exceed 10–20%. This result indirectly confirms the conclusion that the difference between the Mjøltnir tsunami amplitudes, derived from the numerical simulations and from Equation (1) is explained by different mechanisms of tsunami generation in water of different depths rather than by the roughness of the model employed. At the same time, Equation (1) provides a reasonable estimate of the tsunami amplitude for cases in which an impactor diameter is much less than sea depth, and the underwater crater is either not formed at all or turns out to be too small to significantly influence the evolution of the water crater. Such a situation was released in the process of formation of the Eltanin underwater impact structure.

6 CONCLUSIONS

The existing experimental and theoretical studies show that the cratering process is largely determined by the ratio d/H , where d is the projectile size (diameter), and H is the water depth. If $d/H < 0.2$, no underwater crater is formed at all. The projectile undergoes fragmentation and decelerates, not reaching the floor. A considerable part of its mass remains unmelted. Eltanin is an example of such an impact.

Table 1. Tsunami-wave amplitude. The table is adapted from Shuvalov and Trubetskaya (2002) and reprinted with the kind permission of Pleiades Publishing Inc.

Distance, m	Wave height measured in Baker experiment, m	Wave height obtained from impact simulations, m
300	28	23
600	14	13
1200	7	6

If $d/H > 1$, the water layer has almost no influence on the cratering flow. In particular, in the Mjølnir case a presence of a 400-m-deep sea very slightly influenced the cratering process. Special morphological features of the Mjølnir crater resulted from a special structure of the target, in particular, from a thick layer of low strength sediments covering the crystalline basement. A powerful resurge flow (with velocity up to $70 \text{ km}\cdot\text{s}^{-1}$) resulting from the collapse of a water transient cavity could strongly influence deposition of ejected material. Moreover, even such shallow water can strongly influence the formation and deposition of distal ejecta.

If $0.2 < d/H < 1$, the water layer strongly influences the cratering flow, the formation and deposition of distal ejecta, and the morphology of the final crater. In this case concentric craters (a central depression in a crystalline basement surrounded by a shallow outer crater in sediments) can be formed.

There are two main mechanisms of impact-induced tsunami generation. If water depth considerably (by a factor of 3–4) exceeds a projectile size, tsunami results from the collapse of a water transient crater and the wave amplitude can be estimated from the relations derived from underwater nuclear tests. If, on the contrary, $d/H > 1$, the tsunami appears due to repulsion of sea water by the growing crater rim and the structural uplift of the sea floor. In this case the wave amplitude can be considerably higher than that estimated from relations derived from underwater nuclear tests.

REFERENCES

- Adushkin VV, Nemchinov IV (1994) Consequences of impacts of cosmic bodies on the surface of the Earth. In: Gehrels T (ed) Hazards due to comets and asteroids, University Arizona Press, Tucson, pp 721–778
- Artemieva NA, Shuvalov VV (2002) Shock metamorphism on the ocean floor (numerical simulations). Deep-sea research. Part II. Topical studies in oceanography 49(6):959–968
- Dalwigk I, Ormö J (2001) Formation of resurge gullies at impacts at sea: the Lockne crater, Sweden. Meteoritics Planetary Sci 36:359–369
- Dienes JK, Walsh JM (1970) Theory of impact: Some general principles and the method of Eulerian codes. In: Kinslow R (ed) High-velocity impact phenomena. Academic Press, New York, pp 46–104
- Gault DE, Sonnet CP (1982) Laboratory simulations of pelagic asteroidal impact: Atmospheric injection, benthic topography, and the surface radiation field. In: Silver LT, Shultz PH (eds) Geological

- implications of impacts of large asteroids and comets on the Earth. Geological Society of America Special Paper 190, pp 69–92
- Gault DE, Wedekind JA (1978) Experimental studies of oblique impact. Lunar Planetary Science Conference IX, pp 3843–3875
- Gersonde R, Kyte FT (2001) Exploration of the Eltanin impact area (Bellingshausen Sea): expedition ANT XVIII5a. *Meteoritics Planetary Sci Suppl* 36:A64
- Gersonde R, Kyte FT, Bleil U et al (1997) Geological record and reconstruction of the late Pliocene impact of the Eltanin asteroid in the Southern Ocean. *Nature* 390:357–363
- Glasstone S, Dolan PJ (1977) The effects of nuclear weapons. US Department of Defense and US Department of Energy, US Government Printing Office, Washington, DC, p 653
- Hills JG, Nemchinov IV, Popov SP, Teterov AV (1994) Tsunami generated by small asteroid impacts. In: Gehrels T (ed) *Hazards due to comets and asteroids*, University of Arizona Press, Tucson, pp 779–789
- Kuznetsov NM (1965) Thermodynamic functions and impact adiabatic curves of air at high temperatures. *Mashinostroenie, Moscow* (in Russian)
- Kyte FT, Zhou Z, Wasson JT (1981) High noble metal concentration in a late Pliocene sediment. *Nature* 292:417–420
- McGlaun JM, Thompson SL, Elrick MG (1990) CTH: a three-dimensional shock wave physics code. *Int J Impact Engng* 10:351–360
- Melosh HJ (1989) *Impact cratering: a geologic process* (Oxford Monographs on Geology and Geophysics, No. 11). Clarendon Press, New York, p 245
- Melosh HJ, Ivanov BA (1999) Impact crater collapse. *Ann Rev Earth Planet Sci* 27:385–415
- Movshovich EV, Milyavskii AE (1990) The morphology and the interior structure of impact craters Kamensk and Gusev. In: *Impact Craters at the Mesozoic–Cenozoic Boundary*. Nauka, Leningrad, pp 110–146
- Nemchinov IV, Jacobs C, Tagliaferri E (1997c) Analysis of satellite observations of large meteoroid impacts. In: Remo J (ed) *Near-Earth Objects*. *Ann NY Acad Sci* 822, pp 303–317
- Nemchinov IV, Loseva TV, Teterov AV (1996) Impacts into oceans and seas. *Earth Moon Planets* 72(1–3):405–418
- Nemchinov IV, Shuvalov VV, Kosarev IB et al (1997a) Assessment of comet Shoemaker-Levy 9 fragment sizes using light curves measured by Galileo spacecraft instruments. *Planet Space Sci* 45(3):311–326
- Nemchinov IV, Svetsov VV, Kosarev IB et al (1997b) Assessment of kinetic energy of meteoroids detected by satellite-based light sensors. *Icarus* 130(2):259–274
- O’Keefe JD, Ahrens T (1982b) The interaction of the Cretaceous/Tertiary extinction bolide with the atmosphere, ocean, and solid Earth. In: Silver LT, Schultz PH (eds) *Geological implications of impacts of large asteroids and comets on the Earth*. Geological Society of America Special Paper 190, pp 103–120
- O’Keefe JD, Ahrens TJ (1999) Complex crater: relationship of stratigraphy and rings to impact conditions. *J Geophys Res* 104(E11):27091–27104
- Ormö J, Lindström M (2000) When a cosmic impact strikes the sea bed. *Geol Mag* 137(1):67–80
- Ormö J, Shuvalov VV, Lindström M (2002) Numerical modeling for target water depth estimation of marine-target impact craters. *J Geophys Res* 107(E12), doi:10.1029/2002JE001865
- Pierazzo E, Chyba CF (1999) Amino acid survival in large cometary impacts. *Meteoritics Planetary Sci* 34:909–918
- Pierazzo E, Melosh HJ (2000) Melt production in oblique impacts. *Icarus* 145:252–261
- Quaide WL, Oberbeck VR (1968) Thickness determinations of the lunar surface layer from lunar impact craters. *J Geophys Res* 73(16):5247–5270
- Roddy DJ, Shuster S, Rosenblatt M et al (1987) Computer simulations of large asteroid impacts into oceanic and continental sites—preliminary results on atmospheric, cratering and ejecta dynamics. *Int J Impact Engng* 5(1–4):525–541
- Schultz PH (1999) Ejecta distributions from oblique impacts into particulate targets. *Lunar Planet Sci XXX*. LPSI, Houston, #1919

- Shuvalov VV (1999a) Multi-dimensional hydrodynamic code SOVA for interfacial flows: application to thermal layer effect. *Shock Waves* 9(6):381–390
- Shuvalov VV (1999b) Atmospheric plumes created by meteoroids impacting the Earth. *J Geophys Res* 104(E3):5877–5889
- Shuvalov V (2000) Numerical modeling of the impacts into shallow sea. In: Plado J, Pesonen LJ (eds), *Abstracts of ESF Workshop: Meteorite impacts in Precambrian shields*. Lappajärvi, Finland, p 57
- Shuvalov VV (2003b) Numerical modeling of the Eltanin impact. *Lunar Planet Sci XXXIV*. Houston. #1101
- Shuvalov V, Dalwigk I (2002) Numerical Modeling of resurge flow and Lockne gullies formation: Preliminary results. In: Dalwigk I (ed.), *Abstracts of ESF Workshop: Impact Tectonism*. Mora, Sweden, p. 57
- Shuvalov V, Dypvik H (2004) Electra formation and crater development of the Mjølñir impact. *Meteoritics Planetary Sci* 39(3):467–479
- Shuvalov VV, Trubetskaya IA (2002) Numerical modeling of marine target impacts. *Solar System Res* 36(5):417–430
- Shuvalov VV, Trubetskaya IA (2004a) The 1815 eruption of Tambora volcano: overview of field investigations and numerical modeling. In: *Dynamics of interacting geospheres*. Institute of Geosphere Dynamics, RAS. Moscow, pp 336–343
- Shuvalov VV, Trubetskaya IA (2004b) Numerical modeling of the eltanin impact. In: *Dynamics of interacting geospheres*. Institute of Geosphere Dynamics, RAS. Moscow, pp 344–350
- Shuvalov VV, Artem'eva NA, Kosarev IB (1999) 3D hydrodynamic code SOVA for multimaterial flows, application to Shoemaker-Levy 9 comet impact problem. *Int J Impact Engng* 23(1):847–858
- Shuvalov V, Dypvik H, Tsikalas F (2002) Numerical simulations of the Mjølñir marine impact crater. *J Geophys Res* 107(E7), 10.1029/2001JE001698
- Shuvalov VV, Ormö J, Lindström M (2005) Hydrocode simulation of the Lockne marine target impact event. In: Koeberl C, Henkel H (eds) *Impact tectonics impact studies*. Springer, Berlin, pp 405–422
- Thompson SL, Lauson HS (1972) Improvements in the chart D radiation-hydrodynamic CODE III: Revised analytic equations of state. Report SC-RR-71 0714. Sandia National Laboratory, Albuquerque, p 119
- Tillotson JH (1962) Metallic equations of state for hypervelocity impact. *Gen Atomic Rep* GA-3216 p 137
- Tsikalas F, Gudlaugsson ST, Faleide JI (1998a) Collapse, infilling, and postimpact deformation at the Mjølñir impact crater, Barents Sea. *Geological Soc Amer Bull* 110:537–552
- Tsikalas F, Gudlaugsson ST, Faleide JI (1998b) The anatomy of a buried complex impact structure: the Mjølñir structure, Barents Sea. *J Geophys Res* 103:30469–30484

CHAPTER 10

IONOSPHERIC AND MAGNETOSPHERIC EFFECT

IVAN NEMCHINOV, VALERY SHUVALOV, ALEKSEY KOVALEV,
IGOR KOSAREV AND YULIUS ZETZER

*Institute for Dynamics of Geospheres, Russian Academy of Sciences, Moscow 119334, Russia
E-mail: ivvan@idg.chph.ras.ru; shuvalov@idg.chph.ras.ru; akoval@idg.chph.ras.ru;
kosarev@idg.chph.ras.ru; zetzer@idg.chph.ras.ru*

The generally recognized hazardous consequences of the impacts of comets and asteroids include crater formation, fall back of ejected material, destructive action of shock and seismic waves, thermal radiation of the fireball and reentering high-velocity ejecta, fires, changes in the atmosphere transparency due to dust and soot from the fires, and tsunamis. The impacts of large bodies can destroy the fragile ecological system of the entire planet and cause mass extinctions, similar to the extinction at the K/T boundary 65 million years ago. Humankind is more vulnerable than were dinosaurs. Today it is generally accepted that impacts of bodies with diameters of 1–2 km are highly dangerous for modern civilization. In addition to the mentioned consequences of impacts, there are some others that have not yet been thoroughly studied, such as ionospheric and magnetospheric disturbances. Nemchinov et al. (1993) and Adushkin and Nemchinov (1994) have shown that the impact of a cosmic body with a diameter of 1–2 km or larger creates a plume with a maximum velocity on the order of the entry velocity of the impactor. Results of simulations for the vertical impact of a SiO_2 body with the initial velocity $50 \text{ km}\cdot\text{s}^{-1}$ on a silicate Earth surface are shown in Figs. 1 and 2. The average velocity of the rising plume in 1–2 s is $25 \text{ km}\cdot\text{s}^{-1}$. The temperature of the plume is rather large (1.8 eV at $t = 0.6 \text{ s}$ and 1 eV at $t = 2 \text{ s}$), so the plume is substantially ionized and can interact with the Earth's magnetic field. Moreover, the air is heated in the shock wave moving ahead of the plume (3.1 eV at $t = 2 \text{ s}$). The rising and expanding plume gradually becomes cooler and less ionized, but at the moment of 2 s it reaches 70 km, where the first ionized layers of the atmosphere begin (the so-called D-layer of the ionosphere), and the interaction with the magnetic field continues.

The fastest part of the plume moves with a velocity greater than the escape velocity, and the Earth's gravity field cannot stop its penetration into the ionosphere

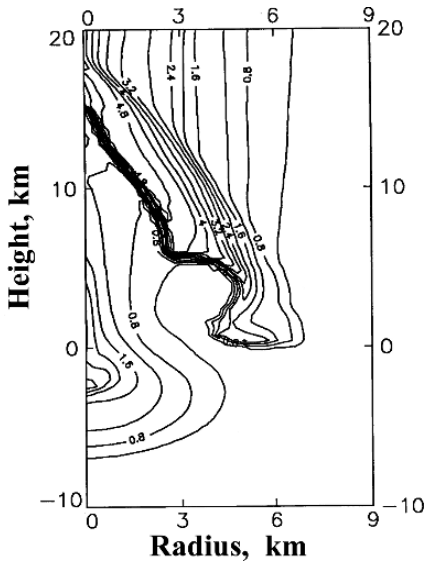


Figure 1. Plot of constant temperature contours after a vertical impact of a 2-km-diameter SiO_2 body at a velocity $50 \text{ km}\cdot\text{s}^{-1}$ on the Earth at $t = 0.62 \text{ s}$. Sharp changes in the temperature coincide with the location of the interface between silicate vapor and the air. The shock wave in the air can be seen above this interface. Maximum temperature in the vapor is 1.8 eV ; in the air it is more than 4.8 eV . Figures 10.1 and 10.2 are adapted from Adushkin and Nemchinov (1994) and reprinted with the kind permission of the University of Arizona Press

and magnetosphere. The energy of such large impactors is so huge (for a 2-km body it is equivalent to the energy of 10^4 Mt TNT) that the energy of the high-velocity part of the plume becomes comparable to or exceeds the total energy of the magnetosphere (equal to about 200 Mt TNT) and the Earth's magnetic field also cannot stop the rising plume, so the magnetosphere can be severely deformed. This can cause not only strong magnetic disturbances, but also destruction of Van Allen radiation belts and creation of new ones. Even before the plasma plume passes through the magnetosphere, this plume can generate intense field-aligned currents, which are short-circuited in the ionosphere. The subsequent energy release heats the lower ionospheric layers.

A gigantic MHD generator is formed and transforms the kinetic energy of the plume E_p into the thermal energy of the ionosphere Q_i (Nemchinov et al. 1993b). The coefficient of transformation $\zeta = Q_i/E_p$ can be estimated from the following relation:

$$\zeta = U^2 B^2 t^3 / (V_A M_f), \quad (1)$$

where B is the magnetic field, V_A is the Alfvénic velocity in the ionosphere, and U is the plume velocity. Let us assume that the characteristic duration of the interaction

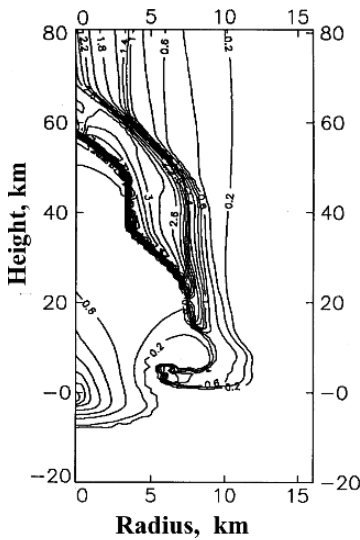


Figure 2. Plot of constant temperature contours after a vertical impact of a 2-km silicate body at $t = 2$ s. The maximum temperature in the vapor is 1.1 eV and in the air it is more than 3.1 eV. The ionized jet interacts with the Earth's magnetic field

process is $t = R_E/U \sim 600$ s, where R_E is the Earth's radius. As ζ is on the order of 10^{-2} – 10^{-3} , the energy released in the lower layers of the ionosphere for the energy of impactors 10^4 – 10^5 Mt TNT is on the order of 10^2 – 10^3 Mt TNT. This can cause substantial heating of the ionosphere around the rising plume. Destruction of radiation belts and precipitation of trapped particles cause additional ionization in much larger regions of the Earth.

The impacts of bodies with sizes 1–2 km and larger are rare and magnetospheric and ionospheric disturbances seem to be less dangerous than other hazardous effects of the impacts. However, the impacts of smaller bodies are much more frequent and can also cause ionospheric effects in regions larger than zones in which strong effects are caused by shock waves and fires. The intensity of these ionospheric disturbances strongly depends on the size of impactors. As an example, the 1908 Tunguska event caused a moderate magnetic storm (Ivanov 1961, 1964; Vasilyev 1998) at a distance of 900 km from the epicenter. The amplitudes of these long-lasting (about 4-hour) disturbances were not very large (~ 70 nT). Theoretical analysis of this event (Nemchinov et al. 1999) is based on the assumption that the plume rises upward through the wake. Simulations by Boslough and Crawford (1997) have shown that the maximum altitude of the plume is ~ 400 – 500 km. The plume, after reaching the maximum height, falls back at some distance from the epicenter of explosion. A reflected shock wave is formed at an altitude of about 100 km (Shuvalov and Artemieva 2002a) and slowly decaying oscillations of the atmosphere arise (Nemchinov et al. 1999). Air behind the reflected shock wave

is heated to temperatures 600–1,000°. This leads to long-lasting changes in the atmosphere conductivity, and formation of a large-scale quasistationary current system in the ionosphere (Nemchinov et al. 1999). Long-period oscillations of the conducting *D*, *E*, and *F* layers of the ionosphere cause geomagnetic disturbances.

At the dawn of the radio era it was not possible to detect short-period ionospheric disturbances after the Tunguska event. However, such disturbances have been observed much later at several thousand km from Novaya Zemlya, the test site of the nuclear weapons. The yield of the most powerful nuclear explosion 58 Mt TNT and its altitude 3.6 km are close to the amount of released energy and the altitude of the Tunguska explosion. In the case of the Tunguska event, ionosphere disturbances caused by the impact were not catastrophic. However, the dependence of modern civilization on radio and TV communications and observations from space increases each year, as well information traffic through space. Thus it seems reasonable to study the amplitudes and character of ionospheric and magnetospheric disturbances for impactors with sizes larger than that of the Tunguska meteoroid, but <1 km, in the size range 0.1–1 km.

1 GAS DYNAMIC SIMULATIONS

A cosmic body moving through the atmosphere deforms and becomes disrupted due to aerodynamic forces. The simulation of such processes has been fulfilled using the gas dynamic code SOVA (Shuvalov et al. 1999; Shuvalov and Artemieva 2002a). The same code was used for simulations of meteoroid interaction with the ground or water, and the plume rising to high altitudes at which the magnetic field play a substantial role.

1.1 Impacts of Icy Bodies

Simulations for icy bodies have been fulfilled for impactors with sizes >30 m (Shuvalov and Artemieva 2000; Nemchinov and Shuvalov 2003). The increase in a body size leads to the increase in the mass capable of escaping the Earth's gravity. For meteoroids with 200, 300, and 1,000 m diameters, 1 g·cm⁻³ initial density, and 50 km·s⁻¹ initial velocity, the atmospheric mass that can overcome the Earth's gravity, i.e., move with a velocity exceeding 11.2 km·s⁻¹ is equal to 5.6, 8.0 and 1% of the impactor mass, respectively (Shuvalov and Artemieva 2000). The energy of the plume reaching the magnetosphere can be estimated as 0.28, 0.38, and 0.05% of the initial kinetic energy. Thus, for the meteoroid kinetic energy 1.25·10³, 4.22·10³, and 1.56·10⁵ Mt TNT, the energy of the high-velocity part of the plume (with velocity higher than 11 km·s⁻¹) is no less than 3.5, 16, and 80 Mt TNT, respectively. This energy, at least in the latter case, is comparable to the total energy of the entire magnetosphere.

The following describes some results of simulations for an icy body with an initial velocity of 50 km·s⁻¹, a density of 1 g·cm⁻³, and a diameter of 200 m. A few seconds after the impact the plume is formed. The distributions of temperature

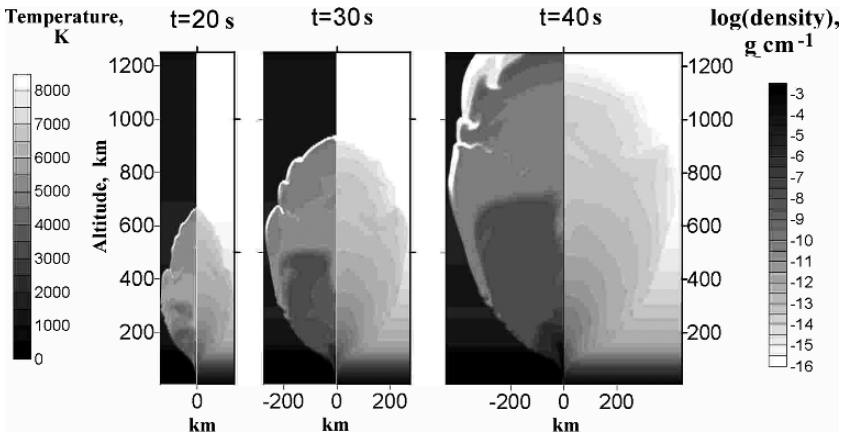


Figure 3. Temperature (left panels) and density (right panels) in 20, 30, and 40 s. Figures 10.3 to 10.6 are adapted from Kovalev et al. (2006) and reprinted with the kind permission of Pleiades Publishing Inc

and density are shown in Fig. 3. In 10 s a conical stream is formed at an altitude of about 100 km with an angle of divergence much wider than that at lower altitudes. The energy and mass of this stream are derived from air ejected from denser layers of the atmosphere. In 20, 30, and 40 s the maximum radius of the plume is 100, 250, and 400 km (at altitudes 300, 600, and 700 km), respectively. The velocity profile along the axis of symmetry is shown in Fig. 4. The maximum velocity in 20, 30, and 40 s is about 25, 30, and 40 km·s⁻¹. One can see that the shock wave propagating upward through the atmosphere with decreasing density accelerates. The distribution of the ratio of the density to the undisturbed atmospheric density at the same altitude is shown in Fig. 5.

In 20 s the density at high altitudes (up to 500 km) is higher than the ambient density by 1–2 orders of magnitude, and in 40 s at altitudes of 700–1,300 km is higher by 4–5 orders of magnitude. The distribution of the excess energy (in comparison with the energy of the background atmosphere per unit height) is shown in Fig. 6. In 40 s the excess energy at altitudes <600 km have ceased to change, as the gas flow from the lower altitudes stopped.

1.2 Impacts of Stony Bodies

Most of the Earth’s surface is covered by the water of oceans and seas. This section describes the results of numerical simulations of the impact of a stony asteroid with an initial density of 2.65 g·cm⁻³, diameter of 400 m, and entry velocity of 17 km·s⁻¹. This velocity and diameter are close to those of recently found asteroid 99942 Apophis. The initial phase of the impact into the ocean with a depth of 4 km

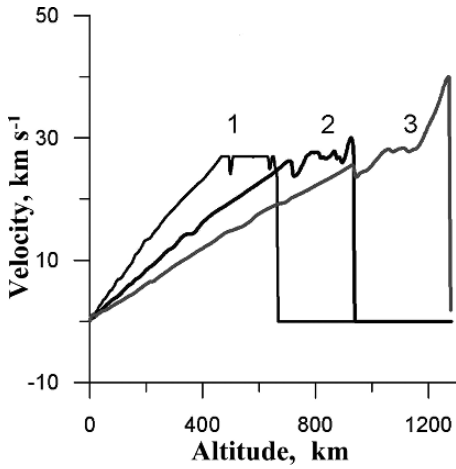


Figure 4. Velocity along the symmetry axis in 20 s (1), 30 s (2), and 40 s (3)

is shown in Fig. 7. At $t = 0$ one can see a shock wave and a wake behind the body. During the motion through the water the cosmic body melts and substantially deforms. In 0.2 s the body penetrates to a depth of about 1.5 km and a plume is formed around the wake. An unstable water crater collapses, creating water waves

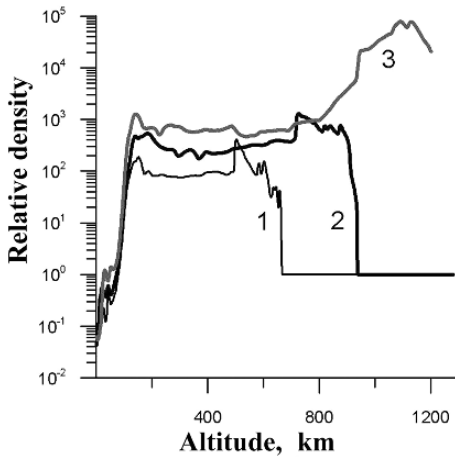


Figure 5. Jet to background density ratio along the axis in 20 s (1), 30 s (2), and 40 s (3)

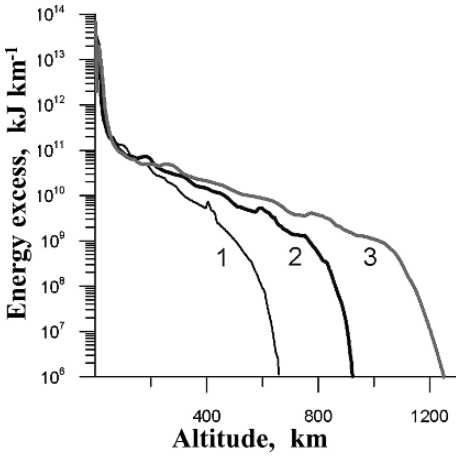


Figure 6. Profile of energy excess along the axis. $t = 20$ s (1), $t = 30$ s (2), $t = 40$ s (3)

going outward. This process can lead to tsunamis, but in this chapter concentrates on the processes in the atmosphere, ionosphere and magnetosphere.

The later phases of the plume rise are shown in Fig. 8. One can see a rather thin dense plume core that consists mainly of water vapor. At altitudes 100–150 km the plume obtains a much larger angle of divergence and the disturbed region consists of practically pure air ejected from the dense layers of the atmosphere. In 20 s

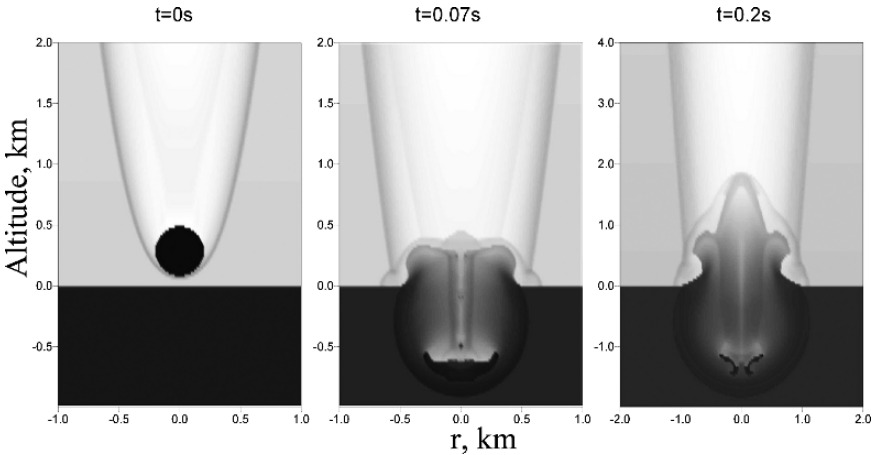


Figure 7. Initial stage of the 400-m-diameter asteroid impact into 4-km-deep ocean, density plots are shown

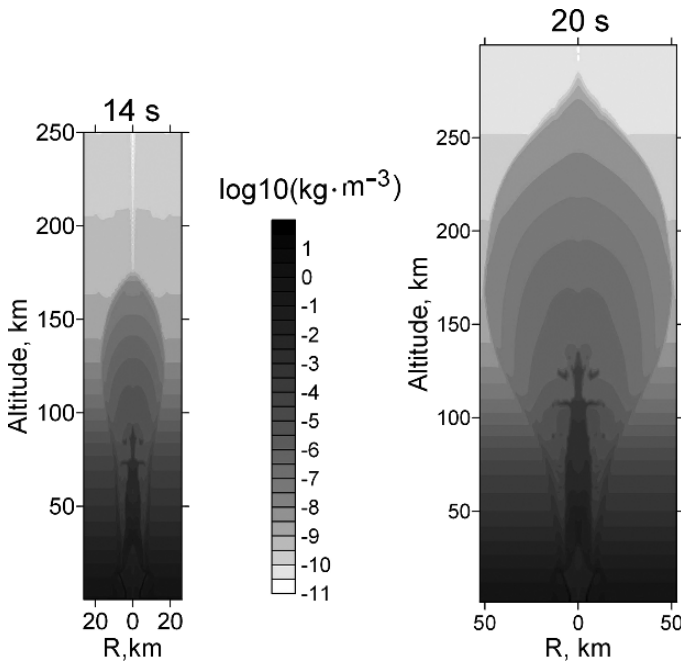


Figure 8. Density in 14 s and 20 s after the impact

the upper part of the shock wave reaches 270 km, while the dense core is only at 120 km. Later, the air plume reaches much higher altitudes, whereas the core also continues to rise, but much slower.

In Fig. 9 the excess energy (left side) and mass (right side) for moments 40–200 s after the impact are shown. One can see that in 200 s the excess energy at altitudes 100–300 km is on the order of 100 Mt TNT, that is comparable to the energy of the whole magnetosphere.

The distribution of density in 420 s is shown in Fig. 10. (It is quite similar in 200–600 s). In a cylinder with a radius of 1,700 km and a height of 2,000 km the density is about 10^{-14} g·cm $^{-3}$, which corresponds to the normal air density at an altitude of ~ 250 km. This increases the absorption of solar radiation and cosmic rays; the effect is likely to be similar to rising the F $_2$ layer of the ionosphere up to altitudes of 1,000–2,000 km.

The average radial velocity of the shock wave for $t < 600$ s is on the order of 10 km·s $^{-1}$, which causes strong heating of the gas behind the shock wave. The shock wave velocity slowly decreases with time. Lower parts of the plume, rising with lower velocities, fall back due to gravity, causing intense oscillations of the ionosphere for a long time; therefore, these impacts cause global effects in the ionosphere.

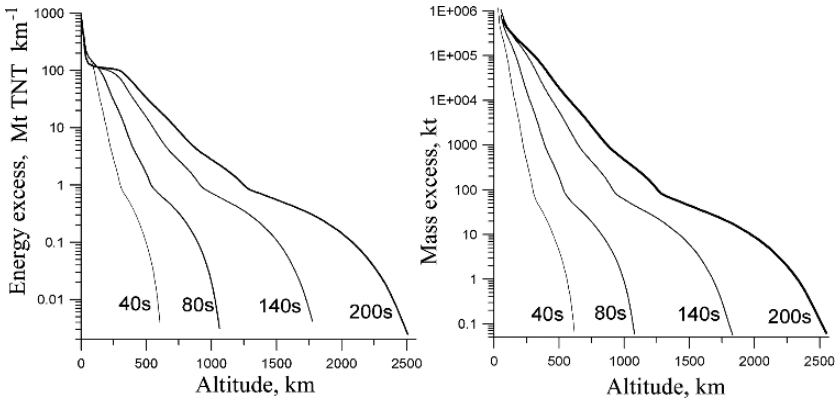


Figure 9. The impact of a 400 m stony body with initial velocity $17 \text{ km}\cdot\text{s}^{-1}$. Excess energy (left) and mass (right) at times 40 to 200 s after impact

1.3 MHD Simulations

To take into account the interaction with the geomagnetic field, 2D MHD simulations of vertical impacts have been conducted. The rising plume was subdivided into ions, neutral atoms, and molecules. To solve the MHD equations the

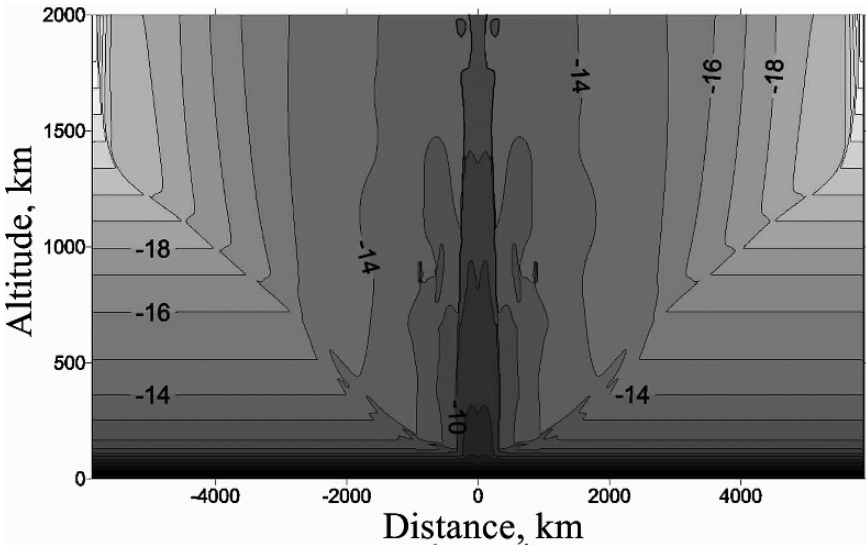


Figure 10. The impact of a 400-m stony body with initial velocity $17 \text{ km}\cdot\text{s}^{-1}$. Common logarithm of density expressed in $\text{g}\cdot\text{cm}^{-3}$ is shown in 420 s. The figure is adapted from Nemchinov et al. (2006) and reprinted with the kind permission of Pleiades Publishing Inc

flux-corrected-transport (FCT) numerical method was used (Colella and Woodward 1984; DeVore 1991). The same technique was used for simulations of the motion of a neutral part of the jet, neglecting electric and magnetic fields. The momentum exchange between ions and neutrals via elastic collisions was taken into account.

Some simplified assumption of ionization equilibrium (Zel'dovitch and Raiser 1967) was taken:

$$\frac{\alpha^2}{1-\alpha} = \frac{AT^{3/2}S_1}{\delta S_2} \exp(-I_1/T), \quad (2)$$

where α is the ionization degree, A is a constant, T is the temperature, I_1 is the first ionization potential, δ is the ratio of the density to the normal density at the same altitude, and S_1 and S_2 are the statistical sums of ions and neutrals, respectively. Outside the plume the degree of ionization was determined from the standard model of the daytime atmosphere. In regions of the plume with densities $<10^{-9} \text{ g}\cdot\text{cm}^{-3}$ recombination was neglected. Ionization by electronic impact was calculated with the cross-sections borrowed from Laher and Gilmore (1990).

For an icy body with entry velocity of $50 \text{ km}\cdot\text{s}^{-1}$ the MHD simulations started in $t = 5 \text{ s}$ after the body reached the surface. The initial data for the MHD problem were taken from the results of purely gas dynamic simulations. The direction of the magnetic field was assumed to be vertical. This corresponds to an impact in the polar region. The jet expands in the radial direction, and although the velocity of the radial expansion of the jet (about $5 \text{ km}\cdot\text{s}^{-1}$) is small in comparison to the entry velocity of the impactor and the upward velocity of the plume, interaction of the plume with the geomagnetic field takes place, but with less intensity than it would for impacts near the equator. Thus, neutral and ionized components of the plume separate in the radial direction. This is evident from Fig. 11a, which shows the distribution of neutrals and ions after the impact of a 200-m-diameter body. At a height of 500 km, the ion density is appreciably higher than the density of neutrals. Figure 11b shows the altitude dependence of the excess mass of ions and neutrals and the ionization degree in the plume above the altitude that is an argument of these functions. The mass of ions ejected to altitudes $H > 400 \text{ km}$ is twice as large as that of neutral atoms, and the ionization degree at $H \geq 1000 \text{ km}$ is close to 0.8. The flow velocities at $H \geq 400 \text{ km}$ exceed $11 \text{ km}\cdot\text{s}^{-1}$, i.e., this part of the plume overcomes gravity. The total mass of this part of the jet is equal to 20 kt.

The MHD momentum transfer from jet ions to background ions sets the background ions outside the jet in motion with a velocity equal to that of the transversal expansion of the jet.

The expanding plasma expels the magnetic field and forms a geomagnetic cavern (Fig. 12a). The shape of the geomagnetic cavern mimics that of the jet. The size of the region of magnetic disturbance is much larger than that of the diamagnetic cavern because ions move outside the plume (Fig. 13). MHD computations show that during the first seconds a fast magnetosonic wave is formed. It propagates with the local Alfvén velocity (see Fig. 12b, where Z component of the magnetic

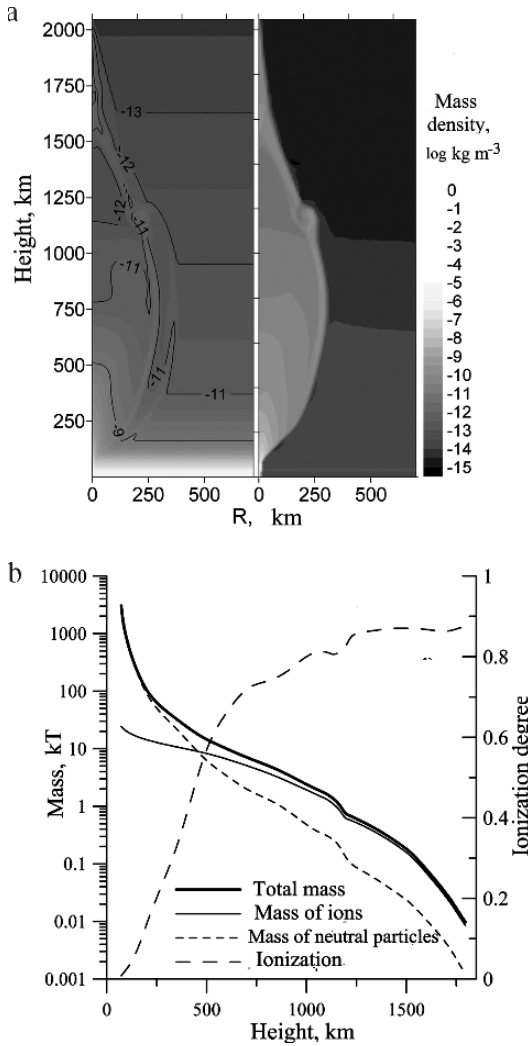


Figure 11. The impact of a 200-m body: (a) distribution of the mass density of neutral atoms (left panel) and ions (right panel) at $t = 60$ s; (b) the ionization degree and the excess mass of ions and neutral atoms in the jet at $t = 40$ s. Figures 10.11 to 10.13 are adapted from Kovalev et al. (2006) and reprinted with the kind permission of Pleiades Publishing Inc

disturbance is shown). The amplitude of this wave is small at large distances from the plume injection point (about 10 nT at a distance of 300 km).

MHD simulations for a 400 m-diameter icy body (Fig. 14) compared with those for a 200-m body (Fig. 11) show that at the same moments of time the jet produced by the larger body rises slightly higher (2,200 compared with 2,000 km). The excess

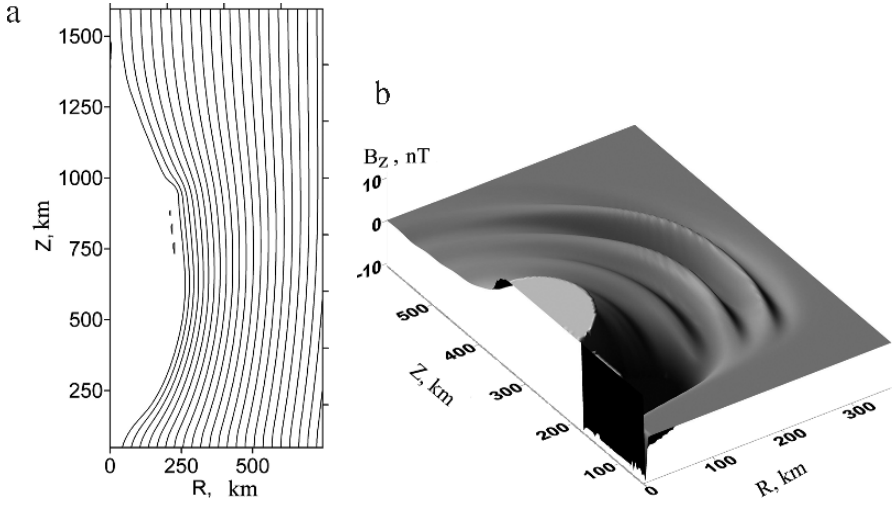


Figure 12. The impact of a 200-m body: (a) magnetic field lines at $t = 20$ s; (b) Z-component of magnetic-field disturbance at $t = 7$ s (the values beyond an interval [near the jet] ± 10 nT are not shown)

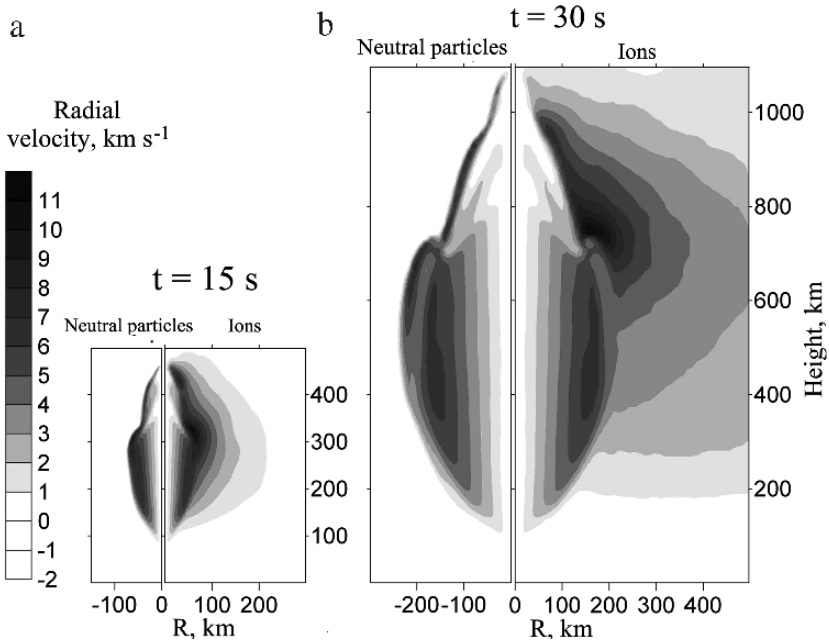


Figure 13. The impact of a 200-m body: distribution of radial velocity of ions and neutral atoms at $t = 15$ s (left panel) and $t = 30$ s (right panel)

mass and excess energy at high altitudes at 40 s are approximately proportional to the impactor energy.

In Fig. 15 radial velocities of ions and neutral atoms are shown at 40 and 80 s. One can see that ions move upward and laterally at small angles to the horizontal in a region much larger than the plume.

In Fig. 16 the magnetic field disturbances, the absolute value of magnetic disturbance ΔB and radial component B_r , at 40 and 80 s are shown. One can see the formation of diamagnetic cavity. A small region with a very high amplitude of magnetic field disturbances, on the order of 15,000 nT, appears around this cavity, less significant disturbances are far from the plume. The maximum radius of intense magnetic disturbances exceeds that of the plume by several times.

Magnetic disturbances (large-amplitude Alfvén waves and whistler mode waves) reaching the Van Allen radiation belts can influence the pitch angles of electrons and ions and cause precipitation of trapped particles into the atmosphere, leading to additional ionization in the atmosphere. The plume flow imposed on the ionosphere is a driven MHD-dynamo. The flow acts as a dynamo and the magnetically conjugate ionosphere is a load with Birkeland (magnetic field aligned) currents connecting the dynamo to the load. This gives rise to auroral UV and nonthermal radio emissions in the conjugate region of the ionosphere.

In the future the flow of gas should be studied taking nonequilibrium thermodynamics into account, because at high altitudes the mean free path of various species may become comparable to the characteristic size of the atmosphere and/or the diameter of the plume. In the plume, mutual penetration of particles can take place, 2D and 3D current systems can be formed, and magnetic diffusion can become anomalous. Therefore, more sophisticated models should be used instead of this two-fluid (one neutral and one ionized fluid) MHD approximation. However, all these models should be checked by modeling experiments.

2 MODELING EXPERIMENTS

Large-scale experiments can be performed for modeling geophysical processes in the high-velocity plume produced by impacts. High-velocity jets have already been released into space using the so-called shape-charged devices producing barium or strontium vapor streams at various altitudes. Being illuminated by solar light, the jets become ionized and start to interact with the geomagnetic field and ambient ionosphere. Such experiments have been conducted to better understand the natural space environments, and study fundamental plasma physics, including the critical ionization velocity effects. The results of such active geophysical experiments and their analysis have been published in a multitude of papers, e.g., Haerendel and Sagdeev (1981), Pongratz (1981), Torbert and Newell (1986), Stenbaek-Nielsen et al. (1990, 1993), Kelley et al. (1991), and Delamere et al. (1996, 1999). The maximum velocity of these jets is on the order of 13–15 km·s⁻¹.

Other types of such cumulative explosive devices—the so-called explosive type generators (ETG)—have been specially designed, constructed, produced, and tested

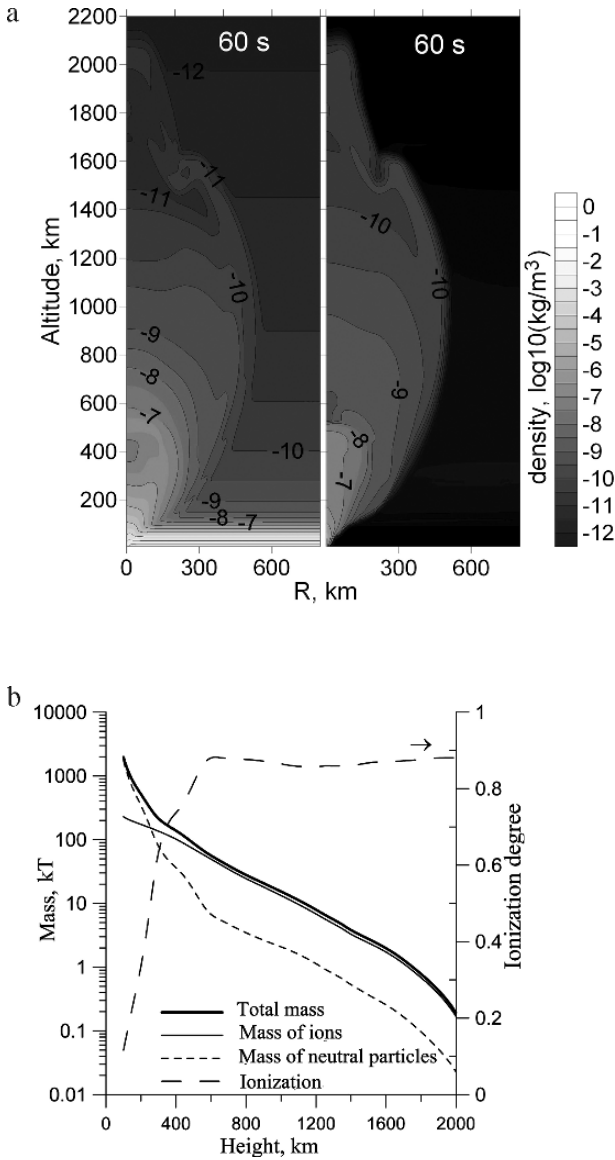


Figure 14. The impact of a 400-m body: (a) distribution of the mass density of neutral atoms (left panel) and ions (right panel) at $t = 30$ s; (b) the ionization degree and the excess mass of ions and neutral atoms in the jet at $t = 40$ s. Figure 10.14b is adapted from Kovalev et al. (2006) and reprinted with the kind permission of Pleiades Publishing Inc

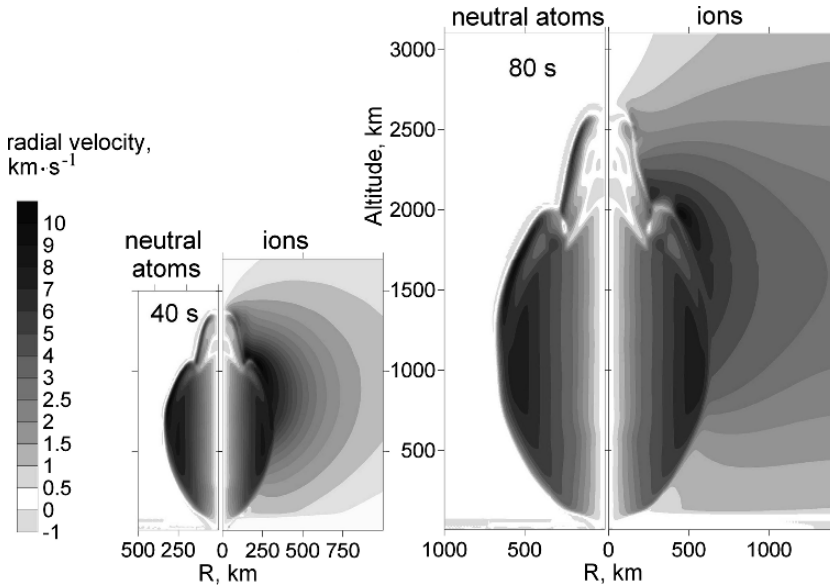


Figure 15. 400 m body: radial velocity of ions (right panels) and neutral atoms (left panels)

in space by the Institute for Geospheres Dynamics RAS over the last almost 40 years. The first phase of this research program was described in Tsikulin and Popov (1977). The maximum velocity of jets produced by ETG reaches 30–50 km·s⁻¹. Modern ETG has high efficiency of transformation of the chemical energy of

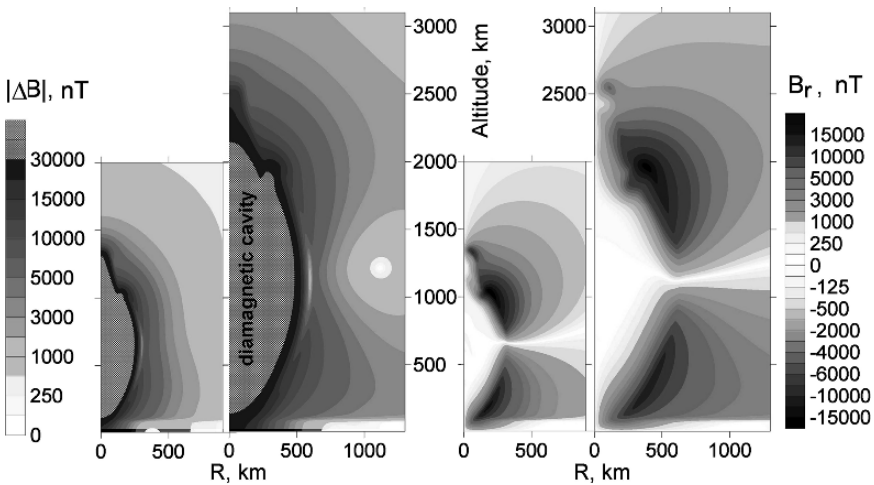


Figure 16. 400 m body: magnetic field disturbances

explosives into the kinetic energy of a jet—up to 14–20%. The ETGs are compact and can be risen by rockets to high altitudes. The released jets interact with the Earth's magnetic field and air.

A number of the Active Geophysical Rocket Experiments (AGRE) (Adushkin et al. 1993) and the so-called Fluxus-1 and Fluxus-2 experiments (Erlandson et al. 1996; Gavrilov et al. 1999; Zetzer et al. 2002), have been conducted at altitudes of 140–150 km. In the Fluxus experiments the jet axis was directed at a small angle to the magnetic field. The North Star Active Plasma Experiment (APEX) was conducted at altitudes of 260 km and 380 km (Delamere et al. 2004; Erlandson et al. 2002, 2004a; Gatsonis 2004; Gavrilov et al. 2004; Lynch et al. 2004; Pfaff et al. 2004). The jet was directed perpendicular to the geomagnetic field.

In the experiment at an altitude of 360 km a canister of compressed air was opened 0.2 s prior to the ETG detonation. The number density in the artificial air cloud decreased from $2 \cdot 10^{11} \text{ cm}^{-3}$ at 10 m from the ETG orifice to $2 \cdot 10^{10} \text{ cm}^{-3}$ at 150 m from the ETG. This is much higher than the number density of $1.6 \cdot 10^8 \text{ cm}^{-3}$ at the altitude of 360 km and is comparable with the density $5 \cdot 10^{10} \text{ cm}^{-3}$ at 150 km (Fluxus altitude). The aluminium jet interacted with the air cloud, heated it, and a new jet consisting of aluminum and air was formed. The average density in the artificial cloud was chosen to connect the APEX results with the Fluxus-1 and -2 results. On the other hand this density is of the same order of magnitude as in the impact-generated plume at altitudes where the wide-angle stream is formed.

The modeling experiments do not reproduce the whole process of plume formation and its interaction with the geomagnetic field. However, it is possible to study the interaction with the magnetic field and background air at various altitudes. It is guessed that general features of the interaction processes after impacts are the same as in the modeling experiments: The density of the jet is much higher than in the background plasma, the magnetic field is expelled and diamagnetic cavity formed, fast magnetohydrodynamic waves propagate to large distances from the jet, and momentum transfer from the jet to the ambient air occurs. Moreover, some quantitative coincidence takes place: The maximum velocity of the ETG jet is the same as in the impact-produced plume, and density and composition of the air ahead of the jet are the same as ahead of the impact-generated plume. The amplitude and direction of the geomagnetic field in the modeling experiments coincide with those in the impact events. It is obvious that there is a difference in the radius of the jet in the modeling experiments (0.1–1 km) and the radius of a plume in the impact events (10–100 km), as well as differences in the sizes of disturbed regions, the mean free paths of particles, and the gyro radii in the geomagnetic field. However, in the modeling experiments one can study in situ such very complicated processes as instability, turbulence, anomalous magnetic diffusion, and critical ionization phenomena, which present problems for numerical simulations.

In two of the AGRE experiments the mass of the explosives was 2.3 kg, energy of the jet 1.6 MJ, maximum velocity $30 \text{ km} \cdot \text{s}^{-1}$, and total mass of the jet 30 g.

A large luminous volume was formed. In 0.3 s its maximum diameter was 1.5 km and the maximum distance from the ETG detonation point was 2 km. At the initial, bright phase of the experiment the radiation was emitted in the continuum.

In the Fluxus-1 and -2 experiments (Zetzer et al. 2002), conducted at an altitude of 140 km, the jet was released parallel to the magnetic field. For the jet energy 3 MJ and maximum velocity $40 \text{ km}\cdot\text{s}^{-1}$ the maximum diameter of the luminous volume is about 1.2 km and intensity of radiation at $t = 0.1 \text{ s}$ is about 200 W/ster. At a distance of 130 m from ETG the plasma jet density exceeded 10^9 cm^{-3} and the magnetic field was reduced by 50% due to the diamagnetic effect.

Theoretical 2D MHD simulations have been conducted for analysis of the experiments. As an example, the ion and neutral density and the magnetic field lines in 30 ms after injection of the plasma jet parallel to the magnetic field are shown in Fig. 17. Expulsion of the geomagnetic field by the plume and formation of the diamagnetic cavern have been confirmed by the in situ measurements.

In the North Star APEX, the total mass of the explosive in the ETG was 9.7 kg and the chemical energy of the explosives was about 40 MJ (Erlandson et al. 2004b). In this experiment the axis of the jet was almost perpendicular to the geomagnetic field. The initial velocity of the aluminum vapor jet was about $43 \text{ km}\cdot\text{s}^{-1}$. The plasma density at a distance of 470 m was $3\cdot 10^9 \text{ cm}^{-2}$. The plasma jet injected through the artificial air cloud produced a diamagnetic cavity (Gavrilov et al. 2004).

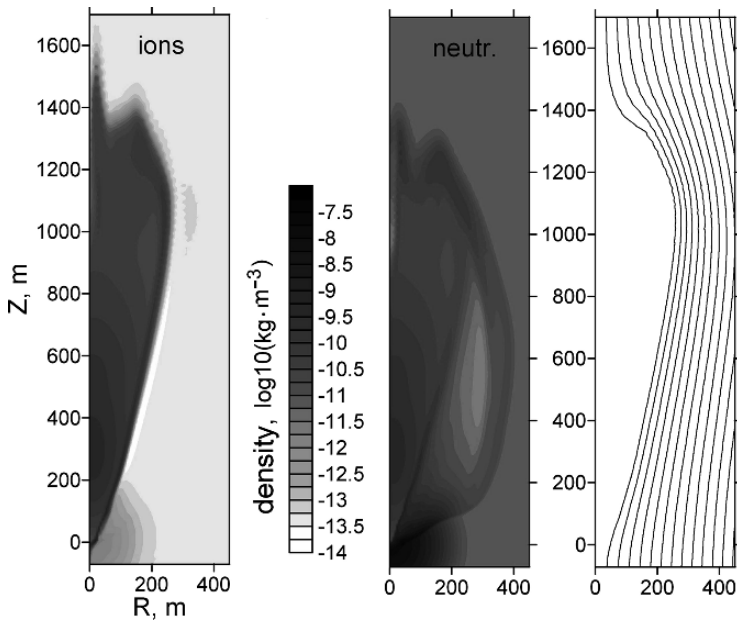


Figure 17. Artificial plasma jet parallel to the magnetic field: ion and neutral density and magnetic field lines in 30 ms after the injection

Large quasi-dc electric fields and also parallel to the magnetic field electric fields were observed on the edges of the cavity. The payload instrumentation registered in the nearby arrear. Waves and turbulence prior to the arrival of the jet, within the jet, and after the jet passed the sensor (Gavrilov et al. 2004; Pfaff et al. 2004).

The average velocity of the jet at distances between 170 m and 550 m is $25 \text{ km}\cdot\text{s}^{-1}$, and at distances between 550 m and 1,020 m is $17 \text{ km}\cdot\text{s}^{-1}$. These velocities are larger than the critical ionization velocities (CIV) for Al ($7.3 \text{ km}\cdot\text{s}^{-1}$) and O ($13 \text{ km}\cdot\text{s}^{-1}$). Lynch et al. (2004) assumed that CIV effects dominated the dynamics of the disturbed regions, but there is no direct evidence approving this assertion. Gavrilov et al. (2004) assumed that the jet deceleration is a result of a field-aligned current generation. The evidence of existence of these currents is a bipolar parallel electric field at the leading edge of the cavity (Pfaff et al. 2004). Delamere et al. modeled the ETG plasma jet using a 3D hybrid simulation code. They investigated coupling of the plasma jet with the ambient plasma. The quasineutrality was assumed, so the polarization electric field resulted from the difference in gyro radius of ions ($\sim 400 \text{ m}$ for Al^+) and electrons rather than from the formation of space charge. Delamere et al. (2004) claimed that the exact nature of the coupling of the jet in the ambient plasma is not known.

All the main effects of plasma–jet interaction (formation of a diamagnetic cavity, substantial depletion of the magnetic field, emission of fast waves) in the sophisticated models are the same as in the simple MHD models, but of course, the quantitative results may be substantially different. It seems reasonable not only to further analyze the results of already conducted modeling experiments but also to study the possibility of new experiments with increased energy of a jet and increased size of a disturbed region.

REFERENCES

- Adushkin VV, Nemchinov IV (1994) Consequences of impacts of cosmic bodies on the surface of the Earth. In: Gehrels T (ed) Hazards due to comets and asteroids, University Arizona Press, Tucson, pp 721–778
- Adushkin VV, Zetzer JI, Kiselev YN et al (1993) Active geophysical rocket experiments in the ionosphere with the high velocity plasma jet injection. *Doklady RAS* 331(4):486–489
- Boslough MB, Crawford DA (1997) Shoemaker-Levy 9 and plume-forming collisions on Earth. In: Remo JL (ed) Near Earth objects. *Ann NY Acad Sci* 822:236–282
- Colella P, Woodward PR (1984) The piecewise parabolic method (PPM) for gas-dynamical simulations. *J Comput Phys* 54:174–201
- Delamere PA, Stenbaek-Nielsen HC, Hampton DL, Wescott EM (1996) Optical observations of the early ($t < 5 \text{ s}$) ion dynamics of the CRRES G1, G9 and G11A releases. *J Geophys Res* 101(A8):17,243–17,257
- Delamere PA, Stenbaek-Nielsen HC, Pfaff RF et al (2004) Dynamics of the Active Plasma Experiment North Star artificial plasma jet. *J Spacecraft Rockets* 41(4):503–508
- Delamere PA, Swift DW, Stenbaek-Nielsen HC (1999) A three-dimensional hybrid code simulation of the December 1984 solar wind AMPTE release. *Geophys Res Lett* 26(18):2837–2840
- DeVore CR (1991) Flux-corrected transport techniques for multidimensional compressible magneto-hydrodynamics. *J Comput Phys* 92:142–160
- Erlanson RE, Meng CI, Zetzer JI (2004a) Introduction to the North Star active Plasma-jet space experiment. *J Spacecraft Rockets* 41(4):481–482

- Erlanson RE, Meng C-I, Swaminathan PK et al (2004b) North star Plasma-jet space experiment. *J Spacecraft Rockets* 41(4):483–489
- Erlanson RE, Meng C-I, Zetzer JI et al (2002) The APEX North Star experiment: observations of high-speed plasma jets injected perpendicular to the magnetic field. *Adv Space Res* 29(9):1317–1326
- Erlanson RE, Mursula K, Bösinger T (1996) Simultaneous ground-satellite observations of structured Pc 1 pulsations. *J Geophys Res* 101(A12):27,149–27,156
- Ernst CM, Schulz PH, A'Hearn MF, the Deep Impact Science Team (2006) Photometric evolution of the Deep Impact flash. *Lunar Planet Sci XXXVII*. LPSI. Houston. # 2192.pdf
- Gatsonis N, Demagistris M, Erlanson RE (2004) Three-dimensional magnetohydrodynamic modeling of plasma jet in the North Star space experiment. *J Spacecraft Rockets* 41(4):509–520
- Gavrilov BG, Podgorny AI, Podgorny IM et al (1999) Diamagnetic effect produced by the Fluxus-1 and -2 artificial plasma jet. *Geophys Res Lett* 26(11):1549–1552
- Gavrilov BG, Podgorny IM, Sobyenin DB et al (2004) North Star plasma-jet experiment particles and electric and magnetic field measurements. *J Spacecraft Rockets* 41(4):490–495
- Haerendel G, Sagdeev RZ (1981) Artificial plasma jet in the ionosphere. *Adv Space Res* 1:29–46
- Ivanov KG (1961) Geomagnetic phenomena observed at Irkutsk Magnetic Observatory after explosion of the Tunguska meteorite. *Meteoritika* 21:46–48. Nauka Publishers, Moscow (in Russian)
- Ivanov KG (1964) Geomagnetic effect of Tunguska catastrophe. *Meteoritika* 24:141–151. Nauka Publishers, Moscow (in Russian)
- Kelley MC, Swenson CM, Brenning N, Baker K, Pfaff R (1991) Electric and magnetic field measurements inside a high-velocity neutral beam undergoing ionization. *J Geophys Res* 96(A6):9703–9718
- Kovalev AT, Nemchinov IV, Shuvalov VV (2006) Ionospheric and magnetospheric disturbances caused by impacts of small comets and asteroids. *Solar System Research* 40(1):57–67
- Laher RR, Gilmore FR (1990) Updated excitation and ionization cross sections for electron impact on atomic oxygen. *J Phys Chem Ref Data* 19(1):277–305
- Lynch KA, Torbert RB, Chutter M et al (2004) Active Plasma experiment: North Star particle data. *J Spacecraft Rockets* 41(4):496–502
- Nemchinov IV, Shuvalov VV (2003) Geophysical effect of shocks of small asteroids and comets. In: *Geophysical processes in the lower and upper shells of an Earth*. Book 2. *Trans Inst Dynamics Geospheres RAS Moscow*, pp 36–47 (in Russian)
- Nemchinov IV, Losseva TV, Merkin VG (1999) Estimate of geomagnetic effect at a falling of Tunguska meteoroid. In: *Physical processes in geospheres: their developments and interacting (Geophysics of the strong disturbances)*. *Trans Inst Dynamics Geospheres RAS Moscow*, pp 324–338 (in Russian)
- Nemchinov IV, Alexandrov PE, Artemiev VI et al (1993) On magnetodynamic effects initiated by a high-speed impact of a large cosmic body upon the Earth's surface. *Lunar Planet Sci Conf XXIV*, Houston, pp 1063–1064
- Nemchinov IV, Zetzer YuI, Kovalev AT, Shuvalov VV (2006) Perturbations in the ionosphere and magnetosphere during the fall of cosmic bodies onto land or ocean *Doklady Earth Sciences* 409(5):736–738
- Pfaff RF, Freudenreich HT, Bounds SR et al (2004) Electric field, magnetic field, and density measurements on the active plasma experiment. *J Spacecraft Rockets* 41(4):521–532
- Pongratz MB (1981) Large scientific releases. *Adv Space Res* 1:253–273
- Shuvalov VV, Artemieva NA (2000) Atmospheric erosion and radiation impulse induced by impacts. *Catastrophic events and mass extinctions: impacts and beyond*. July 9–12, 2000. *Geozentrum University of Vienna, Austria*. LPI Contribution 1053, Houston, pp 199–200
- Shuvalov VV, Artemieva NA (2002a) Numerical modeling of Tunguska-like impacts. *Planet Space Sci* 50:181–192
- Shuvalov VV, Artem'eva NA, Kosarev IB (1999) 3D hydrodynamic code SOVA for multimaterial flows, application to Shoemaker-Levy 9 Comet impact problem. *Intern J Impact Engng* 23(1):847–858
- Stenbaek-Nielsen HC, Wescott EM, Hallinan TJ (1993) Observed barium emission rates. *J Geophys Res* 98(A10):17491–17500
- Stenbaek-Nielsen HC, Wescott EM, Haerendel G, Valenzuela A (1990) Optical observations on the CRIT-II critical ionization velocity experiment. *Geophys Res Lett* 17(10):1601–1604

- Torbert RB, Newell PT (1986) A magnetospheric critical velocity experiment: particle results. *J Geophys Res* 91(A9):9947–9955
- Tsikulin MA, Popov EG (1977) Radiative properties of the shock waves in gases. Nauka, Moscow, p 174 (in Russian)
- Vasilyev NV (1998) The Tunguska meteorite problem today. *Planet Space Sci* 46(2/3):129–150
- Zel'dovitch Ya B, Raiser Yu P (1967) *Physics of shock waves and high-temperature hydrodynamic phenomena*. Academic Press, New York
- Zetzer JJ, Kozlov SI, Rybakov VA et al (2002) Air glow in the visible and infrared spectral ranges of the disturbed upper atmosphere under conditions of high-velocity plasma jet injection. 1. Experimental data. *Kosm Issled* 40(3):252–260

CHAPTER 11

IMPACTS AND EVOLUTION OF EARLY EARTH

GALINA PECHERNIKOVA AND ANDREI VITYAZEV

Institute for Dynamics of Geospheres, Russian Academy of Sciences, Moscow 119334, Russia
E-mail: pechernikova@idg.chph.ras.ru; avit@idg.chph.ras.ru

1 INTRODUCTION

The problem of the first half-billion years of Earth's existence is fundamental for all Earth sciences because it was in this period that the Earth and its envelopes were formed. During the last decades of the twentieth century joint efforts of scientists from different countries made it possible to develop a standard scenario of the origin of the Solar System and the planets that satisfied basic observational data accumulated by astrophysics and comparative planetology. The general description of this scenario, as well as solutions of related problems, can be found in Safronov and Vityazev (1985), Vityazev et al. 1990, Vityazev and Pechernikova (1991), and the multiauthor book, *The Origin of the Earth and the Moon* (2000). The use of a number of isotope systems (space- and geo-chronometers) provides a way of estimating the duration of the most essential stages of Earth's formation. It was established that physical and chemical evolution of the preplanetary disk matter incorporated into growing planets began at the early stages of their formation. The basic exogenic source of energy and material for the growing planets was falling bodies, with sizes up to 1,000 km (Vityazev et al. 1990; Pechernikova and Vityazev 1996; Vityazev and Pechernikova 1996). The Earth's core and mantle formation took place during the final stages of Earth's growth (30–100 Ma after the Sun's formation), actually simultaneously with the formation of the primitive crust, hydrosphere, and atmosphere. The impact events determined the influence of the formation of the Earth's outer envelopes (Pechernikova and Vityazev, 1996; Vityazev and Pechernikova 1996). This chapter offers a brief overview of the modern understanding of the role of impacts during the first 500 Ma of the Earth's evolution.

The overview begins with a brief discussion of a recent modification in the theory of the Earth's growth and a generalized formula of the mass accumulation rate. The it discusses spectra of mass and velocities of falling bodies and their composition and describes simulation of the frequency of falls of bodies with different sizes.

Using the formula of the Earth's growth rate and the estimate of the mass velocity spectrum of planetesimals, the rate of input of kinetic energy and the depth of mixing of the near-surface layers of growing planets are obtained. Then the interpretation of available scarce experimental data and observable relict signals from Hadean are presented, which for the first time enabled researchers to obtain the characteristics of compositions and conditions of the early upper geospheres, including the climate of the primary Earth.

2 THE EARTH'S GROWTH RATE

The duration of formation of the Earth and other planets is a fundamental question of planetary cosmogony. The time of the Earth's growth is also a most important parameter in Earth sciences. The present estimates of the total age of the Solar System (4.6 Ga) and duration of the final stages of the Earth's formation (~ 100 Ma) confirmed by isotopic data are not subject to question. However, the Earth's growth rate at the early stages, a crucial period for its future evolution, has so far remained unclear. A consistent consideration of the role of large bodies in the evolution of the preplanetary swarm, based on the general approach, allowed researchers for the first time to obtain durations of formation of massive (but probably differentiated) bodies (Vityazev et al. 1990; Vityazev and Pechernikova 1991). These durations conform with modern isotopic data generated by the Hf-W system (Pechernikova 2004, 2005).

The mass distribution of preplanetary bodies is generally represented in the form of a simple power law:

$$n(m', t)dm' = n_0(t)(m')^{-q}dm', \quad (1 < q < 2), \quad (1)$$

where $n(m', t)dm'$ is the number of bodies with masses in an interval from m' to $m' + dm'$ at the moment of time t , $q < 2$ designates the fact that the main mass of the system is concentrated in large bodies, and $n_0(t)$ is the normalizing coefficient. To find $n_0(t)$, normalize $n(m', t)$ by the density of condensed matter in the feeding zone ρ_d :

$$n_0(t) = (2 - q)M_1(t)^{q-2}\rho_d, \quad (2)$$

where $M_1(t)$ and m_0 are upper and lower distribution limits. Using Equations (1) and (2) the time of the Earth's growth up to relative radius $z = (m(t)/m_{\oplus})^{1/3}$ is obtained, taking into account the influence of large bodies (for more details see Pechernikova 2004, 2005):

$$t = \frac{b \delta r_{\max}}{\sigma_0} \left(\ln \frac{1+z}{1-z} - 0.43 z - 0.04 z^3 \right), \text{ years.} \quad (3)$$

Here δ is the Earth's mean density, r_{\max} is its maximum (modern) radius, $b = 0.07$ (weakly depending both on q and Safronov's parameter $\theta(\theta \sim 1)$). The values of q according to the coagulation theory were obtained within the limit of $1.5 \div 2$ (Safronov 1969; Vityazev et al. 1990). The interpretation of ancient cratering

surfaces and the size distribution of asteroidal populations give the same q estimate. The derived Equation (3) takes into account the changes in the surface density of the solid matter in the feeding zone of the planet $\sigma_d(t)$ from its initial value σ_0 , the upper limit of the distribution $M_1(t)$, the relative velocity of planetesimals (the root-mean-square velocity relative to the circular velocity) in the feeding zone of the growing planet in the process of the planet's growth:

$$\sigma_d(t) = \sigma_0(1 - z^2), \bar{v}^2 = Gm/\theta r. \quad (4)$$

The equipartition of the energy of random motion between the growing planet m , the bodies with a mean mass of \bar{m}' in the distribution and large bodies m' in the mass interval from \bar{m}' to M_1 (see the following) was also taken into account. The increase in the relative mass of the Earth $m(t)/m_\oplus$ calculated from Equation (3) at its mean density over the growth time of $\delta = 4.5 \text{ g}\cdot\text{cm}^{-3}$, $\sigma_0 = 10 \text{ g}\cdot\text{cm}^{-2}$ and $\theta = 2$ is shown as curve 1 in Fig. 1. Curves 2 and 3 derived from the early models are shown for comparison. In the model with expanding feeding zones (Vityazev et al. 1990) it was assumed that the masses of bodies falling onto the growing planet are $m' \ll m(t)$ and that the orbit of the planet is circular. In the early model by Schmidt-Safronov (1969) it was additionally assumed that the planet “was aware” of the future final mass m_\oplus .

Figure 1a shows that taking into account the role of large bodies in the suggested model significantly accelerates mass accumulation by the planet at the early and main stages of its growth: The Earth gains the mass of Mars ($\approx 0.1 m_\oplus$) in approximately 17 Ma. After 50 Ma its mass becomes twice as large as in the earlier models. Figure 1b shows that bodies with thousands of kilometers in size are formed during the first few millions of years. However, the time of growth up to $0.97m_\oplus$. (i.e., to $r = 0.99r_\oplus$.) remains the same, $\sim 10^8$ years.

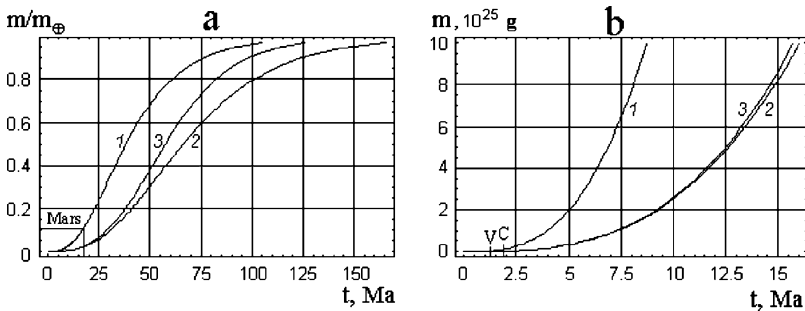


Figure 1. a. Increase in the relative mass of the Earth: 1—model (Pechernikova 2004, 2005), which takes into account the role of large bodies; the time is shown of the formation of the largest bodies with masses of modern Mars; 2—model with expanding feeding zones (Vityazev et al. 1990); 3—model suggested by Schmidt and Safronov (1969). b. Mass of the growing Earth during the first 15 Ma (notations are the same as in panel a), the letters V and C show the times of formation of the largest bodies with masses of the order of the Vesta and the Ceres, respectively

The new model yields the times for the growth of the bodies' masses at the early stages (see Fig. 1*b*) that are consistent with the isotopic data for the formation of bodies with the masses of Vesta and Mars, whereas the solution of the problem associated with a threefold difference in the cosmochemical and dynamic scales of the Earth's formation was suggested in Vityazev et al. (2003a,b) and Allegre et al. (2004). These works show that the formation of bodies thousands of kilometers in size during the first millions of years (see the preceding) and their heating to a temperature of interior melting both by the short-living ^{26}Al (half-life period 0.72 Ma) and impacts enable researchers to interpret the Hf-W geochronometer (Kleine et al. 2002; Yin et al. 2002; Schoenberg et al. 2002) as an indication both of melting and differentiation in parental planetesimals, as well as of the absence of any further significant rehomogenization of this material in the course of subsequent accumulation of the terrestrial planets.

Therefore, unlike the earlier models, the consistent consideration of the role of large bodies in the processes of the Earth's accumulation renders a short time scale of its growth at the early stage and eliminates any remaining contradictions with the Hf-W geochronometer date.

3 MASSES, VELOCITIES AND COMPOSITION OF FALLING BODIES

From these calculations under a standard scenario of the Earth's formation the spectrum of mass and relative velocities of bodies forming the planet was obtained (Vityazev et al. 1990; Vityazev and Pechernikova 2003). The authors have taken into account a change in mass m_1 of the second (relative to the growing planet in terms of mass) body (or the value of the upper limit of mass distribution $M_1(t)$ practically coinciding with m_1):

$$M_1(t) \approx (1 - z^2)m(t), \quad (5)$$

Equation (5) indicates that at the early stages of planet accumulation, when $z = r(t)/r_{\text{max}} \ll 1$, the largest bodies in the feeding zone are comparable with the growing planet in terms of mass. Only when $m(t)$ becomes as large as a notable portion of the mass of matter in the feeding zone and the decrease in the surface density of matter becomes significant due to depletion, does the growing planet outpace the other bodies in its zone in terms of mass. This formula, obtained by the authors in 1980 (Vityazev et al. 1990), perfectly correlates with later results of numerical simulations of the process of terrestrial planet accumulation (Wetherill 1985; Ipatov 1987).

Table 1 and Fig. 2 give a demonstrative idea of the mass of bodies in the zone of the growing planet and bodies falling on it.

Figure 2 shows two versions of the realization of the stochastic process of fall of bodies in a given range of D sizes (km): (1) for the time interval from 160 to 161 Ma (i.e., for a period of 1 Ma) conforming to the Earth's mass of $0.9988m_{\oplus}$ (left column); and (2) for the time interval, from 190 to 191 Ma conforming to the Earth's

Table 1. Distribution of large bodies in the feeding zone of the growing Earth

Mass of the growing Earth $m(t)$	0.7 m_{\oplus}	0.9 m_{\oplus}	0.99 m_{\oplus}
Time of the Earth's growth, 10^6 years	~ 50	~ 80	~ 100
Mass and radius of largest bodies			
m_1 , g	$3.1 \cdot 10^{26}$	$1.1 \cdot 10^{26}$	$1.2 \cdot 10^{25}$
r_1 , km	2600	1900	900
m_2 , g	$9.0 \cdot 10^{25}$	$3.1 \cdot 10^{25}$	$3.2 \cdot 10^{24}$
r_2 , km	1700	1200	570
m_3 , g	$5.1 \cdot 10^{25}$	$1.8 \cdot 10^{25}$	$1.8 \cdot 10^{24}$
r_3 , km	1400	1000	470
m_4 , g	$3.5 \cdot 10^{25}$	$1.2 \cdot 10^{25}$	$1.2 \cdot 10^{24}$
r_4 , km	1300	900	420
m_5 , g	$2.6 \cdot 10^{25}$	$9.0 \cdot 10^{24}$	$9.0 \cdot 10^{23}$
r_5 , km	1200	800	380
Radius ranges, km	Numbers of bodies $N(r)$ in the feeding zone of the planet		
500–100	2150	870	127
100–10	$6.9 \cdot 10^5$	$2.8 \cdot 10^5$	$4.1 \cdot 10^4$
10–1	$2.2 \cdot 10^8$	$8.8 \cdot 10^7$	$1.3 \cdot 10^7$

mass of $0.9990m_{\oplus}$ (right column). For the purpose of calculation, Equations (1)–(3) and (5) and a pseudorandom number generator were used to estimate the diameter of a falling body (in a given range of sizes) and the moment of fall in the interval of 0–1,000,000 years. The first four panels show an increase in the number of impactors with a decrease in their sizes from 40–50 to 10–20 km.

The bottom panels show the total number of impactors in a diameter range from 20 to 100 km, making it obvious that during the first time interval five bodies with the sizes of 90–100 km fell, whereas during the second interval their number was reduced to two. The maximum size of bodies in the first time interval was 200–400 km and in the second 150–200 km. Figure 6 demonstrates the falls of large bodies (Pechernikova and Davidenko 2003).

The mean relative velocity of planetesimals in the feeding zone of the growing planet is determined by its mass m (Equation (4)) and increases as $v(t) \propto r(t)$. Using the solutions obtained in (Vityazev et al. 1990) one can express the root-mean-square velocity relative to the circular velocity of the growing planet moving along the ellipse as (Pechernikova 2005):

$$v^2(m) = \bar{m}' \bar{v}^2 / m, \tag{6}$$

$$\bar{m}' = (2 - q)M_1 / (3 - q), \tag{7}$$

where \bar{v}^2 is determined by Equation (4), and \bar{m}' is the mean mass (with a weight function $m' n(m') dm'$) of the body in distribution Equation (1). It is logical to suggest that the equipartition of the energy of random motion Equation (6) between the

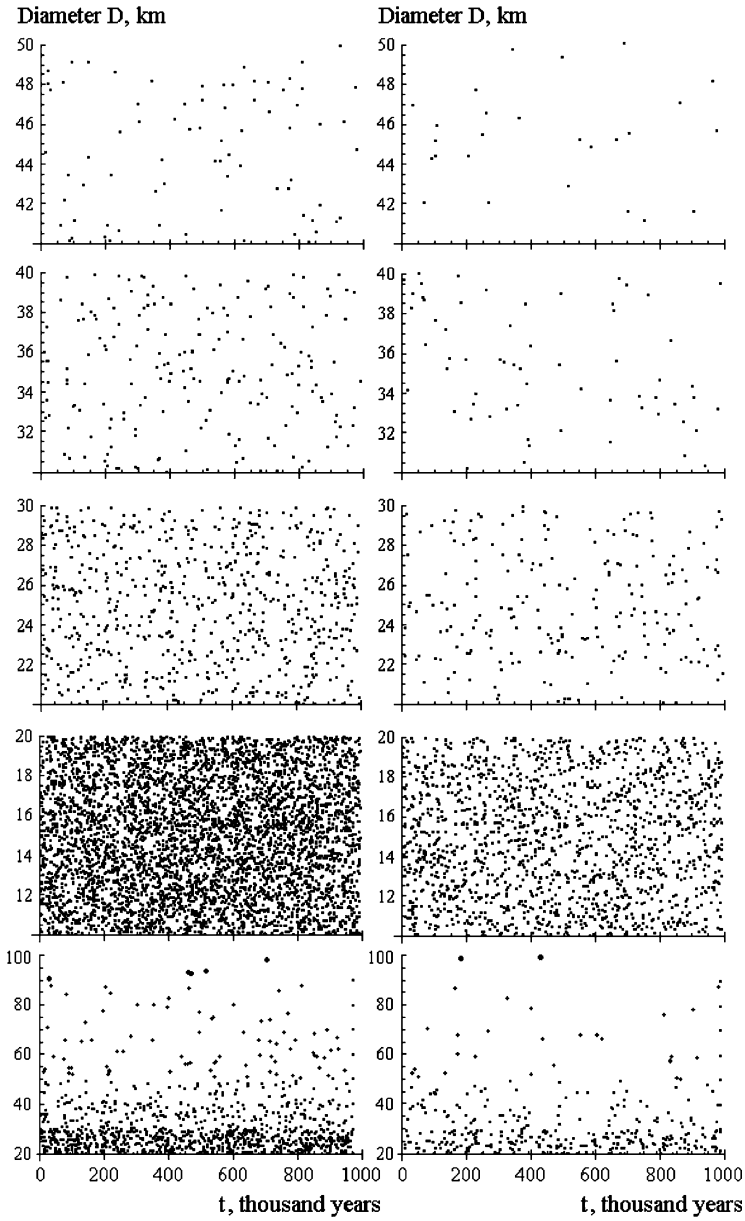


Figure 2. Frequency of falls of bodies of different sizes onto the growing Earth in relation to the mass of the growing planet (stochastic model)

growing planet m and the bodies with mean mass \bar{m}' in the distribution is also valid for large planetesimals m' in the mass interval from \bar{m}' to M_1 , i.e.:

$$v^2(m') = \bar{m}'\bar{v}^2/m'. \quad (8)$$

For other planetesimals with masses $m' < \bar{m}'$, in view of their frequent collisions and approaches, assume $v^2(m') = \bar{v}^2$. Thus, Equations (4), (6), and (8) determine the spectrum of relative velocities of preplanetary bodies up to the “embryo” planet.

The averaged composition of bodies in the zone of terrestrial planets, including the asteroid belt zone, according to the modern paradigm, is similar to the composition of chondrites. At the same time it has been long shown that the Earth cannot have been constructed from a single class of carbonaceous (CI, CL, CV, CO, CR), ordinary (H, L, LL), enstatites (EH, EL) etc. chondrites and achondrites. It is possible to select a mix of material from the known meteorite classes kept in terrestrial collections that would simultaneously match isotopic, geochemical, and geophysical criteria (Vityazev et al. 1990). However, there is no guarantee that a significant portion of substance was introduced by planetesimals on average of chondritic but otherwise of rather variable composition (contents of iron, degree of oxidation, etc.), which either have fallen onto the planets and completely disappeared or have not yet been found, e.g., are in the asteroid belt.

The uncertainty of some percent in the composition of a light admixture in the core and mantle does not present a crucial challenge for attempts to simulate the division of the primary Earth into the core and the mantle (Vityazev et al. 1990; Vityazev and Pechernikova 2003). However, when an attempt is made to describe possible compositions of a primitive crust, hydrosphere, and atmosphere, such uncertainty in the bulk composition of Earth-forming bodies results in a several-times-higher uncertainty in the abundance of volatiles (H_2O , CO_2 , etc.). The integrated data on the isotopic composition of oxygen ($^{16}\text{O}/^{17}\text{O}/^{18}\text{O}$), D/H, Ar/ H_2O ratios, etc. show that the cometary material and carbonaceous chondrites could introduce no more than several percent of the Earth’s mass (Vityazev et al. 1990; Pechernikova and Vityazev 1996; Vityazev and Pechernikova 1996; Vityazev and Pechernikova 2003). In terms of H_2O it can nevertheless range from several units to ten masses of modern hydrosphere ($2 \cdot 10^{24}$ g). Ordinary chondrites have a considerably lower content of volatiles ($\sim 0.1\%$ H_2O); however, it is more than sufficient (with a small surplus) for the formation of the hydrosphere. At the same time the calculation of impact crater formation during the planet’s growth period suggests that a detectable fraction (up to several percent) of planetesimals’ material and the surface of the growing planet could be ejected to geocentric and even heliocentric orbits (Melosh and Sonet 1986; Pechernikova and Vityazev 1996, 1998; Vityazev and Pechernikova 1996; Teterev et al. 2004). A large share of volatiles could be lost; and the loss of water up to several masses of the modern ocean ($1.4 \cdot 10^{24}$ g) is not considered impossible. Finally, one should also know how many volatiles can be contained in the mantle. Available geochemical and geophysical estimates differ strongly, whereas conservative estimates give $\sim (1-3) \cdot 10^{24}$ g. SNC

meteorites, probably of Martian origin, contain from 0.04 to 0.4% of water by weight. For the terrestrial mantle the corresponding water mass would amount to one to several masses of the modern ocean. This chapter omits the situation with other volatiles (P, S, K, Na) and only notes that the lower estimate of carbon mass content in the Earth has been long known. If all carbon of terrestrial carbonates were transferred to the atmosphere, its mass and composition would be close to the Venus atmosphere ($\sim 4.5 \cdot 10^{23}$ g). In these circumstances it is apparently necessary first of all to consider two extreme classes of models with minimum and maximum volatiles content. In the maximum case it is possible to assume the greatest addition (in terms of mass) by carbonaceous meteorites and cometary bodies, which is 10% of the Earth's mass. The essence of this variant was discussed by Ringwood, but it confronted harsh objections (see, e.g., Vityazev et al. 1990) and today is no longer considered. For the "dry" version of the Earth with a minimum abundance of volatiles, a model composition may be assumed with >90% of ordinary chondrites material and <5% of carbonaceous chondrites material to take into account the minimum content of volatiles subject to the inevitable loss due to impact degassing. Under such an approach a reconstruction of the primary atmosphere and hydrosphere may be based on the results of experiments in step annealing of meteorite samples. The study of samples heated to melting might give evidence of differentiation, as was done in experiments with the Tsarev meteorite (Zetzer and Vityazev 1996). The study showed that in addition to primary differentiation to silicate and metal components both of these components are exposed to secondary liquation processes. In laboratory conditions (small pressure) FeS is separated from FeNi in the metal melt, whereas in the silicate component the separation of a very small part of the component with anortositic composition (similar to primary crust?) from the other generally ultrabasic component (primitive mantle?) is recorded. This result confirms early experiments on melting the samples of the Allende carbonaceous chondrite and the silicate part of the Jilin ordinary chondrite but requires further contemplation. The authors suggested that researchers search the ancient (over 4 Ga) lunar high mountain areas to look for traces of impact material ejections from the surface of the Hadean Earth (Pechernikova and Vityazev 1998). Finding such material could essentially increase the knowledge about the surface envelopes of the ancient Earth. Recently American researchers offered a relevant research project.

4 IMPACT ENERGY AND HEAT AND MASS TRANSFER

Table 2 contains the summary of the energy balance of the early Earth (Vityazev and Pechernikova 2003).

4.1 Brief Comment on the Table

The energy of short-living isotopes is released in the first millions of years and is essential for heating the largest planetesimals and deep interiors of future planets. Gravitational energy is the most powerful source at the stage of the planets' growth, but only $\sim 10\%$ thereof remains buried in interiors. At the same time the energy

Table 2. The power balance of the Earth during the first 500 Ma

Energy sources		Erg
1	Short-living radio-isotopes ^{26}Al , ^{60}Fe	10^{37}
2	Long-living radio-isotopes U, Th, ^{40}K	$4 \cdot 10^{37}$
3	Impact energy of bodies	$2 \cdot 10^{39}$
4	Energy of elastic compression	10^{37}
5	Energy of differentiation	$1.5 \cdot 10^{38}$
6	Energy of tidal dissipation	10^{37}
7	Enthalpy of falling planetesimals	10^{37}
8	Energy of chemical reactions* and phase transitions*	10^{37}
9	Solar energy IR–UV + solar wind	$2.5 \cdot 10^{41}$
Processes of heat-mass transfer		Nu
1	Impact mixing	$10^2 - 10^5$
2	Advective flows	$10^2 - 10^5$
3	Convective heat transfer	10
4	Conductive heat transfer	1
5	Diffusion mass transfer	1
6	Fluidal heat-mass transfer	?
7	Tidal penepletion	10
8	Impact ejection into geo- and gelio-centric orbits	$1-10\% M_{\oplus}$

*Depending on endo- or exothermic process the sign is – or +.

of gravitational differentiation during the formation of the two largest reservoirs, the core and mantle, is almost completely spent on the heating of interiors. In the second part of Table 2 the values of the effective Nusselt number are shown and the extreme values at different times for the relevant geospheres are specified. It is obvious from Table 2 that mixing and advective motions took place at the stage of the Earth's growth impact. These processes accompanied sinking of the heavy fraction to the core and were more powerful than the modern geodynamic motions by orders of magnitude.

The estimate of energy liberated by impacts is calculated using the latest model of the Earth's growth (Pechernikova 2005), which takes into account the role of large bodies. In the system of coordinates connected with the center of masses of the bodies m and m' their kinetic energy before approaching T_0 is equal to:

$$T_0 = \frac{mm'}{2(m+m')} V^2, \quad V = \sqrt{v^2(m) + v'^2(m')}, \quad (9)$$

where V is the relative velocity of bodies before the approach for which its mean value has been assumed, $v(m)$ is the relative velocity of the growing planet in Equation (6), and $v'(m')$ is the relative velocity of the planetesimal, which is determined by Equations (4) or (8) depending on its mass m' . The conservation of the system's total energy before the approach and after the collision, assuming complete sticking (here the authors neglect the ejection), is expressed as:

$$T_0 + U + U' = Q' + U'', \quad (10)$$

where U , U' and U'' are potential energies of the bodies m and m' and of the body with a total mass of $m'' = m + m'$, Q' is the energy spent on the fragmentation and converted into heat at the collision of the growing planet m with the body m' . Integrating Q' (m') with the distribution function Equations (1), (2), and the frequency of the planet's collisions with the bodies m' , depending on their masses and velocities (see Pechernikova 2004, 2005), one obtains dQ/dt , which is the amount of impact energy converted into heat in a time unit in the processes of the Earth's accumulation (this is the upper estimate). Its integral over time gives the value of $2.26 \cdot 10^{39}$ erg, which is naturally slightly higher than that indicated in Table 2.

Figure 3 shows the flux of "impact" energy turning into heat and, for comparison, the flow of solar radiation (the solar constant is reduced to early times). It follows from Fig. 3 that in the interval of approximately 17–57 Ma (which corresponds to the Earth's growth from $m \approx 0.08m_{\oplus}$ to $m \approx 0.72m_{\oplus}$) the flow of impact energy exceeded that of solar radiation. Figure 4 shows the change in the impact energy received by the growing Earth per year: at first, with the increase of the planet's mass, relative velocities of planetesimals increase (see Equations (4), (6), (8), and (9)), the flow of falling bodies grows and the impact energy increases; then, although the velocities continue to grow, the number of falls quickly reduces due to material depletion in the planet's feeding zone (Fig. 5) and dQ/dt decreases.

In the work of Vityazev and Pechernikova (1996) it was shown that unlike the modern crust the primitive crust did not represent a shell of definite thickness. The falls of different-sized bodies resulted in continuous mixing of allocated magma of picritic composition with residual peridotitic material. In Vityazev and Pechernikova (1996) the effective thickness of this mixed layer was estimated, taking into account the function of mass distribution of preplanetary-body Equations (1) and (2), the frequency of their falls, and the theory of impact craters' formation. Figures 7 and 8 show the new results of calculations of the Earth's growth, its radius, and the change in the average thickness of the layer of impact mixing $H(t)$, taking into account a shorter scale of the Earth's growth Equation (3).

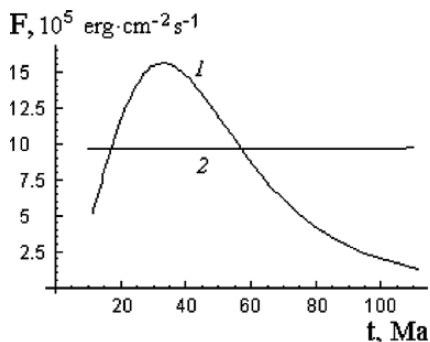


Figure 3. Energy received by the Earth during its growth as a result of impacts—curve 1; and solar heating—curve 2

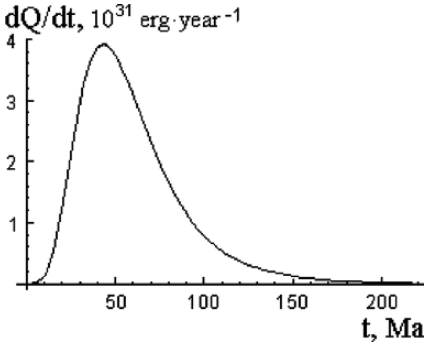


Figure 4. Impact energy turning into heat during the Earth's growth

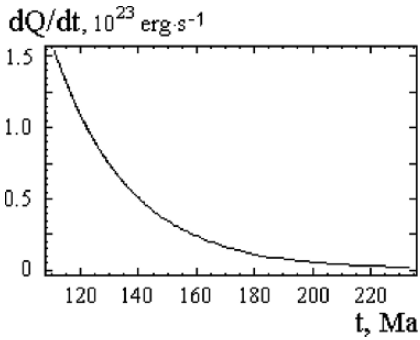


Figure 5. Energy received by the Earth as a result of impacts of planetesimals at the final stage of its growth

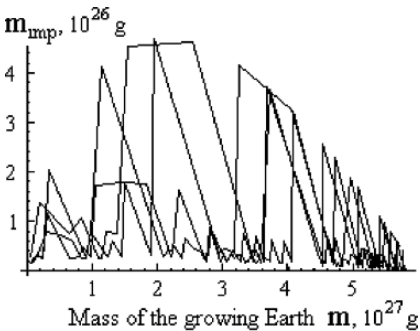


Figure 6. Falls of large ($>10^{26}$ g) bodies to the growing planet as stochastic process. Four runs are shown (Pechernikova and Davidenko 2003)

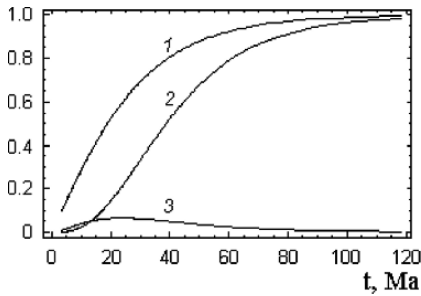


Figure 7. Growth of the Earth's relative radius $r(t)/r_{\oplus}$ and relative mass $m(t)/m_{\oplus}$ (curves 1 and 2, respectively) and time-dependent average thickness of the layer of impact mixing $H(t)/r_{\oplus}$ (curve 3). The averaging was carried out on mass of the falling matter accounting for $\beta = 0.25$ of the matter mass in the planet's feeding zone

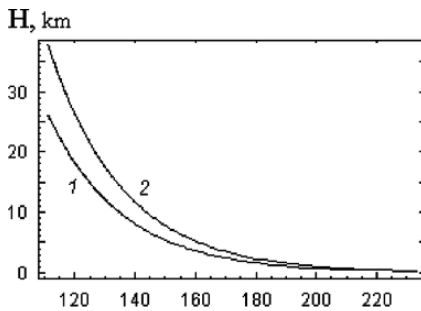


Figure 8. Average thickness of the layer of impact mixing $H(t)$ at the final stage of the Earth's growth. Curve 1 is calculated at $\beta = 0.25$, curve 2 – at $\beta = 0.5$

5 DATA ON RELICT ZIRCONS AND XENON AND CLIMATE OF THE EARLY EARTH

The absence of ancient terrestrial rocks (older than 4 Ga) bears the evidence of intensive impact processing that decayed by the end of the first 500 Ma. Nevertheless, an expensive search in Western Australia (Jack Hills metaconglomerates of Yilgran craton) gave relict minerals—detritic zircons with ages from 4.1 to 4.4 Ga (the famous W74 sample, sizes $\sim 30 \mu\text{m}$) (Peck et al. 2001). Precise investigations of their composition and structure, including REE and isotopism, indicate (Peck et al. 2001) the existence of primitive continental (S-granites) crust exposed to denudation and erosion at the presence of water pools. No estimates of the hydrosphere mass based on this data have been reported.

The search in modern geospheres for an informative relict isotope label showing the composition and character of processes during the first half-billion years has a long history. The basic gases in the atmosphere and water of the hydrosphere

are continuously recycling and some of volatiles together with ocean deposits in the subduction zones drag into the mantle and come back again to the surface in volcanic provinces and rift zones. The inert gases of the atmosphere are subject to such processes to a much lesser extent. The pleiad of nine Xe-isotopes appears to be the most informative. In some works (see, for example, Ozima and Podosek 1999, 2001) the antiquity of the Xe part (on ^{129}Xe) is shown. However, here the researchers are confronted with the so-called “missing Xe problem.”

The missing Xe problem is an old geochemical and cosmochemical problem connected with the observational abundance of inert gases in the atmospheres of the Earth and Mars. Given the added radiogenic Ar and with the deduction of He and, to a lesser extent, Ne escaping through dissipation, the content of inert gases is similar to meteoritic (the so-called planetary gases) except for 10–20-multiple Xe deficiency (Fig. 9).

The search for a possible terrestrial reservoir enriched by xenon in relation to other inert gases Ne, Ar, and Kr took more than 30 years. In the ice caps of Antarctica and Greenland, various sedimentary rocks were checked; and experiments in the possible Xe entry in high-pressure minerals of the core and mantle were performed, giving negative results time and time again. The attempts to find the mechanism extracting from the Earth, at any stage of its evolution, the heaviest of inert gases or, on the contrary, delivering the volatiles depleted by xenon have not resulted in the solution to the Xe deficiency problem. Significant efforts to solve the missing xenon

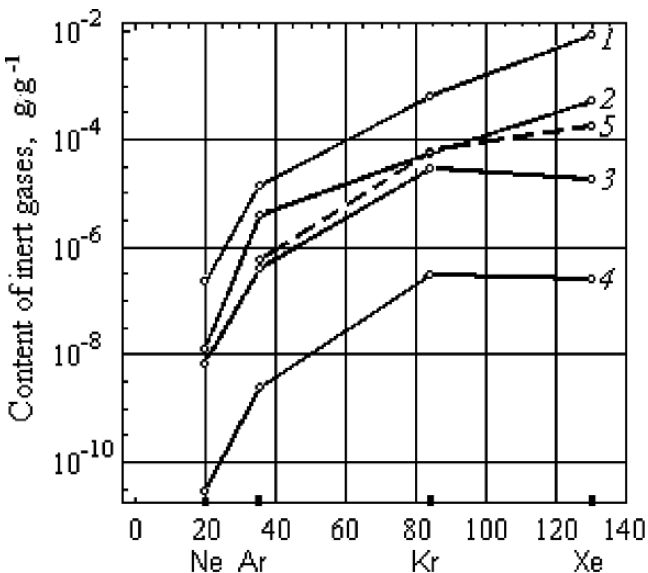


Figure 9. The content (against solar) of inert gases in objects of the Solar system according to the observational data: 1—C1-chondrites; 2—E-chondrites; 3—the Earth; 4—Mars. Dashed curve 5 shows the results of preliminary calculations of terrestrial xenon loss with gas hydrates

problem are driven by the consideration that if xenon is not hidden somewhere in the terrestrial reservoir, then either the material with which it arrived to the Earth is completely different from chondrites (i.e., the basic paradigm of modern cosmochemistry of terrestrial planets is incorrect), or researchers do not take into account an unusual dissipation mechanism that is mainly eliminating the heaviest inert gases.

Recently an almost 20-multiple excess of the Xe content against Ar was discovered in laboratory and natural CH₄-CO₂ gas hydrates (ocean gas hydrates from Blake Ridge near to the US coast; Dickens and Kennedy 2000). According to Dickens and Kennedy (2000), the Xe content in the modern ocean gas hydrates (96% CH₄+ 4% CO₂) is $2 \cdot 10^{-7}$ at the estimated carbon content in gas hydrates of $7.5\text{--}15 \cdot 10^{18}$ g. Thus, the overall Xe content in modern gas hydrates is $1\text{--}2 \cdot 10^{13}$ g, which makes $\approx 1\%$ of its atmospheric abundance. Therefore, this reservoir cannot play an important role in the budget of inert gases of the modern Earth.

There are two facts that enabled Vityazev et al. (2005) to assume rather favorable conditions for a wide spread of gas hydrates in the early Earth: first, available data on the Sun's reduced luminosity (by 25–30%) during the first hundreds Ma of the Earth's history and, hence, a lower average surface temperature; and second, evidence of the intensive interior degasation during the same period obtained in particular from the data on ¹²⁹I–¹²⁹Xe and ²⁴⁴Pu–¹³²Xe isotope systems (Ozima and Podosek 2001).

The third important circumstance suggesting a nontrivial solution to the missing Xe problem is a high flow of planetesimals falling at that time (with asteroid and comet sizes and compositions). A joint consideration of the specific early-Earth features allows a preliminary estimate of the probable Xe primary loss during impact erosion of near-surface terrestrial layers and water pools containing gas hydrates. Estimates for the Earth and Mars based on the uniform approach are provided in the following.

Assume that it is necessary to explain the loss of 10^{16} g of terrestrial Xe (an order higher than its contents in the modern atmosphere). If it entered abiogenic gas hydrates (mainly CO₂·6H₂O) of the early Earth, it is also necessary to remove about 10^{22} g of carbon and $1.5 \cdot 10^{23}$ g of water. The latter figure is suitable for the case of cryosphere impact erosion, but should be considerably increased for gas hydrates in water pools. If it is assumed that the spreading layers of gas hydrates in early water pools settled down on average 500–1,000 m deep together with a part of the gas hydrates layer in impact ejections, some of the above-lying water volumes, capable of making up a mass comparable with that of the modern hydrosphere, should also be lost. Moreover, water is partially lost after impacts in water pools having no gas hydrates. It should be remembered that the mass of water in the modern oceans is $1.4 \cdot 10^{24}$ g and that in the Earth's crust is $0.6 \cdot 10^{24}$ g. In terrestrial carbonates 10^{23} g of CO₂ is connected. Bearing in mind the mantle carbon, the total CO₂ mass can make $\sim 10^{24}$ g, or $\sim 3 \cdot 10^{23}$ g for carbon.

The estimates of the total content of primitive matter of planetesimals falling onto the Earth (90% ordinary chondrites, 10% carbonaceous chondrites, and ice

nucleuses of comet composition $\sim 1\%$) give $1.2 \cdot 10^{23}$ g for carbon and $4.2 \cdot 10^{24}$ for water. What portions of carbon and water were lost during accumulation of the Earth and buried in deep interiors (for water this is the unknown contents in mantle and for carbon the possibility of its presence in the core cannot be excluded) remains a subject of debate.

According to the theory of terrestrial planet formation, assume that by 4.5 Ga ago the Earth collected 95% of its mass and the remaining bodies in its feeding zone with a total mass $3 \cdot 10^{26}$ g were distributed by mass according to the distribution function Equations (1) and (2) at $q \approx 1.8$, with the upper limit close to 1000 km (see Table 1). Roughly speaking, during the subsequent 100–200 Ma about 10^{10} bodies with a kilometer size, $\sim 10^7$ with 10-km and $\sim 10^3$ with 100-km sizes fell onto the Earth. The increase in the Earth's radius during this period makes up the first hundreds of kilometers, and the total area of the cratered surface exceeds the surface of the Earth by three orders. In other words, there is repeated erosion of the near-surface layers to the depth of about impactors' diameters (Vityazev and Pechernikova 1996) (Figs. 7 and 8). For the mentioned sizes of bodies, the depth of craters exceeds probable depths of formation of gas hydrate layers. According to different estimates in cratering models depending on impactor velocities, the ejection of matter to the near-Earth orbits is 1–10% of the impactor mass, or $3 \cdot 10^{24}$ – $4.5 \cdot 10^{25}$ g (Melosh and Sonet 1986; Teterev et al. 2004). One can expect volatile CO_2 – H_2O to account for basic losses and, if gas hydrates occupied an essential portion (dozens of percent) of the Earth's area, the order of figures testifies favorably for the specified mechanism of Xe primary loss (see Fig. 9, curve 5) with the corresponding losses of carbonic acid and water.

Assume that during the period under consideration—100–200 Ma—the part of the surface covered by water was ε_1 ($0 < \varepsilon_1 < 1$) and the part of average-deep pools ($100 \text{ m} < H < 1300 \text{ m}$) with favorable physical and chemical conditions for the existence of inorganic gas hydrates was $0 < \varepsilon_2 < 1$ (for mainly $\text{CO}_2 \cdot 5.7\text{H}_2\text{O}$ it is a known interval in the $20^\circ\text{C} > T > -5^\circ\text{C}$ temperature and $1,000 \text{ bars} > P > 1 \text{ bar}$ pressure phase diagram). The average thickness h of gas hydrate layers should be calculated based on a detailed consideration of the flux of gases from a primitive atmosphere and crust, but one should assume here that it is equal to the typical value for modern terrestrial gas hydrate layers $\sim 200 \text{ m}$. At $\varepsilon_1 = 0.5$, $\varepsilon_2 = 0.5$, the “instant volume” of gas hydrates is about $2 \cdot 10^{22} \text{ cm}^3$, and the loss of water at the chosen average depth of ocean $H_c = 1000 \text{ m}$ is $2 \cdot 10^{23} \text{ g}$. The surface equal to that of the Earth becomes covered with craters created by $N \sim 4 \cdot 10^6$ kilometer-sized bodies over a period of $\sim 100,000$ years. Thus for the Earth, at the ejection efficiency of 1% to the near-Earth orbits, about $2 \cdot 10^{20} \text{ g}$ of gas hydrates and $\sim 2 \cdot 10^{21} \text{ g}$ of water must be lost. At the chosen average ocean depth of $H_c = 500 \text{ m}$, during 200 Ma the mass of lost water should be $2 \cdot 10^{24} \text{ g}$ (approximately as much as the modern ocean and crust now contain, i.e., $2 \cdot 10^{24} \text{ g}$).

For Mars the assumption of the existence of gas hydrate layers in the early cryosphere and water pools seems much less unexpected in light of the continuing discussion of the possible presence of modern near-surface gas hydrates on this

planet. The P-T conditions favorable for the depth of gas hydrates' existence on early Mars are from hundreds of meters in the equatorial areas up to kilometers in the near polar regions. Assuming for the criosphere (up to 1% gas hydrates) that the equivalent thickness of the $\text{CO}_2 \cdot 5.7\text{H}_2\text{O}$ gas hydrate layer is equal to 500 m, there are $5 \cdot 10^{20}$ g gas hydrates whose loss (during the first hundreds of millions of years of evolution) covers the Xe deficiency on Mars.

Consequently, the data on the most ancient Australian zircons indicate that there were water pools at least at the moments of 4.4, 4.3, 4.2, and 4.1 Ga ago. However, it also indicates the presence of an atmosphere of not less than 6–7 mbar (the condition of existence of a threefold point of water). The data about the antiquity of ^{129}Xe show that the Earth's atmosphere did not totally disappear. (If it disappeared completely, no traces of ^{129}Xe —the ^{129}I disintegration product—would have remained in the modern atmosphere.) The data on xenon deficiency suggest its removal after impacts on gas hydrate covers, i.e., in favor of moderately low temperatures according to the phase diagram. At the same time temporarily strong fluctuations in temperature and atmospheric composition could arise after impacts of large bodies.

6 CONCLUSIONS

The modified theory of the Earth's growth (Vityazev et al. 2003a,b; Allegre et al. 2004; Pechernikova 2005), more precisely describing the early and late stages of matter accumulation by the planet, enables the correlation of the latest data on short- and long-lived isotopes. A sufficiently fast growth of the largest bodies (approximately thousands of kilometers in diameter) occurs over periods of about several short-lived ^{26}Al and ^{60}Fe characteristic half-lives. The power of such radioactive sources was sufficient for heating the interiors of such 10–1,000-km sized bodies to melting. An explanation can be given for the existence of iron, pallacite, and mesosideritic meteorites with ages only some Ma younger than the most ancient age (CAI inclusions in the Allende meteorite have the age of 4.567 Ga). At the same time the data on the Hf-W system (^{182}Hf half-life ≈ 9 Ma) become clear. The Hf-W data show that the differentiation of silicates from iron initiated in these bodies and was followed by incomplete homogenization of the matter after falling of these bodies onto the growing planets. On the other hand, the data of the U-Pb geo-chronometer have proven to be true, indicating that the final stage of the Earth's formation actually lasted for about 100 Ma with the accumulation "tail" up to 500 Ma.

The new formula, obtained by the authors for the growth of the Earth's mass accumulating planetesimals, allows the calculation of rates of input of the matter and energy to the Earth's interiors during the first 0.5 Ga. Using this approach, it is possible to obtain improved estimates for the distribution of masses and velocities and the composition of bodies falling onto the Earth. Consequently new estimates have been obtained for the frequency of falls of bodies with different masses and for the depth of processing of upper layers of the growing planet resulting from impacts during the first 500 Ma.

Using a complex of geological and isotope data and bearing in mind the data on impact bombardment of the ancient Earth, the first limitations were obtained for the average temperature and minimum mass of the planetary primary atmosphere 4.4–4.0 Ga ago: a moderately cold climate (average temperatures of about 0°C) interrupted (after falls of large bodies) by high-temperature fluctuations. The pressure of the primitive atmosphere was not less than 0.01 from the modern one. This lower estimate (based on the assumption of the existence of a threefold point of water whose presence is indicated by the most ancient Australian zircons) is presented for the first time.

REFERENCES

- Allegre CJ, Manhès G, Gopel C (2004) Timing and processes of Earth's core differentiation. AGU, Fall Meeting, abstr. No. MR41 A-09 (12/2004)
- Dickens GR, Kennedy BM (2000) In: Paull CK et al (eds) Proceeding of the Ocean Drilling Program. Scientific Results, vol 164. pp 165–170
- Ipatov SI (1987) Solid-body accumulation of the terrestrial planets. *Solar System Res.* 21(3):129–135
- Kleine T, Moenker C, Mezger K et al (2002) Rapid accretion and early core formation on asteroids and the terrestrial planets from Hf-W chronometry. *Nature* 418:952–955
- Melosh HJ, Sonet CP (1986) When worlds collide: jetted vapor plumes and the moon's origin. In: Origin of the Moon. Proceedings Conference, Kona, HI, October 13–16, 1984 (A86-46974 22-91). LPSI, Houston, TX, pp 621–642
- Ozima M, Podosek FA (1999) Formation age of Earth from I-129/I-127 and Pu-244/U-238 systematics and the missing Xe. *J Geophys Res Solid Earth* 104(B11):25493–25499
- Ozima M, Podosek FA (2001) Noble gas records of early evolution of the Earth. AGU 2001 Fall Meeting. *Eos, Trans AGU*, 82(47) F24. Abstract U42B-03
- Pechernikova GV (2004) Large bodies reduce the time scale of the Earth's Growth. In: Dynamics of interacting geospheres. Institute of Geosphere Dynamics RAS, Moscow, pp 217–223 (in Russian)
- Pechernikova GV (2005) Time of the Earth's growth. *Dokl Earth Sci* 401A(3):409–412
- Pechernikova GV, Davidenko IW (2003) Estimations of axial moment of the growing Earth. Large Meteorite Impacts. III International Conference, #4015
- Pechernikova GV, Vityazev AV (1996) Statistical model of Earth-Moon coaccretion and macroimpacts. *Lunar Planet Sci XXVII*. LPSI, Houston, pp 1213–1214
- Pechernikova GV, Vityazev AV (1998) Exchange of material during formation of the Earth and Moon. International Conference Origin of the Earth and Moon, Monterey, CA, p 31
- Peck WH, Valley JW, Wilde SA, Graham CM (2001) Oxygen isotope and rare elements in 3.3 to 4.4 Ga zircons: Ion microprobe evidence for high $\delta^{18}\text{O}$ continental crust and oceans in the Early Archean. *Geochim Cosmochim Acta* 65(22):4215–4229
- Safronov VS (1969) Evolution of the protoplanetary cloud and the formation of the Earth and planets. Nauka, Moscow, p 244 (in Russian) [NASA Tech. Transl. F-677, Washington, DC, 1972]
- Safronov VS, Vityazev AV (1985) Origin of the solar system. Soviet Scientific Reviews, Section E. Astrophysics and Space Physics Reviews Syunyaev R (ed) Harwood Academic Publishers, 4:1–98
- Schoenberg R, Kamber BS, Collerson KD et al (2002) New W isotope evidence for rapid terrestrial accretion and very early core formation. *Geochemica et Cosmochemica Acta* 66(17):3151–3160
- Teterev AV, Nemtchinov IV, Rudak LV (2004) Impacts of large planetesimals on the early Earth. *Solar System Res* 38(1):39–48
- Vityazev AV, Pechernikova GV (1991) Late stages of accumulation and early evolution of the planets. Planetary Sciences (American and Soviet Research) Donahue TM, Trivers KK, Abramson DM (eds) National Academy Press, Washington, DC, pp 143–162
- Vityazev AV, Pechernikova GV (1996) Early differentiation of the composition of the Earth and the Moon. *Izvestiya, Physics of the Earth* 32(6):3–16

- Vityazev AV, Pechernikova GV (2003) Origin of geospheres: new results and remaining problems. In: Geophysical processes in the lower and upper shells of the Earth. IDG RAS, Moscow, pp 13–25 (in Russian)
- Vityazev AV, Pechernikova GV, Bashkirov, AG (2003a) Accretion and differentiation of terrestrial protoplanetary bodies and Hf-W chronometry. *Lunar Planet Sci XXXIV*. LPSI, Houston. #1656
- Vityazev AV, Pechernikova GV, Bashkirov AG (2003b) Early accretion and differentiation of protoplanetary bodies and Hf-W chronometry. *Large Meteorite Impacts III*. #4035
- Vityazev AV, Pechernikova GV, Bashkirov AG (2005) “Missing Xenon” problem and climate of the early Earth. *Lunar Planet Sci XXXVI*. LPSI, Houston. #1719
- Vityazev AV, Pechernikova GV, Safronov VS (1990) The terrestrial planets: origin and early evolution. Nauka, Moscow, p 296 (in Russian)
- Wetherill GW (1985) Occurrence of giant impacts during the growth of the terrestrial planets. *Science* 228:877–879
- Yin QZ, Jacobsen SB, Yamashita K et al (2002) A short time scale for terrestrial planets formation from Hf-W chronometry of meteorites. *Nature* 418:949–952
- Zetter JI Vityazev AV (1996) Experiment and differentiation of chondritic bodies. Rickman H, Valtonen MJ (eds), *Worlds in interaction: small bodies and planets of the Solar System*. Kluwer Academic Publishers, Norwell, MA, pp 474–480; *Earth, Moon, and Planets* 72(1–3)

INDEX

- Ablation, 259, 260
Acid rains, 217
Acoustic gravity waves, 148, 218, 236
Acoustic signals, 149
Acoustic system, 148
Active Geophysical Rocket Experiments, 328
Advective motion, 341
Aerial shock waves, 229
Aerodynamic forces, 10
Air-blast, 16
Alfven velocity, 314, 322
Aluminium jet, 328
Alvarez, Luis, 1
ANEOS equation of state, 62, 269, 293
Angara River, 232
Annealing of meteorite samples, 340
Annealing of minerals, 245
Anomalies of elements and isotopes
 in peat, 242
Anomalous atmospheric phenomena, 235, 236
Antipodal point, 216, 217, 219
Apollo lunar samples, 268
Apparent strength, 145
Arago neutral polarization points, 234
Archean, 175, 187
Artificial air cloud, 328, 329
Asteroidal hypothesis, 259
Asteroids, 120
 2002 EM7, 5
 99942 Apophis, 5
 Eros, 61
 Gaspra, 92
 Hermes, 5
 Ida, 92
 Itokawa, 57, 92
 Mathilde, 7, 61, 92, 244
 Toutatis, 5
Atmosphere, 9
 composition, 348
 density, 9
 fluctuation, 348
 temperature, 348, 349
Atmospheric darkening, 207
Atmospheric winds, 239
Auroral phenomena, 238
Australasian strewn field, 272
Australian-Asian tektites, 268
Australites, 267

Baikonur cosmodrome, 238
Ballistic motion, 270
Barents Sea, 293
Barium vapor streams, 325
¹⁰Be, 271, 272
Benesov bolide, 135
Bishop's rings, 234
Block structure, 33
Bodaibo, 232
Bohemia, 273
Bolides, 131
Bottom relief, 41
Brazil, 228
Breakup, 9
Brightness, 233
Bronze Age, 228
Buried explosions, 31, 56
Butterfly-shaped tree fall pattern, 240

Carbon, 208
Carbonaceous chondrites, 242, 243
Carbonates terrestrial, 340, 346
Carbon isotopes ¹³C, ¹⁴C, 243
Casualties, 19, 23
Cenomanian-Turonian boundary, 208
Central European tektite strewn field, 271
Charcoal, 207
Chemical energy of explosives, 327, 328
Chemical plants, 52
Chronology

- lunar impact craters, 93
 - terrestrial impact craters, 109
- Clinopyroxenites, 279
- Clouds, 23, 46
- CO₂, 46
- Coastal areas, 39, 40
- Collapse
 - transient cavity, 106, 173, 174, 178, 179, 181, 185, 190
 - underwater bench, 185
- Colorful sunsets, 234
- Comet(s), 117
 - Borelly, 61, 244
 - C/2000 A2, 8
 - Encke, 126
 - Halley, 60
 - Jacobini-Zinner, 60
 - Shoemaker-Levy 9, 68, 236
 - Tempel 1, 61
 - Wild-2, 61
- Comet albedos, 120
- Cometary bodies, 118, 340
 - material, 339, 347
- Cometary hypothesis, 258
- Comet fading time, 119
- Comet nuclei, 118, 120
- Comet population, 119
- Concrete dams, 54
- Cosmic rays, 124, 281, 320
- Criosphere, 346
 - early, 347, 348
- Critical ionization velocities, 330
- Crown fires, 210
- CSS (Catalina Sky Survey), 2
- Cumulative distribution of fragments, 270
- Cumulative explosive devices, 325
- Cumulative number of impacts, 154
- Czech Republic, 274

- Daily solar currents, 237
- Dangerous objects, 3, 19, 52, 54
- Darwin, Charles, 267
- Debris, 124, 126
- Deceleration, 9, 13
- Deep Impact Mission, 61, 64, 65
- Deep water, 34, 37
- Deflection, 55
- Deformation, 11
- Degassing, 340
- Desert Network, 131
- Deserts, 49
- Destruction of dams, 54

- Deuterium, 243
- Devastation area, 18, 229
- Diamagnetic cavern, 329
- Diamagnetic cavity, 329
- Differentiation, 340
 - primary, 340, 348
- Dinosaurs, 1, 72, 313
- Disruptive collisions, 124
- Distal ejecta, 267, 297
- Don Quijote mission, 66
- Double craters, 7
- Drag coefficient, 138, 247
- Dunite, 281
- Dust, 45
- Dust spreading, 235
- Dusty mantle, 119, 124
- Dynamic mass, 139

- Early Earth, 333, 346
- Early Mars, 347, 348
- Early upper geospheres, 334
- Earth's
 - accumulation, 336, 342, 348
 - "tail", 348
 - atmosphere, 333, 344
 - inert gases, 345
 - modern, 346
 - primitive, 339, 340, 347
 - mass, 349
 - pressure, 349
 - core, 333, 339, 341, 345
 - crust
 - evolution, 333
 - formation, 333, 336, 340
 - growth, 333, 335, 341, 342, 348
 - early stage, 333, 334, 335, 336, 348
 - final stage, 333, 343, 348
 - main stage, 335
 - rate, 334, 334
 - time, 334, 335
 - primitive, 333, 339, 340, 342, 344, 347
 - hydrosphere
 - modern, 346
 - primitive, 333, 339, 340, 344
 - magnetic field, 314, 328
 - mantle, 333, 339, 340, 341, 345
 - mass, 336, 337
 - mean density, 334, 335
- Earthquake(s), 29, 34, 39, 40
- Earthquake magnitude(s), 29, 74
- Ejecta, 25, 44, 59, 164, 172, 176, 180, 183, 191, 268

- Ejecta blanket, 26, 298
- Ejecta curtain, 41, 303
- Ejecta motion, 269
- Ejecta return, 216
- Ejection, 346
 - efficiency, 347
 - of impact material, 340, 347
 - to geocentric orbits, 339
- Electromagnetic impulse, 66
- Energy
 - balance, 340
 - equipartition, 337
 - flux, 342
 - gravitational, 340
 - differentiation, 341
 - of impact, 340, 342, 343
 - kinetic, 334
 - potential, 342
 - of random motion, 335
 - of short-living isotopes, 340
 - sources, 341
- Energy–frequency distribution, 156
- Eocene-Oligocene boundary, 208
- Epicenter zone, 230
- Erosion, 166, 292, 304
- ESA, 61, 66
- Escape, 216, 283, 313
- Europe, 55, 236
- Explosive type generators, 325
- Eyewitness reports, 212, 230

- F₂ layer of the ionosphere, 320
- Fading of comets, 119
- Fading rate, 119
- Falling bodies, 336, 337, 343
 - composition, 348
 - flow, 342, 346
 - frequency, 333, 338, 342, 348
 - masses, 335
 - mass spectrum, 333, 348
 - velocity spectrum, 333, 348
- Feeding zone, 334, 335, 336, 337, 342
 - expanding, 335
- Ferromagnetic material, 245
- Final crater, 26
- Fire(s), 22
- Fireball, 16, 23, 210
- Fire propagation, 211
- Flares, 154
- Flattened trees, 210
- Fluxus experiments, 328
- Focused solar light, 56

- Fragmentation, 41, 58, 59, 134
- Fragment–vapor cloud, 135

- Galileo spacecraft, 70
- Gas hydrates, 345, 346, 347
 - in the early earth, 346
 - layers, 347, 348
- Geo-chronometer, 333
 - Hf-W, 336, 348
 - U-Pb, 348
- Geomagnetic cavern, 322
- Geomagnetic effect, 237
- Geomagnetic field, 68
- Geophysical experiments, 325
- Ghana, 274
- Global fire, 207, 215, 223
- Grady-Kipp distribution, 278
- Gravity-dominated regime, 62, 63
- Grazing impact, 213
- Greenland bolide, 151
- Ground telescopes, 70, 229
- Ground water, 210
- Growing planet (Earth), 333, 334, 335, 336, 337, 338, 339, 342, 343
 - root-mean-square velocity, 337
- Gullies, 292, 304
- Gyro radius of ions, 330

- Hadean, 334, 340
- Halley-type comets, 117, 122
- Hayabusa mission, 57
- Hazard mitigation, 21
- Heat transfer coefficient, 212
- High-velocity jets, 325
- Hiroshima, 19, 23
- Hubble Space Telescope, 70
- Hydrodynamic instabilities, 255
- Hydroelectric dams, 52

- Icy bodies, 17, 35, 233, 316
- Ignition, 22, 23, 25, 210, 215
- Impact crater(s)
 - accumulation rate, 109, 165
 - formation, 35
 - mode of formation
 - strength/gravity, 105, 106, 110
 - morphology
 - simple/complex, 105, 106, 168
 - lunar
 - Oriente basin, 107
 - terrestrial

- Arkenu, 50
- Barringer Meteorite Crater, 229
- Bosumtwi, 271, 275
- Chesapeake Bay impact structure, 271
- Chicxulub, 180, 208, 217
- Elgygytgyn, 27, 283
- Eltanin impact structure, 293, 304, 307
- Henbury, 229
- Kaali, 10
- Kamensk, 292, 304
- Kara, 27
- Lockne, 292, 293, 299
- Macha crater group, 229
- Mjølnir, 293
- Popigai, 27, 175
- Puchezh-Katunki, 172
- Ries, 27, 271, 272
- Steinheim, 273
- Sterlitamak, 164
- Sudbury, 193
- Ust-Kara, 27
- Vredefort, 187
- Wabar, 51
- Venusian
 - Mead, 165
 - Sascia, 172
- Impact frequency, 103, 111, 166, 169
- Impact glasses, 271
- Impact melt, 177, 181, 183, 190, 194
- Impact probability, 99, 102, 103
- Impact rate, 93, 102
- Impacts into water, 39
- Impacts of large bodies, 348
- Impact velocity, 102–104
- Indochina, 271
- Infrasound waves, 148
- Injuries, 24
- Innisfree meteorite, 132
- Integral luminous efficiency, 140
- Internal waves, 222
- International agreements, 56
- International laws, 60
- Ionization equilibrium, 322
- Ionization potential, 322
- Ionosphere, 67, 238, 314
- Ionospheric current system, 238
- Ionospheric disturbances, 315
- Ionospheric effects, 315
- Iridium, 207, 242
- Irkutsk, 237
- Isothermal atmosphere, 218
- Ivory Coast strewn fields, 271
- Ivory Coast tektites, 271, 275
- Jena, 237
- Jet engine, 56
- Jiotto spaceship, 60
- Jovian moons, 122
- Jupiter, 68
- Jupiter-family comets, 117
- K/T (Cretaceous/Tertiary) boundary, 44, 45, 207, 208, 223
- K/T event, 25
- Kamenskoe, 232
- Kelvin-Helmholtz instabilities, 11, 14, 73
- Kezhma, 232
- Kinetic energy of a jet, 328
- Kinetic weapon, 56
- Krakatau, 218
- Kuiper belt, 118
- Kulik, Leonid, 212
- Laboratory modeling experiments, 239
- Lake Bosumtwi, 274
- Lamb wave, 218, 219
- Landing speed, 57
- Large craters, 27
- Laser, 56
- Late heavy bombardment, 93, 95
- Lateral velocity, 137
- Layers
 - mixing, 334, 342
 - average thickness, 344
 - near-surface, 334, 347
- Lena River, 232
- Libyan desert glass, 50
- Lifetimes of minor bodies, 127
- Lifetimes of small comets, 126
- Light curves, 133
- Light flashes, 151
- Lightning, 210, 222, 230
- Light phenomena, 231
- Light twilights, 234
- LINEAR (Lincoln Laboratory's Near-Earth Asteroid Research), 2
- Lithosphere, 34, 187
- LONEOS (Lowell Near-Earth Objects Survey), 2
- Long-period comets, 117, 122, 127
- Lost City meteorite, 132
- Luminous efficiency, 137
- Lunar crust, 283

- Lunar meteorites, 267, 283
- Lusatia, 273

- Mach number, 47
- Magnetic diffusion, 328
- Magnetic disturbances, 314, 322
- Magnetic field, 322
- Magnetic field variations, 238
- Magnetic storm, 315
- Magnetic susceptibility, 245
- Magnetodynamic disturbances, 238
- Magnetohydrodynamic waves, 68, 328
- Magnetosphere, 67, 238, 314
- Malyshevka, 232
- Manhattan Project, 56
- Mantle, 123
- Mars, 49, 269, 278, 283
- Martian atmosphere, 277
- Martian meteorites, 268, 280
- Mass accumulation, 335
- Mass extinctions, 180, 207, 208, 218, 312
- Matter in the feeding zone, 335
 - condensed, 335
 - density, 334
 - surface density, 335, 336
- Mesosphere, 44
- Meteorite Committee, 241
- Meteorite Neuschwanstein, 132
- Meteorites
 - achondrites, 339
 - chondrites, 339, 346
 - carbonaceous, 339, 340, 345, 346
 - Allende, 340, 348
 - ordinary, 339, 340, 346
 - Jilin, 340
 - enstatites, 339, 345
 - SNC, 268, 276, 339
- Meteoroid(s), 132
- Meteoroid disintegration, 253
- Meteoroid explosion, 231
- Meteoroid strength, 142
- Meteors, 58, 131, 233, 260
- MHD-dynamo, 325
- MHD equations, 321
- MHD simulations, 67, 321
- Microbes transfer, 284
- Microorganism transfer, 284
- Microspherules, 241
- Microtektites, 267
- Microwave beams, 56
- Mineral resources
 - diamonds, 177
 - gold, 193
 - oil, 185
- Modeling of the Tunguska event, 249
- Moho boundary, 28, 33
- Moldavites, 273
- Moon, 229, 268, 283
- Moravia, 273
- Morávka meteorite, 132
- Morphologic anomalies, 246
- Morphometric anomalies, 246
- Mortality, 18, 19
- Multiphase hydrodynamics, 269
- Muong Nong tektites, 271
- Mutative changes, 246

- Nagasaki, 18, 19, 23
- NASA, 1, 60, 61
- NEAR (Near Earth Asteroid Rendezvous), 61
- Near-Earth Asteroids, 110, 112
- Near-Earth Objects, 4, 272
- NEAT(Near-Earth Asteroid Tracking), 2
- Neutron, 55
- Nitrogen isotope, 244
- Nizhnyaya Tunguska River, 232
- Noctilucent clouds, 235, 236
- Nonuniform atmosphere, 20
- North American strewn field, 271
- North Star Active Plasma Experiment, 328
- Nuclear explosions, 18
- Nuclear power stations, 52, 53
- Nuclear tests, 4, 24, 29, 40, 211
 - Blanca, 30
 - CANNIKIN, 29, 30
 - Novaya Zemlya, 42, 258, 316
 - Rainier, 29
- Nuclear waste depositaries, 52
- Numerical methods, 11
 - free-Lagrangian method, 11
- Numerical models
 - ablating piston, 138
 - approximate models, 17
 - liquid-like fragmentation, 135
 - pancake model, 10
 - progressive fragmentation, 137
 - sand bag, 11
 - semianalytical models, 248
- Numerical simulations, 11
- Nusselt number, 341

- Oblique impact, 26
- Ocean floor, 291

- Ocean(s), 291
 Oort cloud, 118
 Optical anomalies, 234, 236
 Orbital evolution, 119, 127
 Origin of the Solar system, 333
 Overpressure, 18, 20
 Ozone, 46
- Palladium, 242
 Peat bogs, 242
 Peat columns, 242
 Peat layers, 242
 Peekskill, 132
 Permafrost, 242, 244, 261
 Phanerozoic, 213
 Photographic bolide network, 131
 Physical theory of meteors, 137
 Pine three-needle tufts, 246
 Planetary cosmogony, 334
 Planetesimals, 334, 339
 differentiation, 336
 large, 339
 mass spectrum, 334, 336
 melting, 336
 relative velocity, 335, 336, 337,
 341, 342
 velocity spectrum, 334, 339
 Plasma jet, 330
 Plasma-jet interaction, 330
 Plasma physics, 325
 Plume, 15, 25, 67, 73, 234, 255, 313, 328
 Podkamennaya Tunguska River, 227
 Population, 19, 119, 127
 Porosity, 7
 Prairie Network, 131, 132
 Precursor, 47, 49
 Preobrazhenka, 232
 Preplanetary bodies
 averaged composition, 339
 bulk composition, 339
 mass distribution, 334, 336, 337, 339,
 342, 347
 upper limit, 335, 336
 mean mass, 337, 339
 time of growth, 336
 Preplanetary disk, 333
 Pribram meteorite, 132
 Progressive fragmentation, 136
 Pulverization of, 59
 P-waves, 29
- Radar observations, 5, 6, 68, 91
 Radiance exposure, 22
 Radiation, 23, 24, 56
 Radiation efficiency, 24
 Radiation flux, 214, 216, 249
 Radiation impulse, 24
 Radiation intensity, 137
 Radiation passband, 138, 141
 Radiation pressure, 56
 Radiation spectrum, 138
 Radiative mass, 139
 Radiative radius, 139
 Radioactive waste depository, 53
 Radioactivity leakage, 54
 Radio communications, 238
 Rare-earth elements, 242
 Rayleigh-Taylor instabilities, 11, 250
 Regional fires, 223
 Regolith, 284
 Relict signals from Hadean, 334
 Relict zircons, 344, 348, 349
 Residual magnetization, 245
 Role of large bodies, 334, 335, 336, 341
 Rosetta mission, 61
 Rotation, 7
 Roughness number, 39
 Rubble piles, 7
- Satellite Network, 133
 Scaling law, 26, 42, 105, 106
 coupling parameter, 181
 porous/nonporous, 105, 106
 Sea(s), 291
 Sedimentary rocks, 294
 Seismic efficiency, 30
 Seismic energy, 29
 Seismic magnitude, 32
 Seismic shaking, 186
 Seismic waves, 28, 33, 54, 237
 Seismogenic zone, 34
 Shallow sediments, 303
 Shallow water, 308
 Shape-charged devices, 325
 Shergottite, 268, 280, 282
 Shock waves, 15
 Short-living isotopes, 336, 340, 341
 ²⁶Al, 336, 348
 ⁶⁰Fe, 348
 Short-period comets, 117, 121
 Short-period ionospheric disturbances, 316
 Sikhote-Alin meteorite, 10, 228
- Quench of fire, 213

- Silica, 268
 Size-frequency distribution, 118, 121, 122
 asteroids, 110, 112
 craters, 92, 95, 101, 105
 Small comets, 123, 124
 Small cosmic bodies, 3, 51, 55, 57, 60, 73
 Smoky trail, 234
 Solar halos, 234
 Solar radiation, 342
 Solar sail, 56
 Solar wind, 341
 Soot, 207
 SOVA code, 11, 269, 293, 316
 Spacewatch program, 2
 Sphagnum moss, 242, 244
 Spherical explosion, 15
 Stardust spaceship, 61
 Statistical strength theory, 142
 Stokes drag, 270
 Stratopause, 44
 Stream of fragments, 13
 Strength of cosmic bodies, 9
 Strewn field, 10
 Strontium vapor streams, 325
 Sulfur aerosols, 217
 Sun-grazing comets, 118, 126
 Superbolides, 133
 Surface waves, 28
 S-waves, 29
 System of isotopes
 Hf-W, 334, 348
 ^{129}I - ^{129}Xe , 346, 348
 ^{244}Pu - ^{132}Xe , 346, 348

 Taganov's criterion, 48
 Tagish Lake meteorite, 132
 Tashkent, 237
 Tectonic energy, 34
 Tektites, 267
 Tektite strewn field, 268
 Terrestrial aerosols, 243
 Terrestrial planets, 336
 Tertiary sands, 274
 Thermal burn, 240
 Thermal layer, 47, 49
 Thermal radiation, 46, 210, 211
 Thermoluminescence, 245
 Tiflis, 237
 Tillotson equation of state, 293, 294
 Tracer particles, 269
 Trajectory azimuth, 232

 Trajectory inclination, 232
 Transient cavity, 105, 106, 179, 199
 Transient crater, 26, 35, 44, 295
 Tree resin, 242
 Tree rings, 242
 Tropopause, 44
 Tsunami, 34, 37, 38, 291
 Tunguska cosmic object, 227
 Tunguska event, 3, 22, 42, 66, 73, 126, 209,
 227, 316
 Two-phase hydrodynamic, 278

 Underground explosions, 28
 Underwater crater, 291, 292, 308
 Underwater explosion, 35, 37

 Van Allen radiation belts, 314, 325
 Vanavara, 231
 Vapor-air jet, 250
 Vapor layer, 138
 Vega spaceship, 60
 Vertical impacts, 250, 302, 321
 Villalbeto de la Peña meteorite, 132
 Vitim bolide, 152
 Volatiles, 339, 340, 345

 Wake, 12, 13, 315
 Water basin, 300
 Water crater, 318
 Water pools, 346, 348
 Water surge, 295
 Water wave, 35
 Waveguide modes, 32
 Wave height, 41

 Xenon, 346
 missing Xe problem, 345
 pleiad of nine isotopes, 345
 primary, 347
 relict, 344
 X-rays, 55

 Yarkovsky effect, 6
 Yenisei River, 234
 Yucatan peninsula, 180, 186

 Zigzags of the Tunguska cosmic object, 234
 Zircon, 344, 348